

RADC-TR-82-335
Final Technical Report
January 1983



POLARIZATION NUL CHARACTERISTICS OF SIMPLE TARGETS

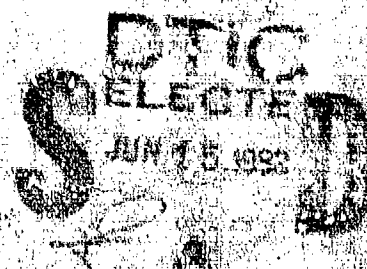
Sperry Research Center

**H. Mieras, R. M. Barnes, G. M. Vachula, J. W. Buchnam, C. L. Bennett
and Wolfgang A. Boerner**

APPROVED FOR PUBLIC RELEASE DISTRIBUTION UNLIMITED

This effort was funded totally by the Laboratory Directors' Fund

**ROME AIR DEVELOPMENT CENTER
Air Force Systems Command
Griffins Air Force Base, NY 12441**



AD A129303
DTIC FILE COPY

1

This report has been reviewed by the E. Public Affairs Office (PA) and is releasable to the National Technical Information Service (NTIS). At NTIS it will be releasable to the general public, including foreign nations.

RADC-IR-87-335 has been reviewed and is approved for publication.

APPROVED:

Daniel L. Tauronky
DANIEL L. TAURONKY
Project Engineer

APPROVED:

Frank J. Barr
FRANK J. BARR, Technical Director
Surveillance Division

FOR THE DIRECTOR:

John P. Bess
JOHN P. BESS
Acting Chief, Plans Office

If your address has changed or if you wish to be removed from our mailing list, or if the information is no longer relevant to your organization, please notify RADC (OCOS), Griffiss AFB, NY 13446-5000, or the nearest RADC office.

Do not return to us any of this report unless we request it. If you have a specific document required that is not included in this report, please contact the nearest RADC office.

UNCLASSIFIED

SECURITY CLASSIFICATION OF THIS PAGE (When Data Entered)

REPORT DOCUMENTATION PAGE		READ INSTRUCTIONS BEFORE COMPLETING FORM
1. REPORT NUMBER RADC-TR-82-335	2. GOVT ACCESSION NO. A129303	3. RECIPIENT'S CATALOG NUMBER
4. TITLE (and Subtitle) POLARIZATION NULL CHARACTERISTICS OF SIMPLE TARGETS		5. TYPE OF REPORT & PERIOD COVERED Final Technical Report 26 Aug 81 - 25 Aug 82
		6. PERFORMING ORG. REPORT NUMBER SRC-CR-82-33
7. AUTHOR(s) H. Mieras J.N. Buchnam R.M. Barnes C.L. Bennett G.M. Vachula Wolfgang M. Boerner		8. CONTRACT OR GRANT NUMBER(s) F30602-81-C-0254
9. PERFORMING ORGANIZATION NAME AND ADDRESS Sperry Research 100 North Road Sudbury MA 01776		10. PROGRAM ELEMENT, PROJECT, TASK AREA & WORK UNIT NUMBERS 61101F LDFF20C1
11. CONTROLLING OFFICE NAME AND ADDRESS Rome Air Development Center (OCDS) Griffiss AFB NY 13441		12. REPORT DATE January 1983
		13. NUMBER OF PAGES 254
14. MONITORING AGENCY NAME & ADDRESS (if different from Controlling Office) Same		15. SECURITY CLASS. (of this report) UNCLASSIFIED
		15a. DECLASSIFICATION/DOWNGRADING SCHEDULE N/A
16. DISTRIBUTION STATEMENT (of this Report) Approved for public release; distribution unlimited		
17. DISTRIBUTION STATEMENT (of the abstract entered in Block 20, if different from Report) Same		
18. SUPPLEMENTARY NOTES RADC Project Engineers: Daniel L. Tauroney (OCDS) David Stein, Capt, USAF (COTA) This effort was funded totally by the Laboratory Directors' Fund		
19. KEY WORDS (Continue on reverse side if necessary and identify by block number) Polarization Null Stokes Parameters Polarization Maximum Poincaré Sphere Simple Compound Targets ECM w/Polarization Single Scattering Centers EUM w/Polarization Target Discrimination		
20. ABSTRACT (Continue on reverse side if necessary and identify by block number) The polarization null and maximum characteristics of simple compound targets are studied; with the objective of assessing the applicability of these concepts to target discrimination. The polarization characteristics of single scattering centers are derived in theoretical detail and shown to be highly distinctive according to scattering center type. However, the dynamic behavior of the characteristics with changing aspect for compound targets is shown to be very complex. It is concluded that these concepts		

UNCLASSIFIED

SECURITY CLASSIFICATION OF THIS PAGE (When Data Entered)

UNCLASSIFIED

SECURITY CLASSIFICATION OF THIS PAGE(When Data Entered)

are not generally useful for target discriminations if an extended target is viewed at a single frequency. Extensions are suggested to make the approach useful.

Accession For	
NTIS GRA&I	<input checked="checked" type="checkbox"/>
NTIC TAB	<input type="checkbox"/>
Unannounced	<input type="checkbox"/>
Justification	
By	
Distribution/	
Availability Codes	
Dist	Avail and/or Special



UNCLASSIFIED

SECURITY CLASSIFICATION OF THIS PAGE(When Data Entered)

TABLE OF CONTENTS

<u>Section</u>	<u>Page</u>
1 INTRODUCTION	1
2 CHARACTERIZATION OF POLARIZATION PROPERTIES OF SIMPLE TARGETS	5
2.1 Representation of Polarization States	6
2.2 Polarization Transformations	10
2.3 The Polarization Scattering Matrix, Mueller Matrix, and Canonical Forms	11
2.4 Polarization Nulls and Maxima	15
2.5 Nulls and Maxima for General Symmetric Target	22
2.6 Simple Approximate Descriptions of Scattering Characteristics: Single-Bounce, Double-Bounce, Dipole.	26
2.7 Dynamic Behavior of Nulls and Maxima for Dumbbell Targets	28
2.8 Depolarization Due to Averaging Over a Scintillation Period	34
2.9 Co-Pol Null Locus for Right-Circular Cylinder	35
2.10 Extension of Previous Results to a Non-Diagonal Scattering Matrix	49
2.11 Effect of Polarization Calibration Errors on Null Measurements	51
3 COMPUTED POLARIZATION PROPERTIES OF SIMPLE AIRCRAFT MODELS	54
3.1 Description of the Aircraft Models	56
3.2 Computed Aircraft Characteristics at 0° Elevation	59
3.3 Computed Aircraft Characteristics at 10° Elevation	80
3.4 Average Polarization Characteristics of Aircraft Models	92
4 MEASURED POLARIZATION PROPERTIES OF SIMPLE AIRCRAFT MODELS	97
4.1 Description of Dual-Polarized Radar	97
4.2 Measurement of Stokes Vectors	108
4.3 Polarization Calibration	111
4.4 Other Concerns	113
4.4.1 System	113
4.4.2 Geometry	114
4.4.3 Target	116
4.4.4 Clutter	117
4.5 Measurement Results	119
4.6 Comparison of Measured and Calculated Results	152
5 EFFECTS OF NOISE, CHAFF, AND JAMMING OF POLARIZATION NULLS	162
5.1 Interference Effects	162
5.1.1 Return Model	162
5.1.2 Fisher Information Matrix for Estimating ν and γ	166

TABLE OF CONTENTS (Continued)

<u>Section</u>	<u>Page</u>
5.1.3 Effects of Chaff and Jamming Using Nominal Polarization Sets	169
5.2 ECCM Techniques	170
5.2.1 Example Case	170
5.2.2 Calculation of ECCM Effectiveness for Six Jammer Polarizations	178
6 SUMMARY AND CONCLUSIONS	180
7 REFERENCES	182
8 APPENDICES	184
8.1 Unitary Transformation Properties	184
8.2 The Elementary Transformations of Polarization and Stokes Vectors	186
8.3 Symmetry Relations for Scattering Matrix and Transmit-Receive Conventions	190
8.4 Diagonalization of Scattering Matrix and Eigenvalues	193
8.5 Equal Area Projection for Polarization Chart	196
8.6 Modeled Response of Right-Circular Cylinder	196
8.7 Modeled Response of Fins	203
8.8 Multiple Scattering — Aircraft Models	208
8.9 Fresnel Region Responses	208
8.10 Relation Between Symmetric PSM and Six Power Measurements	212
8.11 Relation Between PSM and Twelve Power Measurements	214
8.12 Historical Development of Radar Polarimetry	219

LIST OF ILLUSTRATIONS

<u>Figure</u>	<u>Title</u>	<u>Page</u>
1	Normalized polarization ellipses for right-sense polarization.	8
2	Normalized Poincaré sphere.	8
3	Great circle cut ($S_2 = 0$) on Poincaré sphere, showing nulls and maxima for canonical (positive real diagonal) scattering matrix.	19
4	Polarization nulls and maxima for plane symmetric targets for various values of parameters ν , γ . One hemisphere shown. Note: shown for $ a_{HH} > a_{VV} $. For $ a_{VV} > a_{HH} $ turn disc upside down.	24
5	Copol null locus for one scintillation period of dumbbell target on equal area polarization chart.	30
6	Copol null loci for one scintillation period of rotating dumbbell target for various dumbbell parameters.	31
7	Copol maxima as function of scatterer phase, corresponding to cases of figure 6.	33
8	Backscatter RCS, HH and VV, of right circular cylinder, $L/D = 5$ at $ka = 2.4$.	36
9	Parameters m , 2ν , and 2γ of scattering matrix vs. aspect, for RCC with $L/D = 5$, at $ka = 2.4$.	38
10	Partial copol null locus for RCC, $L/D = 5$, at $ka = 2.4$. Aspect change 35° to 52.5° (ticks at 2.5° steps).	40
11	Backscatter RCS, HH and VV, of right circular cylinders at $ka = 2.4$; (a) $L/D = 5$, (b) $L/D = 10$.	42
12	Parameters m , 2ν , and 2γ of scattering matrix vs. aspect for RCC with $L/D = 5$ and for RCC with $L/D = 10$; at $ka = 2.4$.	43
13	Copol null loci over various aspect intervals. Left column: RCC with $L/D = 5$, right column RCC with $L/D = 10$; at $ka = 2.4$.	44
14	Parameters m , 2ν , and 2γ vs. aspect for RCC, $L/D = 10$ at $ka = 5.24$ (left column) and $ka = 8.15$ (right column).	45
15	Copol null loci over various aspect intervals for RCC, $L/D = 10$; at $ka = 5.24$ (left column) and at $ka = 8.15$ (right column).	46
16	Copol null locus over aspect change $\alpha = 50^\circ$ to 60° ; for RCC, $L/D = 10$; at $ka = 5.24$; showing spiral behavior.	48
17	Copol loci, showing effect of error in VV channel of 10% magnitude, 30° phase. Compare this with figure 6.	53
18	Target models, with approximate full scale dimensions.	57
19	Polarization characteristics vs. aspect of model 1; $ka = 2.4$; $\theta = 0^\circ$.	60
20	Polarization characteristics vs. aspect of model 1 wings alone; $ka = 2.4$; $\theta = 0^\circ$.	62

LIST OF ILLUSTRATIONS (Continued)

<u>Figure</u>	<u>Title</u>	<u>Page</u>
21	Polarization characteristics vs. aspect of model 2 wings alone; $k_a = 2.4$; $\theta = 0^\circ$.	63
22	Polarization characteristics vs. aspect of model 1 and model 2; $k_a = 2.4$; $\theta = 0^\circ$.	64
23	Polarization characteristics vs. aspect of cylinder, Scale A; $k_a = 5.24$; $\theta = 0^\circ$.	66
24	Polarization characteristics vs. aspect of model 1, Scale A; $k_a = 5.24$; $\theta = 0^\circ$.	67
25	Polarization characteristics vs. aspect of model 2, Scale A; $k_a = 5.24$; $\theta = 0^\circ$.	68
26	Polarization characteristics vs. aspect of model 3, Scale A; $k_a = 8.14$; $\theta = 0^\circ$.	69
27	Polarization characteristics vs. aspect of cylinder, Scale B; $k_a = 8.14$; $\theta = 0^\circ$.	70
28	Polarization characteristics vs. aspect of model 1, Scale B; $k_a = 8.14$; $\theta = 0^\circ$.	71
29	Polarization characteristics vs. aspect of model 2, Scale B; $k_a = 8.14$; $\theta = 0^\circ$.	72
30	Polarization characteristics vs. aspect of model 3, Scale B; $k_a = 12.8$; $\theta = 0^\circ$.	73
31	Polarization characteristics vs. aspect of model 1, Scale C; $k_a = 12.8$; $\theta = 0^\circ$.	74
32	Polarization characteristics vs. aspect of model 2, Scale C; $k_a = 12.8$; $\theta = 0^\circ$.	75
33	Polarization characteristics vs. aspect of model 3, Scale C; $k_a = 18.6$; $\theta = 0^\circ$.	76
34	Polarization characteristics vs. aspect of model 1, Scale D; $k_a = 18.6$; $\theta = 0^\circ$.	77
35	Polarization characteristics vs. aspect of model 2, Scale D; $k_a = 18.6$; $\theta = 0^\circ$.	78
36	Polarization characteristics vs. aspect of model 3, Scale D; $k_a = 27.9$; $\theta = 0^\circ$.	79
37	Copol max polarization vs. aspect of model 1 and model 2; $k_a = 2.4$; $\theta = 10^\circ$.	82
38	Polarization characteristics vs. aspect of model 1 and model 2; $k_a = 2.4$; $\theta = 10^\circ$.	83
39	Copol max polarization vs. aspect of cylinder, Scale A; $k_a = 5.24$; $\theta = 10^\circ$.	84

LIST OF ILLUSTRATIONS (Continued)

<u>Figure</u>	<u>Title</u>	<u>Page</u>
40	Polarization characteristics vs. aspect of cylinder, Scale A; $ka = 5.24$; $\theta = 10^\circ$.	85
41	Copol max polarization vs. aspect of model 1, Scale A; $ka = 5.24$; $\theta = 10^\circ$.	86
42	Polarization characteristics vs. aspect of model 1, Scale A; $ka = 5.24$; $\theta = 10^\circ$.	87
43	Copol max polarization vs. aspect of model 2, Scale A; $ka = 5.24$; $\theta = 10^\circ$.	88
44	Polarization characteristics vs. aspect of model 2, Scale A; $ka = 5.24$; $\theta = 10^\circ$.	89
45	Copol max polarization vs. aspect of model 3, Scale A; $ka = 8.14$; $\theta = 10^\circ$.	90
46	Polarization characteristics vs. aspect of model 3, Scale A; $ka = 8.14$; $\theta = 10^\circ$.	91
47	Expected value of average polarization characteristics; cylinder, Scale A; $ka = 5.24$; $\theta = 0^\circ$.	93
48	Expected value of average polarization characteristics; model 1, Scale A; $ka = 5.24$; $\theta = 0^\circ$.	94
49	Expected value of average polarization characteristics; model 2, Scale A; $ka = 5.24$; $\theta = 0^\circ$.	95
50	Illustration of FMCW range bin system.	98
51	Dual polarized radar for measuring Stokes parameters.	99
52	SRC radar data acquisition system.	100
53	Power vs. range for clutter, noise, and targets.	103
54	Test geometry for polarization measurements.	104
55	Polyfoam support cone and pedestal.	104
56	Radar transmitter and antenna.	106
57	Radar receiver/signal processor.	106
58	Support pylon and target viewed from radar.	107
59	Two targets (Scales A and C) and cone tips.	107
60	Power due to noise and to support cone clutter.	115
61	Response of half-inch spheres (-41 dBsm).	118
62	Error in mean S+C due to clutter effects.	120
63	Measured Stokes parameters vs. aspect of cylinder, Scale A; $ka = 5.24$; $\theta = 0^\circ$.	124
64	Measured Stokes parameters vs. aspect of model 1, Scale A; $ka = 5.24$; $\theta = 0^\circ$.	125

LIST OF ILLUSTRATIONS (Continued)

<u>Figure</u>	<u>Title</u>	<u>Page</u>
65	Measured Stokes parameters vs. aspect of model 2, Scale A; $ka = 5.24$; $\theta = 0^\circ$.	126
66	Measured Stokes parameters vs. aspect of model 3, Scale A; $ka = 8.14$; $\theta = 0^\circ$.	127
67	Measured Stokes parameters vs. aspect of cylinder, Scale B; $ka = 8.14$; $\theta = 0^\circ$.	128
68	Measured Stokes parameters vs. aspect of model 1, Scale B; $ka = 8.14$; $\theta = 0^\circ$.	129
69	Measured Stokes parameters vs. aspect of model 2, Scale B; $ka = 8.14$; $\theta = 0^\circ$.	130
70	Measured Stokes parameters vs. aspect of model 3, Scale B; $ka = 12.8$; $\theta = 0^\circ$.	131
71	Measured Stokes parameters vs. aspect of model 1, Scale C; $ka = 12.8$; $\theta = 0^\circ$.	132
72	Measured Stokes parameters vs. aspect of model 2, Scale C; $ka = 12.8$; $\theta = 0^\circ$.	133
73	Measured Stokes parameters vs. aspect of model 3, Scale C; $ka = 18.6$; $\theta = 0^\circ$.	134
74	Measured Stokes parameters vs. aspect of model 1, Scale D; $ka = 18.6$; $\theta = 0^\circ$.	135
75	Measured Stokes parameters vs. aspect of model 2, Scale D; $ka = 18.6$; $\theta = 0^\circ$.	136
76	Measured Stokes parameters vs. aspect of model 3, Scale D; $ka = 27.9$; $\theta = 0^\circ$.	137
77	Measured Stokes parameters vs. aspect of model 1, Scale A; $ka = 5.24$; $\theta = 10^\circ$.	138
78	Measured Stokes parameters vs. aspect of model 2, Scale A; $ka = 5.24$; $\theta = 10^\circ$.	139
79	Measured Stokes parameters vs. aspect of model 3, Scale A; $ka = 8.14$; $\theta = 10^\circ$.	140
80	Measured Stokes parameters vs. aspect of model 1, Scale B; $ka = 8.14$; $\theta = 10^\circ$.	141
81	Measured Stokes parameters vs. aspect of model 2, Scale B; $ka = 8.14$; $\theta = 10^\circ$.	142
82	Measured Stokes parameters vs. aspect of model 3, Scale B; $ka = 12.8$; $\theta = 10^\circ$.	143
83	Measured Stokes parameters vs. aspect of model 1, Scale C; $ka = 12.8$; $\theta = 10^\circ$.	144

LIST OF ILLUSTRATIONS (Continued)

<u>Figure</u>	<u>Title</u>	<u>Page</u>
84	Measured Stokes parameters vs. aspect of model 2, Scale C; $ka = 12.8$; $\theta = 10^\circ$.	145
85	Measured Stokes parameters vs. aspect of model 3, Scale C; $ka = 18.6$; $\theta = 10^\circ$.	146
86	Measured Stokes parameters vs. aspect of model 1, Scale D; $ka = 18.6$; $\theta = 10^\circ$.	147
87	Measured Stokes parameters vs. aspect of model 2, Scale D; $ka = 18.6$; $\theta = 10^\circ$.	148
88	Measured Stokes parameters vs. aspect of model 3, Scale D; $ka = 27.9$; $\theta = 10^\circ$.	149
89	Measured Stokes parameters vs. aspect of model 2, Scale A; $ka = 5.24$; $\theta = 0^\circ$. Note: demonstrates redundant data for symmetric target.	150
90	Predicted Stokes parameters vs. aspect of cylinder, Scale A; $ka = 5.24$; $\theta = 0^\circ$.	153
91	Predicted Stokes parameters vs. aspect of model 1, Scale A; $ka = 5.24$; $\theta = 0^\circ$.	154
92	Predicted Stokes parameters vs. aspect of model 2, Scale A; $ka = 5.24$; $\theta = 0^\circ$.	155
93	Predicted Stokes parameters vs. aspect of model 3, Scale A; $ka = 8.14$; $\theta = 0^\circ$.	156
94	Predicted and measured polarization characteristics of cylinder, Scale A; $ka = 5.24$; $\theta = 0^\circ$.	158
95	Predicted and measured polarization characteristics of model 1, Scale A; $ka = 5.24$; $\theta = 0^\circ$.	159
96	Predicted and measured polarization characteristics of model 2, Scale A; $ka = 5.24$; $\theta = 0^\circ$.	160
97	Predicted and measured polarization characteristics of model 3, Scale A; $ka = 8.14$; $\theta = 0^\circ$.	161
98	Polarization null estimation accuracy of chaff.	171
99	Jammer polarization on the Poincaré sphere.	172
100	Polarization null estimation accuracy in jamming.	173
101	Polarization null estimation accuracy using counter-jamming scheme.	179
102	Propagation and scattering sign conventions.	191
103	Equal area polarization chart, showing left-sense hemisphere.	197
104	Backscatter RCS of right circular cylinder, $L/D = 10$, at $ka = 5.24$; (a) HH, (b) VV.	201
105	Backscatter RCS of right circular cylinder, $L/D = 10$, at $ka = 8.25$; (a) HH, (b) VV.	

LIST OF ILLUSTRATIONS (Concluded)

<u>Figure</u>	<u>Title</u>	<u>Page</u>
106	Flat Wing Model, showing leading and trailing edge responses and traveling wave interaction.	205
107	Computed wing response versus aspect. At 0° and 10° elevation. (Wing for aircraft model 1 at $ka = 2.4$.)	207
108	Two-way Fresnel pattern factor vs. off-axis position at $Z = 12$ m.	211
109	Two-way Fresnel pattern factor vs. off-axis position at $Z = 21$ m.	213

LIST OF TABLES

<u>Table</u>	<u>Title</u>	<u>Page</u>
1	Polarization Coordinates	9
2	Optimal Polarizations and Powers	20
3	Target Dimensions in Units of Cylinder Radius, a	58
4	Target Size Scale	58
5	Radar System Parameters	102
6	File Header and Name Conventions	121
7	Test Run Log	122
3	Elements of B Matrix for Example Case (Symmetric Target, $\gamma = 45^\circ$, $\nu = 0^\circ$)	175

SECTION 1

INTRODUCTION

This is the final report on work performed under Contract No. F30602-81-C-0254, August 1981 to August 1982, with the Rome Air Development Center, Rome, NY.

The objective of this effort was to study the polarization null patterns and maximum patterns of simple aircraft models, at practical radar frequencies, and to assess the feasibility of using the nulls or maxima for target classification in both benign and hostile electronic environments.

The approach to this problem included combined theoretical and experimental studies. The null and maximum characteristics were computed for theoretical target models of increasing complexity: single scattering centers of various types, combinations of scattering centers, and complete modeled aircraft. This study provided insight into the behavior of polarization characteristics as functions of aspect, frequency, and target geometry. Considerable effort was expended to assure realistic modeling of the target returns. Measurements were performed using a dual-polarization 35 GHz radar. Three aircraft models of slightly differing shapes and each at four different size scales were measured. Measurements were made over 0° - 90° aspect variation and at 0° and 10° elevation angles. The data is presented in the form of scattered Stokes vectors, from which the nulls and maxima are derived. Agreement between computed and measured polarization characteristics was good, so that conclusions could be drawn with confidence from the more readily manipulated computed characteristics.

This study was limited to the monostatic case, which results in a significant simplification due to the symmetry of the scattering matrix. The bistatic case is theoretically more complicated and will not exhibit some of the symmetry relations between null and max polarizations derived here for the monostatic case. However, the dynamic behavior of nulls and maxima can be expected to be similar.

The study was also originally limited to single frequency illumination. It was found that this resulted in a limitation on the usefulness of polarization characteristics for target identification, for targets distributed over many wavelengths. Hence some tentative extensions were made to multifrequency illumination. More work in this area is expected to yield a highly effective target discrimination technique.

It is known, and is detailed in this report, that scattering centers of different types (e.g. plates, dihedrals, edges) have highly distinctive polarization characteristics. It is therefore possible to infer scatterer type from a set of radar returns at judiciously chosen transmit and receive polarizations. Combinations of uncoupled scattering centers (such as an aircraft at practical radar frequencies) also have distinctive characteristics, dependent on the characteristics of the parts and on the spatial relations between them. It might be expected that two aircraft, which are similar in overall appearance but differ in detail, can exhibit sufficiently distinctive polarization behavior to permit discrimination. This study shows that this is indeed the case: at any particular aspect and frequency, two such aircraft do exhibit different polarization characteristics. However, the dynamic behavior with aspect or frequency of the characteristics is so complicated that their usefulness for target discrimination is problematic without further processing. This is the major result of this study: the instantaneous polarization null and maximum behavior of compound targets is too complex to permit effective target discrimination based on single frequency/aspect data, except possibly over certain (narrow) aspect bins. In particular it is shown that none of the polarization characteristics are invariant with aspect, as has at times been speculated in the literature. The difficulty is very similar to (and, in fact, has the same cause as) the rapid fluctuations of RCS versus aspect - while the patterns may be distinctive, they are too complex for direct use in a classifier. There are two ways to overcome the difficulties of rapidly fluctuating null patterns: either by averaging over aspect/frequency diverse data; or by utilizing the measured fluctuations to resolve parts of the target. The simpler averaging method is discussed to some extent in this report. It is seen that discrimination may be possible at those aspects where a distinctive scattering center is dominant. The second method is also

considered to show great promise. It is similar to range or cross-range profile methods, but with the single amplitude in a resolution cell replaced by a multi-dimensional polarization characteristic. Further discussion of this method is beyond the scope of this report; it is mentioned here to soften the blow of the rather negative conclusions drawn here regarding target discrimination under restrictive operating conditions.

The polarization characteristics upon which most emphasis is placed in this report are the co- and cross-polarized null and maximum polarizations and their respective powers. In particular, there is a set of five real parameters, m , 2γ , 2ν , 2τ , and 2ψ , an amplitude factor and four angles, in terms of which these polarizations and powers are defined. The usefulness of these five parameters lies in that they form a set of independent and complete target descriptors, which are invariant under polarization transformations. That is, the five parameters are characteristic features of the target at a particular aspect and frequency and are independent of the transmit and receive polarizations used to measure them. They are also invariant under target roll about the RLOS. However, they are not invariant under more general target orientation changes (aspect), nor under frequency changes. The completeness of the five parameters holds only for static, deterministic targets, for which the scattered radiation is fully polarized. For time-variant and random targets (meaning, really, that the relative orientations of the scattering centers of a distributed target, such as chaff, are changing during the measurement interval), the scattered radiation becomes depolarized, requiring four additional parameters. This is related to the fact that five independent real numbers characterize the relative phase scattering matrix, which fully describes coherent scattering, while nine independent real numbers characterize the Mueller matrix which fully describes incoherent scattering.

Only three parameters, namely m , 2γ , 2ν , are required to characterize a plane-symmetric coherent target (with the RLOS in the plane of symmetry). The aircraft models studied here at 0° elevation are of this type. This case is studied in detail, because of the more readily assimilable insight it provides.

The polarization nulls and maxima were not measured directly. Rather, two (fixed) orthogonal transmit polarizations were used. At each transmit polarization, the received power was measured for each of six different receiver polarizations. (Only one transmit polarization is required for the plane symmetric cases.) The procedure and data recording was done under computer control. From the power measurements, the Stokes vectors and polarization characteristics are derived. Great care was taken to develop a good polarization calibration procedure.

In Section 2, the theoretical background is presented, including a discussion of the characteristics of simple compound targets. In Section 3, the computed polarization characteristics are presented for each of the aircraft models. The measurement system and measurement results are given in Section 4. In Section 5, the effects of noise, chaff, and jamming on polarization null and maxima concepts are discussed. The use of polarization agility as an ECCM to reduce the effect of jamming is analyzed. A summary is given in Section 6; followed by References and an Appendix containing some mathematical details.

Wolfgang-M. Boerner gives an excellent history and extensive bibliography of polarimetry (See Appendix, page 8.12).

SECTION 2

CHARACTERIZATION OF POLARIZATION PROPERTIES OF SIMPLE TARGETS

In this section definitions and standards of polarimetry are presented, and the polarization properties of elementary and simple compound targets are investigated. The literature abounds with conflicting and sometimes self-inconsistent definitions of the descriptive parameters of polarization phenomena. An effort has been made here to present a consistent set of definitions which is compatible with other engineering standards. The results are almost identical to the work of Chan and Boerner [1], although there are some notational differences, due to the independent history of subject development at Sperry Research Center (SRC).

Much of the material in this section is not new, being a compendium of earlier development. However, emphasis will be put here on the concepts which are useful to this report. Section 2 concludes with a detailed investigation of the polarization properties of dumbbells and cylinders. Those results are extremely useful; first, for developing a feeling and understanding for polarization concepts; and second, for the direct applicability to more complicated targets.

The polarization properties of radar targets, utilizing null and maxima concepts ("optimal polarizations"), were investigated by Kennaugh [2] in the late 1940's and early 1950's, and received comprehensive treatment by Huynen in the 1950's [7] and in his 1970 Thesis [3]. More recently, Poelman has built an experimental polarimetric radar and made progress in using polarization properties to increase the detection capability of radar systems [17]. (See References [16,4] and Volume II of this report [18] for an extensive collection of references and historical notes.) Some of the standards used in this report differ from the above works for the sake of ease and compatibility with engineering practice, as will be noted.

2.1 REPRESENTATION OF POLARIZATION STATES

For a plane TEM wave propagating in the +z direction, we write

$$\vec{E}(z,t) = \text{Re} \left\{ E_0 \hat{E} e^{j(\omega t - kz + \phi)} \right\}, \quad (1)$$

where the (complex) unit polarization vector is

$$\hat{E} = \begin{bmatrix} e_x \\ e_y \end{bmatrix} = \begin{bmatrix} |e_x| \\ |e_y| e^{j\delta} \end{bmatrix}, \quad (2)$$

with $|e_x|^2 + |e_y|^2 = 1$. We will associate x and y with horizontal (H) and vertical (V) polarizations. For linear polarization, we have $\delta = 0$, and we can define the rotation ψ in the x-y plane: $\tan \psi = |e_y|/|e_x|$. For circular polarization, we have $|e_x| = |e_y| = 1/\sqrt{2}$ and $\delta = \pm \pi/2$. We choose $\delta = -\pi/2$ for right circular (RC) and $\delta = \pi/2$ for left circular (LC). That is:

$$\hat{E}_{RC} = \begin{bmatrix} 1 \\ -j \end{bmatrix} \quad \text{and} \quad \hat{E}_{LC} = \begin{bmatrix} 1 \\ j \end{bmatrix}.$$

This convention agrees with engineering usage and is contrary to that of Huynen and of physics texts. This convention corresponds to the sense of rotation of the \vec{E} vector in time at a fixed point in space. The general elliptical polarization of Equation (2) can be related to the motion of a point on the perimeter of the polarization ellipse illustrated in Figure 1. The illustration is for right-sense polarization, for which the ellipticity angle τ is defined to be negative. For linear polarization $\tau = 0$; and for left-sense polarization $\tau > 0$. For consistency, we require the restrictions $-\pi/4 \leq \tau \leq \pi/4$ and $-\pi/2 \leq \psi \leq \pi/2$. Using τ, ψ we can represent

$$\begin{bmatrix} e_x \\ e_y \end{bmatrix} = \begin{bmatrix} \cos \psi & -\sin \psi \\ \sin \psi & \cos \psi \end{bmatrix} \begin{pmatrix} \cos \tau \\ j \sin \tau \end{pmatrix} e^{j\alpha}, \quad (3)$$

the phase α is adjusted so that the phase of e_x is zero as in Equation (2). The reason for this form will become clear in the next section when transformations are discussed.

The normalized polarization vector can be represented in terms of power measurements as the normalized Stokes vector s :

$$s = \begin{bmatrix} |e_x|^2 + |e_y|^2 \\ |e_x|^2 - |e_y|^2 \\ 2 \operatorname{Re} \{e_x e_y^*\} \\ -2 \operatorname{Im} \{e_x e_y^*\} \end{bmatrix} = \begin{bmatrix} s_0 \\ s_1 \\ s_2 \\ s_3 \end{bmatrix} \quad (4)$$

(The above definition of s applies to a right-handed system $\hat{x}, \hat{y}, \hat{k}$. Use of the monostatic convention (see Section 2.3 and Appendix A-3) also introduces a left-hand system. In a left-hand system, s_3 has the opposite sign.) For the fully polarized wave of this section $s_0^2 = 1 = s_1^2 + s_2^2 + s_3^2$ which does not hold for partial polarization. Evaluating the Stokes vector for the forms (2) and (3), we obtain

$$\begin{bmatrix} s_0 \\ s_1 \\ s_2 \\ s_3 \end{bmatrix} = \begin{bmatrix} 1 \\ |e_x|^2 - |e_y|^2 \\ 2 |e_x| |e_y| \cos \delta \\ 2 |e_x| |e_y| \sin \delta \end{bmatrix} = \begin{bmatrix} 1 \\ \cos 2\tau \cos 2\psi \\ \cos 2\tau \sin 2\psi \\ \sin 2\tau \end{bmatrix} \quad (5)$$

as is shown by Huynen, but with a different order of the s_i .

The right-handed triplet (s_1, s_2, s_3) is conveniently plotted as a point on the surface of the normalized Poincare sphere, as in Figure 2. The Cartesian coordinates on the sphere are (s_1, s_2, s_3) and the polar coordinates (r, θ, ϕ) are $(1, \pi/2 - 2\tau, 2\psi)$. Orthogonal polarizations are antipodal on the sphere, where \bar{E}_1 and \bar{E}_2 are orthogonal if $\bar{E}_1 \cdot \bar{E}_2^* = 0$. Note that two polarization vectors which differ only by a relative phase ($e^{j\alpha}$ in Equation (3)), are mapped into the same Stokes vector s . Table 1 summarizes the coordinates of some basic polarizations.

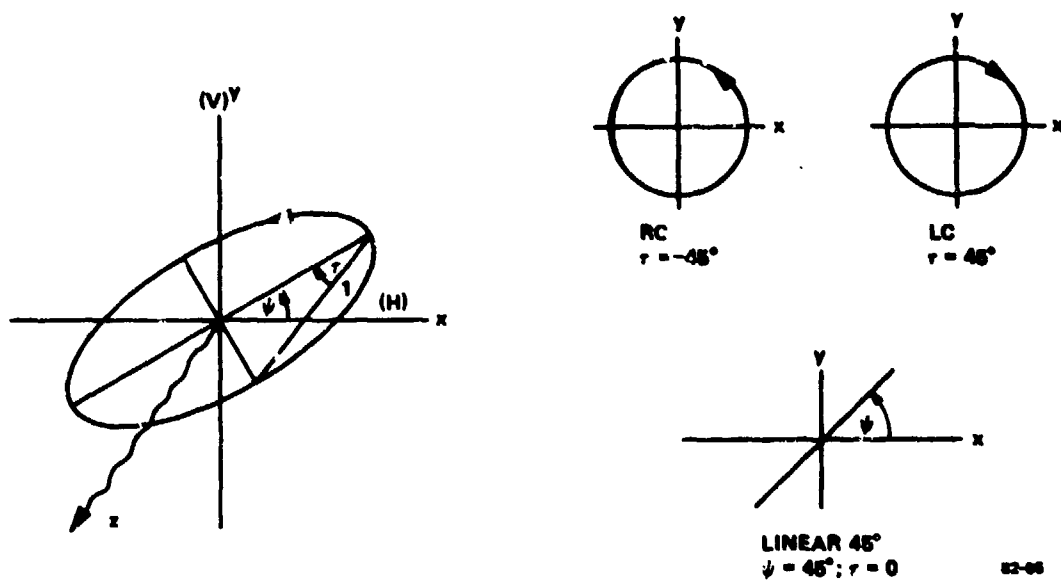


FIG. 1 Normalized polarization ellipse for right-sense polarization.

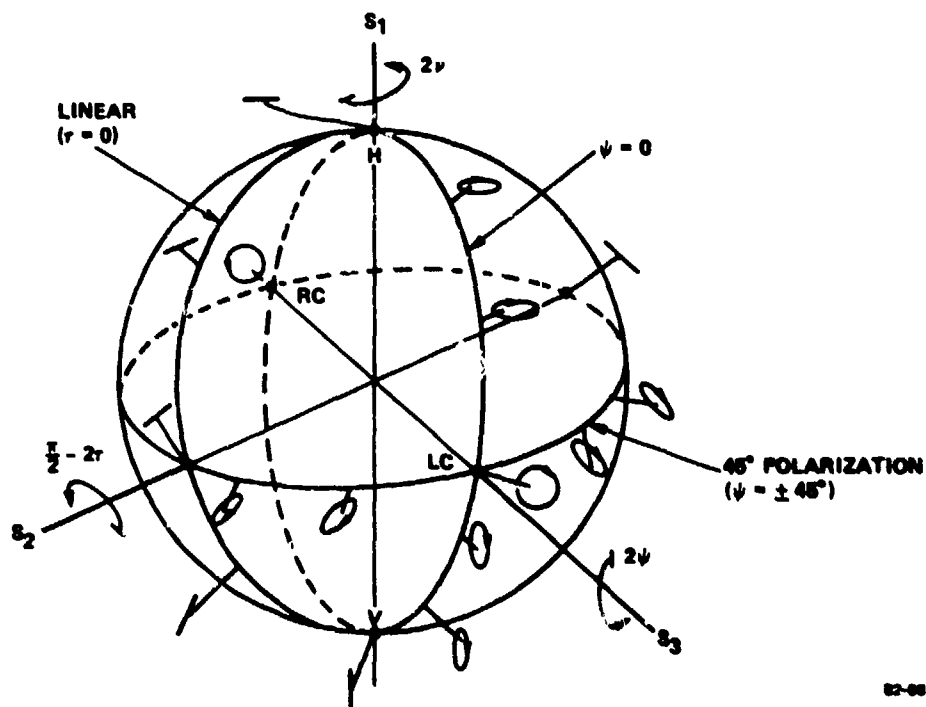


FIG. 2 Normalized Poincaré sphere.

TABLE 1

POLARIZATION COORDINATES

	\hat{E}	S
H	$\begin{pmatrix} 1 \\ 0 \end{pmatrix}$	$\begin{pmatrix} 1 \\ 1 \\ 0 \\ 0 \end{pmatrix}$
V	$\begin{pmatrix} 0 \\ 1 \end{pmatrix}$	$\begin{pmatrix} 1 \\ -1 \\ 0 \\ 0 \end{pmatrix}$
RC	$\frac{1}{\sqrt{2}} \begin{pmatrix} 1 \\ -j \end{pmatrix}$ (or) $\frac{1}{\sqrt{2}} \begin{pmatrix} j \\ 1 \end{pmatrix}$	$\begin{pmatrix} 1 \\ 0 \\ 0 \\ -1 \end{pmatrix}$
LC	$\frac{1}{\sqrt{2}} \begin{pmatrix} 1 \\ j \end{pmatrix}$	$\begin{pmatrix} 1 \\ 0 \\ 0 \\ 1 \end{pmatrix}$
45° Linear	$\frac{1}{\sqrt{2}} \begin{pmatrix} 1 \\ 1 \end{pmatrix}$	$\begin{pmatrix} 1 \\ 0 \\ 1 \\ 0 \end{pmatrix}$

2.2 POLARIZATION TRANSFORMATIONS

The transformation from one polarization basis to another, $\bar{E}_2 = Q\bar{E}_1$, can be (and has been) written in many forms. Most convenient is to write Q in the form

$$Q = \begin{bmatrix} q_1 & q_2 \\ -q_2^* & q_1^* \end{bmatrix}, \quad (6)$$

a unitary transformation with the property $Q^*Q^T = I$ and $\text{Det}(Q) = |q_1|^2 + |q_2|^2 = 1$ (See Appendix 8.1 for some details and generalizations.) If two polarizations are considered equivalent when they differ only by a relative phase, then there exists a unique Q of the above form, which takes one orthonormal basis pair of vectors into another. In particular we have

$$\begin{pmatrix} E_R \\ E_L \end{pmatrix}_c = Q_{lc} \begin{pmatrix} E_H \\ E_V \end{pmatrix}_l \quad (7)$$

for transforming from a linear to a circular basis,

$$\text{where} \quad Q_{lc} = \frac{1}{\sqrt{2}} \begin{pmatrix} 1 & j \\ j & 1 \end{pmatrix}, \quad (8)$$

$$\text{with} \quad Q_{cl} = Q_{lc}^{-1} = \frac{1}{\sqrt{2}} \begin{pmatrix} 1 & -j \\ -j & 1 \end{pmatrix}.$$

We see that right-circular polarization is transformed as

$$Q_{lc} \begin{pmatrix} j \\ 1 \end{pmatrix}_l = \begin{pmatrix} 1 \\ 0 \end{pmatrix}_c,$$

and left circular as

$$Q_{lc} \begin{pmatrix} 1 \\ j \end{pmatrix}_l = \begin{pmatrix} 0 \\ 1 \end{pmatrix}_c.$$

Corresponding to a transformation Q is a 4×4 transformation, V , of the Stokes vector. This is worked out in Appendix 8.2. Reference to Figure 2 of the Poincare sphere suggests the decomposition of Q into a product of three transformations

$$Q = Q_{\Psi} Q_{\tau} Q_{\nu} \quad (9)$$

corresponding to the Euler rotations 2ν , $\pi/2 - 2\tau$, and 2Ψ of the Poincare sphere, with corresponding

$$V = V_{\Psi} V_{\tau} V_{\nu} \quad (10)$$

These matrices are derived and tabulated in Appendix 8.2. The angles τ and Ψ have already been introduced in Section 2.1 as descriptors of the polarization vector; namely ellipticity and spatial rotation. The angle ν , called the "skip angle" by Huynen, will be seen to be more intrinsically associated with the target scattering matrix. Q_{ν} changes the relative phase between the two components of \hat{E} , without changing their magnitude. The subset of unitary transformations containing only Ψ and τ will be called "polarization transformations".

2.3 THE POLARIZATION SCATTERING MATRIX, MUELLER MATRIX, AND CANONICAL FORMS

The general polarization scattering matrix in a linear basis is written

$$A_G = \begin{pmatrix} a_{HH} & a_{HV} \\ a_{VH} & a_{HH} \end{pmatrix} \quad (11)$$

for the monostatic case $a_{HV} = a_{VH}$ (see Appendix 8.3 and [5]). Further, we will always deal with the relative phase scattering matrix so that we can write

$$A = \begin{pmatrix} |a_H| e^{j\phi_H} & |a_{HV}| \\ |a_{HV}| & |a_V| e^{j\phi_V} \end{pmatrix} \quad (12)$$

which consists of five distinct real numbers. (This matrix is usually called S .)

The scattered field is

$$\vec{E}^s = A \hat{E}^t . \quad (13)$$

In the so-called "monostatic convention" (Appendix 8.3), the H and V components of \hat{E}^t and \vec{E}^s have the same polarity, although the propagation vectors are opposite directed (Note that this convention makes the $(\hat{H}, \hat{V}, \hat{k})$ triplets have opposite handedness!). With this convention the received voltage is

$$V = \hat{E}^r \cdot \vec{E}^s ,$$

where \hat{E}^r is the receiver polarization, and the power is $P = VV^*$. A convenient way to write this is

$$V = r^T A t \quad (14)$$

where t and r are the transmit and receive unit polarization vectors, respectively. By reciprocity, a single antenna receives the same polarization it transmits ($r = t$).

Under a change of basis, say $t = Qt'$ and $r = Qr'$, we have

$$V = r^T A t = r'^T Q^T A Q t' = r'^T A' t' ,$$

with $A' = Q^T A Q . \quad (15)$

In particular, suppose that $r = t = \hat{E}_R = \begin{pmatrix} j \\ 1 \end{pmatrix}$, right circular in a linear basis, and that $A = I$, the scattering matrix for a simple specular return (e.g. a sphere). Using linear coordinates we obtain $V = [j \ 1] \begin{bmatrix} j \\ 1 \end{bmatrix} = 0$, as expected, since a single bounce reflector changes the sense of circular polarization, which cannot be received by the same antenna. In a circular

basis, we have $r' = t' = Q_{\ell c} t = \begin{pmatrix} 1 \\ 0 \end{pmatrix}$ and $A' = Q_{\ell c}^T A Q_{\ell c} = 1/2 \begin{pmatrix} 1 & j \\ j & 1 \end{pmatrix} \begin{pmatrix} 1 & j \\ j & 1 \end{pmatrix} = \begin{pmatrix} 0 & j \\ j & 0 \end{pmatrix}$ resulting in $V = [1 \ 0] \begin{pmatrix} 0 & j \\ j & 0 \end{pmatrix} \begin{pmatrix} 1 \\ 0 \end{pmatrix} = [1 \ 0] \begin{pmatrix} 0 \\ j \end{pmatrix} = 0$, as desired.

We now want to find a canonical form of A under a unitary transformation. In Appendix 8.4, it is shown that A can be diagonalized by solving the eigenvalue problem $Ae = \lambda e^*$, obtaining

$$S_0 = \begin{pmatrix} m & 0 \\ 0 & s \end{pmatrix} = e^{j\beta} Q^T A Q, \quad (16)$$

where β is an arbitrary phase angle which cancels that of $\det(A)$, and where m and s are real. The significance of this is that we can investigate the behavior of the simpler form S_0 and obtain the behavior of A by application of a unitary transformation. As shown in Appendix 8.4, a by-product of the derivation of (16) is the observation that invariants of any transformation Q (when A is symmetric) are the norm and determinant of A ,

$$\left. \begin{aligned} \text{where} \quad \text{norm}(A) &= \sqrt{|a_{11}|^2 + |a_{22}|^2 + 2|a_{12}|^2} \\ \det(A) &= a_{11} a_{22} - a_{12}^2 \end{aligned} \right\} \text{invariant}$$

(For the more general Q_G , which may have $\det(Q_G) = e^{j\beta/2}$, we can absorb $e^{j\beta}$ in Equation (17) into Q_a , with the result that $|\det(A)|$ is invariant.)

The columns of Q are the orthonormal eigenvectors e_1, e_2 . (The orthogonality is obtained only if A is symmetric.) The entries m and s are related to the eigenvalues by $m = |\lambda_1|$, $s = |\lambda_2|$, and where we choose m to correspond to the largest eigenvalue.

Then following Huynen, we introduce the angle γ , writing S_0 in the form

$$S_0 = m \begin{pmatrix} 1 & 0 \\ 0 & \tan^2 \gamma \end{pmatrix}, \quad 0 \leq |\gamma| \leq \frac{\pi}{4} \quad (17)$$

It is also possible to form a 4×4 matrix, M , representing scattering which operates on the Stokes vector. This has been called the Mueller matrix. Similar to Equation (13) we write

$$s_s = M s_t$$

where s_t and s_s are the Stokes vectors of the transmitted and scattered radiation respectively. (Since these have opposite handedness in accordance with our monostatic convention, remember that s_3 is defined with opposite sign for the transmitted and scattered vectors; see Appendix 8.3.) The received power can then be shown to be

$$P = \frac{1}{2} s_r^T M s_t \quad (18)$$

The receiver Stokes vector is defined to have the same handedness as though the receiver were operated as transmitter.

For the corresponding transformations Q , V , we can form (as in Equation 15),

$$P = \frac{1}{2} s_r^T M' s_t = \frac{1}{2} s_r'^T V^T M V s_t' = \frac{1}{2} s_r'^T M' s_t' \quad (19)$$

with $M' = V^T M V$

In particular, corresponding to the canonical form S , there is a canonical form M_0 . This can readily be found by writing out the Stokes vectors of t and s in $s = S t$ for four independent cases of t and solving for M in $s_s = M_0 s_t$. The result is

$$M_0 = \begin{pmatrix} \frac{m^2 + s^2}{2} & \frac{m^2 - s^2}{2} & 0 & 0 \\ \frac{m^2 - s^2}{2} & \frac{m^2 + s^2}{2} & 0 & 0 \\ 0 & 0 & ms & 0 \\ 0 & 0 & 0 & -ms \end{pmatrix} \quad (20)$$

This can also be written in the form

$$M_0 = \frac{m^2}{4 \cos^4 \gamma} \begin{pmatrix} 1 + \cos^2 2\gamma & 2 \cos 2\gamma & 0 & 0 \\ 2 \cos 2\gamma & 1 + \cos^2 2\gamma & 0 & 0 \\ 0 & 0 & \sin^2 2\gamma & 0 \\ 0 & 0 & 0 & -\sin^2 2\gamma \end{pmatrix} \quad (20')$$

In particular, the unit scattering matrix $S_0 = \begin{pmatrix} 1 & 0 \\ 0 & 1 \end{pmatrix}$ corresponds to

$$M_0 = \begin{pmatrix} 1 & 0 & 0 & 0 \\ 0 & 1 & 0 & 0 \\ 0 & 0 & 1 & 0 \\ 0 & 0 & 0 & -1 \end{pmatrix}.$$

(Note, Huynen includes a factor of $1/2$ in his definition of M .) The Mueller matrix is symmetric if and only if the scattering matrix is symmetric. A more elegant way to relate A , M , Q , and V is given at the end of Appendix 8.2

2.4 POLARIZATION NULLS AND MAXIMA

The received voltage can now be written as (see Equation 15)

$$V = r'^T S_0 t',$$

where r', t' are the polarization vectors in the transformed basis (we have dropped the phase term $e^{j\beta}$, since it is arbitrary). The co-polarized

voltage ($r' = t' = \begin{pmatrix} t_1 \\ t_2 \end{pmatrix}$) is

$$V_C = t'^T S t' = t_1^2 m + t_2^2 s. \quad (21)$$

The cross-polarized voltage ($r'^T t' = 0$) is

$$V_X = t_1 t_2^* m - t_1^* t_2 s, \quad (22)$$

since r' is orthogonal to t' if $r_1 = t_2^*$, $r_2 = -t_1^*$. We can now immediately obtain the maxima and nulls. Noting that $|t_1|^2 + |t_2|^2 = 1$ write,

$$|V_C| \leq |t_1|^{2m} + |t_2|^{2s} = |t_1|^{2(m-s)} + s,$$

where the equality holds if t_1 and t_2 have the same phase. Since $m > s$, the right side of the inequality is maximized when $|t_1| = 1$, say $t_1 = 1$, hence $|t_2| = t_2 = 0$. Hence the co-pol max polarization and power are

$$t'_M = \begin{pmatrix} 1 \\ 0 \end{pmatrix} \text{ with } P_{CM} = |V_{CM}|^2 = m^2. \quad (23)$$

Writing,

$$|V_C| \leq m - |t_2|^{2(m-s)},$$

we see that the right side is minimized for $|t_2| = 1$, say $t_2 = 1$, but that the left side is maximized (i.e. equality holds) if t_1 and t_2 have the same phase. Therefore, this is a saddle point (maximized subject to constant relative magnitude, but simultaneously minimized subject to constant relative phase). Hence the co-pol saddle point polarization and power are

$$t'_S = \begin{pmatrix} 0 \\ 1 \end{pmatrix} \text{ with } P_{CS} = s^2 = m^2 \tan^4 \gamma \quad (24)$$

Note that t_M and t_S are orthogonal, and that

$$P_{CM} + P_{CS} = m^2 + s^2 = \text{norm}(S) = \text{norm}(A). \quad (25)$$

We see directly from Equation (22) that for each of these polarizations $V_X = 0$. The co-pol max and saddle points also the cross-pol null points.

For the co-pol null, we solve $V_C = 0 = t_1^2 m + t_2^2 s$, obtaining the two solutions

$$t_N' = \frac{1}{\sqrt{m+s}} \begin{pmatrix} \sqrt{s} \\ \pm j \sqrt{m} \end{pmatrix} = \begin{pmatrix} \sin \gamma \\ \pm j \cos \gamma \end{pmatrix} \quad (26)$$

Using the definition of γ in Equation (19), notice that, significantly, the co-pol null locations contain information concerning the relative magnitudes of the eigenvalues of A , whereas the other null and max locations are points on the canonical axes, and hence only serve to orient the diagonalizing transformation, Q .

The cross-pol max location is slightly more difficult to derive, although the result is simple.

$$\text{Form } |V_X|^2 = V_X V_X^* = |t_1|^2 |t_2|^2 (m^2 + s^2) - (t_1^2 t_2^{*2} + t_1^{*2} t_2^2) ms$$

$$\text{or } |V_X|^2 = |t_1|^2 |t_2|^2 \left(m^2 + s^2 - 2ms \operatorname{Re} \left(\frac{t_1^2 t_2^{*2}}{|t_1 t_2|^2} \right) \right)$$

This is maximized when the right-most term is as negative as possible. This happens when $t_2/t_1 = \pm j$ and $|t_1| = |t_2| = 1/\sqrt{2}$. Hence, for the x-pol max polarizations and power, we have

$$t_{XM}' = \frac{1}{\sqrt{2}} \begin{pmatrix} 1 \\ \pm j \end{pmatrix} \text{ with } P_{XX} = \left(\frac{m+s}{2} \right)^2 = \frac{m^2}{4 \cos^2 \gamma} \quad (27)$$

(Note that $P_{XX} = m^2$ at $|\gamma| = \frac{\pi}{4}$).

Also note that for arbitrary transmit polarization, the total power received by the co- and cross-polarized channels of the receiver is

$$P = |V_C|^2 + |V_X|^2 = m^2 (|t_1|^2 + \tan^4 \gamma |t_2|^2) \leq m^2$$

These "optimal polarizations" can be plotted on the Poincare sphere in the canonical basis using definition (4). The results are that t_M' goes into a point at s_1' , t_S' antipodally at $-s_1'$, the two t_X go into $\pm s_3'$, while the co-pol nulls go into

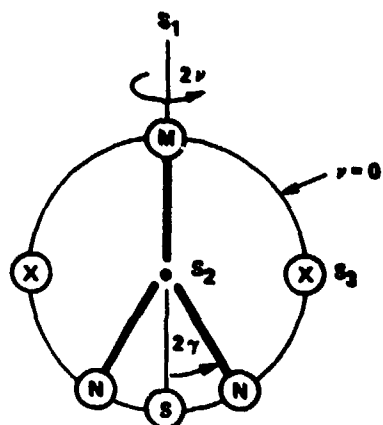
$$\begin{pmatrix} 1 \\ s_1' \\ s_2' \\ s_3' \end{pmatrix} = \begin{pmatrix} 1 \\ -\cos 2\gamma \\ 0 \\ \pm \sin 2\gamma \end{pmatrix}.$$

All these points are in the same plane, $s_2' = 0$; that is, they all lie on a great circle of the Poincare sphere. This is illustrated in Figure 3 and summarized in Table 2. The points are unique, except for two degenerate cases, which are discussed below. The points M , N_1 , N_2 define the polarization (or "Huynen") fork. The diagram for the scattering matrix A is obtained by an Euler rotation of the Poincare sphere, as defined by the transformation, Q .

The maximum power received is $P_{\max} = P_M = m^2$, which occurs for co-polarized reception at t_M . An effective radar cross section is defined by Kennaugh [6] (there is a factor of 4 error in [6]) as

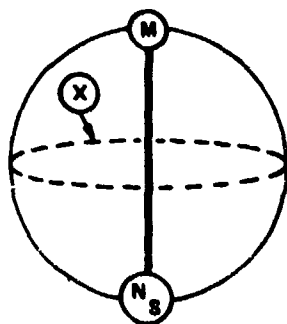
$$ECS = P_E = \left(\frac{m + s}{2} \right)^2 = \frac{m^2}{4} (1 + \tan^2 \gamma)^2 = P_{XX} \quad (28)$$

A subset of the above quantities completely characterize the polarization properties of the target. To obtain the scattering matrix using power measurements, it is necessary to establish the orientation of the Huynen fork, its opening angle 4γ , and the scale factor m . Any combination can be used, for example t_M' , t_N' , and P_{CM} .

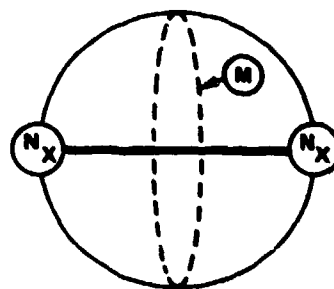


(a) NON-DEGENERATE CASE

DEGENERATE CASES



(b) $\gamma = 0$



(c) $\gamma = 45^\circ$ 82-67

FIG. 3 Great circle cut ($S_2 = 0$) on Poincaré sphere, showing nulls and maxima for canonical (positive real diagonal) scattering matrix.

TABLE 2
Optimal Polarizations and Powers

	In Canonical Basis		Co- and X-Pol Power (Invariant)
	Polarization t'	Stokes Vector s'	
(M) Co-pol max X-pol null	$\begin{pmatrix} 1 \\ 0 \end{pmatrix}$	$\begin{pmatrix} 1 \\ 1 \\ 0 \\ 0 \end{pmatrix}$	$P_{CM} = m^2$ $P_{XM} = 0$
(S) Co-pol saddle X-pol null	$\begin{pmatrix} 0 \\ 1 \end{pmatrix}$	$\begin{pmatrix} 1 \\ -1 \\ 0 \\ 0 \end{pmatrix}$	$P_{CS} = m^2 \tan^4 \gamma$ $P_{XS} = 0$
(N) Co-pol nulls	$\begin{pmatrix} \sin \gamma \\ \pm j \cos \gamma \end{pmatrix}$	$\begin{pmatrix} 1 \\ -\cos 2\gamma \\ 0 \\ \pm \sin 2\gamma \end{pmatrix}$	$P_{CN} = 0$ $P_{XN} = m^2 \tan^2 \gamma$
(X) X-pol maxima	$\frac{1}{\sqrt{2}} \begin{pmatrix} 1 \\ \pm j \end{pmatrix}$	$\begin{pmatrix} 1 \\ 0 \\ 0 \\ \pm 1 \end{pmatrix}$	$P_{CX} = \frac{m^2(1 - \tan^2 \gamma)^2}{4}$ $P_{XX} = \frac{m^2}{4 \cos^4 \gamma}$

Degenerate case $\gamma = 0$, (S) = (N);

$$t_X' = \frac{1}{\sqrt{2}} \begin{pmatrix} e^{j\nu} \\ \pm j e^{-j\nu} \end{pmatrix}; s_X' = \begin{pmatrix} 1 \\ 0 \\ \pm \sin 2\nu \\ \pm \cos 2\nu \end{pmatrix}; \quad -\frac{\pi}{4} \leq \nu \leq \frac{\pi}{4}$$

Degenerate case $\gamma = \frac{\pi}{4}$, (X) = (N);

$$t_M' = \begin{pmatrix} \cos \Psi \\ \sin \Psi \end{pmatrix}; s_M' = \begin{pmatrix} 1 \\ \cos 2\Psi \\ \sin 2\Psi \\ 0 \end{pmatrix}; \quad -\frac{\pi}{2} \leq \Psi \leq \frac{\pi}{2}$$

For all polarizations: Total RCS $P = P_C + P_X = m^2 (|t_1|^2 + \tan^4 \gamma |t_2|^2) \left\{ \begin{array}{l} \leq m^2 \\ \geq 0 \end{array} \right.$

$$\text{Invariant effective RCS: } P_E = \left(\frac{\sqrt{P_{CM}} + \sqrt{P_{CS}}}{2} \right)^2 = \frac{m^2}{4 \cos^4 \gamma} \left\{ \begin{array}{l} \leq m^2 \\ \geq \frac{m^2}{4} \end{array} \right.$$

There are two degenerate cases to this analysis. These are also shown in Figure 3. The first is the case $\gamma = 0$. The canonical scattering matrix is $S_0 = m \begin{pmatrix} 1 & 0 \\ 0 & 0 \end{pmatrix}$; that is, one of the eigenvalues is zero. The co-pol nulls collapse onto the saddle point, and the x-pol max points "flash" into the great circle ($s_1 = 0$) orthogonal to the s_1 axis, with $P_{XX} = m^2/4$. If $Q = I$ so that $A = S_0$, this is the case of a horizontal dipole with a co-pol max at \hat{H} , co-pol null at \hat{V} , and x-pol max at any 45° elliptical polarization.

The second degenerate case is $\gamma = \pm \pi/4$. The canonical scattering matrix is $S_{\pi/4} = m \begin{pmatrix} 1 & 0 \\ 0 & 1 \end{pmatrix}$; that is, the eigenvalues are equal. The co-pol nulls coincide with the x-pol maxima with $P_{XN} = P_{XX} = m^2$. The co-pol maxima "flash" into the great circle $s_3 = 0$ orthogonal to s_3 . If $Q = I$ so that $A = S_0$, this is the case of (circularly symmetric) specular reflection; with a co-pol max at any linear polarization and x-pol maxima at right- and left-circular polarizations.

The important case of a simple double bounce scatterer: $A = \begin{pmatrix} 1 & 0 \\ 0 & -1 \end{pmatrix}$, is not one of our canonical forms. It is obtained from $S_{\pi/4}$ by

$$A = Q_v^* S_{\pi/4} Q_v^{*T}$$

with

$$v = \pm \frac{\pi}{4}.$$

This corresponds to a 90° rotation of Figure 3c about axis s_1' . The result is that the perimeter $s_2' = 0$ is now the great circle of co-pol maxima, corresponding to elliptical polarization with $\psi = 0$, including pure H, V, RC, and LC. The co-pol nulls, coincident with the x-pol maxima, occur at the $\pm 45^\circ$ linear points.

2.5 NULLS AND MAXIMA FOR GENERAL SYMMETRIC TARGET

In order to gain an understanding of the behavior of nulls and maxima, we will first investigate plane symmetric targets. If the plane of symmetry is aligned with H- (or V-) polarization, then the scattering matrix is diagonal. (Note that if the target is rotated about the RLOS, we can simply rotate the polarization reference plane to maintain alignment with the target symmetry plane. Hence, if by H- (or V-) polarization we always mean that \vec{E}_H (or \vec{E}_V) is aligned with the symmetry plane, then our result will apply to all plane symmetric targets, such that the symmetry plane contains the RLOS.) The general form of the scattering matrix is then (see Equation (17)) :

$$A = Q_v^* S_0 Q_v^{*T} = m \begin{pmatrix} e^{j2v} & 0 \\ 0 & \tan^2 \gamma e^{-j2v} \end{pmatrix} \quad (29)$$

where

$$Q_v = \begin{pmatrix} e^{-jv} & 0 \\ 0 & e^{jv} \end{pmatrix}, \quad t = Q_v t'$$

t is the polarization vector in the H-V basis, and t' is the polarization vector in the canonical basis.

The matrix A is completely characterized by the magnitude, m , and the two angles γ and v . 4γ was identified in Section 2.4 as the opening angle of the Huynen fork. The angle v was named the "target skip angle" by Huynen, because it is related to how closely the target resembles an odd- or even-bounce scatterer: If $v = 0$, the target is single (odd) bounce; if $v = \pi/4$ the target is double (even) bounce. Note that v is given by the relative phase of a_{HH} and a_{VV} : $4v = \text{phase}(a_{HH}) - \text{phase}(a_{VV})$; and that γ is given by the relative magnitude: $\tan^2 \gamma = |a_{VV}/a_{HH}|$. In Equation (29), A is written with the assumption that $|a_{HH}| \geq |a_{VV}|$. (In case $|a_{VV}| > |a_{HH}|$, we should reverse the meaning of H and V and maintain the same analysis).

From Table 2 we can immediately obtain the optimal polarizations, using $t = Q_v t'$. In particular, $t_M = \begin{pmatrix} 1 \\ 0 \end{pmatrix}$ (after removing the arbitrary phase factor), with the Stokes representation (1, 1, 0, 0). That is, the co-pol max always occurs at H (or V if $|a_{VV}| > |a_{HH}|$) for plane symmetric targets. (For the degenerate case $|a_{HH}| = |a_{VV}|$, the co-pol max occurs at any linear polarization.)

The co-pol nulls occur at $t_N = \begin{pmatrix} e^{-j\gamma} \sin \gamma \\ \pm j e^{j\gamma} \cos \gamma \end{pmatrix}$. The Stokes vector representation can be obtained either by applying the definition (Equation (4)) or by transforming from Table 2 using V_v (Equation (A-6)):

$$S_N = \begin{pmatrix} 1 \\ -\cos 2\gamma \\ \mp \sin 2v \sin 2\gamma \\ \pm \cos 2v \sin 2\gamma \end{pmatrix} = \begin{pmatrix} 1 \\ \cos 2\tau_N \cos 2\psi_N \\ \cos 2\tau_N \sin 2\psi_N \\ \sin 2\tau_N \end{pmatrix} \quad (30)$$

The right side of the equality comes from Equation (5), giving the Stokes vector in terms of the elliptical polarization parameters ψ , τ . Solving for ψ_N , τ_N , we can plot the co-pol nulls on the polarization chart, which is a projection of the Poincare sphere with s_3 at the center. (An equal area projection is used, see Appendix 8.5.) The nulls and maxima for the gamut of possible symmetric targets are plotted on polarization charts in Figure 4. In these charts, H is at the top, V at the bottom, LC in the center, and the perimeter is linear polarization. The central meridian is $2v = 0^\circ$, while the perimeter is $2v = \pm 90^\circ$. Only the left-sense half of the sphere is represented, so that usually only one of the two co-pol nulls or the two x-pol maxima is plotted; the others of the pair would appear symmetrically on the right-sense chart. Going across the page, the charts are for targets with the same γ (or $|a_{VV}/a_{HH}|$) but with different values of v (or relative phase (a_{HH}/a_{VV})); while going down the page, the charts are for targets with different γ and the same v . Note that **(M)** is always at the top (it could also be at the bottom) and that all the optimal polarizations lie on the projection of a great circle (a meridian), except for the

degenerate cases. In addition to its polarization chart description, the value m is required to characterize a target. The parameters m , γ , ν , are aspect and frequency dependent, so that a complete characterization would consist of null or max loci as functions of aspect and frequency together with m as a function of aspect and frequency.

The position of the co-pol null on the polarization chart can also be interpreted directly as representing the parameters ν , γ of the scattering matrix. The longitude corresponds to 2ν , the latitude corresponds to $(2\gamma - 90^\circ)$.

From Figure 4 we can observe several important properties of the optimal polarization locations pertinent to target classification: (1) As noted above, the co-pol max and saddle (and the x-pol nulls) are always at H or V; (2) the x-pol maxima always occur on the equator, which is 45° elliptical polarization or a linear real combination of RC and LC; (3) the co-pol nulls may appear anywhere. We may think of the locations (M), (X), and (N) as having respectively 0, 1, and 2 degrees of freedom. Hence we can already anticipate that for two symmetric targets, the co-pol null location will be the best discriminant (after, of course, the polarization reference has been established).

There are two ways in which target asymmetry will modify Figure 4. First is the transformation Q_ψ , which is the same as or is equivalent to rotating the target by ψ about the RLOS, and results in a rotation of Figure (4) by 2ψ about the center point. This asymmetry would be removed in practice by establishing the polarization reference plane to be parallel to the symmetry plane, hence restoring Figure 4. That is, polarimetry can be and should be made invariant under target rotation about the RLOS. The second way in which a target may be asymmetric corresponds to a rotation of Figure 4 about s_2 (by the angle 2τ); that is, the polarization chart rotates out of the plane of the paper. Depending on the degree of this asymmetry, it may turn out to be possible to discriminate between a symmetric and a

non-symmetric target (or between two non-symmetric targets) on the basis of this rotation. Whether or not this is true will depend on the mechanism which underlies the structure of the scattering matrix, namely, the spatial and amplitude relations between the scattering centers that make up the scatterer and the dynamic (with frequency and aspect) behavior of these relations. This will be investigated in a later section. It may turn out that the asymmetry character is not a good discriminant, in which case it can be removed by choice of (elliptical) polarization basis, thus again obtaining Figure 4. In any case, the general behavior of Figure 4 can be considered fundamental, as it can be obtained for any target by a suitable choice of the transmit and receive polarizations.

2.6 SIMPLE APPROXIMATE DESCRIPTIONS OF SCATTERING CHARACTERISTICS: SINGLE-BOUNCE, DOUBLE-BOUNCE, DIPOLE.

We can identify some of the charts in Figure 4 as belonging to certain types of scattering centers. Chart (a) represents the single-bounce circularly symmetric specular scatterer with $A = I$ ($2\psi = 0$, $2\gamma = 90^\circ$), while (c) is the double-bounce scatterer (e.g. a dihedral). At low frequency, the specular return from a doubly curved surface (e.g. prolate spheroid) might be represented by (d). A horizontal edge or dipole is represented by (j). A vertical edge is represented by (j) turned upside-down.

The symmetric target rotated about the RLOS is represented by the same figures rotated by 2ψ about the center point (axis s_3).

When discussing polarization characteristics of a target, it is convenient to make use of approximate descriptions. We collect these descriptions in this separate subsection for the sake of reference. We restrict the concepts to symmetric targets aligned with the H-V polarization basis.

By single-bounce we will mean a scatterer with a scattering matrix that is approximately the unit matrix, with no phase difference between the HH and VV terms. The specular return from a sphere or plate is of this type. That is, $2v = 0$ and $2\gamma = 90^\circ$ for a "single-bounce" scatterer. The co-pol nulls occur at LC and RC; that is, $2v = 0, 180^\circ$ and $2\gamma = 90^\circ$; or in terms of the polarization ellipse, at $\tau = \pm 45^\circ$, with Ψ undefined. The nulls are thus located at the center of the polarization chart, as in Figure 4a. When discussing target type, we may identify a "single-bounce" scatterer as one for which these conditions hold only approximately.

By double-bounce we will mean a scatterer having a matrix with approximately unit diagonal entries of opposite sign. An inside corner (dihedral) is of this type. That is, $2v = \pm 90^\circ$, $2\gamma = 90^\circ$ for a "double-bounce" scatterer. The co-pol nulls occur at 45° -linear polarization, that is $2v = \pm 90^\circ$ and $2\gamma = 90^\circ$; or, in terms of the polarization ellipse at $\tau = 0$, $\Psi = \pm 45^\circ$. The nulls are located at the equator end points of the polarization chart, as in Figure 4c.

By dipole we will mean a scatterer with only one non-zero (HH or VV) entry in the scattering matrix. A horizontal dipole has an HH entry. Its co-pol nulls coalesce at VV, that is $2\gamma = 0$ with $2v$ undefined; or in terms of the polarization ellipse, at $\tau = 0$, $\Psi = 0$. The null is located at the bottom of the polarization chart, as in Figure 4g.

A vertical dipole has a scattering matrix with only a non-zero VV entry. Its co-pol null occurs at HH, and thus has the polarization chart representation of Figure 4g turned upside-down, with the co-pol null at $\tau = 0$, $\Psi = 90^\circ$. Although the canonical form description is defined for $0 \leq 2\gamma \leq 90^\circ$, it is convenient to think of the vertical dipole co-pol null as occurring at $2\gamma = 180^\circ$. That is, for the sake of the polarization chart description, 2γ will always be measured with respect to the south pole.

2.7 DYNAMIC BEHAVIOR OF NULLS AND MAXIMA FOR DUMBELL TARGETS

We now begin our investigation of the dynamic properties of the optimal polarizations; that is, the null and maxima locations as functions of aspect and/or frequency. First note that the scattering matrix of a single scattering center is only a slow function of aspect or frequency. For compound targets the dominant effect on the scattering matrix is due to changes in the relative phase between scattering centers. Accordingly we will begin our study with a simple dumbbell target composed of two independent scattering centers, each of which is of the general type discussed in Section 2.5 and each of which can be considered to be approximately constant over a certain region of aspect or frequency variation. The modeling of compound targets as the phase-dependent sum of independent scattering centers is discussed, for example, in Reference [8]. It is valid when scattering centers are separated by more than a few wavelengths (as is the case for the targets considered in this report). The variable is the relative phase between the two scattering centers which can be considered to be due to aspect variation as the dumbbell rotates in the plane of symmetry or (equivalently) due to frequency variation. For aspect, α , variation the relative phase is $\phi_{12} = (4\pi L/\lambda)\cos(\alpha_0 + \Delta\alpha)$, where L is the separation between scatterers. For frequency variation, we can write $\phi_{12} = (4\pi/\lambda_0)(1 + \Delta f/f_0)(L \cos \alpha_0)$. We will observe null and max motion as functions of varying ϕ_{12} . The horizontal and vertical scattering coefficients of scatterer 1 are given by $h_1 e^{j\theta_{H1}}$ and $v_1 e^{j\theta_{V1}}$, and for scatterer 2 by $h_2 e^{j\theta_{H2}}$ and $v_2 e^{j\theta_{V2}}$. Combining these and manipulating to remove the common constant phase, the scattering matrix can be written

$$A = A_1 e^{j\phi_{12}/2} + A_2 e^{-j\phi_{12}/2} = \begin{pmatrix} a_{HH} & 0 \\ 0 & a_{VV} \end{pmatrix}$$

with

$$\begin{aligned} a_{HH} &= h_1 e^{j\phi/2} + h_2 e^{-j\phi/2} \\ a_{VV} &= v_1 e^{j(\phi + \Delta\theta_{VH})/2} + v_2 e^{-j(\phi + \Delta\theta_{VH})/2} \end{aligned} \quad (31)$$

where

$$\Delta\theta_{VH} = \theta_{V1} - \theta_{V2} - \theta_{H1} + \theta_{H2}.$$

This is the most general dumbbell target composed of constant individual scatters, each with its symmetry plane coincident with the symmetry plane of the rotating dumbbell. (A completely general dumbbell would be asymmetric, with the individual scatterers not aligned with the plane of rotation.)

The scattering matrix and null and maxima locations were computed for various combinations of the parameters $h_1, h_2, v_1, v_2, \phi_{VH}$ as ϕ varied from $-\pi$ to $+\pi$, i.e. as the RCS goes through one scintillation period. One case is illustrated in detail in Figure 5. This is the equal area polarization chart described in Appendix 8.5. The center is LC polarization, H is at the north pole and V at the south pole. The egg-shaped curve is the (left-sense) co-pol null locus as the relative phase ϕ between scatterers goes through 360° . The symmetric dashed curve is the locus of the other (right-sense) co-pol null, which appears on the back of the Poincare sphere. The Huynen fork is indicated for a particular value of ϕ , identified by the points (N), (X), and (M). These points lie on a meridian. As ϕ varies, the cross-pol max, (X), moves along the equator. The co-pol max, (M), is always at H (except when the co-pol nulls move to the upper hemisphere, in which case (M) is at V).

As discussed in Section 2.5, the longitude of the co-pol null position corresponds to the parameter 2ψ of the scattering matrix, while the latitude corresponds to $(2\gamma - 90^\circ)$. (It is convenient to think of (2γ) as taking values from 0 to 180° , even though it is defined for 0 to 90° - values of $2\gamma > 90^\circ$ mean that the co-pol max (M) is at V.)

A number of typical dumbbell cases are illustrated in Figure 6. Only the left-sense co-pol null loci are shown. (The point (M) and the (X) locus can be found using the construction of Figure 5.) Some general observations can be made: When one of the scattering centers is dominant (Figures 6a and 6b), the co-pol null makes only small excursions. The relative phase, ϕ_{VH} , between the horizontal and vertical scattering constants affects the average value of 2ψ (Figure 6b). The case illustrated in Figure 6a is for $h_1 \approx v_1$, which is the case if scatterer 1 is a specular point. The

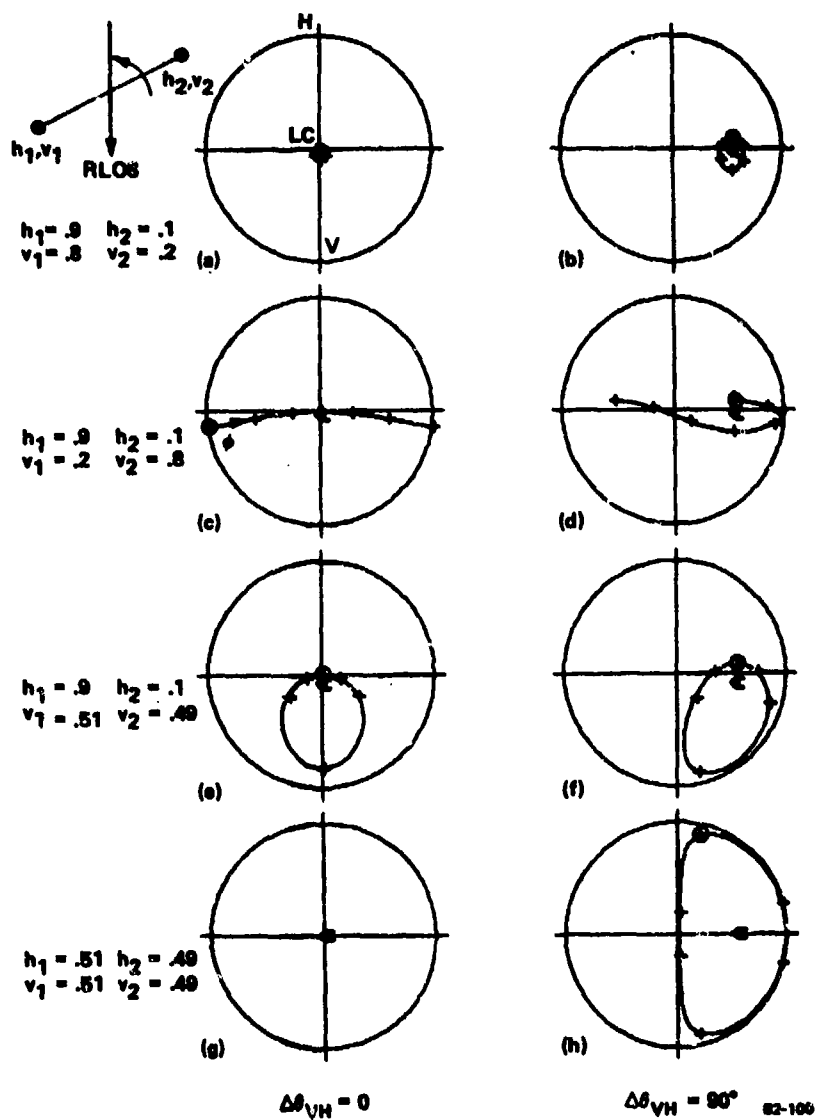


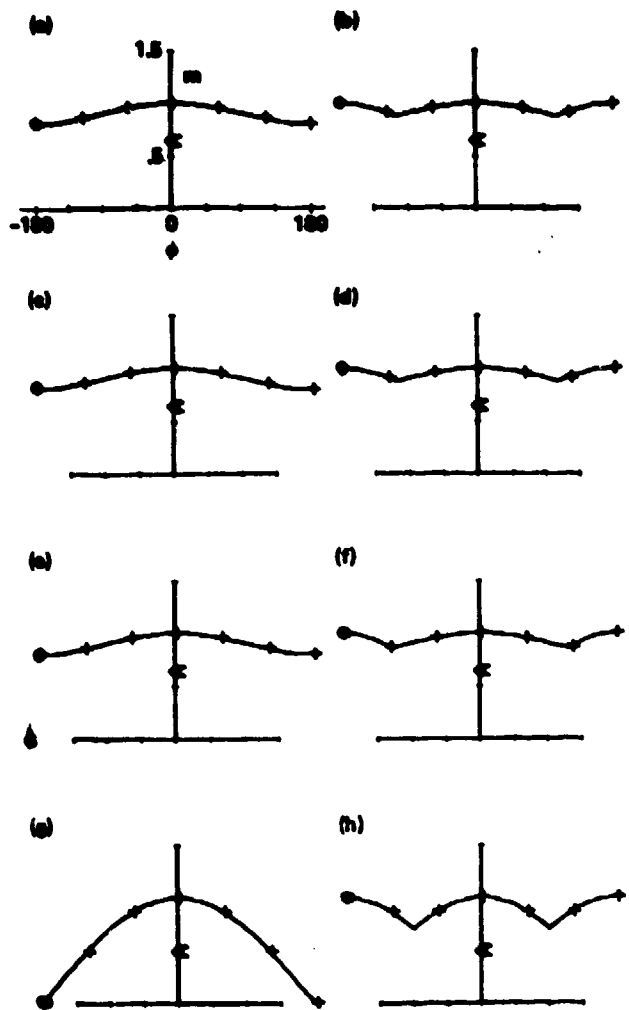
FIG. 8 Copol null loci for one scintillation period of rotating dumbbell target for various dumbbell parameters.

dumbell of Figures 6c and 6d has the same scattering strengths, but now 1 is predominantly horizontal and 2 predominantly vertical. The null locus excursion is small in γ but large in ν . The corresponding variation of m (maximum co-pol voltage) is illustrated in Figures 7a, b, c, d. Because one scatterer is dominant, the fluctuation in m is small.

Figures 6e and 6f show what happens if both scatterers are about equal vertically but scatterer 1 is dominant horizontally. This case could correspond to a specular scatterer 1, and some kind of vertical edge-like structure for scatterer 2. The null trajectory in this case is much larger, showing variation in both the ν and γ parameters. The corresponding plots of m in Figure 7e and 7f show larger fluctuations in m . Finally, the last two cases (Figures 6g, 6h and 7g, 7h) show the case of two nearly equal interfering scatterers. Constructive and destructive interference effects are very large: For Figure 6g, the horizontal and vertical oscillations are in phase, resulting in no movement of the null locus; but for Figure 6h, the oscillations are out of phase, resulting in very large excursions of the co-pol null.

It is important to note that a symmetric target is completely described by a co-pol null locus and the corresponding m -variation.

A significant result of this simulation is that even for simple compound targets the null trajectory can appear just about anywhere on the polarization chart and may exhibit large variations in both parameters 2ν and 2γ . Large excursions in the null locus occur in just the same way as large fluctuations in the RCS when observed as a function of aspect or frequency - namely, as a result of interference effects. The relationship between RCS fluctuations and null position fluctuations is complicated because it involves the relative phase of the HH and VV components of the scattering matrix as well as the "relative phase" between the H and V scintillations. However, it can be said that if RCS fluctuations are rapid, then null location fluctuations are equally rapid.



62-101

FIG. 7 Copol maxima as function of scatterer phase, corresponding to cases of figure 6.

It is possible to anticipate from Figure 6 the null locus behavior for more general 2-scatterer targets: Suppose we observe the target through several scintillation periods, and that the magnitudes of the scattering centers change slowly as a function of aspect (or frequency), as would be the case for a typical radar target. We then expect the shape and centroid of the loci of Figure 5 to change as the null moves around on the locus, resulting in a spiral-like or smeared out locus. This will be seen to be the case for the cylinder (Section 2.9) which over some range of aspect behaves like two or three scattering centers with slowly varying strengths.

2.8 DEPOLARIZATION DUE TO AVERAGING OVER A SCINTILLATION PERIOD

When the separation between two scattering centers is many wavelengths, the fluctuations in RCS and in null locations is rapid for even small changes in aspect (or frequency). In that case it may be impractical or undesirable to follow these fluctuations in a measurement; instead, an average measurement is taken. The result of averaging is that the received power is depolarized. This is equivalent to the statement that for the received Stokes vector defined in Equation (4) we have

$$s_0^2 \neq s_1^2 + s_2^2 + s_3^2. \quad (32)$$

A result is that it is no longer possible to observe a co-pol null, but rather a co-pol minimum. A complete treatment of the depolarized case is beyond the scope of this report. It suffices for our present purposes to note that the location of the co-pol minimum (when the fluctuations are not too large) is approximately given by the average of the instantaneous null locations. The co-pol minimum location is indicated by the point A in each of Figures 6 for the average over one cycle of a fluctuation for the dumbbell. The points A were computed from the average depolarized Stokes vector in just the same manner as the instantaneous null locations were computed from the fully polarized instantaneous Stokes vectors.

Data averaging so as to remove the large fluctuations in the polarization characteristics is pursued to some extent in Section 3 with the aircraft data.

For purposes of target classification, the fluctuations may serve as a discriminant, since they are related to target size and structure. However, the fluctuations are exhibited first and foremost by the received power. It is not clear whether null location fluctuation adds any additional information about the target. It is therefore likely that the average null location is the more useful quantity to be derived from polarimetry. These comments apply to the present case of unresolved scattering centers. When scattering centers are resolved, so that they can be characterized individually, then their polarization properties (discussed in Section 2.5) would, of course, be readily apparent.

2.9 CO-POL NULL LOCUS FOR RIGHT-CIRCULAR CYLINDER

The simple aircraft models which are the ultimate subject of investigation in this report, all consist of right-circular cylinders (RCC) with fins attached. Accordingly, we now investigate the polarization characteristics of the RCC by itself.

The backscatter modeling of the RCC used in this report is given for reference in Appendix 8.6. The cylinder is a symmetric target, and we assume in this discussion that the H-V polarization basis has been aligned with the plane of symmetry (\vec{E}_H in plane of symmetry, \vec{E}_V perpendicular to plane of symmetry). The aspect change is a rotation in the plane of symmetry. The HH and VV radar cross sections for a cylinder with length to diameter ratio $L/D = 1$ and $ka = 2.4$ (where a is the radius and $k = 2\pi/\lambda$) are given in Figure 8, as functions of aspect. Not shown is the relative phase between the HH and VV responses, although of course, this is an important contributor to the polarization characteristics.

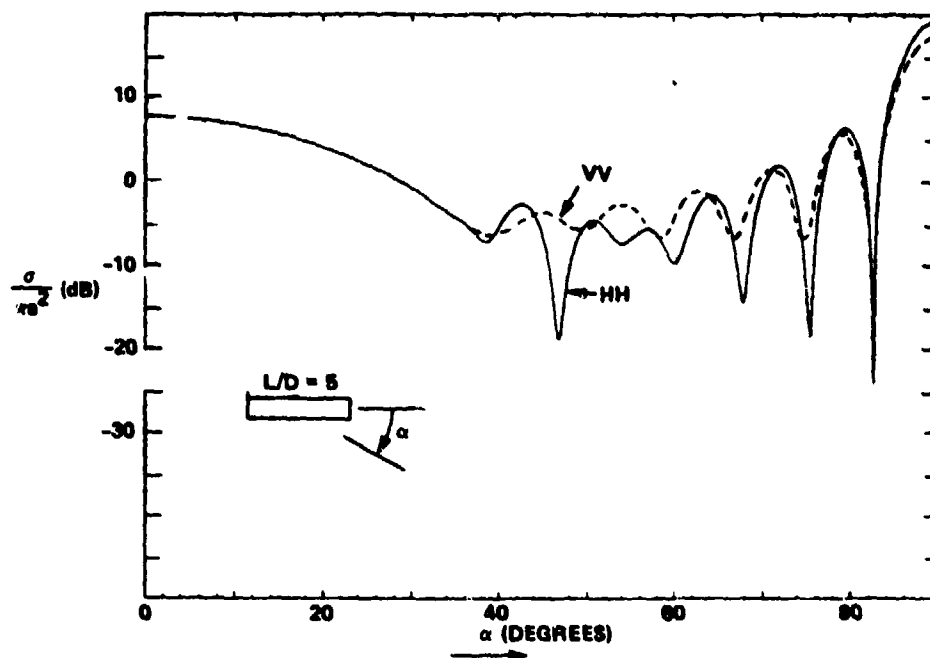


FIG. 8 Backscatter RCS, HH and VV, of right circular cylinder, $L/D = 5$ at $ka = 2.4$.

Near nose-on ($\alpha = 0$), the specular response is that of a circular disc, which is polarization independent. Near broadside ($\alpha = 90^\circ$) the return is again specular and nearly polarization independent. Since this case is in the resonance region, there is a slight difference in the HH and VV responses at broadside, due both to the polarization dependent specular and creeping wave contributions to the response. At intermediate angles, scattering may be considered to occur at the three visible edges of the cylinder. The edge returns are polarization dependent; individually they vary slowly with aspect, but due to the varying relative phase, the total response fluctuates. The HH and VV response fluctuations are different in both phase and amplitude. As a consequence, the co-pol null location will change with aspect.

The scattering matrix behavior as a function of aspect (0 to 90°) is illustrated in Figure 9 in terms of the canonical parameters m , $2v$, and 2γ . These three curves completely describe the scattering properties of the cylinder. The polarization maximum m (max received voltage); Figure 9a, traces the maximum of the HH and VV response curves of Figure 8. Because the target is symmetric, m occurs at either H or V on the polarization chart (i.e. at the poles). Figure 9b is $2v$, which is the relative phase between the HH and VV returns. Note that $2v = 0$ from $\alpha = 0$ to $\alpha = 35^\circ$, where the response is polarization independent. At $\alpha = 90^\circ$, $2v$ is again nearly zero, though not quite because of the slight polarization dependence of the broadside specular. At intermediate aspects, $2v$ is a smoothly varying function, going through several 360° cycles. Also note that there are two solutions for $2v$, so that another curve could be drawn, displaced by 180° . Figure 9c shows that 2γ vs. aspect makes only small deviations from $2\gamma = 90^\circ$. Phenomenologically, the cylinder behaves as a single-bounce scatterer ($2v = 0$, $2\gamma = 90^\circ$) near nose-on and broadside; while at intermediate angles it oscillates between approximate single-bounce and double-bounce ($2v = \pm 90^\circ$, $2\gamma = 90^\circ$) behavior.

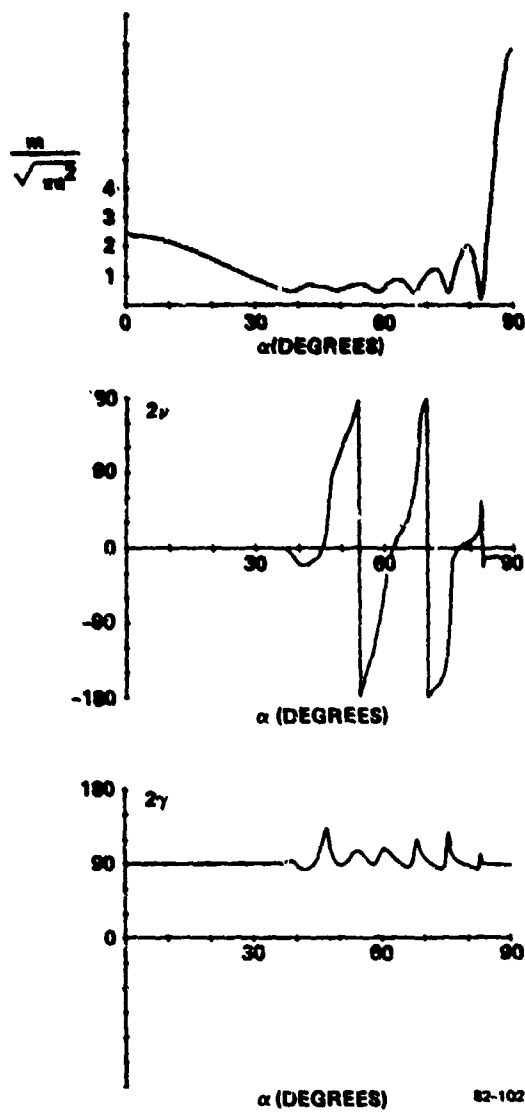


FIG. 9 Parameters m , 2ν , and 2γ of scattering matrix vs. aspect, for RCC with $L/D = 5$, $ka = 2.4$.

The cross-pol maximum polarization, as discussed in Section 2.5, is defined by the parameter 2ν (the longitude on the polarization chart) and occurs on the equator of the polarization chart. The co-pol null polarization is determined by both 2ν and 2γ . (Since the co-pol null locus has one more degree of freedom than the cross-pol max locus, the cross-pol max locus will usually not be discussed - it is simply the projection onto the equator along longitude lines of the co-pol null locus.)

A partial co-pol null locus is plotted on the polarization chart for aspects between 35° and 52.5° (Figure 10). The longitude of the co-pol null is 2ν and the co-latitude is 2γ . Below $\alpha = 35^\circ$, the co-pol null is at the center (LC) and above 50° ; it makes several traversals around the Poincare sphere, near the equator (as indicated by Figures 9b and 9c) before coming to rest near LC (or RC) again for $\alpha = 90^\circ$.

Several comments are in order about these null locus plots to avoid confusion. First, recall that there are actually two loci, displaced by $2\nu = 180^\circ$. We always plot only one locus, the other would appear symmetrically about the H-V axis on the polarization chart. Second, the choice of one null or the other in tracing the locus is completely arbitrary. The computer algorithm used to generate these curves chooses the null closest to the previously computed null, thus tracing out a smooth curve; if a different choice were made, or if the aspect steps between samples were too coarse, the locus would exhibit discontinuous skips from one side of the polarization chart to the other. There is no significance to this skipping; it is not incorrect, but makes a confusing picture. Third, the polarization chart shows only one hemisphere of the Poincare sphere; here, nominally the left-sense hemisphere. In presenting the null-locus, we have here superposed the left- and right-sense hemispheres, in order for the locus to show up as a smooth curve. This means that in Figure 10, as the locus moves from the LC center to the perimeter, it continues on the back-side of the Poincare sphere. In later figures, where the full locus is shown, the apparent figure-eight behavior is actually an undulating curve continuously turning around the sphere.

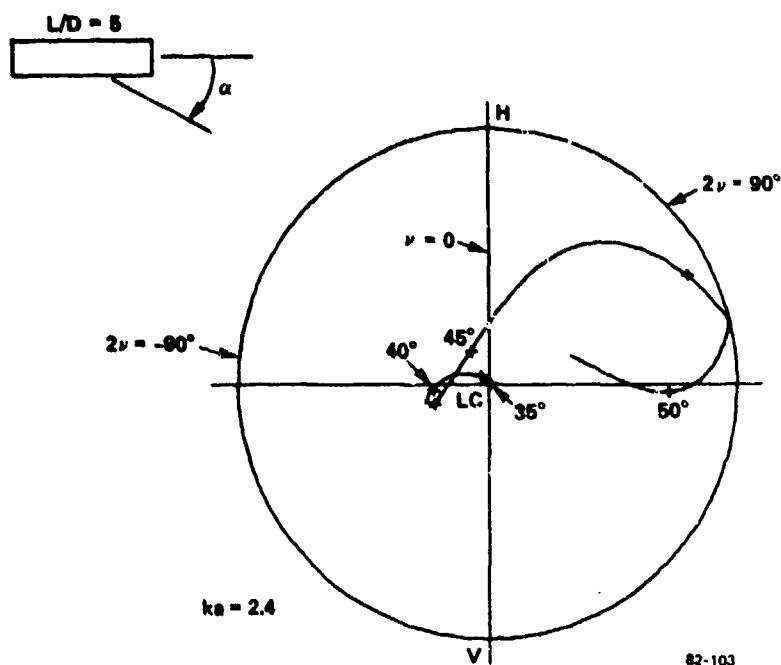
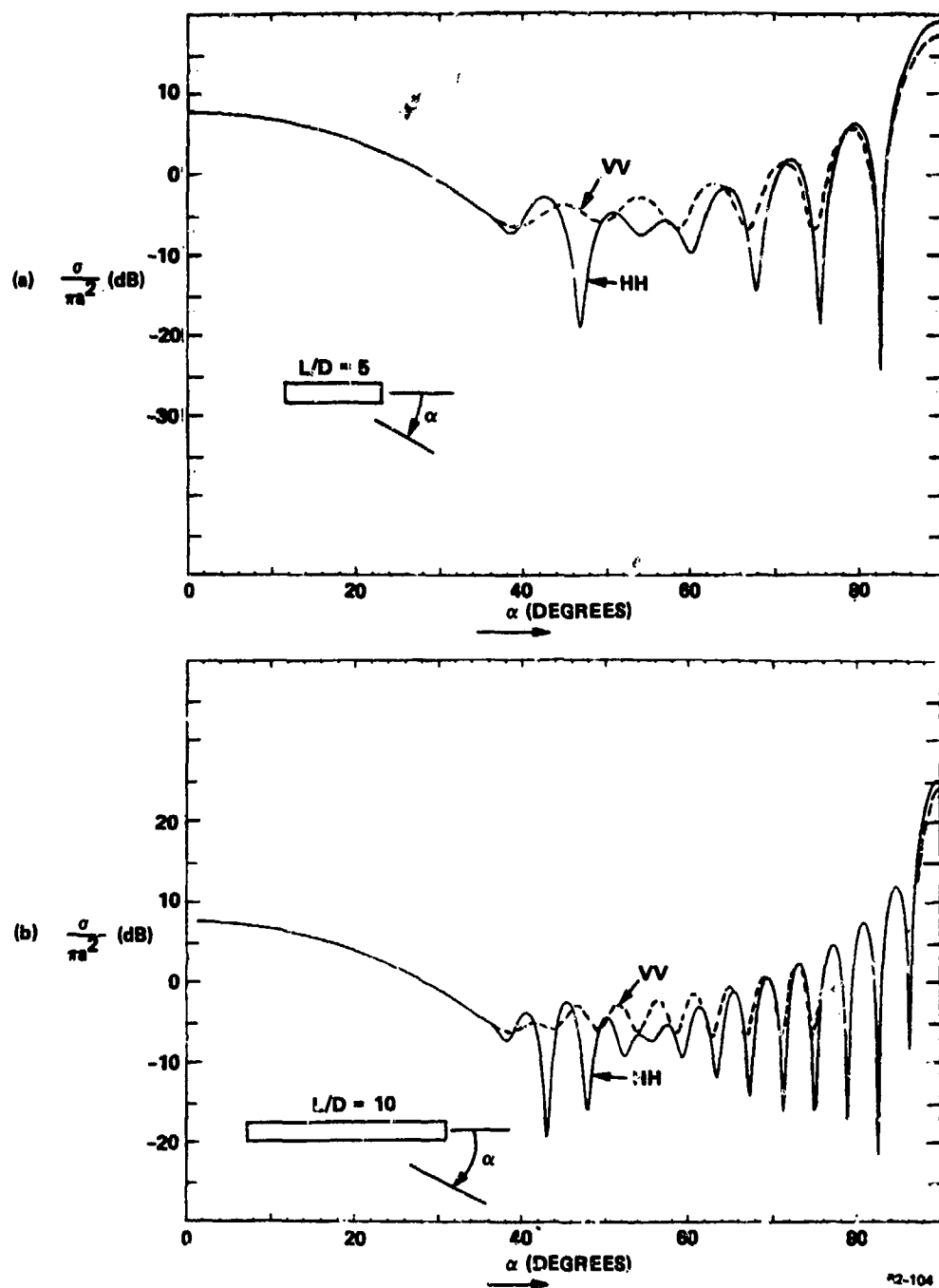


FIG. 10 Partial copol null locus for RCC, $L/D = 5$, at $ka = 2.4$. Aspect change 35° to 52.5° (ticks at 2.5° steps).

For a longer cylinder, the response fluctuations are more rapid. The HH and VV radar cross sections for a $L/D = 10$ cylinder at $ka = 2.4$ are shown in Figure 11b; the responses of the $L/D = 5$ cylinder are duplicated in Figure 11a for easy comparison. The complete characterizations of the scattering matrices for these two cases in terms of m , $2v$, and 2γ are shown in Figure 12. The left column (a,b,c) duplicates previous results for the $L/D = 5$ cylinder, the right column (d,e,f) are the corresponding parameters for the $L/D = 10$ cylinder. The behavior of the two cylinders is very similar, the main difference being the more rapid variation of the larger cylinder. The $(2v, 2\gamma)$ loci, that is the co-pol null loci, are plotted on the polarization charts in Figure 13. The plots have been broken up into four intervals of aspect α , to display the loci more clearly. As before, the left column is the $L/D = 5$ cylinder, the right column is the $L/D = 10$ cylinder. The tick marks on the curves correspond to $2-1/2^\circ$ aspect change. The locus moves around the Poincare sphere in an undulating fashion, except that for $\alpha = 0$ to 40° the null is fixed at the center (circular polarization). We see that the cylinder may act at some aspects like a single-bounce scatterer (null near CP), and at other aspects like a double-bounce scatterer (null near 45° linear polarization, i.e. the extremes of the equator). One traversal around the Poincare sphere looks similar to some of the dumbbell results of Figure 6, as was expected, since the cylinder consists of three scatters; one strong, one weaker, and the third much weaker. The null loci are generally in the upper (H) hemisphere, reflecting the facts that the VV response of the cylinder is somewhat larger than the HH response most of the time and that the HH response minima are deeper. At broadside, the VV response is smaller than the HH response, so that the final null position is in the lower hemisphere (not clear in the figures). For a very thin cylinder (ka small, L/D large), we expect behavior like a dipole (null at V) at broadside.

The aircraft models to be studied in this report scale in the UHF region to higher values of ka , namely $ka = 5.24$ and $ka = 8.15$ with $L/D = 10$. The behavior of cylinders at those scalings are shown in Figures 14 and 15. The organization of these plots is similar to that of the



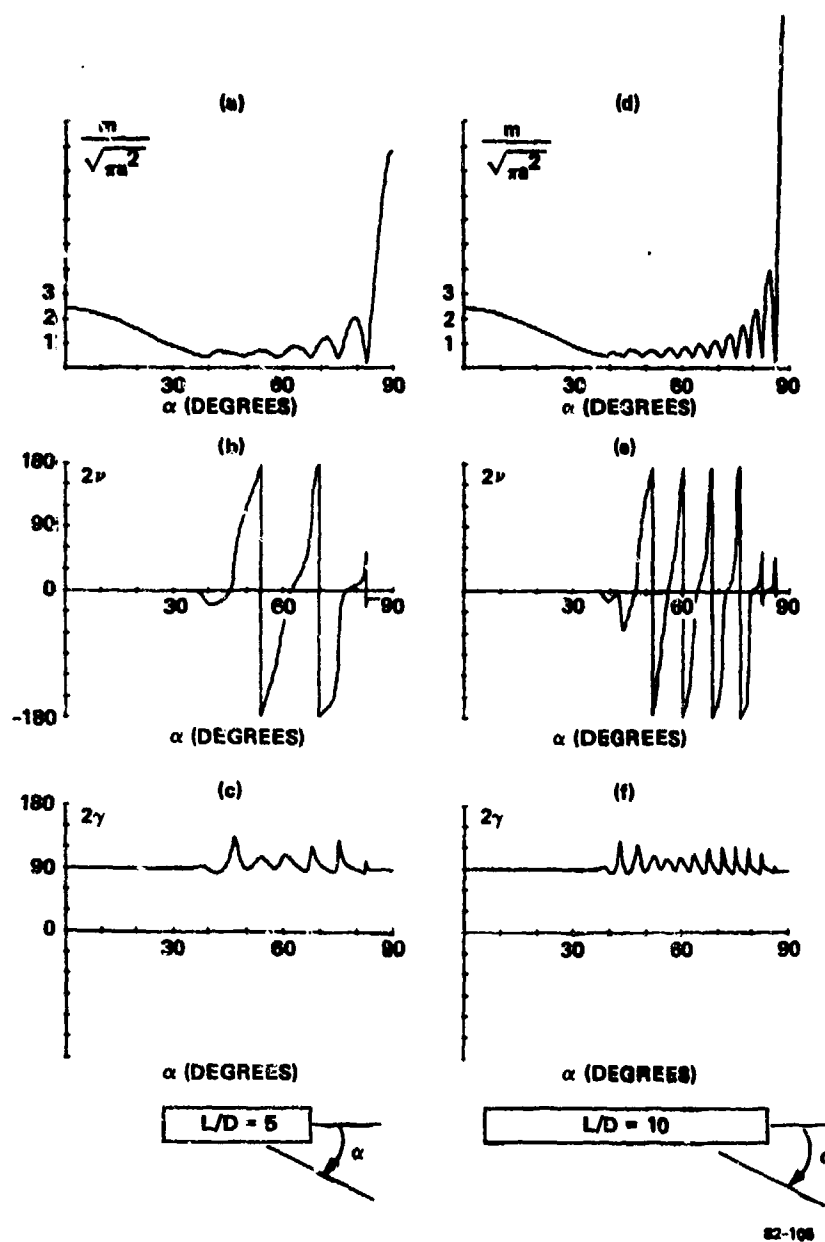


FIG. 12 Parameters m , 2ν , and 2γ of scattering matrix vs. aspect for RCC with $L/D = 5$ and for RCC with $L/D = 10$; at $ka = 2.4$.

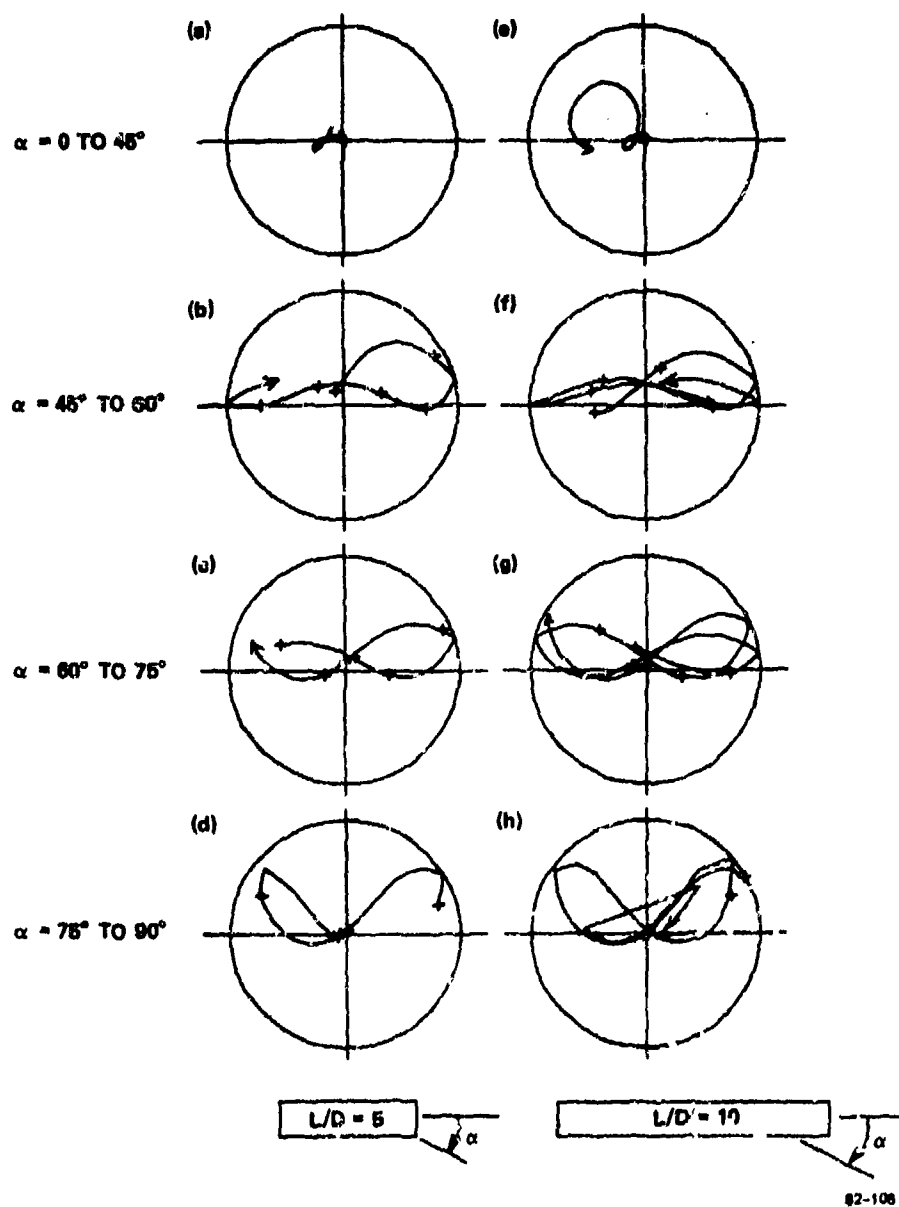
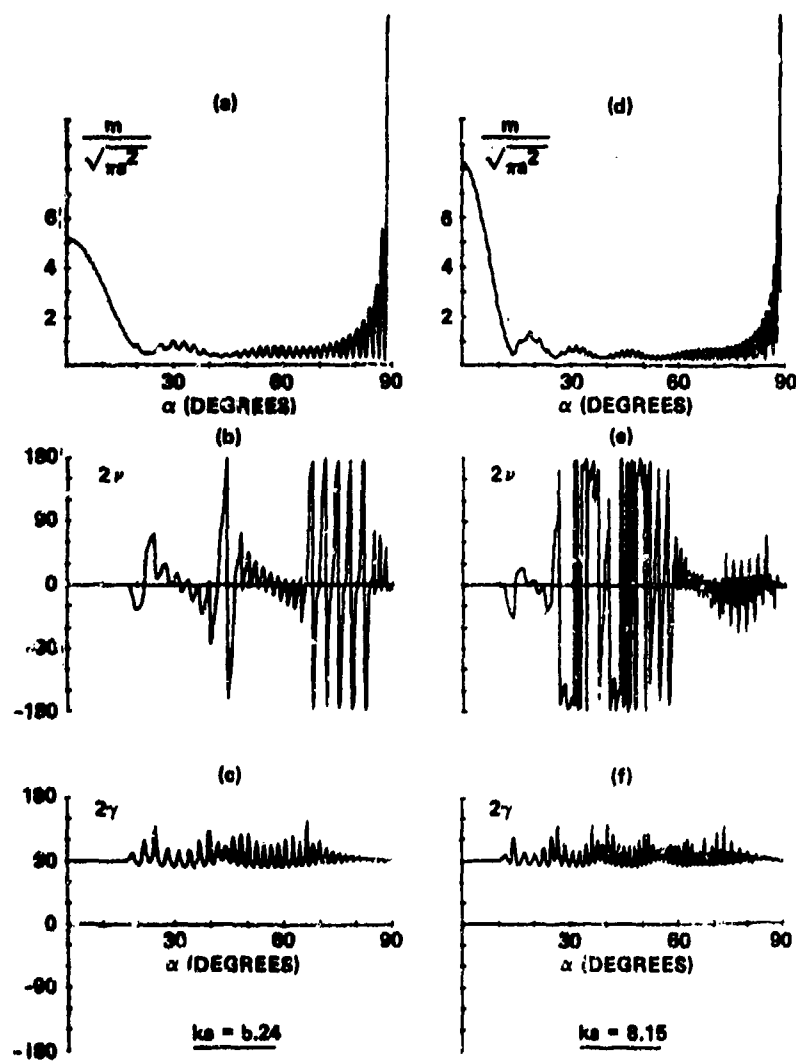


FIG. 13 Copol nuli loci over various aspect intervals. Left column: RCC with $L/D = 5$, right column RCC with $L/D = 10$; at $ka = 2.4$.



82-107

FIG. 14 Parameters m , 2ν and 2γ vs. aspect for RCC, $L/D = 10$ at $ka = 5.24$ (left column) and $ka = 8.15$ (right column).

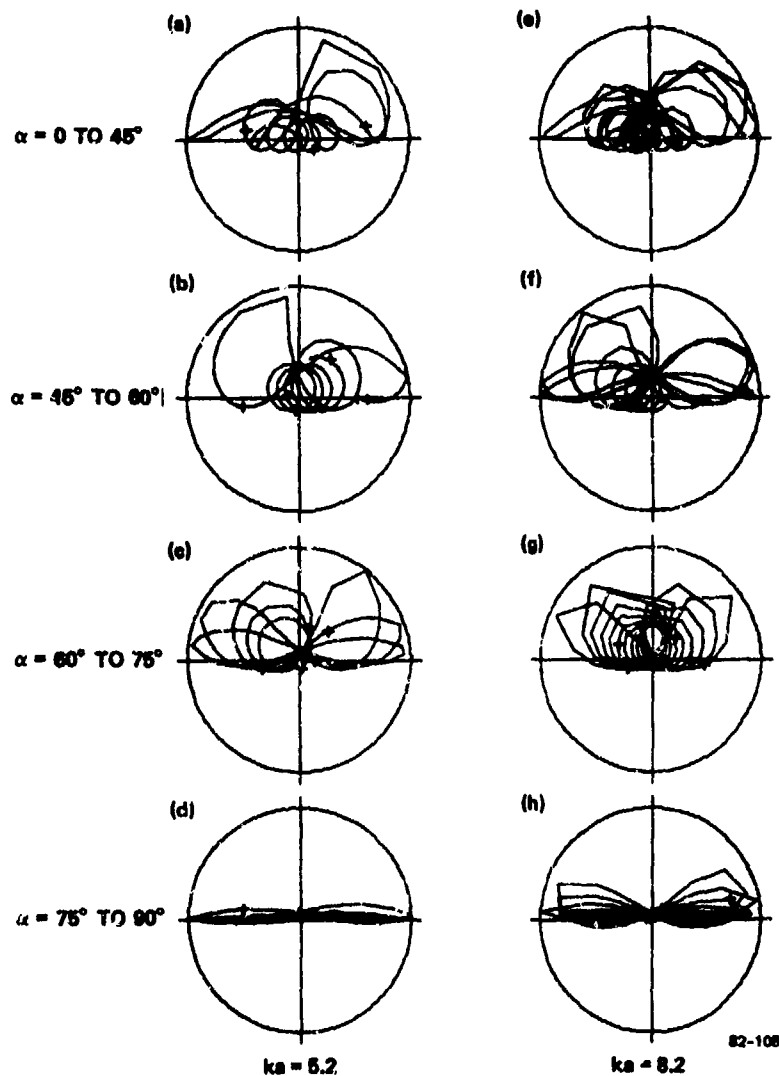


FIG. 15 Copol null loci over various aspect intervals for RCC, $L/D = 10$; at $ka = 5.24$ (left column) and at $ka = 8.15$ (right column).

previous two figures; here the left column is for $ka = 5.24$ and the right column for $ka = 8.15$, with $L/D = 10$ in both. The results are similar to the cases with lower ka , except that the variation with aspect is more rapid. An interesting detail of the locus, which (by coincidence!) didn't show up in the lower ka cases is a spiral motion. Part of the Figure 15b locus is reproduced in Figure 16 to show this behavior more clearly. This effect had been predicted in the dumbbell study earlier in this section. It is caused by one dominant scatterer interfering with a weaker scatterer, through several interference cycles, while the relative strengths of the scatterers change slowly.

Note that for scaling of the aircraft models to S-band or X-band (about a factor of 10 higher in ka) the fluctuations of the null characteristics would be a factor of 10 or so more rapid yet. It is clear that any target discrimination scheme based upon null characteristics of an unresolved target could, at these frequencies, not be used when using a point by point comparison. Rather, average or statistical features would have to be used. For example: For a cylinder, 2γ is on the average slightly greater than 90° , and doesn't go much below 90° . The presence of other large scatterers on the structure are likely to alter this picture. It is therefore pertinent to examine more complex targets, as is done in Section 3.

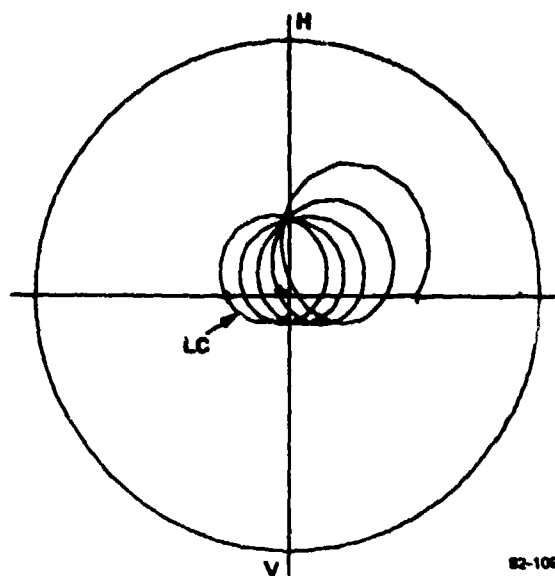


FIG. 16 Copol null locus over aspect change $\alpha = 50^\circ$ to 60° ; for RCC, $L/D = 10$; at $ka = 5.24$; showing spiral behavior.

2.10 EXTENSION OF PREVIOUS RESULTS TO A NON-DIAGONAL SCATTERING MATRIX

So far we have discussed symmetric targets which have a diagonal scattering matrix, and which can be parameterized by the three real quantities m , $2v$, and 2γ . The most general monostatic, relative phase scattering matrix is symmetrical and requires two more real parameters (corresponding to the complex off-diagonal term). From the discussion in Appendices 2 and 4 and Section 2.4, the general scattering matrix A , is related to a diagonal matrix D , by the similarity transformation

$$D = (Q_\Psi Q_\tau)^T A (Q_\Psi Q_\tau), \quad (33)$$

where

$$Q_\tau = \begin{pmatrix} \cos \tau & j \sin \tau \\ j \sin \tau & \cos \tau \end{pmatrix}, \quad (34)$$

$$Q_\Psi = \begin{pmatrix} \cos \Psi & -\sin \Psi \\ \sin \Psi & \cos \Psi \end{pmatrix}, \quad (35)$$

The effect on the Stokes vector representing a point on the Poincare sphere is a rotation of 2τ about the s_2 (45° linear polarization) axis, followed by a rotation of 2Ψ about the s_3 (circular polarization) axis. In particular, the polarization maximum, m , will be rotated by 2τ and 2Ψ from its position at H or V for the diagonal matrix. Now, a rotation of 2Ψ of the Poincare sphere corresponds physically to a rotation by Ψ of the target or of the polarization reference plane) about the RLOS. A rotation of 2τ corresponds to a change of τ in the ellipticity of the polarization ellipse (Figure 1). Considering our polarization chart representation of the null locus (e.g. Figure 5), the chart would be rotated out of the plane of the page and then rotated in the page about the center. This operation destroys some of the convenience of the polarization chart. For instance, the two co-pol nulls will now no longer be located symmetrically about the HV axis. Therefore, in our work with non-symmetric targets, we will usually remove the τ and Ψ transformations from the matrix and continue to plot the polarization characteristics in the standardized way with \textcircled{M} at the top (or

bottom). The complete description of the scatterer will then require the τ and Ψ history in addition to that of m and the co-pol null locus. Alternatively we can present five separate plots of m , 2ν , 2γ , 2τ , and 2Ψ .

The solution for Ψ and τ may be found by writing out Equation (33) in full. The result is

$$\tan 2\Psi = \frac{2\operatorname{Re}((a_{HH} + a_{VV}) a_{HV}^*)}{|a_{HH}|^2 - |a_{VV}|^2} \quad (36)$$

$$\tan 2\tau = \cos 2\Psi \frac{2\operatorname{Im}((a_{HH} - a_{VV}) a_{HV}^*)}{|a_{HH}|^2 - |a_{VV}|^2} \quad (37)$$

The diagonalized matrix is then given by

$$\begin{aligned} D_{11} &= c^2 a_{HH} + s^2 a_{VV} + 2c^* s^* a_{HV}, \\ D_{22} &= c^2 a_{VV} + s^2 a_{HH} - 2cs a_{HV}, \end{aligned} \quad (38)$$

where

$$\begin{aligned} c &= \cos\tau \cos\Psi + j \sin\tau \sin\Psi, \\ s &= \cos\tau \sin\Psi - j \sin\tau \cos\Psi. \end{aligned}$$

The co-pol max polarization before the transformation is given by $(-\Psi, -\tau)$. After the transformation, the co-pol max is either at H or V, as for the diagonal scattering matrices discussed before. 2Ψ and 2τ are both restricted to between $\pm 90^\circ$.

2.11 EFFECT OF POLARIZATION CALIBRATION ERRORS ON NULL MEASUREMENTS

As described in Section 4, great care was taken in the measurement program to assure proper calibration of the two channels of the dual-polarized radar. The calibration procedure is rather complicated due to the fact that a complex 2×2 calibration matrix has to be determined, as opposed to the single real constant required for the single-polarization case. It is of interest to know just how well such a calibration needs to be carried out.

First, consider a calibration error of the form

$$E = k \begin{pmatrix} 1 & 0 \\ 0 & \epsilon e^{j\phi_\epsilon} \end{pmatrix} ; \quad (39)$$

that is, the vertical channel introduces additional attenuation and a phase change. The measured scattering matrix will be of the form $A_M = EA$, where A is the actual scattering matrix. The constant k is just the absolute calibration factor, the same as required for single-polarization measurements, and will not be discussed further.

The effect on the apparent polarization characteristics is seen readily: ϵ changes the relative magnitude of the a_{HH} and a_{VV} components of the matrix and hence changes the value of 2γ . That is, the measured value γ' is related to the true value γ by

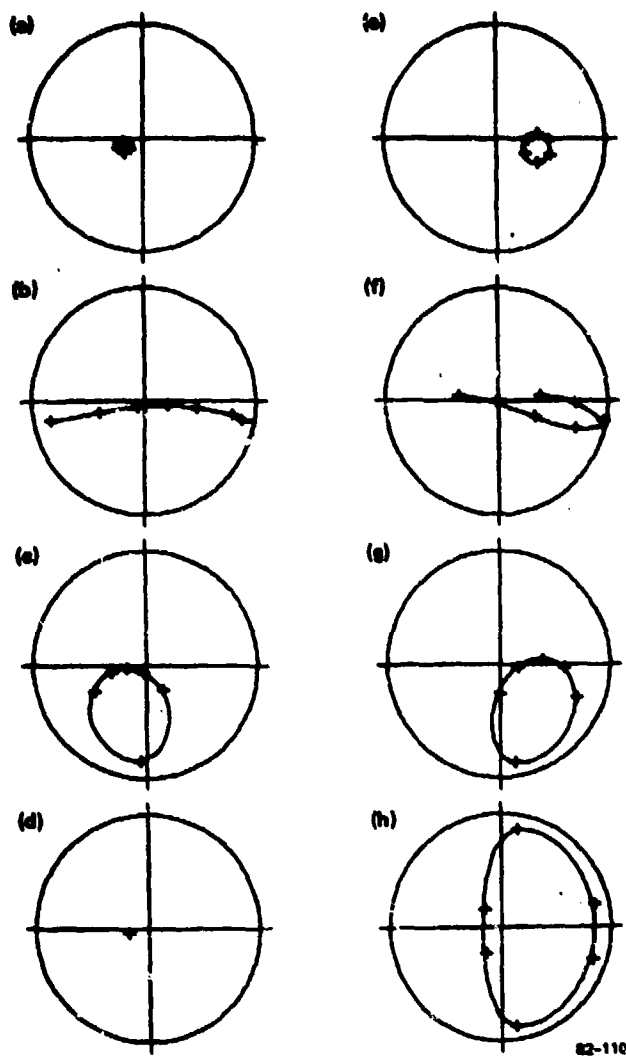
$$\tan^2 \gamma' = \epsilon \tan^2 \gamma .$$

This causes a distortion in the latitude of the polarization chart.

The effect of ϕ_ϵ is to change the apparent phase between the a_{HH} and a_{VV} components and hence change the value of 2ψ . That is, the polarization chart will be rotated about the HV axis. In particular, a point at LC (chart center) will move off-center, hence a single-bounce scatterer will appear as not quite single-bounce. To get some feeling for these errors, the dumbell cases of Figure 6 have been recalculated for an

error of 10 percent in relative amplitude and 30° in phase ($\epsilon = 0.9$, $\phi_\epsilon = 30^\circ$). The results are shown in Figure 17. We see that the effect of calibration errors are not serious unless a precise knowledge of $2v$ or 2γ is desired.

If the error matrix also has off-diagonal terms, the effect is more complicated. If the off-diagonal errors are symmetric (which is unlikely), then the error contains additional rotations in τ and Ψ , as discussed in Section 2.10. If the errors are non-symmetric, the effect depends on just how the data is manipulated to obtain the polarization characteristics. Clearly, it is best to obtain both a_{HV} and a_{VH} by independent measurement, and then average them to remove the non-symmetric part of the error matrix.



82-110

FIG. 17 Copol loci, showing effect of error in VV channel of 10% magnitude, 30° phase. Compare this with figure 6.

SECTION 3

COMPUTED POLARIZATION PROPERTIES OF SIMPLE AIRCRAFT MODELS

This investigation into the polarization characteristics of aircraft models followed two paths simultaneously and interactively: the direct measurement of polarization responses and the computation of the responses, i.e., target modeling. The reasons for pursuing the target modeling approach are compelling; through it, the dependence of polarization characteristics upon target parameters (such as the shapes, sizes, and interrelationships of its parts) and observation parameters can be studied readily without restriction and without the nuisance of noise and other measurement hazards. Phenomena yield more readily to understanding so that predictions can be made for other targets and observation conditions. The problem with target modeling (as a solitary method) is that one is never certain that the modeling is adequate, since the scattering process is usually highly complex. Hence the suspicion could arise that the derived polarization properties are mere artifacts of the target models. Of course, similarly, if only measured responses are analyzed, the results could be coincidental properties of the particular targets or measurement conditions. Our dual modeling/measurement approach attempts to deal with these pitfalls. First: an effort was made to model the target response accurately, though, with computationally efficient algorithms. Second: the computed aircraft model responses and their derived polarization characteristics were compared with the measurements taken of these models. The agreement was, for the most, part very good. The inevitable discrepancies were explained and shown to have no effect on the general conclusions. Conclusions could then be drawn with some confidence from the computed responses.

One difficulty remains: the targets studied here are rather simple, consisting of fewer scattering centers than an actual aircraft. Since the object of this study is to examine the applicability of polarization concepts to discrimination between actual aircraft, one must avoid generalizations based on results which are artifacts of target (relative) simplicity. An example of this is the occurrence of a dominant distinctive response, which for these target models is present at only one aspect (due to the return from the leading edge of a wing). An actual target may have more of these or may have a distinctive response at a strategically important aspect, such as nose-on.

The details of the target modeling effort is collected in the appendices. At the size/wavelength scales of interest here, a complex target can be considered to consist of non-interacting scattering centers. The scattering centers are the edges and specular surfaces of the target model, and also the join regions (inside corners), which give the important double-bounce (or n-bounce) returns. Simple expressions obtained from PO and GTD are used to model the returns, when applicable. Where these expressions fail (such as at grazing incidence) they are modified to obtain agreement with known responses for plates or cylinders. The known responses include published experimental results and exact diffraction integral computations, such as the Sperry Research Center STIE results. It was found possible to describe the polarization and aspect dependent response of scattering centers adequately with simple expressions, although some of these are ad-hoc.

The targets and their computed polarization characteristics are given in the remainder of Section 3. The measured responses and the comparison of measurements with computations are given in Section 4.

3.1 DESCRIPTION OF THE AIRCRAFT MODELS

The general features of the simple aircraft models were specified by RADC. Three targets were to be studied, each at four size-scales. Two of the targets were to be similar in size and shape with a difference in detail such as wing shape or position, the third target was to be dissimilar. The target models constructed (and computed) all consisted of a cylindrical fuselage and flat quadrilateral wings. They are plane symmetric.

Models 1 and 2 are suggestive of the F-5 and MiG-21, respectively. These are roughly the same size and differ in the sweep of the wings (30° and 60° , respectively). Model 3 is suggestive of the MiG-25; it is larger, has a relatively larger wing area, but has a wing angle of 30° like Model 1. The size-scales were chosen to correspond to frequencies ranging from 350 MHz to 1.9 GHz.

The target models are illustrated in Figure 18. The dimensions shown are the approximate full scale dimensions of the aircraft. The dimensions of the models are summarized in Tables 3 and 4. These dimensions appear in the headers of the computer-generated plotted results. Size-scale A corresponds to what is considered to be the lowest practical radar frequency. Even at this low frequency, the targets are many wavelengths long. Scales B, C, D correspond to progressively higher frequencies.

It will be seen that the general characteristics of these targets are similar at all the frequencies considered; the main difference being the rate of fluctuation with changing aspect. No new results are expected at higher equivalent frequencies than size-scale D. In fact, all the important conclusions of this study could be drawn from the results of sizes A and B. Computations were also made for a lower $ka \approx 2.4$ (corresponding to 160 MHz for a full scale model). This is considered near the lower limit of applicability of the scattering center model for these targets. (No measurements were made at this size scale, since the SNR would be too low).

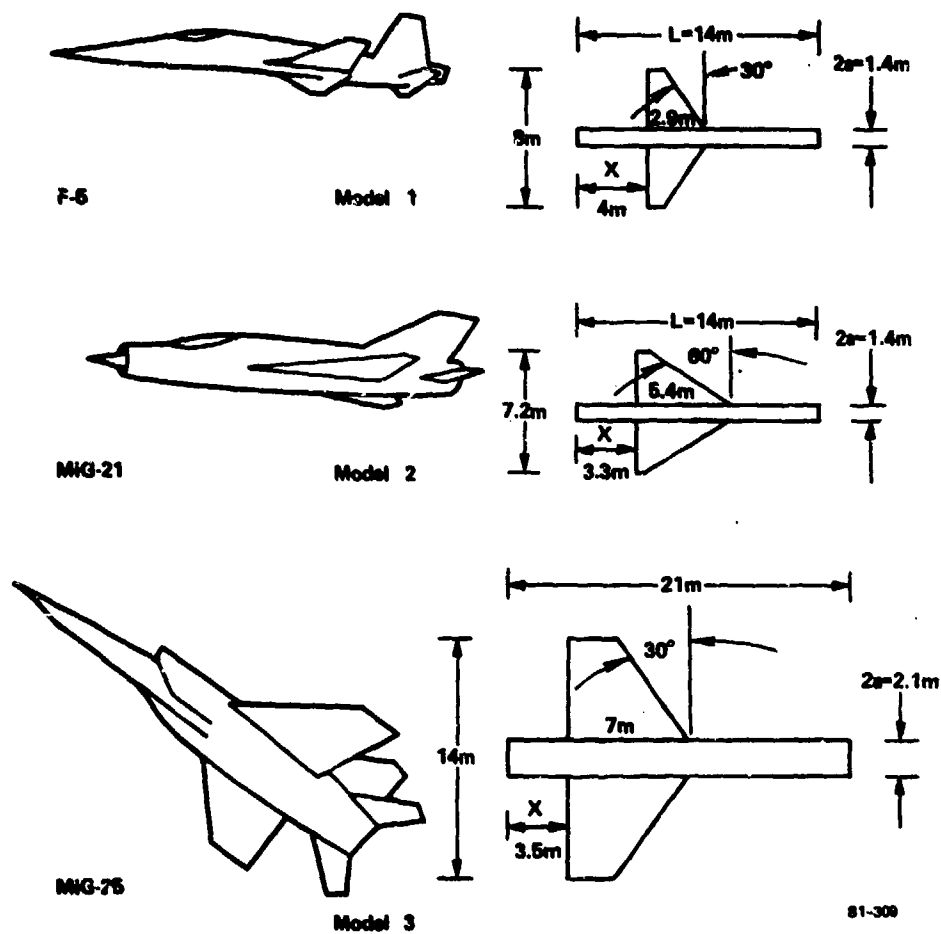


FIG. 18 Target models, with approximate full scale dimensions.

TABLE 3 TARGET DIMENSIONS IN UNITS OF CYLINDER RADIUS, a

Model	H/a	B/a	DZ/a	Z1/a	θ_1 (degrees)
1 (F-5)	10.	4.71	4.0	-0.3	30
2 (MIG-21)	10.	3.85	7.4	2.0	60
3 (MIG-25)	10.	5.85	6.3	-0.3	30

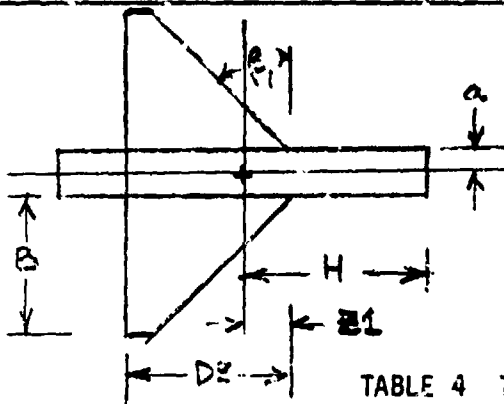


TABLE 4 TARGET SIZE SCALES

Size Scale	Full Scale Frequency	Model	ka	Model Dimension* 20 a (cm)
A	350 MHz	1	5.24	14.3
		2	5.24	14.3
		3	8.14	22.2
B	550 MHz	1	8.14	22.2
		2	8.14	22.2
		3	12.8	34.9
C	870 MHz	1	12.8	34.9
		2	12.8	34.9
		3	18.6	50.8
D	1.27 GHz	1	18.6	50.8
		2	18.6	50.8
		3	27.9	76.2

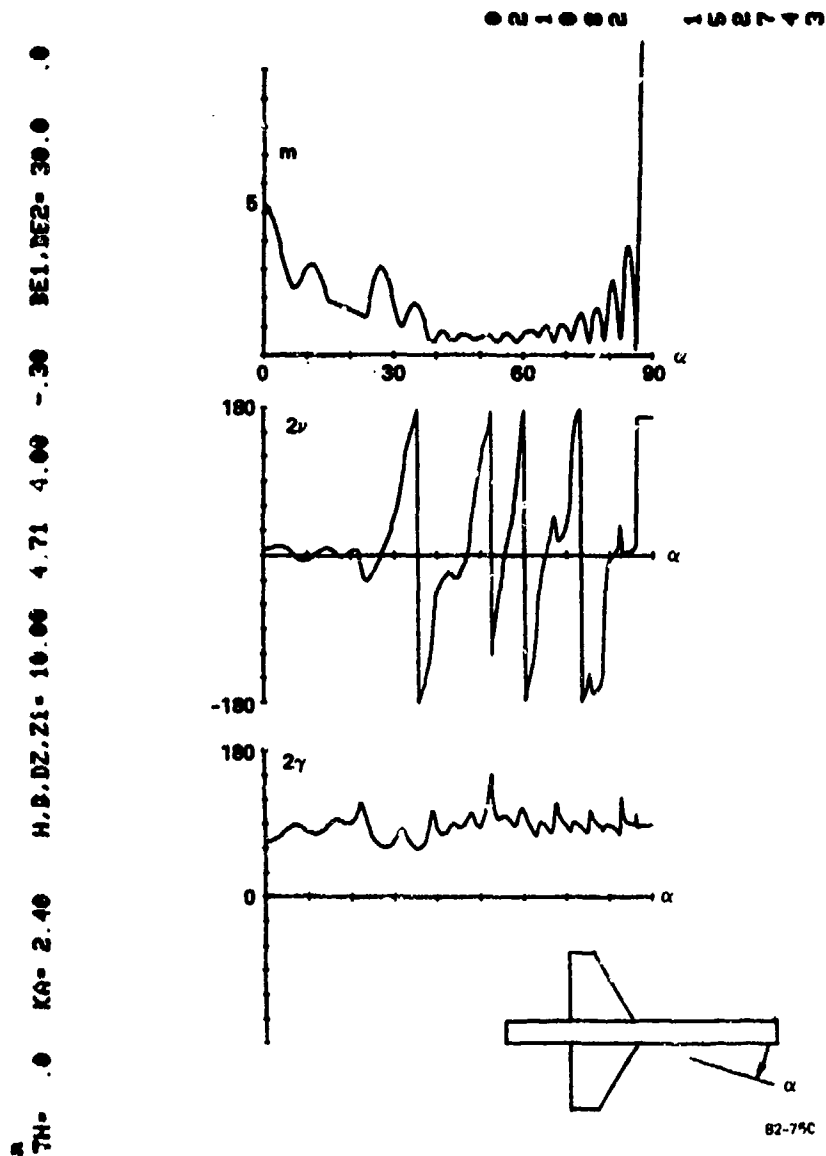
*Model dimension reference (cylinder length) for measurement at 35 GHz

3.2 COMPUTED AIRCRAFT CHARACTERISTICS AT 0° ELEVATION

We will first examine the polarization characteristics of Model 1 at the low frequency $ka = 2.4$. The parameters m , $2v$, 2γ are plotted versus aspect in Figure 19. The target is plane symmetric at 0° elevation, so that the scattering matrix diagonal and the three parameters completely describe the target. The cross-pol null polarizations (one of which is the co-pol max polarization) are at the top and bottom of the Poincare sphere. The co-pol null polarizations (see Section 2) are given by the parameters $\pm 2v$ and 2γ , which are respectively the longitude and co-latitude of the point on the Poincare sphere. The magnitude, m , is the square root of the co-pol max power.

From now on, the parameters m , $2v$, 2γ will be plotted, as in Figure 19, as functions of aspect (0° to 90°), rather than plotted as a locus on the Poincare sphere or polarization chart. The reason is that the locus fluctuation is so rapid it is difficult to follow its detail on the Poincare sphere. A disadvantage is that the plot of the angle $2v$ shows discontinuities as it passes through $+$ or -180° . It should be remembered that $2v$ actually rotates continuously and smoothly around the sphere.

Model 1 consists of a cylinder (of which the polarization characteristics are illustrated in Figure 12) with the addition of wings at a 30° rake angle. The magnitude, m , has additional bumps on it due to the wings, compared with cylinder alone. The angle 2γ shows considerable deviation from the cylinder alone case, particularly at those aspects where the relative contribution of the wings to the response is strong ($\alpha \approx 30^\circ$). The wing has a horizontal return, hence the polarization maximum is at H polarization (top of sphere), and the co-pol nulls are in the lower hemisphere ($2\gamma < 90^\circ$). This last feature thus identifies a horizontal edge. For $\alpha > 40^\circ$, the target looks like a pure cylinder. It should be noted that the rapid little spikes in 2γ occur at minima in the target response (as seen in the plot of m). They occur when the cylinder H return happens to hit a deep null and the (small) response is temporarily mostly vertical. The effect of the wing on the co-pol null polarization is complicated, since it involves



PCAM - POLZN CHARACTERISTICS N. 2NU, 2GA US ASPECT FOR AIRCRAFT

FIG. 19 Polarization characteristics vs. aspect of model 1; $ka = 2.4$; $\theta = 0^\circ$.

the relative phases of the contributions from wing and cylinder. When the wing contribution is not much larger than that of the cylinder, its effect on the null polarizations is unclear. Only when the contribution of the wing is very large (as seen by a large bump in m) is there a distinctive (i.e., downward) change in 2γ .

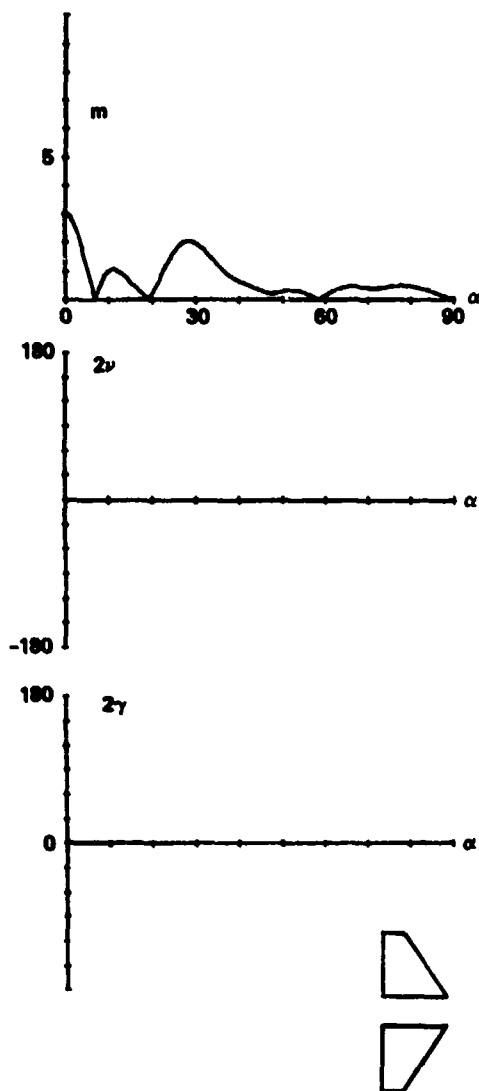
For comparison, the characteristics of wings alone are given in Figure 20. The wing response at $\theta = 0$ is purely horizontal, hence the co-pol null is at V ($2\gamma = 0$) for all aspects. ($2v$ is undefined and here plotted as zero).

As was already noted in the dumbbell investigation of Section 2, the polarization characteristics of the compound target bear little if any relationship to those of its component parts, except when one of the scatterers is dominant. The characteristics change rapidly with aspect; there are no invariants with aspect.

The response of the wings alone for Model 2 is shown in Figure 21. The leading edge of these wings have 60° rake, causing a peak in the response at 60° aspect. The response at 0° is due to the trailing edge return.

In Figure 22 the characteristics of Model 2 are plotted side by side with those of Model 1. We see that the characteristics of the two targets are different near 30° and 60° , where the respective wings have an appreciable effect. One could utilize this difference for target discrimination if the aspect were known. Since $2v$ varies more rapidly with aspect, the characteristic 2γ appears to be a better candidate for use in target discrimination. We note that even in these regions where 2γ show a distinctive departure from its average value, it is still a fluctuating quantity, the result of relative phase dependent interference of multiple scattering centers.

TH= 0 KA= 2.40 H.B.DZ.Z1= 10.00 4.71 4.00 -30 BE1.BE2= 30.0 0



021002 130350

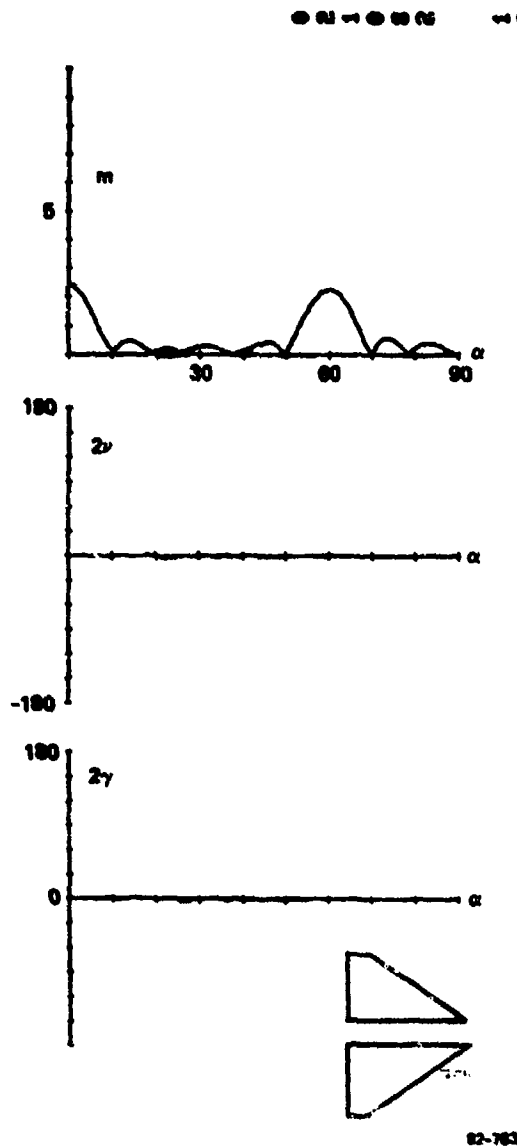
PCUM - POLYN CHARACTERISTICS N. 2NU. 2GA VS ASPECT FOR WINGS

7

82-787

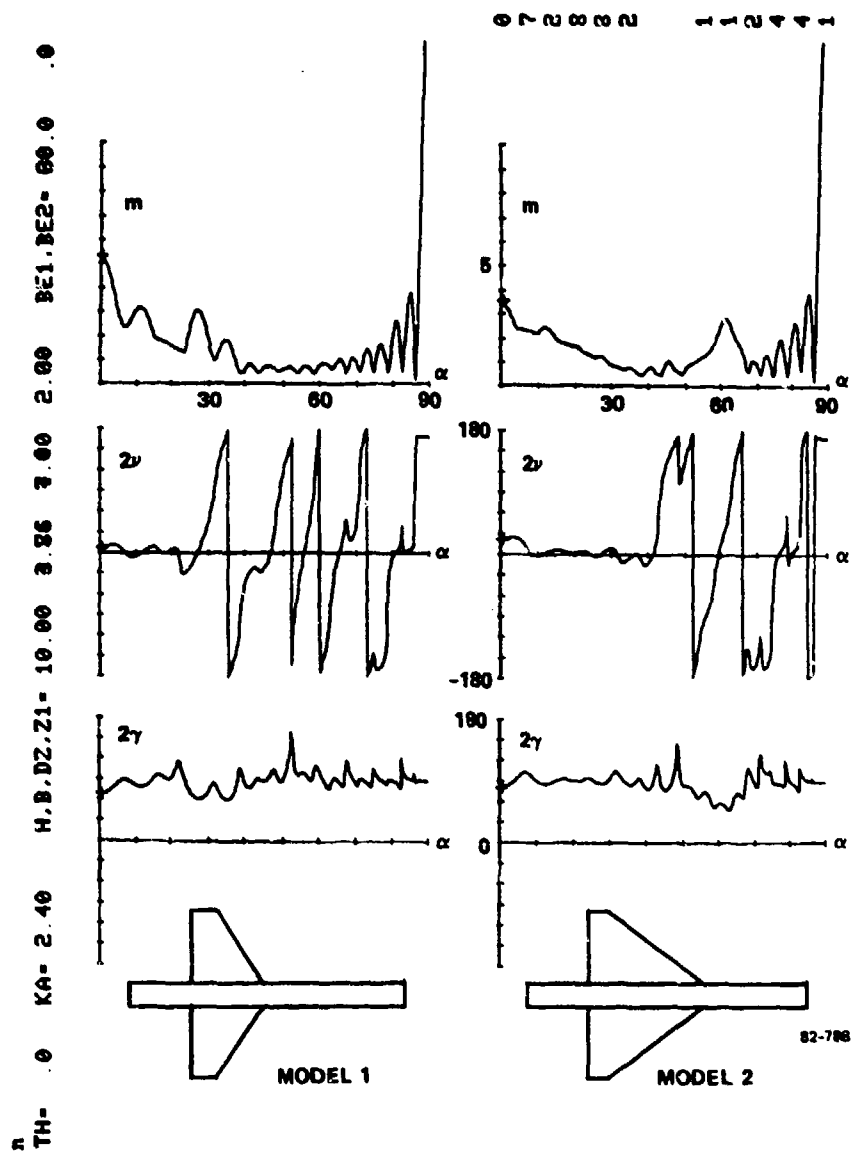
FIG. 20 Polarization characteristics vs. aspect of model 1 wings alone; $ka = 2.4$; $\theta = 0^\circ$.

$\alpha_{TN} = 0$ $ka = 2.40$ $M.B.DZ.21 = 10.50$ 3.86 7.40 2.00 $DE1.DE2 = 60.0$ 0



7 PCUM - POLYN CHARACTERISTICS M. 2MU. 2GA US ASPECT FOR WINGS

FIG. 21 Polarization characteristics vs. aspect of model 2 wings alone; $ka = 2.4$; $\theta = 0^\circ$.



PCAM - POLYN CHARACTERISTICS M. 2NU. 2GA US ASPECT FOR AIRCRAFT

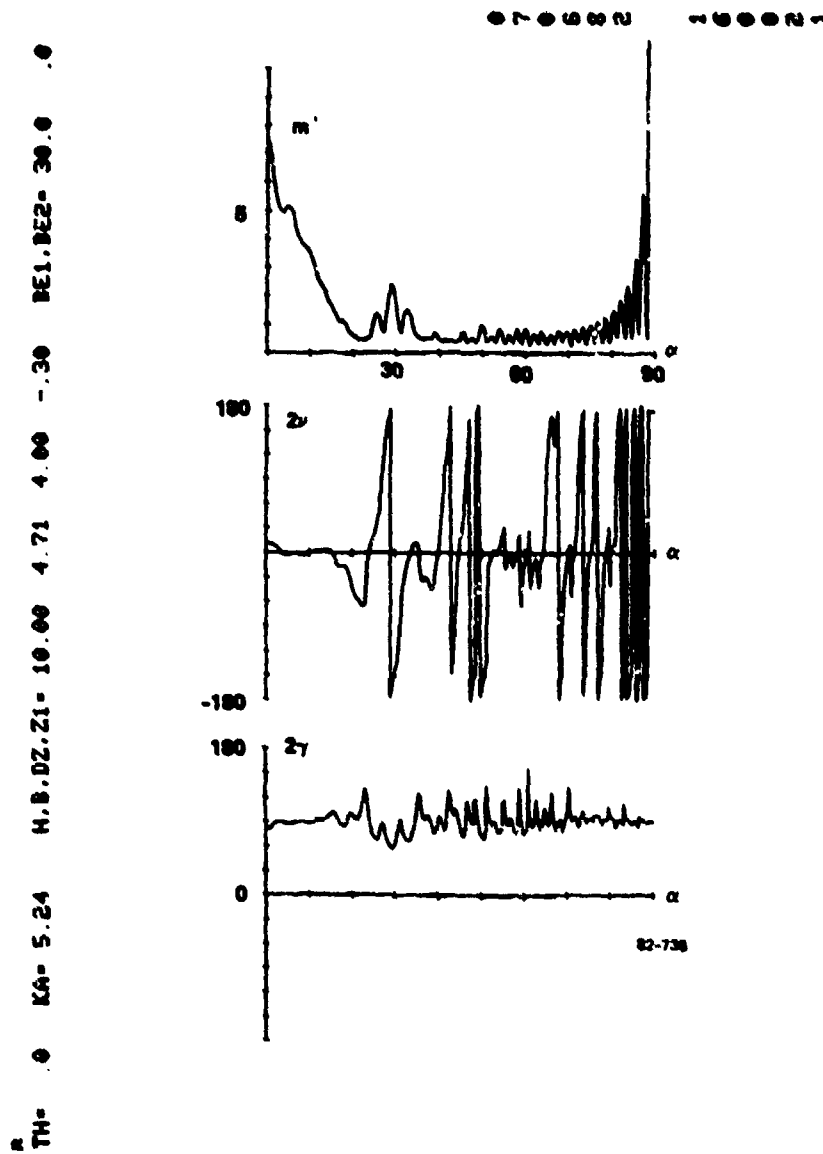
9

FIG. 22 Polarization characteristics vs. aspect of model 1 and model 2; $k_a = 2.4$; $\theta = 0^\circ$.

The frequency scales of interest in this study were higher than considered so far, namely $ka = 5.24$ and higher. We now present the computed null characteristics for all the aircraft models and some cylinders at all size scales, for elevation $\theta = 0$, in Figures 23 through 36. Let us concentrate first on Figures 23 through 26, which are for size scale A; respectively, cylinder 1 or 2 only (23), Model 1 (24), Model 2 (25), and Model 3 (26). The latter has a larger cylinder, which is actually represented by Figure 27, by coincidence of our frequency choices.

The cylinder (Figure 23) has a 2γ characteristic which averages near 90° (meaning that the HH and VV responses are about equal on the average). The angle 2ψ sometimes makes short excursions, sometimes varies continuously around the sphere. The co-pol null locus plotted on the Poincare sphere for aspects between 25° and 40° , a region of small 2ψ variation, would look like Figure 16 (a spiral); the locus for aspects between 65° and 80° , a region of continuous 2ψ variation, would look like Figure 13d (continuous encirclement of the sphere with up and down oscillation). The addition of the Model 1 wings (Figure 24) changes the characteristics profoundly. However, aspect has to be well-known to distinguish between the cylinder and Model 1 on the basis of a few measurements: Any value of 2ψ or 2γ which is taken on by the cylinder is also taken on by Model 1 at a nearby aspect. The exception is near 30° aspect, where the leading wing edge is dominant. The above remarks also apply to Model 2 (Figure 25), except that the distinctive region occurs at 60° . Model 3 (Figure 26) is larger and consequently the null characteristics vary more rapidly with aspect. Again, a distinctive region for 2γ is noted near $\alpha = 30^\circ$, corresponding to the wing rake angle. The characteristics of Model 1 and Model 3 are not readily differentiable except by the rate of fluctuation.

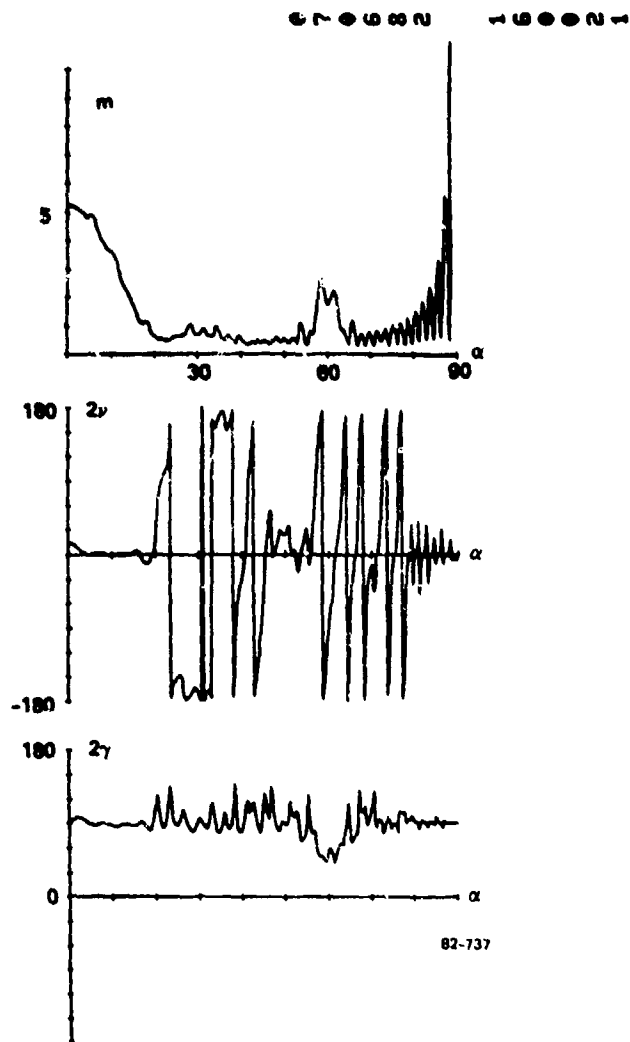
At the higher frequencies (size scales B through D of Figures 27 through 36), the above remarks apply virtually without change. The effect of the wings stands out more clearly in the plots of m and 2γ (the bumps at $\alpha = 30^\circ$ in Figure 36, for example), which is due to the fact that the wing edge response is independent of frequency, while the oblique cylinder response goes down by the square root of the frequency.



7 PCAM - POLYN CHARACTERISTICS N. 2NU. 2CA US ASPECT FOR AIRCRAFT

FIG. 24 Polarization characteristics vs. aspect of model 1, Scale A; $ka = 5.24$; $\theta = 0^\circ$.

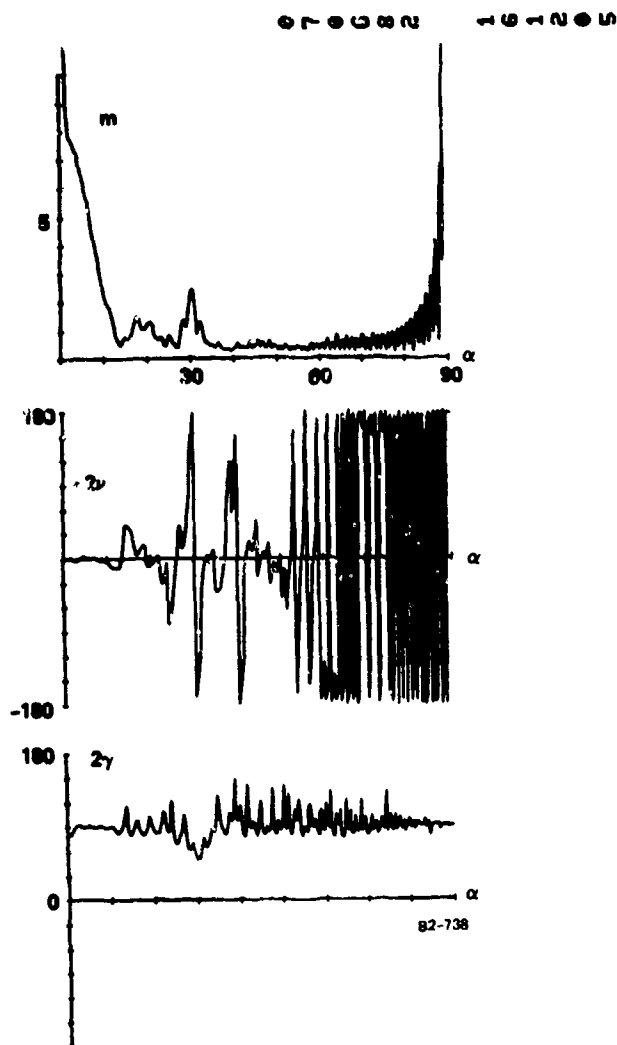
TH= 0 KA= 5.24 H,B,DZ,Z1= 10.00 3.86 7.40 2.00 BE1,BE2= 60.0 0



PCAM - POLYN CHARACTERISTICS M. 2NU, 2GA US ASPECT FOR AIRCRAFT

FIG. 25 Polarization characteristics vs. aspect of model 2, Scale A; $ka = 5.24$; $\theta = 0^\circ$.

TH= .0 KA= 8.14 H.B.D2.Z1= 10.00 5.85 6.30 -.30 BE1,BE2= 30.0 .0



7 PCAF - POLZN CHARACTERISTICS M. 2NU, 2GA VS ASPECT FOR AIRCRAFT

FIG. 26 Polarization characteristics vs. aspect of model 3, Scale A; $ka = 8.14$; $\theta = 0^\circ$.

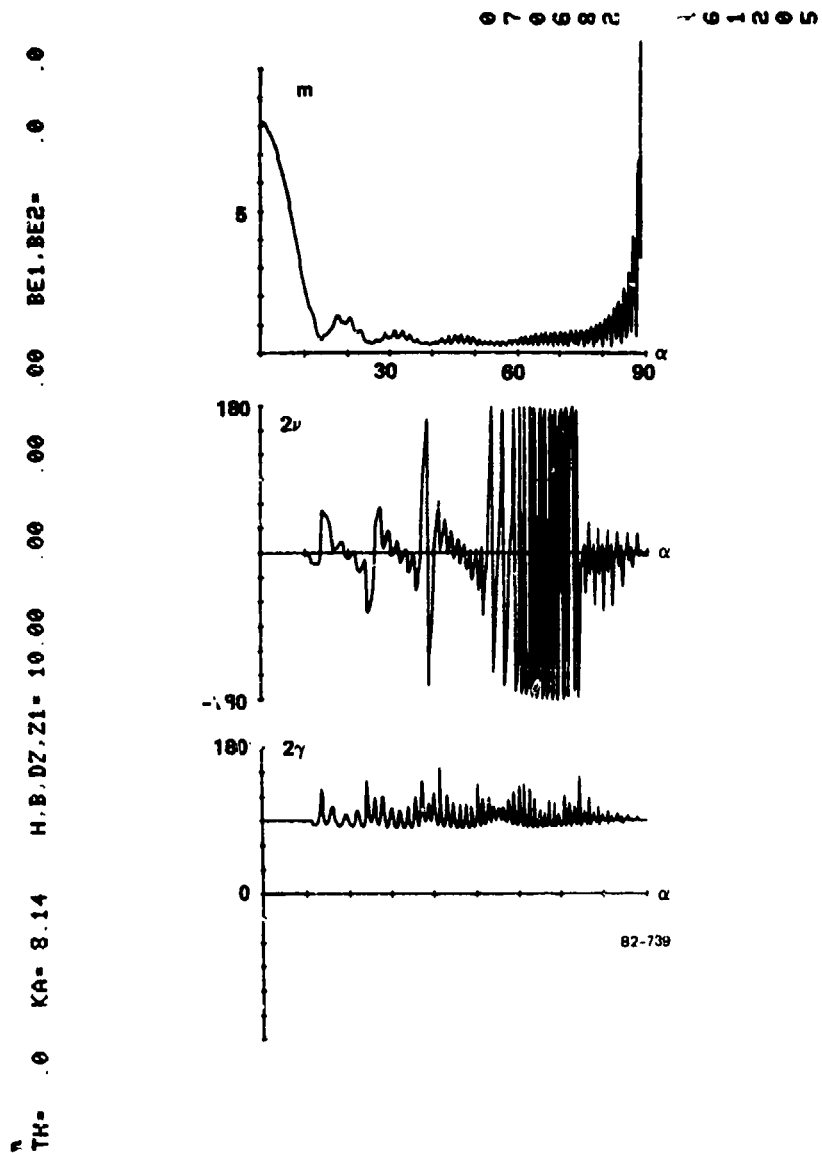
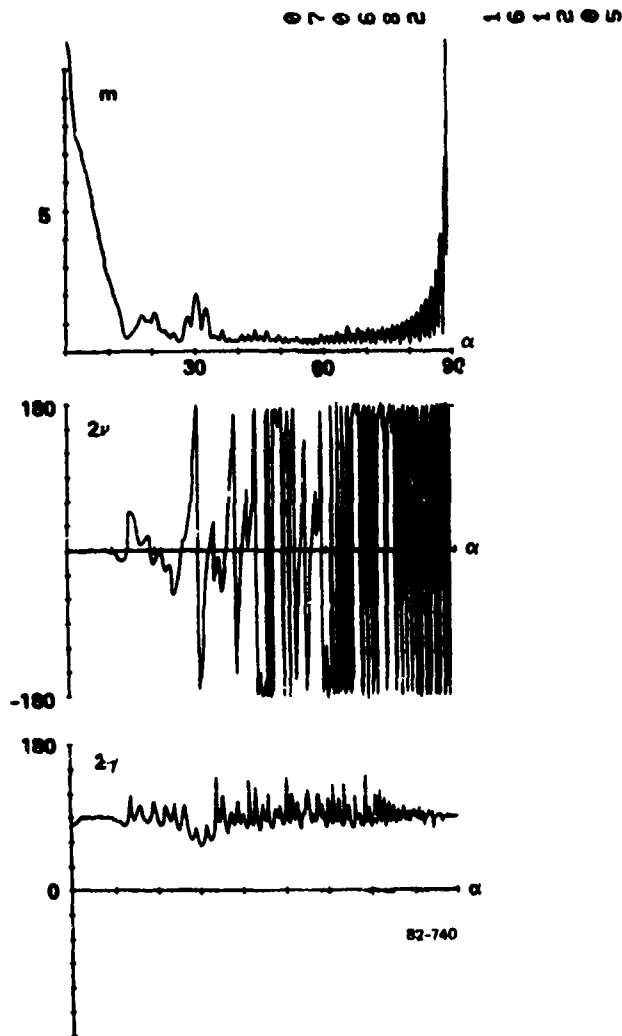


FIG. 27 Polarization characteristics vs. aspect of cylinder, Scale B; $ka = 8.14$; $\theta = 0^\circ$.

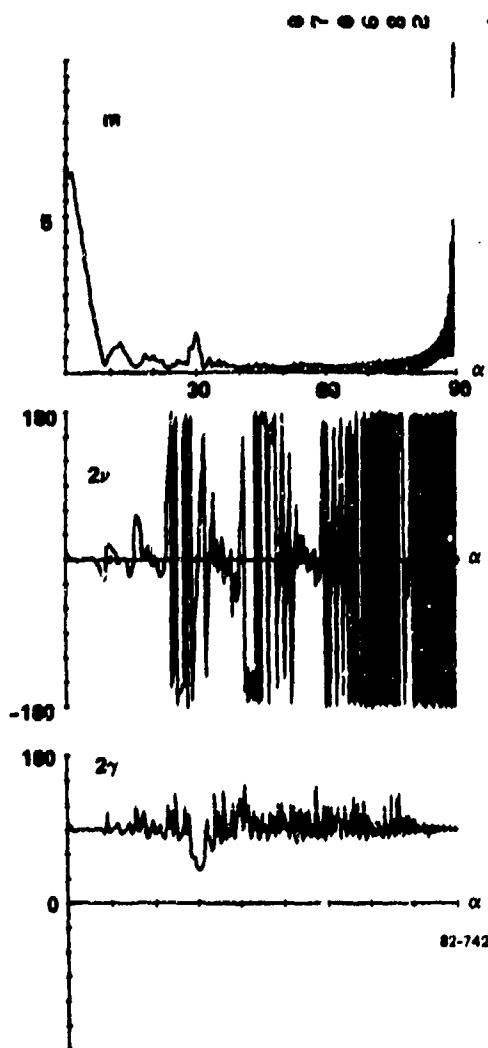
TH= 0 KA= 8.14 M.DZ.Z1= 10.00 4.71 4.00 -30 BE1.BE2= 39.0 0



PCAM - POLZN CHARACTERISTICS M. 2NU. 2GA US ASPECT FOR AIRCRAFT

FIG. 28 Polarization characteristics vs. aspect of model 1, Scale B; $ka = 8.14$; $\theta = 0^\circ$.

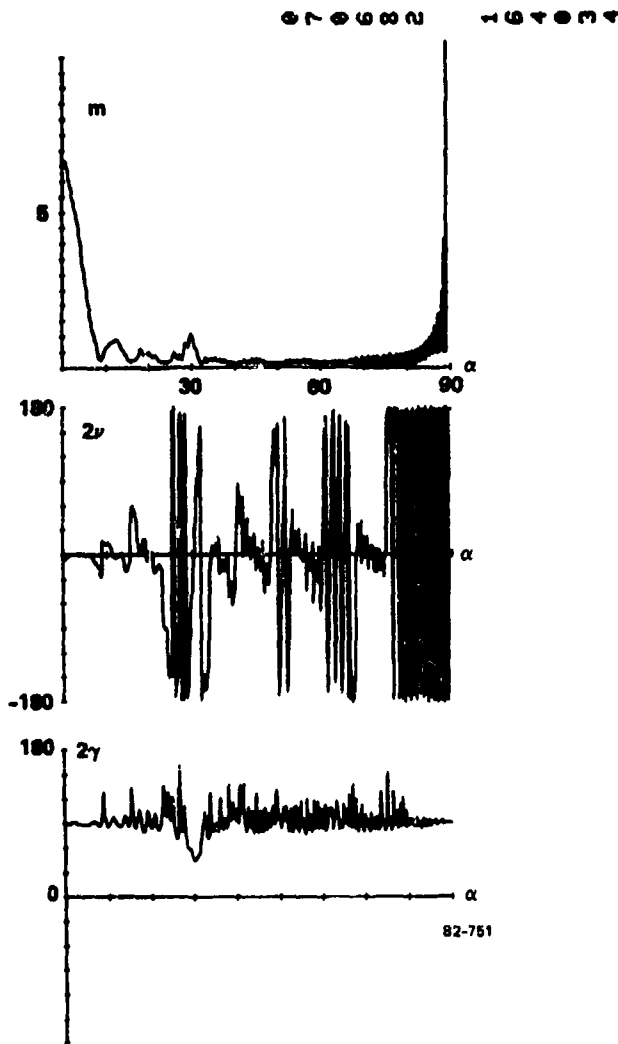
TN- C KA-12.80 H.B.D2.Z1- 10.00 5.85 6.30 - 30 BE1.BE2- 30.0 .0



PCAM - POLYN CHARACTERISTICS N. 2NU. 2GA US ASPECT FOR AIRCRAFT

FIG. 30 Polarization characteristics vs. aspect of model 3, Scale B; $k_3 = 12.8$; $\theta = 0^\circ$.

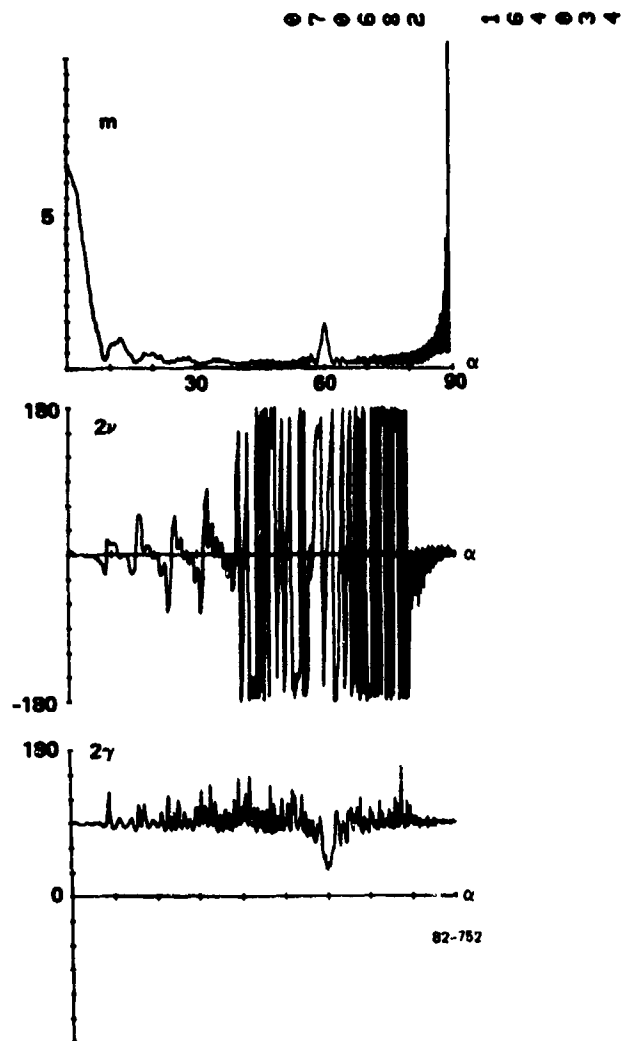
TH= 0 KA=12.80 H.B.D2.Z1= 10.00 4.71 4.00 -30 BE1.BE2= 30.0 0



7 PCAM - POLZN CHARACTERISTICS N. 2NU. 2GA VS ASPECT FOR AIRCRAFT

FIG. 31 Polarization characteristics vs. aspect of model 1, Scale C; $ka = 12.8$; $\theta = 0^\circ$.

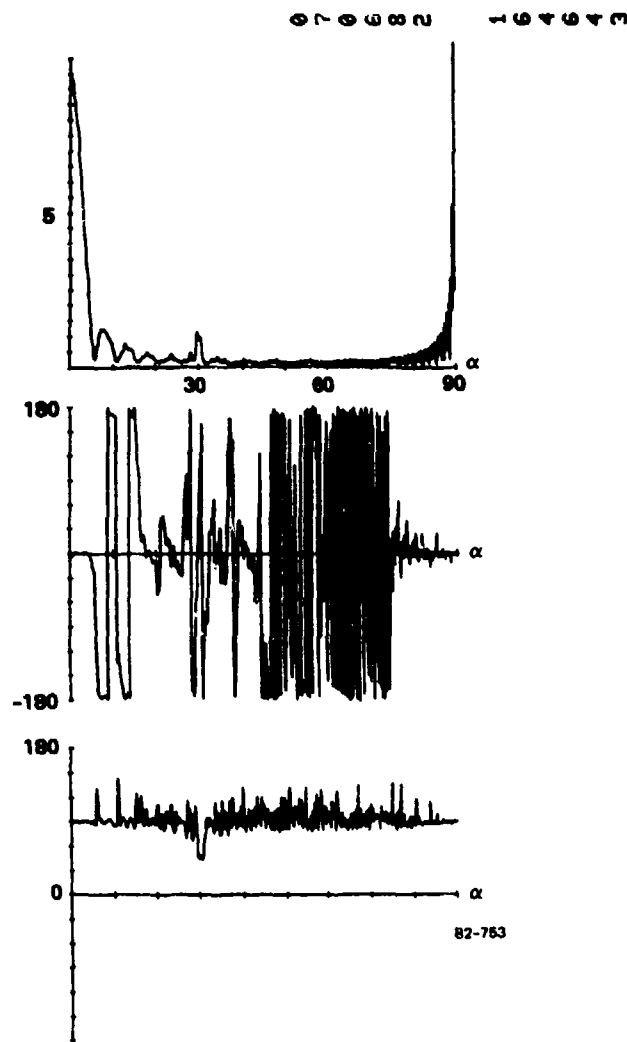
TH- 0 KA=12.80 H.B.DZ.Z1= 10.00 3.86 7.40 2.00 BE1.BE2= 60.0 0



PCAM - POLZN CHARACTERISTICS M. 2NU, 2GA VS ASPECT FOR AIRCRAFT

FIG. 32 Polarization characteristics vs. aspect of model 2, Scale C; $ka = 12.8$; $\theta = 0^\circ$.

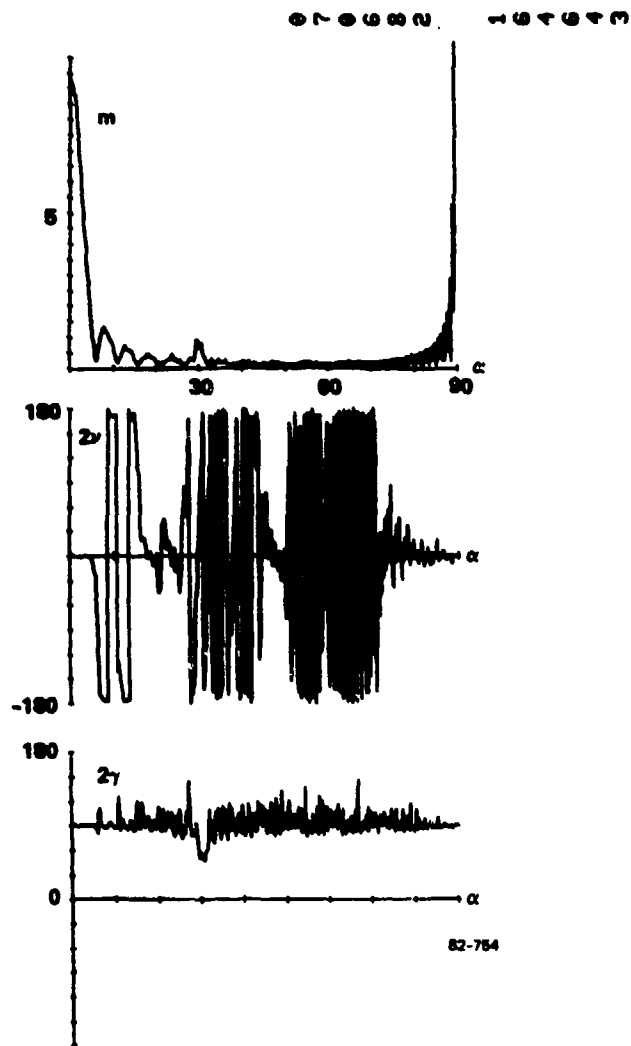
TH= 0 KA=18.60 H.B.D2.21= 10.00 5.85 6.30 - 30 BE1,BE2= 30.0 0



PCAM - POLZN CHARACTERISTICS M. 2NU. 2GA US ASPECT FOR AIRCRAFT

FIG. 33 Polarization characteristics vs. aspect of model 3, Scale C; $ka = 18.6$; $\theta = 0^\circ$.

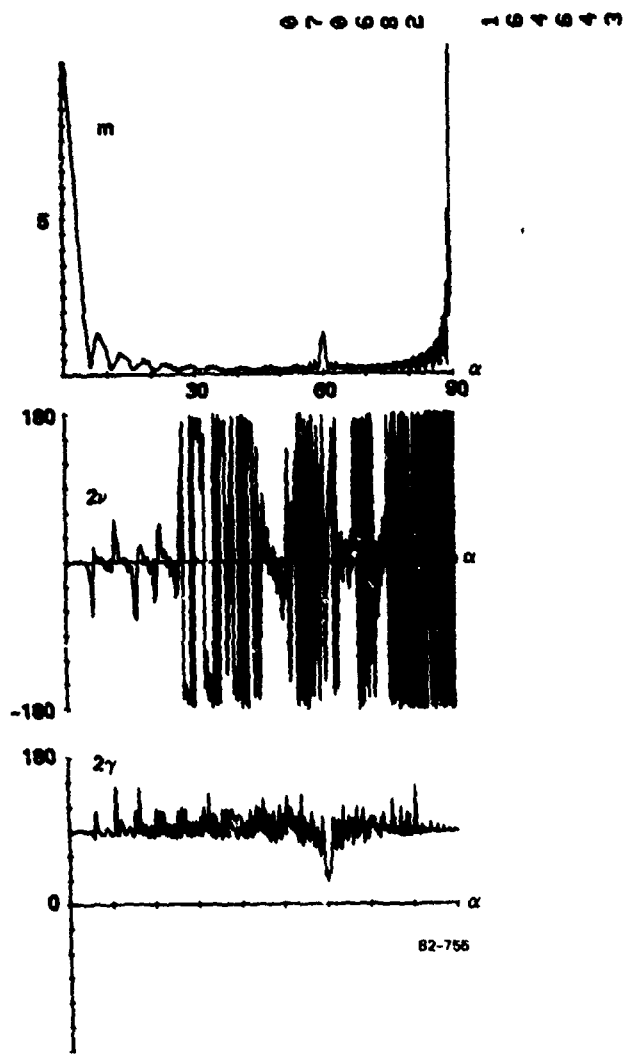
$F_{TH} = 0$ $Ka = 18.60$ $H.B.DZ.Z1 = 10.00$ 4.71 4.00 -30 $DE1.DE2 = 30.0$ 0



7 PCAM - POLZN CHARACTERISTICS M. 2NU. 2GA VS ASPECT FOR AIRCRAFT

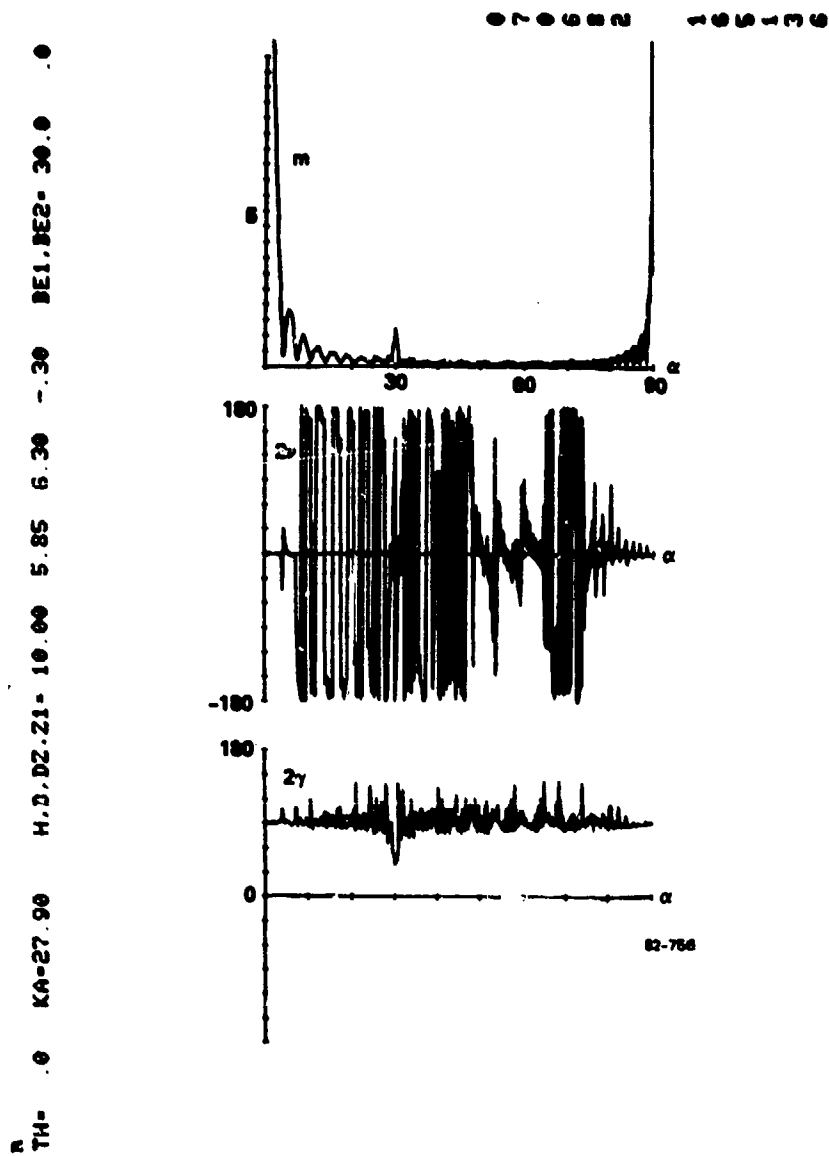
FIG. 34 Polarization characteristics vs. aspect of model 1, Scale D; $ka = 18.6$; $\theta = 0^\circ$.

TH= 0 KA=18.60 H,B,DZ,ZI= 10.00 3.86 7.40 2.00 BE1,BE2= 60.0 0



PCAM - POLZN CHARACTERISTICS M. 2NU. 2GA US ASPECT FOR AIRCRAFT

FIG. 35 Polarization characteristics vs. aspect of model 2, Scale D; $ka = 18.6$; $\theta = 0^\circ$.



7 PCAN - POLZN CHARACTERISTICS K. 2HU, 2GA US ASPECT FOR AIRCRAFT

FIG. 36 Polarization characteristics vs. aspect of model 3, Scale D; $ka = 27.9$; $\theta = 0^\circ$.

It is apparent, particularly at the higher frequencies, that at almost all aspects the polarization characteristics, as they are presented here, are useless for discriminating between these targets (consider Figures 35 and 36, for example).

3.3 COMPUTED AIRCRAFT CHARACTERISTICS AT 10° ELEVATION

For non-zero elevation angle, an aircraft model no longer appears plane symmetric to the radar. Hence the scattering matrix is not diagonal (i.e., there is coupling H-V). The polarization maximum no longer occurs at one of the poles of the Poincare sphere. Five rather than three parameters are needed to characterize the target.

The easiest way to deal with this added complexity is to find first the co-pol maximum polarization, characterized by the polarization parameters Ψ , τ (recall that Ψ , τ are the orientation and ellipticity of the polarization ellipse); then to apply the transformation $Q_\Psi Q_\tau$ to the scattering matrix, which diagonalizes it. This transformation corresponds to the rotations 2Ψ (about \hat{s}_3) and 2τ (about \hat{s}_2) of the Poincare sphere, which places the co-pol maximum at the top, and does not change the location of the co-pol nulls relative to the co-pol max. We then obtain m , 2ν , and 2γ as before for the transformed scattering matrix. This theory was described in Section 2.10. [A detail is the convention that we restrict 2Ψ as well as 2τ to between $\pm 90^\circ$. The co-pol max is then rotated to either top or bottom of the sphere and 2γ has the range 0° to 180° .]

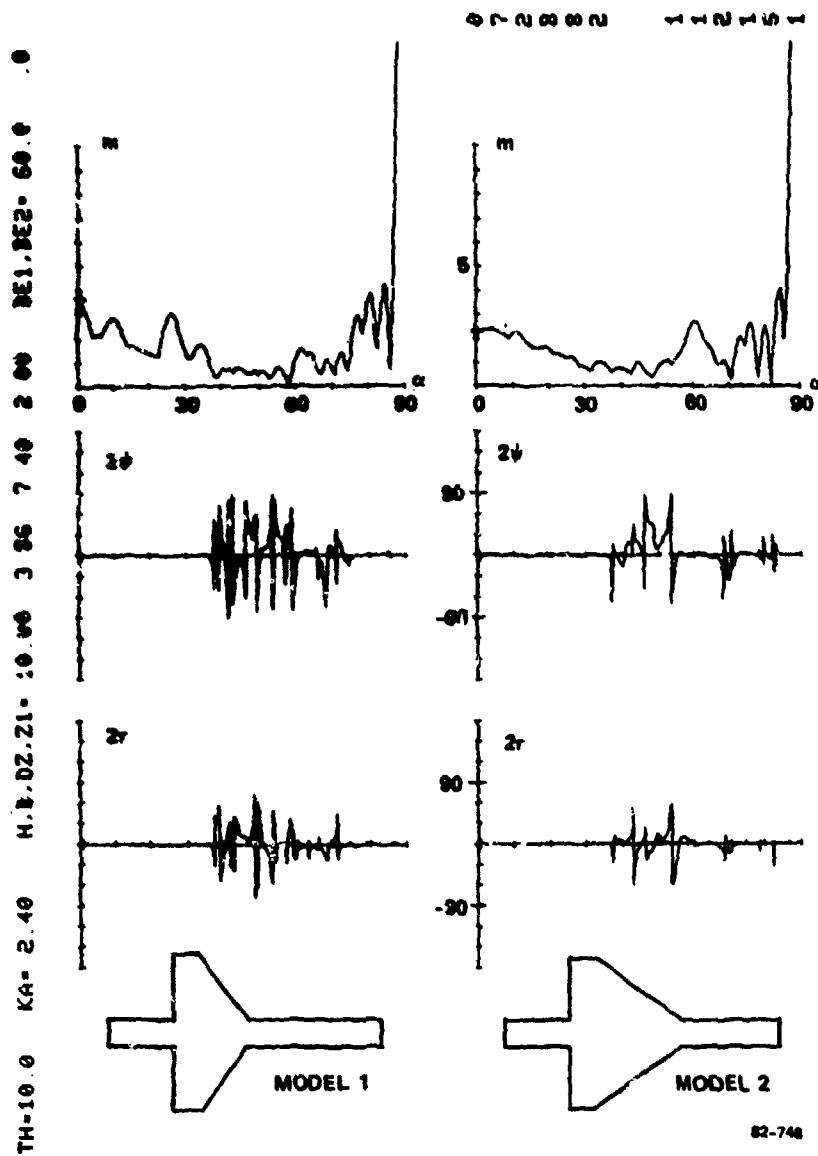
As has been described in Section 2, the rotation by 2Ψ on the Poincare sphere is the same as rotation by Ψ about the RLOS, or a simple reorientation of the radar reference plane. Now, roll-symmetric targets at any orientation in 3-space have a plane of symmetry which contains the RLOS (as one can convince oneself by holding up a cylinder and cocking one's head). For such targets, $\tau = 0$ (i.e., no τ -transformation is required to

diagonalize the matrix). Evidently, 2τ is a measure of the asymmetry of the target. These observations on τ were made by Huynen [14]. However, it will be seen that 2τ is also not an invariant of the target under changes of aspect or frequency.

In Figure 37 the angles 2Ψ and 2τ are plotted, in addition to m , for Models 1 and 2, at the low frequency $ka = 2.4$, at elevation angle $\theta = 10^\circ$. The corresponding characteristics m , 2ν , 2γ are plotted in the usual manner in Figure 38. The fluctuation of 2Ψ and 2τ is seen to be even more erratic than that of 2ν and 2γ . This has been found to be typical of compound targets. It can be understood by the following: So long as 2γ is unequal to 90° , the co-pol max polarization is a point on the Poincare sphere, which wanders about slowly for (very) small changes in aspect; then as 2γ becomes equal to 90° , the co-pol max "flashes" into a great circle (as discussed in Section 2.5); upon coming out of this degeneracy, the co-pol max has switched from one hemisphere to the other. All the while the co-pol nulls are well defined and moving smoothly. [Note that the 180° jumps in 2Ψ are artifacts of our definition of $|\Psi| \leq 90^\circ$, Ψ actually changes continuously and smoothly. It remains true, however, that near the switch of (M) from one hemisphere to the other, that motion is very rapid. This phenomenon occurs frequently: whenever the co-polarized return switches from being larger to smaller than the orthogonal co-polarized return.] Similar behavior is exhibited by 2τ . Because of this erratic behavior, 2Ψ and 2τ (or the co-pol max locus) are not useful for target discrimination for compound targets.

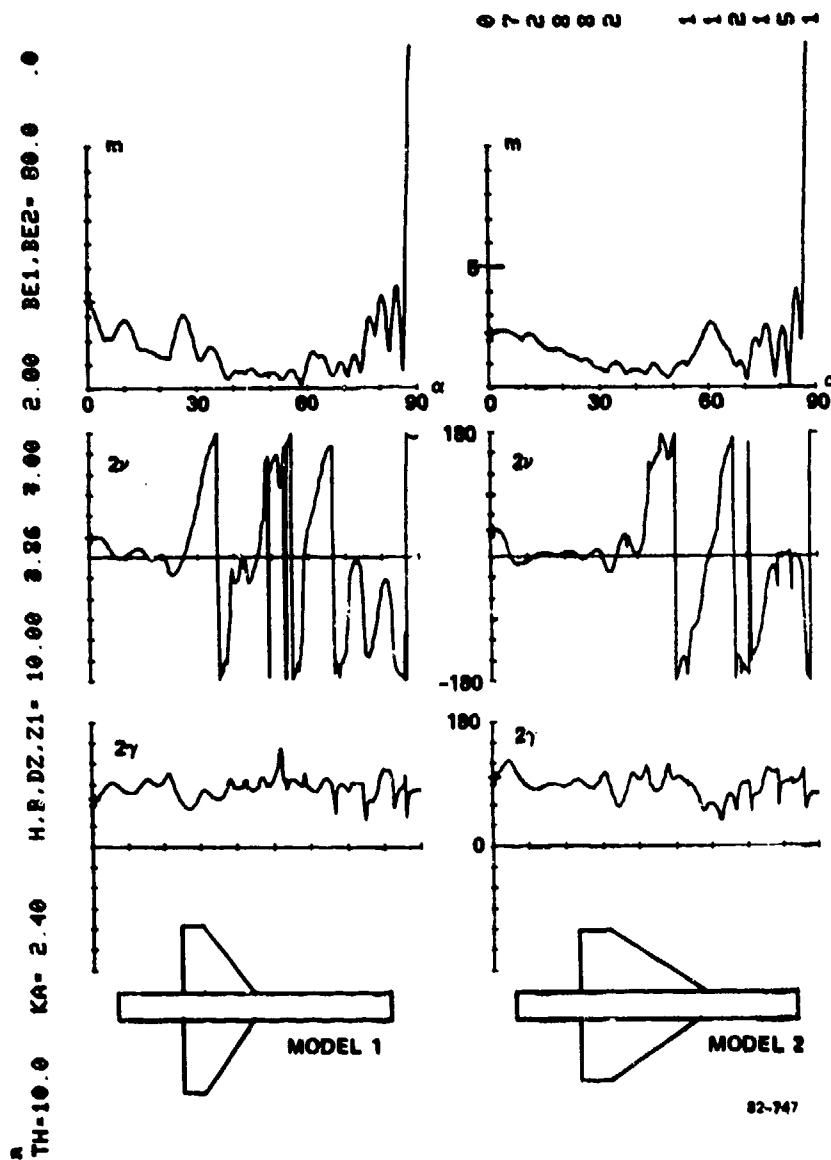
The 2ν and 2γ plots for the $\theta = 10^\circ$ case have properties similar to the $\theta = 0^\circ$ case.

In Figures 39 through 46, these characteristics are given for the cylinder and Models 1, 2, and 3 at $\theta = 10^\circ$ for size scale A. For the sake of much needed brevity, the plots for the other size scales are omitted from this report, as they show no new information.



9 PCAN - POLYN CHARACTERISTICS N. 2PSI.2TAU US ASPECT FOR AIRCRAFT

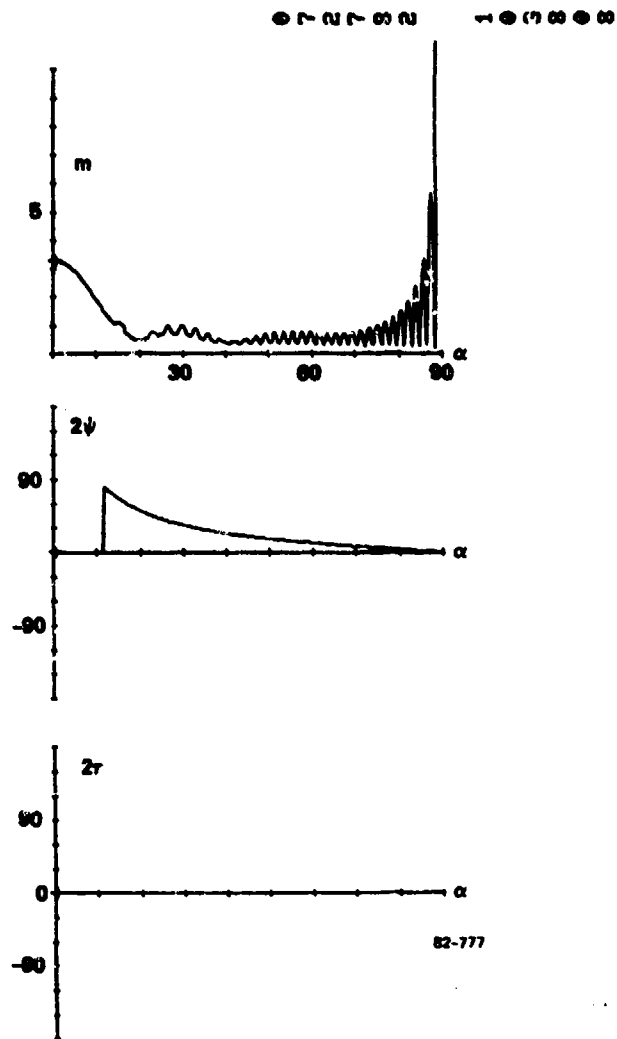
FIG. 37 Copol max polarization vs. aspect of model 1 and model 2; $ka = 2.4$; $\theta = 10^\circ$.



PCAM - POLYN CHARACTERISTICS M. 2NU. 2GA VS ASPECT FOR AIRCRAFT

FIG. 38 Polarization characteristics vs. aspect of model 1 and model 2; $ka = 2.4$; $\theta = 10^\circ$.

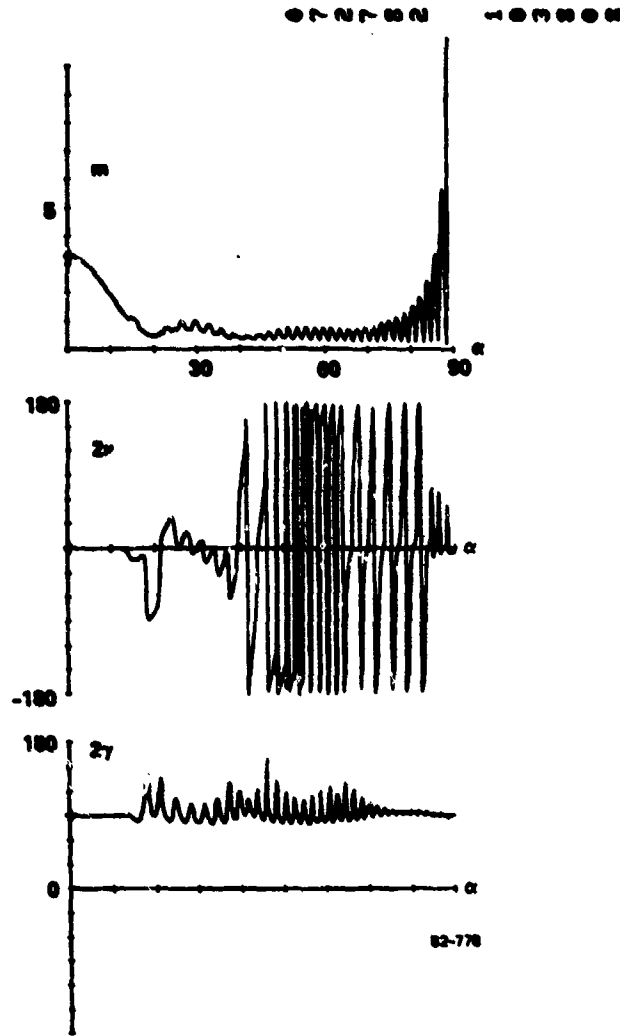
TH=10.0 KA= 5.24 H.B.D2.21= 10.00 .00 .00 BE1,BE2= .0 .0



PCAR - POLZN CHARACTERISTICS N. 2PSI,2TAU VS ASPECT FOR AIRCRAFT

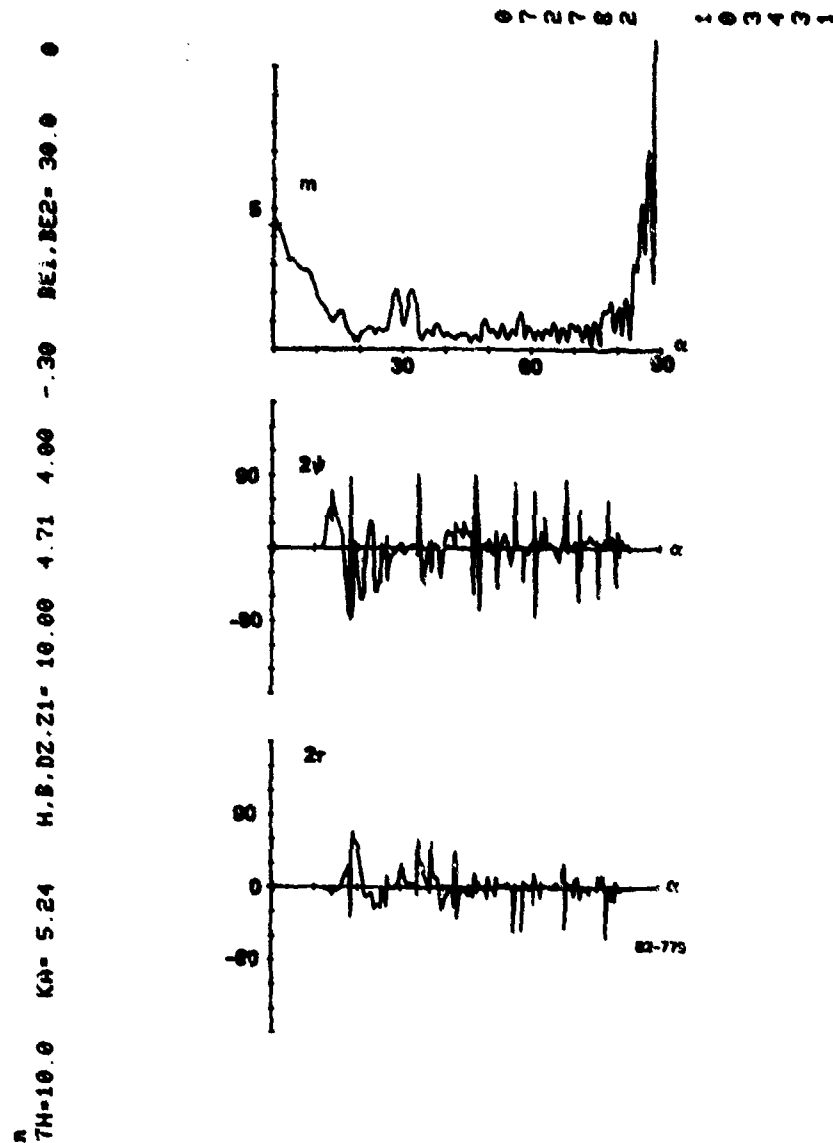
FIG. 39 Copol max polarization vs. aspect of cylinder, Scale A; $ka = 5.24$; $\theta = 10^\circ$.

TH-10.0 KA= 5.24 H.B.DZ.Z1= 10.60 DE1.DE2= .0 .0



7 PCAM - POLZN CHARACTERISTICS M. 21U. 2GA US ASPECT FOR AIRCRAFT

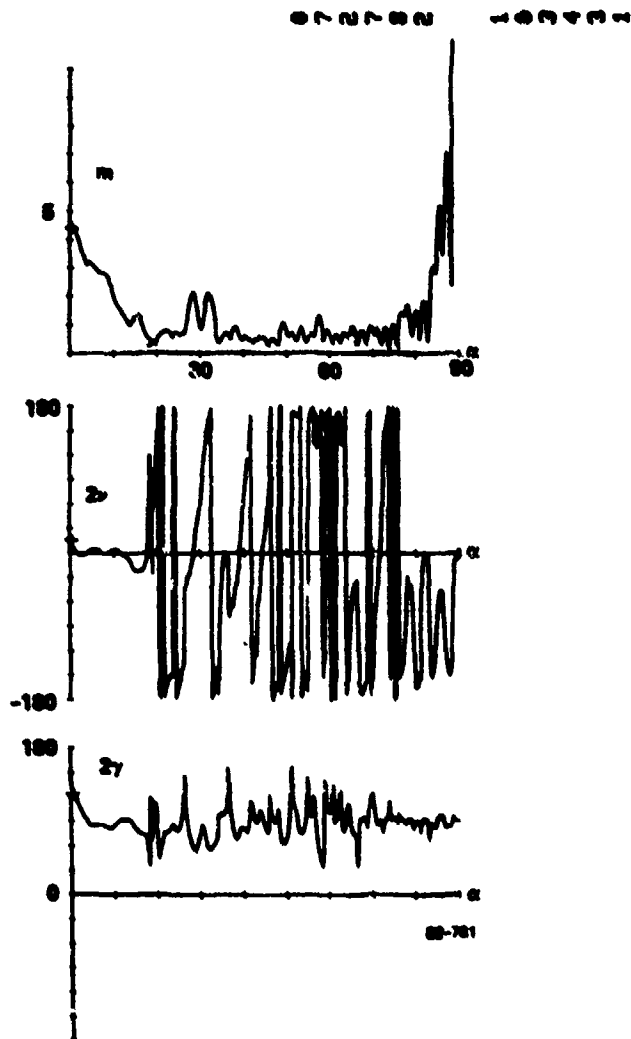
FIG. 40 Polarization characteristics vs. aspect of cylinder, Scale A; $ka = 5.24$; $\theta = 10^\circ$.



7 PCAM - POLZN CHARACTERISTICS M. 2PSI.2TAU VS ASPECT FOR AIRCRAFT

FIG. 41 Copol max polarization vs. aspect of model 1, Scale A; $ka = 5.24$; $\theta = 10^\circ$.

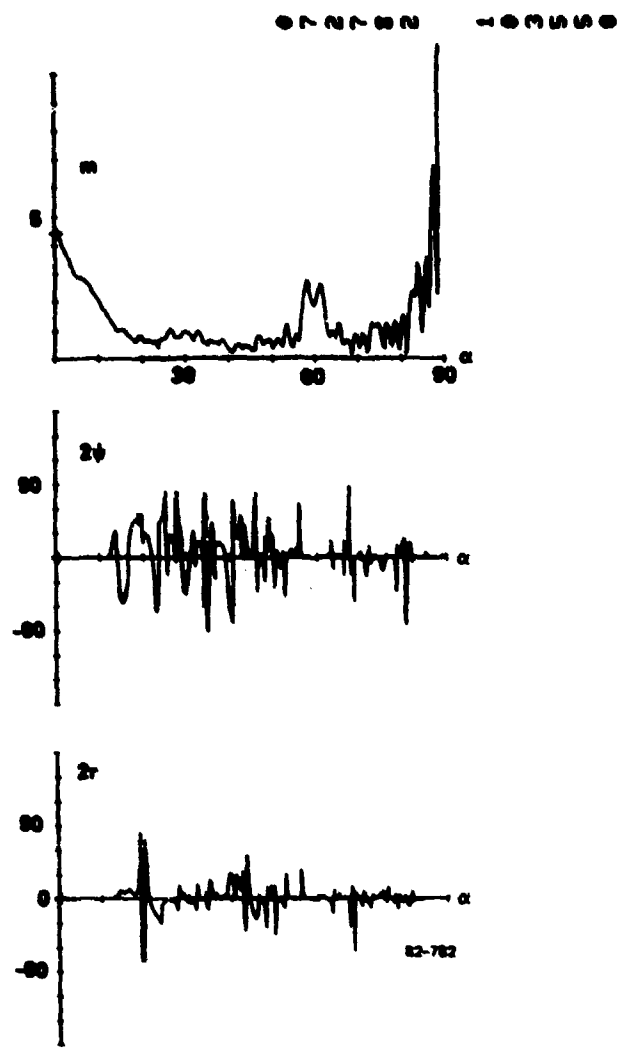
TH=10.0 KA= 5.24 H.B.DZ.Z1= 10.00 4.71 4.60 - .30 DE1.DE2= 30.0 .0



7 PCAM -- POLYN CHARACTERISTICS N. 2NU. 2GA US ASPECT FOR AIRCRAFT

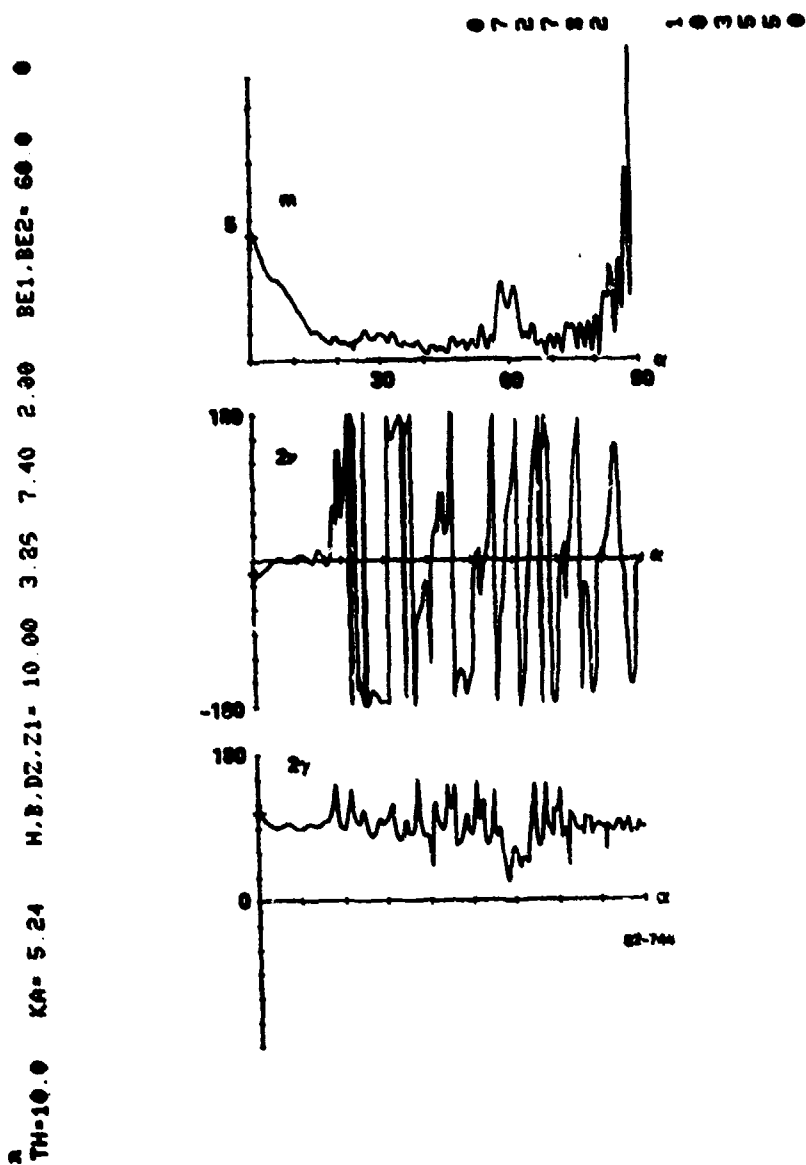
FIG. 42 Polarization characteristics vs. aspect of model 1, Scale A; $ka = 5.24$; $\theta = 10^\circ$.

TH-10.0 KA= 5.24 H.B.DZ.21= 10.00 3.86 7.40 2.00 2E1.2E2= 50.0 .0



7 PCAM - POLZN CHARACTERISTICS M, 2PSI.2TAU VS ASPECT FOR AIRCRAFT

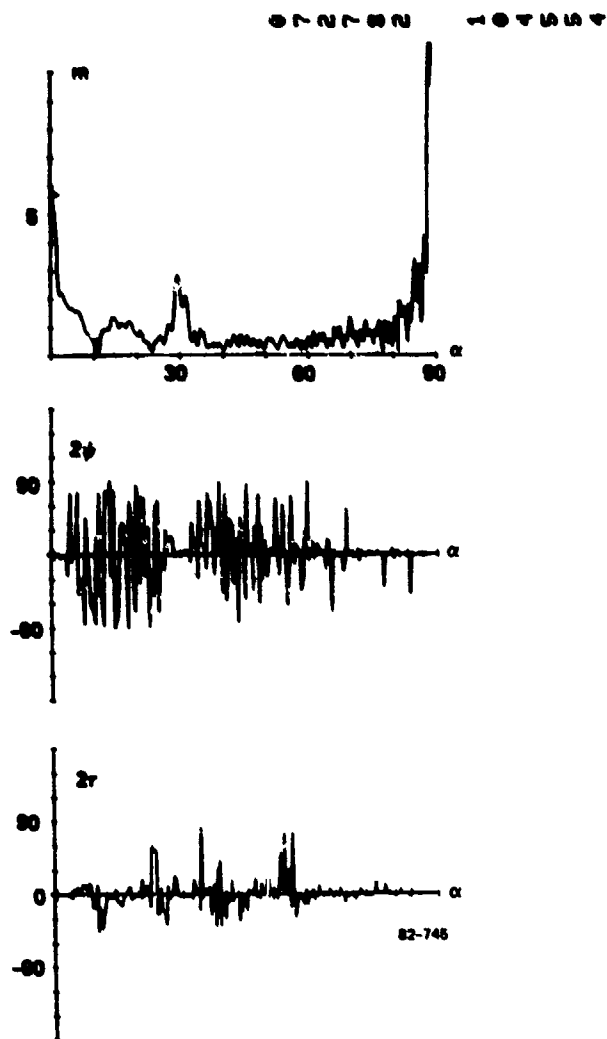
FIG. 43 Copol max polarization vs. aspect of model 2, Scale A; $ka = 5.24$; $\theta = 10^\circ$.



PCAM - POLZII CHARACTERISTICS H. 2NU. 2CA US ASPECT FOR AIRCRAFT

FIG. 44 Polarization characteristics vs. aspect of model 2, Scale A; $k_a = 5.24$; $\theta = 10^\circ$.

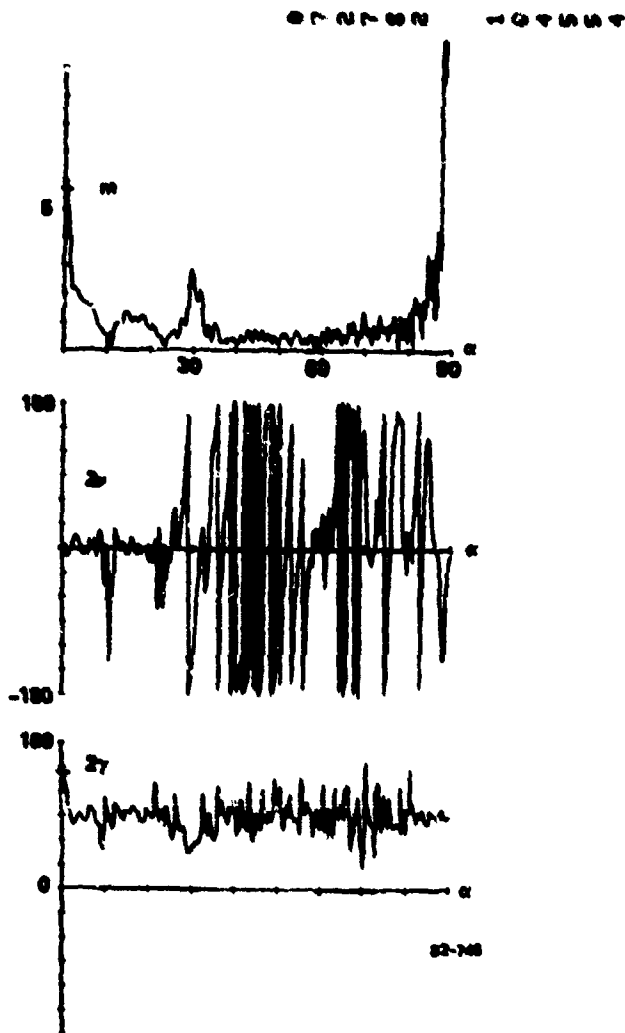
TH-10 0 KA= 8.14 H.B.DZ,Z1= 10.00 5.85 6.30 - 30 BE1,BE2= 30.0 0



PCAM - POLYN CHARACTERISTICS M, 2PSI,2TAU VS ASPECT FOR AIRCRAFT

FIG. 45 Copol max polarization vs. aspect of model 3, Scale A; $ka = 8.14$; $\theta = 10^\circ$.

TM-10.0 KA= 8.14 H.B.DZ.2j= 10.00 5.85 6.30 -30 BE1.BE2= 30.0 0



PCAM - POLZN CHARACTERISTICS N, 2NU, 2GA VS ASPECT FOR AIRCRAFT

7

FIG. 46 Polarization characteristics vs. aspect of model 3, Scale A; $ka = 8.14$; $\theta = 10^\circ$.

3.4 AVERAGE POLARIZATION CHARACTERISTICS OF AIRCRAFT MODELS

The rapid fluctuations in the polarization characteristics with variation in aspect is due to the changes in relative phase between scattering centers. Similar fluctuations at any one aspect occurs with frequency variations. The fluctuations are a nuisance for target ID purposes. We must either utilize them or eliminate them by averaging. The averaging method is illustrated here (refer also to Section 2.8).

It is assumed that measurements are made over a band of frequencies and/or aspect such that at least one cycle of a fluctuation is observed (the bandwidth required for this is just the same as required to resolve the individual scattering centers, as when forming an image or range profile). The powers of the individual measurements are added (incoherent sum). That is, we measure the average Stokes vectors of the scattered radiation. The process is similar to the natural observation of partially coherent light. We may form the expected value of this average. This removes all rapid fluctuations due to relative orientation of the scattering centers.

The results for the cylinder, Model 1, and Model 2, for size scale A, at $\phi = 0$, are shown respectively in Figures 47, 48, and 49 (m is plotted in dBsm in these figures). These are to be compared with Figures 23, 24, and 25. We see that the $2v$ fluctuation is eliminated, in fact $2v = 0$. The rapid fluctuations in 2γ are eliminated. What is left is the distinctive effect of the wing contribution to 2γ near the wing specular. The fact that $2v = 0$ for these targets is because all the strong scatterers are single-bounce and there are no strong double-bounce scattering centers. If a strong double-bounce scatterer were present over some range of aspect, this would show up on the $2v$ plot as an excursion toward $\pm 90^\circ$.

It should be noted (see Section 2.8) that $2v$ and 2γ here do not represent a co-pol null, but rather a co-pol minimum. The effect of averaging is to depolarize the received power.

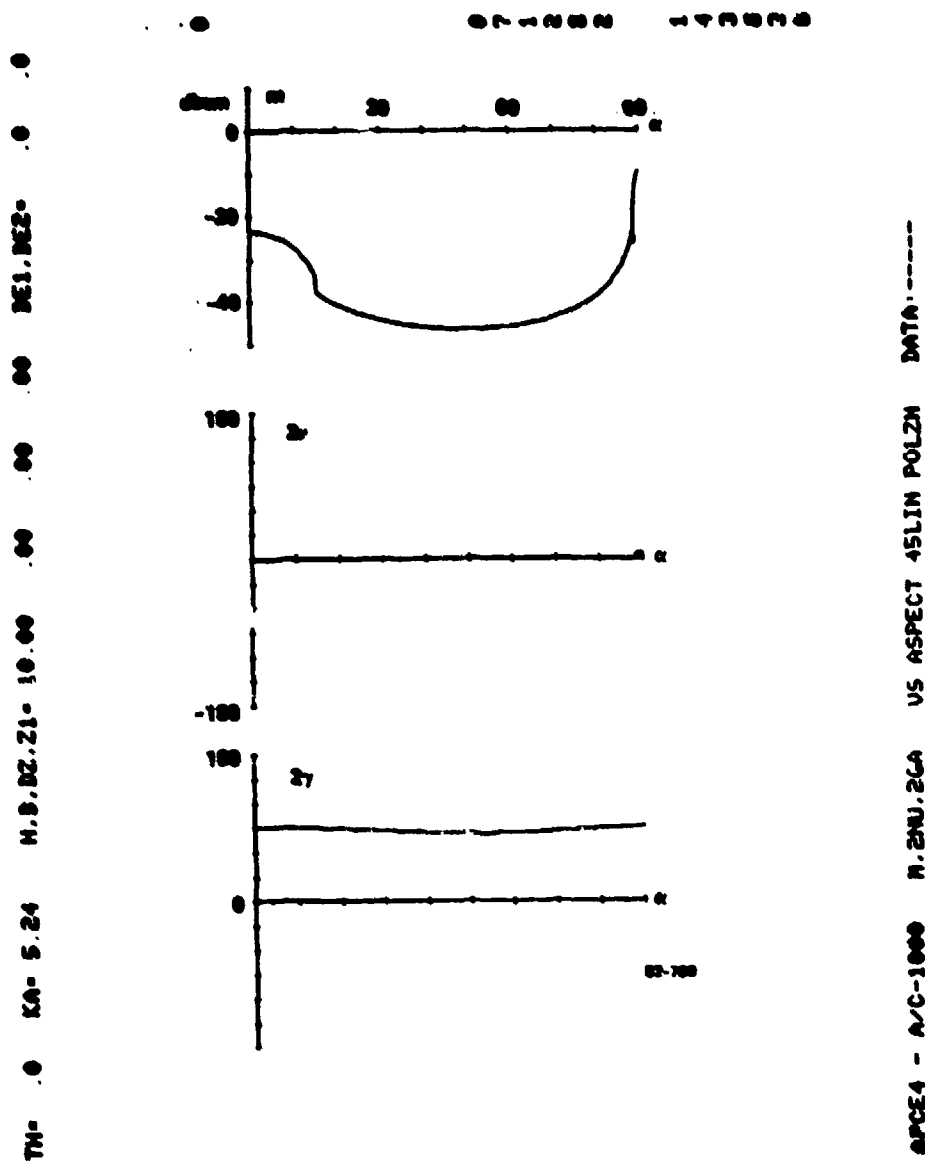


FIG. 47 Expected value of average polarization characteristics; cylinder, Scale A; $k_a = 5.24$; $\theta = 0^\circ$.

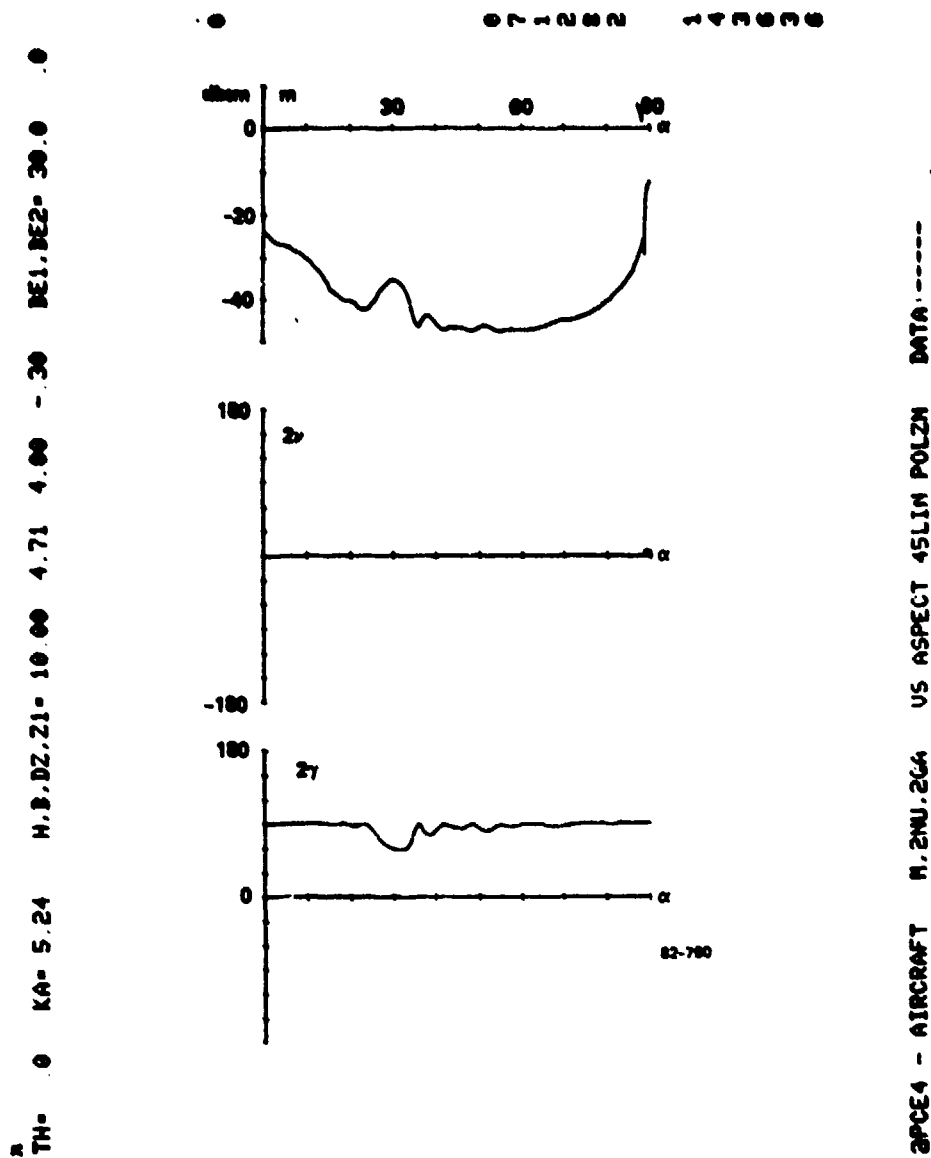


FIG. 48 Expected value of average polarization characteristics; model 1, Scale A; $k_a = 5.24$; $\theta = 0^\circ$.

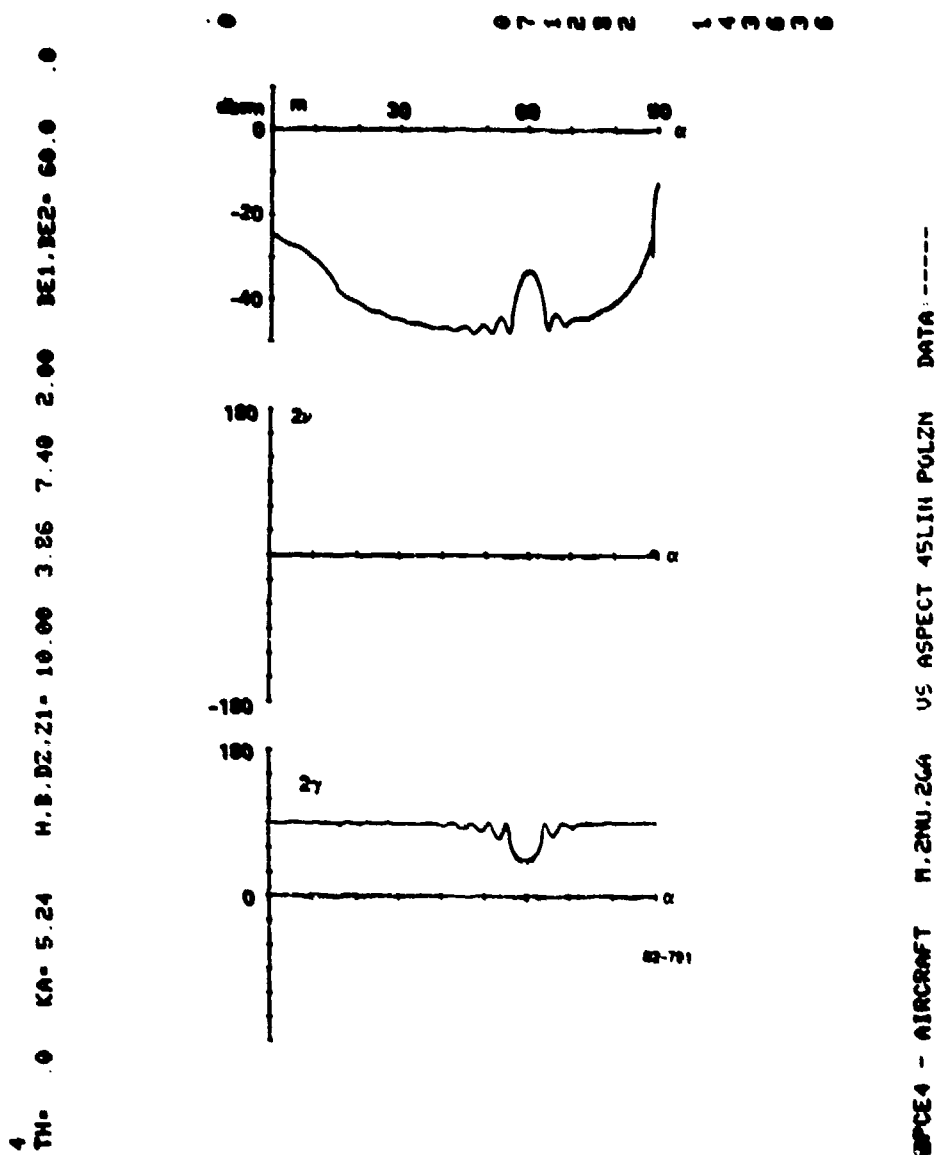


FIG. 49 Expected value of average polarization characteristics; model 2, Scale A; $k_a = 5.24$; $\theta = 0^\circ$.

This preliminary investigation shows that averaging may prove to be the method by which polarization characteristics become viable target discriminants. It would require a wideband radar, but simple incoherent processing. The adequate treatment of this approach requires a statistical analysis of the measured polarization characteristics. This is beyond the scope of this report.

SECTION 4

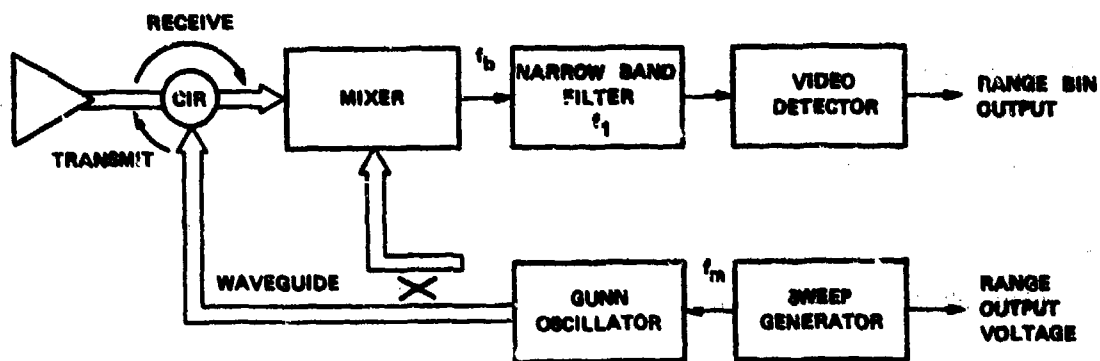
MEASURED POLARIZATION PROPERTIES OF SIMPLE AIRCRAFT MODELS

4.1 DESCRIPTION OF DUAL-POLARIZED RADAR

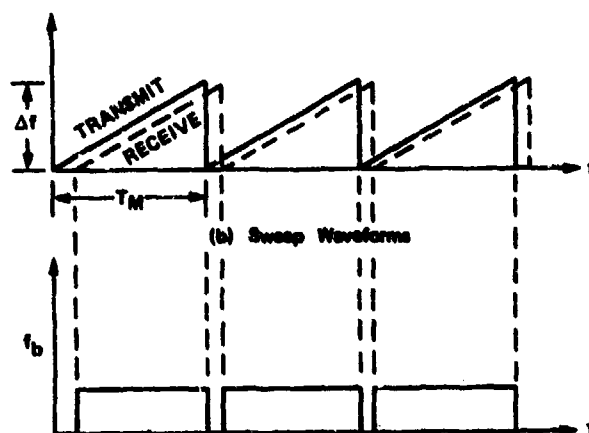
A simple yet versatile testbed radar system has evolved at Sperry Research Center to meet our needs for target and clutter data gathering and algorithm testing. Figures 50-52 show block diagrams of the measurement system (for which we hold two patents, with others pending).

The operation of the system may be understood by referring to Figure 50. An FMCW (frequency modulated, continuous wave) radar (Figure 50a) achieves range resolution by transmitting a chirp, i.e., a signal which has a frequency versus time resembling a sawtooth (Figure 50b), mixing the received signal with the transmitted signal, (resulting in an i.f. signal (Figure 50c) for which frequency is proportional to target range), narrowband filtering at i.f., and detecting. If the resulting signal is integrated over many chirps, it contains broadband target information (the transmit bandwidth is equal to 500 MHz for our system); however, if the detected video is sampled each chirp at the same point in the chirp, it contains target information only at a single transmit frequency (i.e., CW information). Either of these modes is possible; the latter was used for measurements under this effort.

In Figure 51, the FMCW Gunn oscillator (the transmitter), together with the circulator, antenna, and mixer can be recognized from the simple single-polarized FMCW system of Figure 50. A 3 dB power splitter has been inserted immediately after the transmitter (which breaks up the transmitter power into two branches, vertical and horizontal); also added are computer-controlled attenuators in both branches and a manual phase shifter in the vertical branch. If the phase shifter is set for 90° , either left-hand circular, vertical, or horizontal polarized radiation can be transmitted under computer control.



(a) Block Diagram



(a) IF Frequency

61-310

FIG. 50 Illustration of FMCW range bin system.

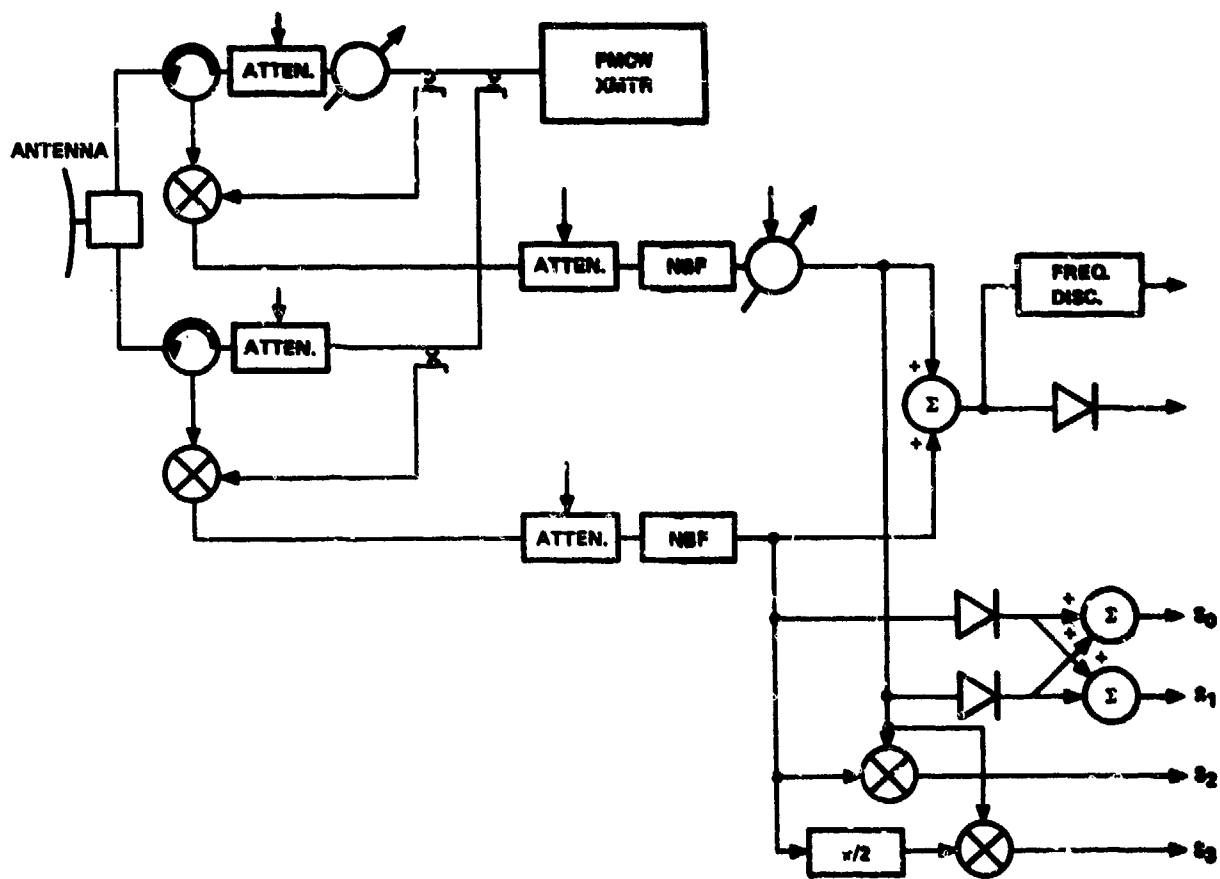


FIG. 51 Dual polarized radar for measuring Stokes parameters.

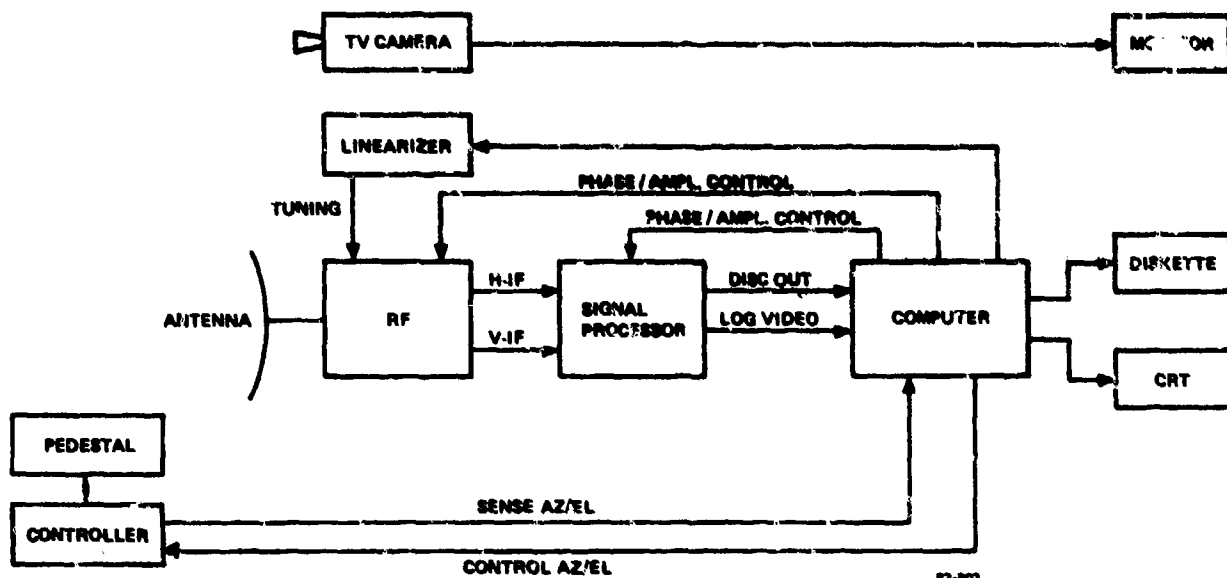


FIG. 52 SRC radar data acquisition system.

The two i.f. signals (the outputs of the two mixers) go to a dual-polarized signal processor which has two modes of operation. In the "sequential" mode, computer controlled attenuators and phase shifter in the receive signal processor are used to change (from chirp to chirp) the effective polarization of the receive antenna, independent of the polarization of the transmit antenna. Any arbitrary elliptical receive polarization can be synthesized by the controls shown. It is shown in Section 4.2 that for any transmit polarization, a complete set of Stokes parameters, and therefore one of the columns of the relative phase scattering matrix, can be calculated using detected power from four chirps by suitably varying the receive polarization (viz., vertical, horizontal, 45° linear, and left-hand circular). In fact, six receive chirps were used for each of two transmit polarizations (the above four, plus 135° linear and right-hand circular) to provide redundant information for reduction of noise effects.

Only the sequential mode was used for the measurements in this contract, since the simultaneous mode requires bilinear multipliers (mixers) and precision square law detectors of quality exceeding that available for easily obtainable i.f. signal processing components.

Figure 52 shows the overall radar system integrated with ancillary components such as a pedestal with controller, a boresighted TV camera (together with video monitor), and data storage means (eight-inch floppy diskette). The figure indicates the central role that the DEC MINC computer plays in system operation and data recording. We used the somewhat slow BASIC MINC operating system for hardware/software development and translated to the faster FORTRAN language for an order-of-magnitude improvement in data-taking run time.

Table 5 gives the parameters of the RF subsystem.

TABLE 5

Radar System Parameters

Center Frequency	35 GHz
Swept Bandwidth	500 MHz
Antenna Beam Width	2 degrees
Antenna Gain	35 dB
Transmit Power	25 mW (linear polarization) 50 mW (circular polarization)
Receive Noise Figure	4 dB DSB

Figure 53 shows receive antenna output power in dBm as a function of range to the target in meters. Receive noise, transmitter noise, ground clutter (assumed to be in a -25 dB sidelobe) and two signal levels (radar cross section or RCS of -40 to -20 dBsm, or 10^{-4} to 10^{-2} m²) are shown. It is clear that, especially for the smaller target RCS, a range of 20 m or less is desirable to ensure an adequate S/C level. In fact, all the data runs were at 12 m or 20 m range. The larger target sizes (above 0.1 m²) should remain adequately above both clutter and noise out to 100 m or more.

Figure 54 shows the measurement test geometry. A radar fence between radar and support structure is useful in blocking backscatter from the pedestal and surrounding ground.

As shown in Figure 54 for the short range (12 m) 0° aspect runs, the transmitter was placed at position S_1 , the fence at S_2 , and the pedestal at S_3 . For 10° aspect runs, the transmitter was raised 2.1 m to position S_4 . For the long range (20 m) runs, the positions L_1 , L_2 , and L_3 , respectively, were used for transmitter, fence, and pedestal. In every case, the fence was carefully positioned using a large RCS target at the top of the support cone so as to simultaneously minimize knife-edge-diffraction distortion of the signal and sidelobe scatter from the pedestal.

The target support pylon (Figure 55) was a conical polyfoam block shaped so that its RCS was below -50 dBsm. The polyfoam cylinder rested on a remote-controlled pedestal which rotated it in azimuth. A 14-bit digital shaft encoder (Figure 52) reported azimuth angle to 0.03° accuracy.

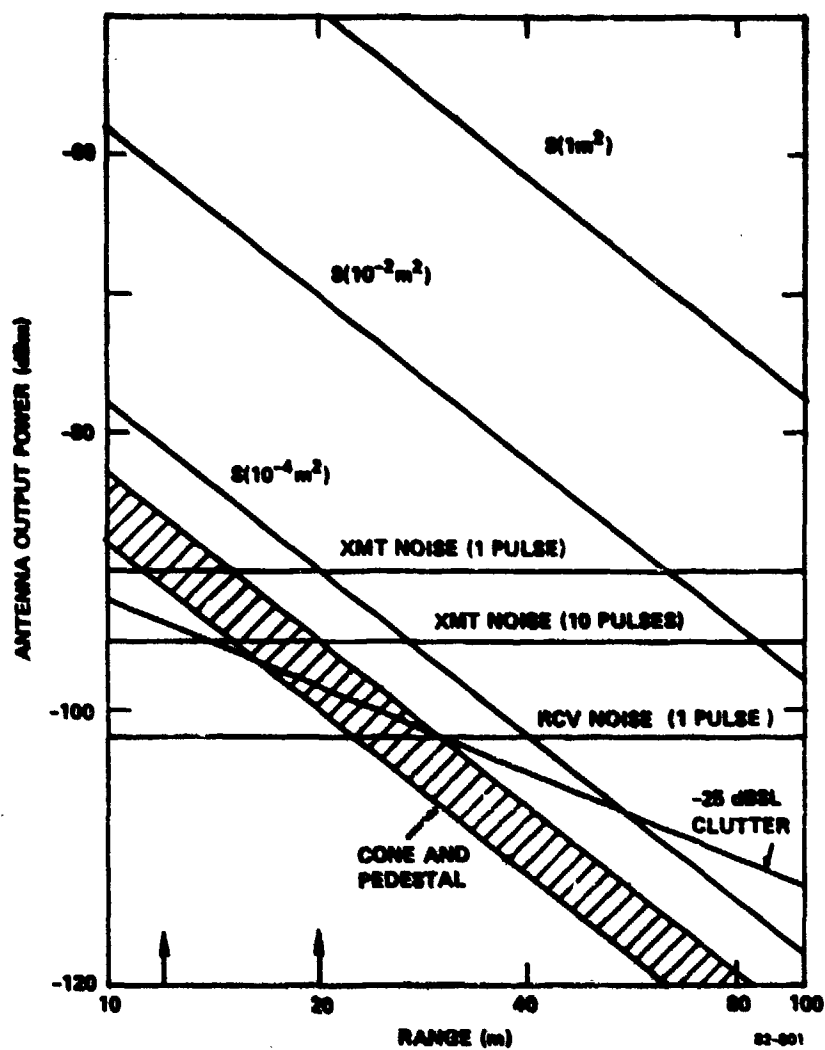


FIG. 53 Power vs. range for clutter, noise, and targets.

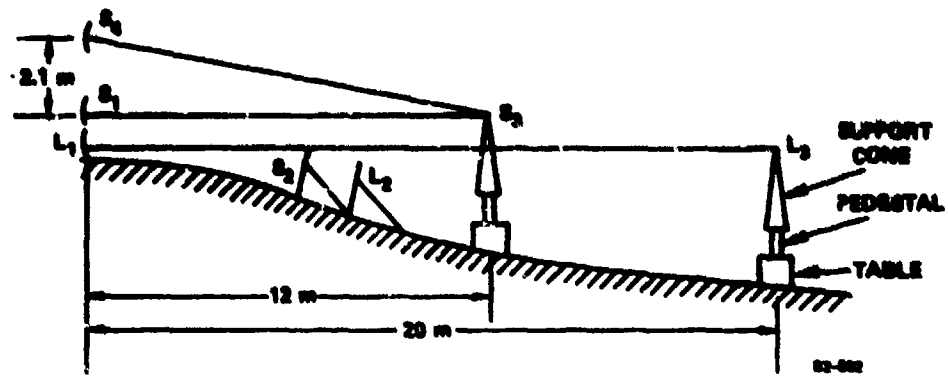


FIG. 54 Test geometry for polarization measurements.



FIG. 55 Polyfoam support cone and pedestal.

As suggested in Figure 52, a central computer (a Digital Equipment Corporation MINC 11) was used to control the radar configuration, acquire and condition radar scattering data, and record these data (along with calibration and ancillary data in header blocks) on eight-inch floppy diskettes. The data on these diskettes was in the form of square-law detected power for different transmit-receive polarization pairs. These data were then read from the floppy into the Univac 1106 where power data were mapped into co-pol nulls and cross-pol nulls for each aspect.

Figures 56-59 show photographs of the RF subsystem, the receiver signal processor, the 20 m range target as viewed from the antenna, and two targets mounted on polyfoam cone tips.

Since targets which are symmetric with respect to earth vertical have zero HV response (i.e., zero off-diagonal elements in the earth-basis scattering matrix), horizontal and vertical polarization are poor choices for transmit polarization for relative phase measurements between the HH and VV responses (the diagonal elements of the scattering matrix). Figure 56 shows a simple solution: tilt the radar 45° so that one transmit attenuator really controls linear polarized radiation at 135° with respect to earth horizontal, and the other attenuator really controls 45° linear polarization. These two polarizations were referred to as V prime and H prime, respectively.

Figure 57 indicates the receiver signal processor layout, with 60 MHz i.f. components (Avantex voltage-controlled amplifiers, bandpass filters, 3 dB power splitters, Olektron phase shifter, and RHG log detector) on the lowest level and video processing/sampling circuitry on the uppermost level.

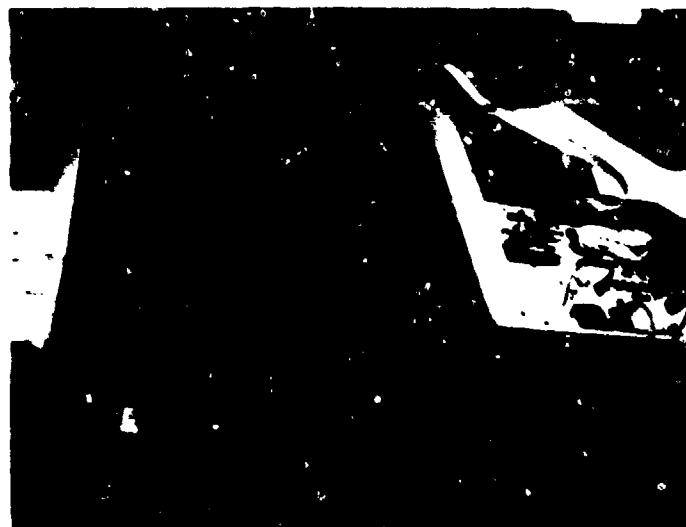
Figure 58 indicates the relative geometry of the polyfoam support, target, radar fence, and surrounding ground, as viewed by the radar.

Figure 59 shows two targets, scales A and D respectively, sitting on their polyfoam cone tips.



82-857

FIG. 56 Radar transmitter and antenna.



82-851

FIG. 57 Radar receiver/signal processor.



82-858

FIG. 58 Support pylon and target viewed from radar.



82-850

FIG. 59 Two targets (Scales A and C) and cone tips.

4.2 MEASUREMENT OF STOKES VECTORS

The null and maximum polarizations and the Stokes parameters (SP) are both sets of polarization descriptors that completely describe the elements of the relative phase polarization scattering matrix (RPSM) of an object. The polarization nulls and maxima have the advantage that they are invariant with respect to a radar's transmit and receive polarization for a given target orientation. The SP do not have this advantage. However, since in a practical radar system the transmit and receive polarizations are usually known, and it is the elements of the RPSM that are measured; and since the relation between these measurements and the SP is more apparent than that between the measurements and the nulls and maxima, the focus here will be on the SP.

The measurements for the target sets required to satisfy this contract consist of two groups: one at a 0° radar-to-target depression angle and another at approximately a 10° depression angle. In the 0° depression angle case, the aircraft models are plane-symmetric in that they lie in a plane of symmetry relative to the radar resulting in a polarization scattering matrix which has only diagonal terms that are in general non-zero. Since the RPSM is desired, it is clear that three real numbers, two magnitudes and a relative phase, completely describe the diagonal matrix for this plane-symmetric target case:

$$\text{RPSM} = \begin{bmatrix} |a_{11}| & 0 \\ 0 & |a_{22}|e^{j\Delta\phi} \end{bmatrix} \quad (40)$$

where a_{11} and a_{22} are the complex elements of the scattering matrix and $a_{11} = |a_{11}|e^{j\phi_{11}}$, $a_{22} = |a_{22}|e^{j\phi_{22}}$ and $\Delta\phi = \phi_{22} - \phi_{11}$.

It was found that a single transmit polarization (135° linear was chosen) and a minimum of four receive polarizations are sufficient to determine the elements in the matrix above. A theoretical minimum of four receive polarizations is necessary instead of three, to ensure that the relative phase is measured unambiguously. That is, since $\Delta\phi$ is measured as either $\sin \Delta\phi$ or $\cos \Delta\phi$, both must be measured to unambiguously determine $\Delta\phi$. Practically it was decided to measure the power in six receive polarizations: V and H linear, 135° and 45° linear, and LH and RH circular. These received powers are denoted by P_1, P_2, P_3, P_4, P_5 , and P_6 , respectively. The SP for a received electric field may then easily be constructed as follows:

$$\begin{aligned}
 s_0 &= \sqrt{(P_2 - P_1)^2 + (P_4 - P_3)^2 + (P_6 - P_5)^2} \\
 s_1/s_0 &= (P_2 - P_1)/s_0 \\
 s_2/s_0 &= (P_4 - P_3)/s_0 \\
 s_3/s_0 &= (P_6 - P_5)/s_0
 \end{aligned}
 \tag{41}$$

This approach ensures that the SP s_1, s_2 , and s_3 sum square to s_0 and thus that the degree of polarization is one as it should be for monochromatic electric fields. The SP, three of which are independent, completely describe the three numbers that represent the symmetric target RPSM from which the polarization nulls and maxima and in particular m , 2γ , and 2ν are derived. See Appendix 8.10 for a description of the relationship between the SP and the elements of the RPSM.

In the 10° depression angle case, the aircraft models do not lie in a plane of symmetry relative to the radar, resulting in a RPSM all of whose elements are in general non-zero. That is, for such an asymmetric target

$$\text{RPSM} = \begin{bmatrix} |a_{11}|e^{j\Delta\phi_{11}} & |a_{12}| \\ |a_{12}| & |a_{22}|e^{j\Delta\phi_{22}} \end{bmatrix} \quad (42)$$

where once again the complex elements of the scattering matrix are $a_{11} = |a_{11}|e^{j\phi_{11}}$, $a_{12} = |a_{12}|e^{j\phi_{12}}$, $a_{22} = |a_{22}|e^{j\phi_{22}}$, and $\Delta\phi_{11} = \phi_{11} - \phi_{12}$ and $\Delta\phi_{22} = \phi_{22} - \phi_{12}$. Five real numbers completely describe this matrix.

In order to measure these five numbers, it was found that at least two transmit polarizations are necessary. The two chosen here are the orthogonal pair 45° linear and 135° linear. Once again, as in the symmetric target case, it was decided to measure the powers in six receive polarizations, V and H linear, 135° and 45° linear, and LH and RH circular, for each of the transmit polarizations resulting in a total of twelve power measurements at each target aspect. Some of these measurements are redundant. However, by combining them as was done in Equation 41, it can be ensured that the normalized SP for each transmit sum square to one independently of each other. Thus all twelve measurements are used to determine the five real numbers that completely describe the RPSM (see Appendix 8.11).

Two different minimal sets of seven measurements, one for each of the three magnitudes desired $|a_{11}|$, $|a_{12}|$, and $|a_{22}|$ and two each (to avoid any sign ambiguity) for each of the relative phases desired, were also found. It was not clear, however, that using one of these minimal sets of measurements was better than using all twelve measurements, which has the advantage of decreasing the effects of noise and sampling jitter.

4.3 POLARIZATION CALIBRATION

The calibration of the SRC dual-polarized radar was separated into two parts. The first part consisted of the calibration of the individual components in the system, including the Gunn oscillator power source, the log-detector, the transmit and receive attenuators, the receive amplifiers, and the transmit and receive phase shifters. The second part consisted of the system polarization calibration, which ensured that indeed the transmit and receive polarization was that which was desired. The component calibration is described further in Section 4.4. The focus in the remainder of this subsection will be on the system polarization calibration.

A one-way calibration procedure was performed to ensure that the transmit polarization was as desired. Since 135° linear and 45° linear polarizations are the desired transmit polarizations, it was decided that these two polarizations could be best transmitted by rotating the radar 45° relative to earth horizontal, and transmitting vertical or horizontal polarization (in radar coordinates). If one thinks in terms of a V, H coordinate system for the target, and a V', H' coordinate system for the radar, where V', H' is rotated by $+45^\circ$ relative to V, H ; then V' transmit alone is 135° linear polarization and H' transmit alone is $+45^\circ$ linear polarization in the target coordinate system. This procedure allows the two desired transmit polarizations to be realized with one transmit channel ON while the other is completely OFF. The effects of cross-polarization leakage, frequency pulling on the Gunn oscillator, and uncertainties in the path lengths of the two channels which affect the relative phase and hence the polarization of the transmitted signal, are thus minimized. Each transmit attenuator may then be calibrated individually to ensure that the power is identical for each transmit polarization, 45° and 135° linear.

The receive attenuators and amplifiers were initially calibrated individually with a laboratory reference 60 MHz input signal. In order to calibrate the entire system receive polarization; that is, the receive amplifiers and phase shifter which determine the radar receiver polarization, a two-way automatic calibration procedure was developed. Basically this procedure consists of illuminating a known cross section, 1 square meter, dihedral corner reflector with the crease oriented at 22.5° relative to horizontal with either a 45° or 135° linear polarization (the transmit polarizations used to measure the elements of the RPSM). This calibration target returns a vertically or horizontally polarized signal, respectively; either of which has equal power in both the V' and H' channels of the radar receiver. Knowing that this is the case, the electronically controlled digital phase shifter may then be stepped through all possible phases under computer control, and the resulting log-detected power stored for each phase shift. The phase shift corresponding to maximum received power must then be 0° relative phase between the two channels, while the minimum received power corresponds to a 180° phase shift between the two channels. All other phase shifts, and in particular those allowing LH and RH circular polarization reception, may be inferred from these.

The power difference between the maximum and minimum received power gives an indication of the balance of the amplification in each receive channel. If this difference (measured in decibels) is small, it can be improved; that is, made larger by adjusting one of the receive amplifiers to balance or equalize the amplification in both channels. The automatic phase calibration program may then be run once more producing the phase settings required to configure the receiver to the receive polarizations desired.

The power difference between the maximum and minimum received power also gives an indication of the polarization purity of the receiver. It was found that the cross-polarized power was from 25 dB to 30 dB below the co-polarized power.

Since the calibration target, the dihedral corner reflector, is a 0 dBsm or 1 square meter reflector at 35 GHz; it was also used to determine a conversion factor relating the power measured by the log detector in dBm to the actual target size in units of dBsm. Comparison of predicted and measured responses in Section 4.6 shows this power calibration to be fairly accurate.

The accuracy of this two-way calibration procedure strongly depends on the accuracy of the angles involved in setting up the calibration experiment. The radar should be tilted at exactly 45° relative to horizontal and the dihedral should be tilted at exactly 22.5° relative to horizontal. A bubble level with an accuracy of $\pm 0.5^\circ$ was used to set these angles and was found to be acceptable.

4.4 OTHER CONCERNS

Even after careful polarization calibration there are several potential sources for error in a radar system measuring polarization effects which sometimes can be of very small magnitude. These potential error sources can be grouped into radar-system-induced errors, errors associated with geometry, errors due to the construction of the target, and errors from ambient clutter.

4.4.1 System

System errors come from three major sources: additive noise, system nonlinearities, and drift.

Transmitter noise, which dominates receiver noise in our system, (see Figure 53), is due to FM sidebands on the carrier of the Gunn diode transmitter, which leak through the system and appear at the i.f. frequency. (In our system, the major leakage path is a bounce off the subreflector of the Cassegrain antenna). By using radar absorbing material on the subreflector,

transmitter noise is kept to 12 dB above receiver noise; averaging ten pulses further reduces both noise sources by 5 dB, resulting in a noise "baseline" which corresponds to a target cross section of -54 dBsm (six millionths of a square meter) at a range of 12 m. This was measured as part of run P29R01, data from which is shown in Figure 60. The total backscattered power (in dB relative to a square meter) is plotted as the pedestal turns; at aspects of 25° , 45° , 50° , 52.5° , 55° , 75° , and 90° , the "target" was quickly replaced. The data from 0° - 52.5° and 55° - 90° represents several varieties of polyfoam support cone tips, while the data from 52.5° - 50° and 90° - 100° represents essentially system noise; note that it has an average level of about -54 dBsm. Actually, this "noise" data also includes ambient clutter from the pedestal and nearby ground, which is evidently well screened by the radar fence.

The other system-induced errors, nonlinearities and drift, require careful calibration for those aspects which are highly nonlinear but stable (e.g. log detector deviation from true linear volts-per-dB characteristic, voltage controlled amplifier gain-versus-volts characteristic), and frequent calibration for those aspects which indicate drift (e.g. phase/gain characteristics of the RF mixers, which potentially can change as the Gunn VCO frequency changes with time or temperature). The stable nonlinear elements of the radar were calibrated both with a CW 60 MHz i.f. laboratory source and with scattered power from a 1 square meter reference dihedral target. These calibration runs were automated with the MINC computer as master controller; typically 100 measurements were averaged to drive measurement noise errors in the calibration process to 0.2 dB or less. The drift-prone components of the system (primarily the two mixers) were calibrated hourly using a special dual-polarized computer controlled algorithm described in Section 4.3, which simultaneously closed-loop corrected both relative gain and relative phase in the two receiver channels.

4.4.2 Geometry

Potential error sources associated with geometry include target orientation, antenna orientation, placement of the radar fence, and near field

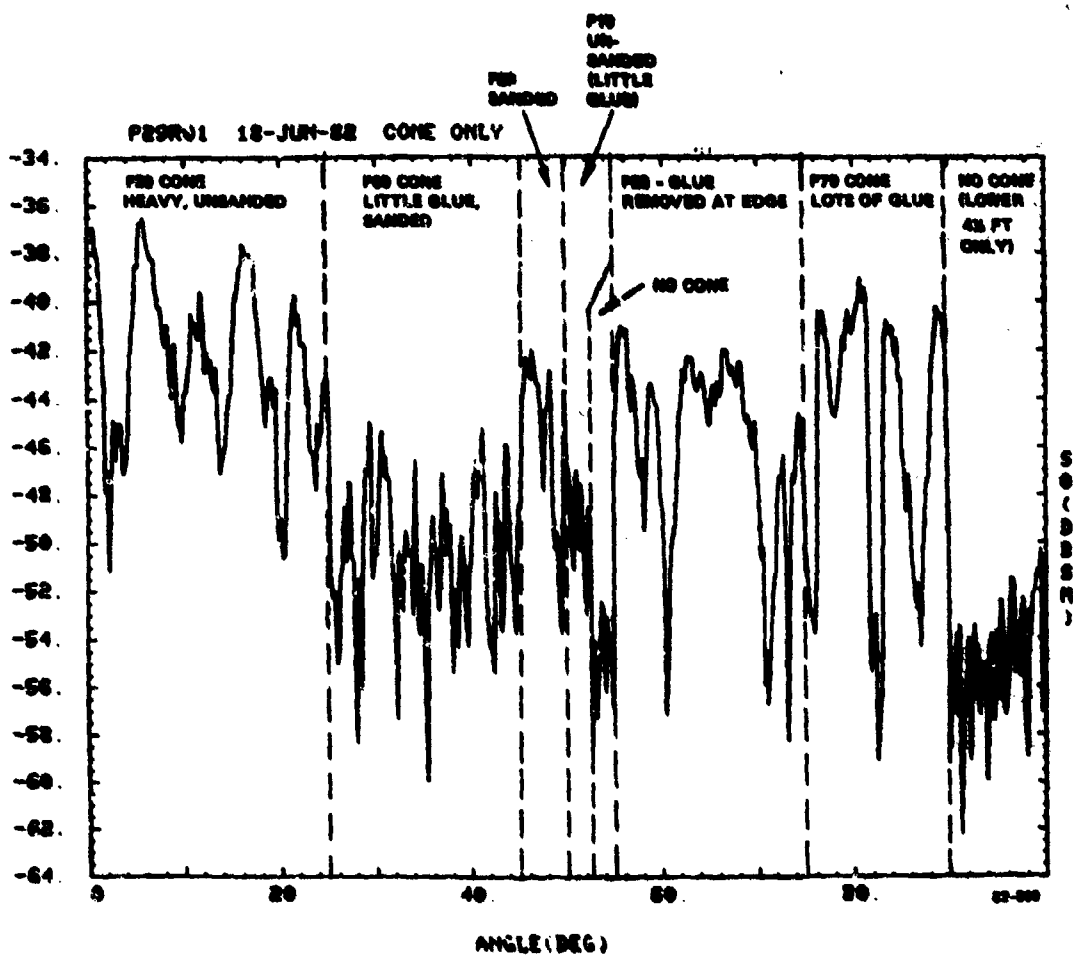


FIG. C0 Power due to noise and to support cone clutter.

effects. Target aspect was controlled via the following chain: the MINC computer interfaced a motor controller, which determined the direction and speed of a dc motor, which was linked by a pulley to a synchro driver. The synchro receiver in the pedestal then turned the polyfoam support and target. Any backlash or other angle errors would be measured by a synchro-to-digital converter which was accurate to 0.03° . Target pitch (which was nominal zero degrees) was carefully measured each run with bubble levels accurate to 0.5° .

Antenna orientation was facilitated with the use of a co-mounted TV camera with remote monitor. The camera was carefully bore-sighted using a physically small target with large RCS (the 4.1-cm-wide dihedral with 1 square meter RCS) at the range of interest (either 12 m or 20 m). Later, the radar-TV combination could be pointed at a small RCS target with 0.1° accuracy, ensuring that the peak of the 2° beam is on target. The 45° tilt of the radar (Figure 56) was ensured using a bubble level.

The radar fence (Figures 54 and 58) was carefully placed to minimize the sidelobe response of the metal pedestal, while at the same time minimizing distortion of the target response due to knife-edge scatter over the top of the radar fence.

Near field effects (see Section 8.9) were deemed to be serious enough at 12 m range for the largest three target scales (C, D, E) that runs were made at 20 m range, even though the S/N ratio decreased 9dB by moving out to that range.

4.4.3 Target

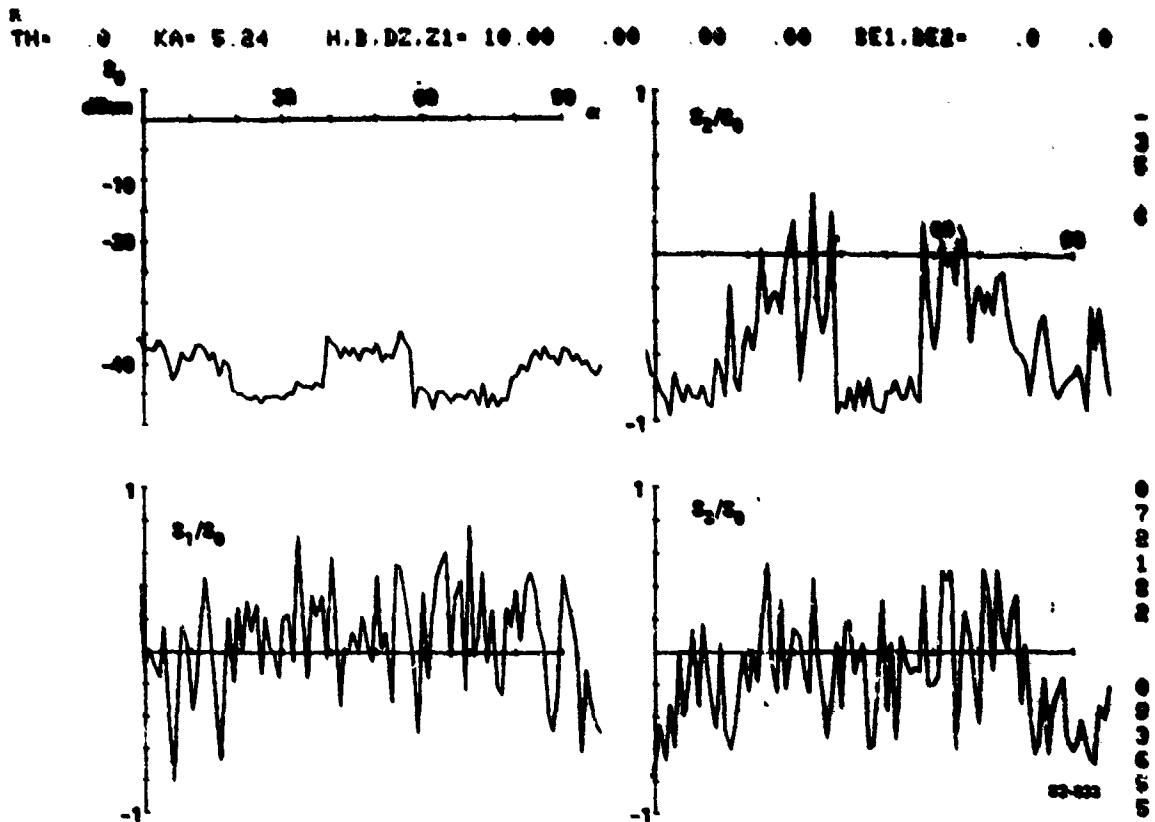
Potential target-induced errors included unwanted scattering from mounting screws, wing slots, and incorrect assembly. The screw and slot errors were minimized by covering them with conductive tape, which was carefully smoothed. The major assembly problem, wing/body alignment, was identified in an early test run when the local RCS peak due to the wing leading edge appeared at an azimuth of 32° instead of 30° ; for all runs after this, wing alignment accurate to 0.5° was ensured by careful assembly.

4.4.4 Clutter

Unwanted responses from scatterers near the target (i.e., radar clutter) dominated the interference at the 12 m range (see Figure 53), while at 20 m, transmitter noise is dominant. The major contributor to clutter is the polyfoam support cone; of this, the tip is dominant. Other scatterers include the pedestal and nearby ground, both of which are reduced to below transmitter noise (even at 12 m range) by the radar fence. Scatterers at long range (for example the tower visible in Figure 58) are easily range-gated out, using the FMCW 3 MHz range gate filters (labelled "NBF" for "narrowband filter" in Figure 51).

The upper 12-inch tip of the 60-inch polyfoam support was detachable; in fact, several tips were fabricated. Two types are shown in Figure 59. The cone tip on the right had three sections, held together with a heavy application of low RCS glue, giving a relatively poor RCS of -37 dBsm to -44 dBsm, as shown in Figure 60 (0° - 25° azimuth). Other three-section tips had better performance (below -45° dBsm typically, as shown in Figure 60, 25° - 50°). The best low RCS cone tip consisted of only one section with no glue, as shown to the left in Figure 59; this cone tip had an RCS of -50 dBsm.

An indication of the clutter-limited sensitivity of the system at 12 m range is given in Figure 61, which shows polarization data for a half-inch ball bearing (with an RCS of -41 dBsm). The ball bearing was removed between 20° and 40° and between 60° and 80° , leaving only the cone tip (one of the -45 dBsm low-glue cones). Note that the presence of the ball bearing is clearly evident in both the s_0 and s_2 plots, as it should be, and does not appear in the s_1 and s_3 plots, as it in fact should not. (Remember that for 135° linear illumination and a specular one-bounce scatterer, all the scattered radiation is at 135° : $s_1 = 0$, $s_3 = 0$, $s_2/s_0 = -1$.)



PCA3 - AIRCRAFT 50.1.2.3 US ASPECT 45LIN POLIN DATA P70R02 30-JUN-82

FIG. 61 Response of half-inch sphere (-41 dBsm).

One might ask just how large should the signal-to-clutter ratio be to cause acceptably low distortion to a measured power level. For signal power S , clutter power C and relative signal/clutter phase θ the $S+C$ power is

$$p = |\sqrt{S} + \sqrt{C} e^{j\theta}|^2 \quad (43)$$

which has a maximum of $S + C + 2\sqrt{SC}$ and a minimum of $S + C - 2\sqrt{SC}$. These bounds are shown in Figure 62. Note that 20 dB S/C ensures error less than ± 1 dB, while 10 dB S/C results in errors between -3.3 dB and +2.4 dB. Consulting Figures 53 and 62, we see that -50 dBsm cones can cause ± 3 dB errors in -40 dBsm target measurements, but only ± 0.3 dB errors in -20 dBsm target measurements.

4.5 MEASUREMENT RESULTS

In all, over fifty target runs were recorded. Table 6 describes the information recorded in the disk file header for each run, and also describes the file name convention used. The first letter is always P (for polarization). The next two numbers describe the target body and configuration, respectively. (Target body scales A-D correspond loosely to body types 1-5). The next letter is R for 0° single-transmit (symmetric) targets; A for 10° dual-transmit (asymmetric) targets; or D for dual-transmit runs with symmetric targets. The last two digits form the run number.

Table 7 gives a brief listing of the files, along with the date recorded, five header data items, and header comments. The header data items include attenuator setting (identical switched attenuators were used before both horizontal and vertical receive amplifiers to preclude input saturation), azimuth step size of the pedestal in degrees, target range in meters, and calibration target responses in vertical and horizontal channels.

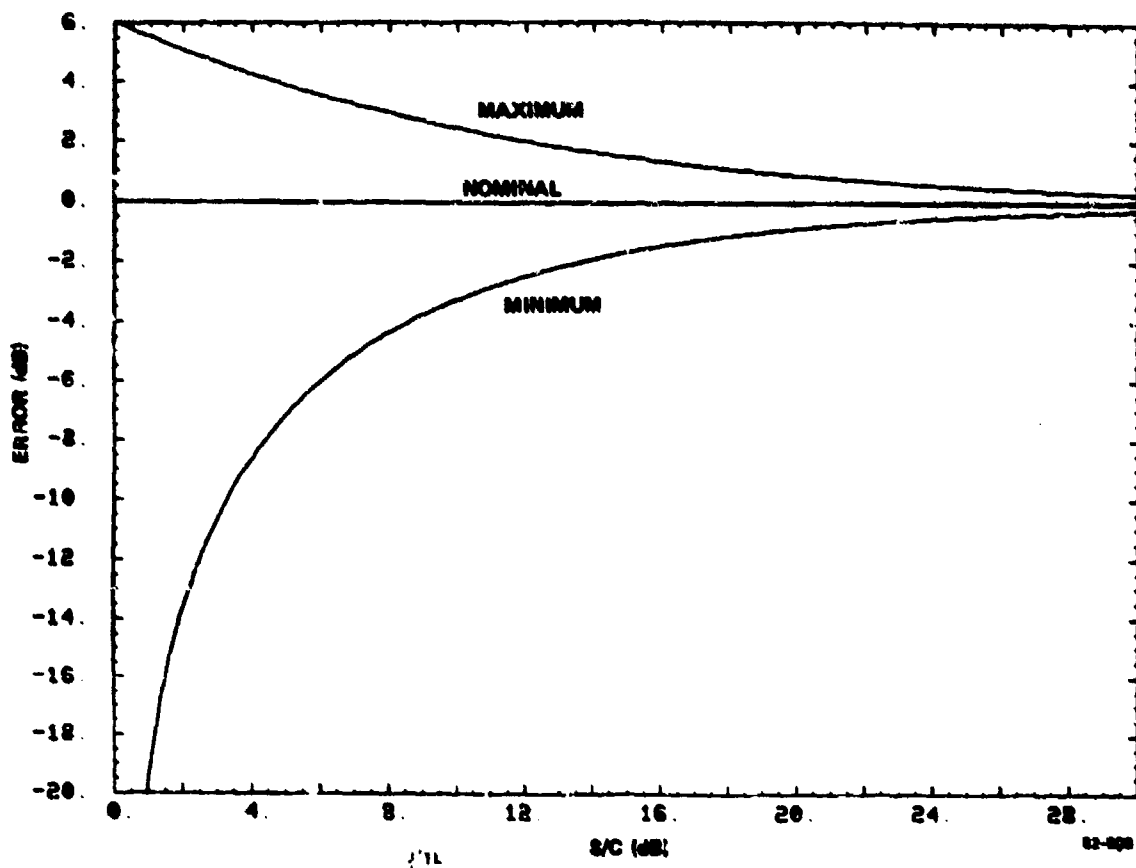


FIG. 62 Error in mean S+C due to clutter effects.

HEADER INFORMATION*****

1	# LINES OF DATA ON FILE AFTER HEADER
2	H' XMT GAIN (DB)
3	V' XMT GAIN (DB)
4	XMT PHASE SETTING
5	FIXED ATTENUATOR (DB) IN H RCV PATH (-100,0)
6	FIXED ATTENUATOR (DB) IN V RCV PATH (-100,0)
7	MAX H' RCV GAIN (DB),V' XMT
8	MAX V' RCV GAIN (DB),V' XMT
9	RCV PHASE SHIFTER SETTING FOR IN-PHASE,V' XMT
10	TOTAL AZIMUTH SCAN (DEG)
11	AZIMUTH STEP SIZE (DEG)
12	AZIMUTH START ANGLE (DEG)
13	SAMPLE TIME IN NSEC
14	NUMBER OF SAMPLES AVERAGED
15	RANGE TO TGT (M)
16	IF PREAMP OUTPUT (DBM) FOR 1 SQ M TGT,V' XMT
17	RCV PHASE SHIFTER SETTING FOR IN-PHASE,H' XMT
18	IF PREAMP OUTPUT (DBM) FOR 1 SQ M TGT,H' XMT
19	MAX H' RCV GAIN (DB),H' XMT
20	MAX V' RCV GAIN (DB),H' XMT

FILE NAME CONVENTION*****

PIJR01.DAT

I BODY TYPE

1	14 CM AIRCRAFT (SCALE A)
2	22 CM AIRCRAFT (SCALE A-B)
3	35 CM AIRCRAFT (SCALE B-C)
4	43 CM AIRCRAFT (SCALE C-D)
5	64 CM AIRCRAFT (SCALE D)
6	1 SQ M DIHEDRAL
7	1/2 IN BB
8	1 FT SPHERE
9	CONE ONLY

J CONFIGURATION

0	BODY ONLY (WITH SLOTS AND TAPE)
1	30 DEG THIN WING
2	60 DEG WING
3	30 DEG FAT WING
4	+45 DEG DIHEDRAL
5	-22.5 DEG DIHEDRAL
6	VERT DIHEDRAL
7	HOR DIHEDRAL
8	SMOOTH RCC AIRCRAFT BODY
9	CONE ONLY

TABLE 6
FILE HEADER AND NAME CONVENTIONS

TABLE 7 TEST RUN LOG

FILE,DATE,ATTEN,AZSTEP,RANGE,DBHV',DBMH',COMMENT

P32D02	19-JUL-8	-20	0.50	20.000	-12.700	-14.200
P43D03	19-JUL-8	-30	0.50	20.000	-12.700	-14.200
P31D02	19-JUL-8	-20	0.50	20.000	-12.700	-14.200
P42D02	16-JUL-8	-30	0.50	20.000	-14.000	-15.200
P41D02	16-JUL-8	-30	0.50	20.000	-13.000	-13.200
P53D02	16-JUL-8	-30	0.50	20.000	-14.000	-13.200
P12D01	16-JUL-8	-20	0.20	12.000	-4.400	-4.900
P53D01	16-JUL-8	-40	0.50	12.000	-4.400	-4.900

DISK 4

LONG RANGE
LONG RANGE -- RADAR FENCE
LONG RANGE
LONG RANGE -- RADAR FENCE
LONG RANGE -- RADAR FENCE
FIRST 20N RUN- RADAR FENCE
RADAR FENCE -- CALM
RADAR FENCE-CALM DAY

FILE,DATE,ATTEN,AZSTEP,RANGE,DBHV',DBMH',COMMENT

P41D01	16-JUL-8	-40	0.50	12.000	-4.400	-4.900
P31D01	16-JUL-8	-30	0.50	12.000	-5.400	-5.300
P42D01	16-JUL-8	-40	0.50	12.000	-5.400	-5.300
P32D01	16-JUL-8	-30	0.50	12.000	-5.400	-5.300
P43D02	16-JUL-8	-40	0.50	12.000	-5.400	-5.300
P43D01	16-JUL-8	-30	0.50	12.000	-5.400	-5.300
P80D01	15-JUL-8	-40	1.00	12.000	-5.800	-6.100
P99A01	13-JUL-8	0	1.00	12.000	-4.000	-4.100
P43A01	13-JUL-8	-40	0.50	12.000	-4.000	-4.100
P42A01	13-JUL-8	-40	0.50	12.000	-4.000	-4.100
P32A01	13-JUL-8	-40	0.50	12.000	-4.000	-4.100
P41A01	13-JUL-8	-40	0.50	12.000	-4.700	-5.800
P31A01	13-JUL-8	-30	0.50	12.000	-7.000	-6.300
P23A01	13-JUL-8	-30	0.20	12.000	-4.400	-5.700
P21A01	13-JUL-8	-30	0.20	12.000	-4.700	-6.500

DISK 3

RADAR FENCE-- CALM AIR
RADAR FENCE
RADAR FENCE
RADAR FENCE
RADAR FENCE
RADAR FENCE
HERBIE IN MAIN BEAM

STILL WINDY
WINDY
WINDY
WINDY--BOBS NOSE DOWN
INTERMITTENT WIND
WINDY
WINDY

FILE,DATE,ATTEN,AZSTEP,RANGE,DBHV',DBMH',COMMENT

P65D02	13-JUL-8	-40	0.00	12.200	-5.100	-5.100
P65D01	13-JUL-8	-40	0.00	12.200	-5.100	-5.100
PA0R01	14-JUL-8	-20	0.10	12.200	-3.700	-5.400
P12A01	13-JUL-8	-20	0.20	12.000	-5.400	-4.600
P22A01	13-JUL-8	-30	0.20	12.000	-5.400	-5.800
P11A01	13-JUL-8	-20	0.20	12.000	-4.700	-5.900
P33A01	13-JUL-8	-30	0.20	12.000	-4.700	-5.900
P33R02	09-JUL-8	-40	0.20	12.200	-4.000	0.000
P20R01	09-JUL-8	-40	0.20	12.200	-4.000	0.000
P28R02	09-JUL-8	-40	0.20	12.200	-4.000	0.000
P23R03	09-JUL-8	-40	0.20	12.200	-4.000	0.000
P22R01	08-JUL-8	-40	0.20	12.200	-4.000	0.000
P21R02	08-JUL-8	-40	0.20	12.200	-4.000	0.000

DISK 2

-30 AND DOWN BY 10 DB STE
-30 DB TO - 90 DB IN 10 D

NO WIND
A LITTLE WINDY
NOT WINDY
FIRST ROOF RUN--HOT SUN--
WINDY
WINDY
WINDY

SLIGHT WIND- MASKING TAPE
MASKING TAPE

FILE,DATE,ATTEN,AZSTEP,RANGE,DBHV',DBMH',COMMENT

P10R01	30-JUN-82	NEW CON	-30	0.50	12.200	-11.200	0.000	
P70R02	30-JUN-82	NEW CONE	-20 ON- 20 OFF -ET	0	1.00	12.200	-11.200	0.000
P18R01	18-JUN-82	ON GOOD CON	-30	0.50	12.200	-4.000	0.000	
P29R01	18-JUN-82	CONE ONL	0	0.20	12.200	-4.000	0.000	
P70R01	15-JUN-8	HALF IN SPHERE ON OFF EVERY 20 POINTS	15-JUN-8	0	1.00	12.200	-8.900	
P21R01	15-JUN-8	SCREW STICKS UP	-30	0.20	12.200	-4.000	0.000	
P12R04	15-JUN-8	NEW TAPE- WINGS SQUARED	-20	0.50	12.200	-4.000	0.000	
P80R01	15-JUN-8	WINDY- ON TABLE	-30	0.10	12.200	-4.000	0.000	
P28R01	15-JUN-8	RCC RUN ON STAND	-30	0.20	12.200	-4.000	0.000	
P23R04	10-JUN-8	SQUARED WINGS - .1 DEG. AZ STEP	-30	0.10	12.200	-4.600	0.00	
P33R01	03-JUN-8	FIRST RUN - TAPED - 3 MHZ FILTER	-30	1.00	12.200	-4.600	0.0	
P12R03	03-JUN-8	TAPED - 3 MHZ FILTER	-30	1.00	12.200	-4.600	0.000	
P23R03	03-JUN-8	10 DEG TO 20 DEG- .1 DEG STEPS	-30	0.10	12.200	-4.600	0.000	
P23R02	03-JUN-8	TAPE ON SCREWS - 3 MHZ FILTER	-30	1.00	12.200	-4.600	0.000	
P66R01	03-JUN-8	REPRODUCE BOERNER RESULTS	-30	1.00	12.200	-4.600	0.000	
P23R01	27-MAY-8	FIRST RUN WITH TOT 2-WINDY AND HOT	-35	1.00	12.200	-4.600	0	
P12R02	27-MAY-8	25 DB ATTEN - 10 SAMPLES AVERD - 20.4 - 22	-20	1.00	12.200	-4.6		
P63R01	20-MAY-8	TEST	-30	1.00	0.900	0.000	0.000	
P12R01	20-MAY-8	FIRST TARGET RUN	-30	1.00	12.200	-4.600	0.000	

DISK 1 - BASIC

Figures 63 through 76 plot measured Stokes parameter data for targets at 0° aspect, while Figures 77 through 88 plot these data for targets at 10° aspect. As described in Section 4.2, one transmit polarization (135° linear) is sufficient for the first set, while two transmit polarizations (45° and 135°) are required for the second set. The model and scale conventions used can be interpreted by consulting Table 4; for example, Figure 70, which represents Model 3, scale B, in turn corresponds to a MiG-25 at 550 MHz scaled frequency.

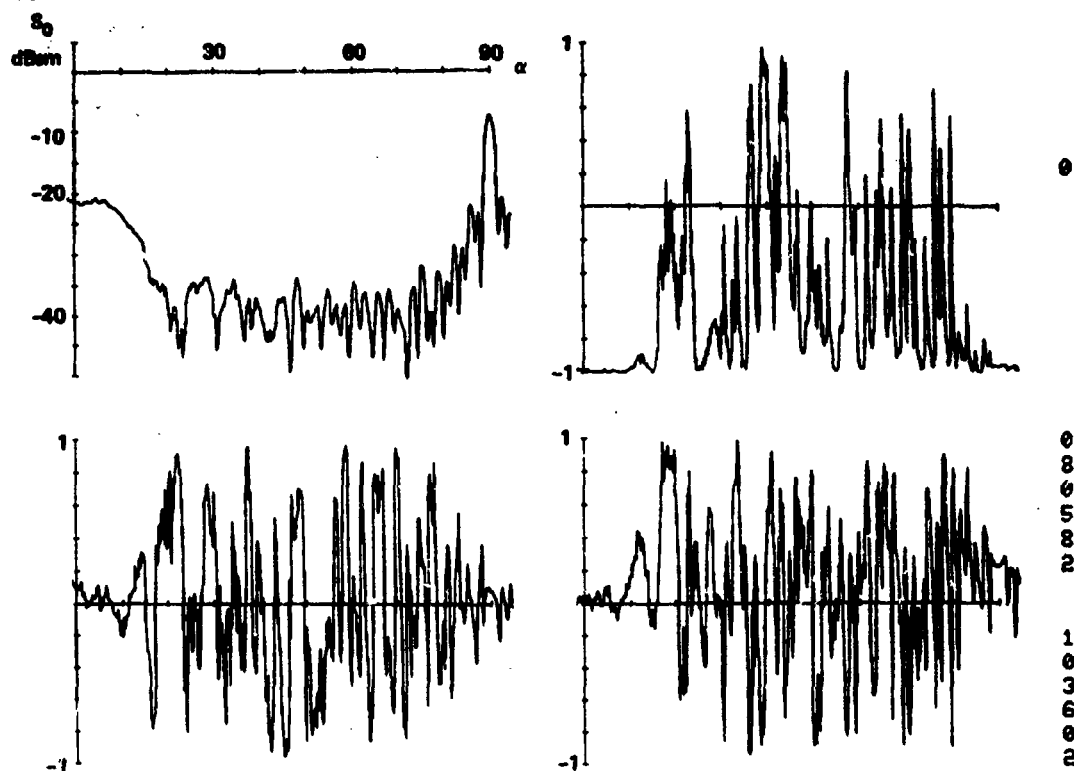
Several target polarization features emerge clearly from these data. By far, the most striking and potentially useful is the horizontal dipole formed by the leading edge of the target wing. The characteristic Stokes parameter response for such a dipole is $s_1/s_0 = 1$, $s_2/s_0 = 0$, $s_3/s_0 = 0$. In fact, the figures with Models 1 and 3 tend to show s_1/s_0 near +1 at 30°, while s_2 and s_3 both fluctuate around zero (e.g. Figure 76); the figures with Model 2 show this behavior at $\alpha = 60^\circ$ (e.g. Figure 72). The effect is stronger at 60°, since this is further away from the sidelobes from the nose-on disk.

The 0° aspect runs all show a strong specular scatterer near nose-on. This scatterer has a Stokes response of $s_1/s_0 = 0$, $s_2/s_0 = -1$,

$s_3/s_0 = 0$ if the illumination is 135° linear (such a flat plate target leaves linear polarization unchanged). All the figures from 63 to 76 demonstrate this specular response near nose-on.

The width of the nose-on response as a function of aspect, particularly measured using s_2/s_0 , is an indication of the diameter of the flat plate nose of the aircraft models. As the scale size of the models increases from A to D, the azimuth extent over which s_2/s_0 remains near -1 decreases as the inverse of the scale size.

TH= .0 KA= 5.24 H.B.DZ.21= 10.00 .00 .00 .00 BE1,BE2= 0 0

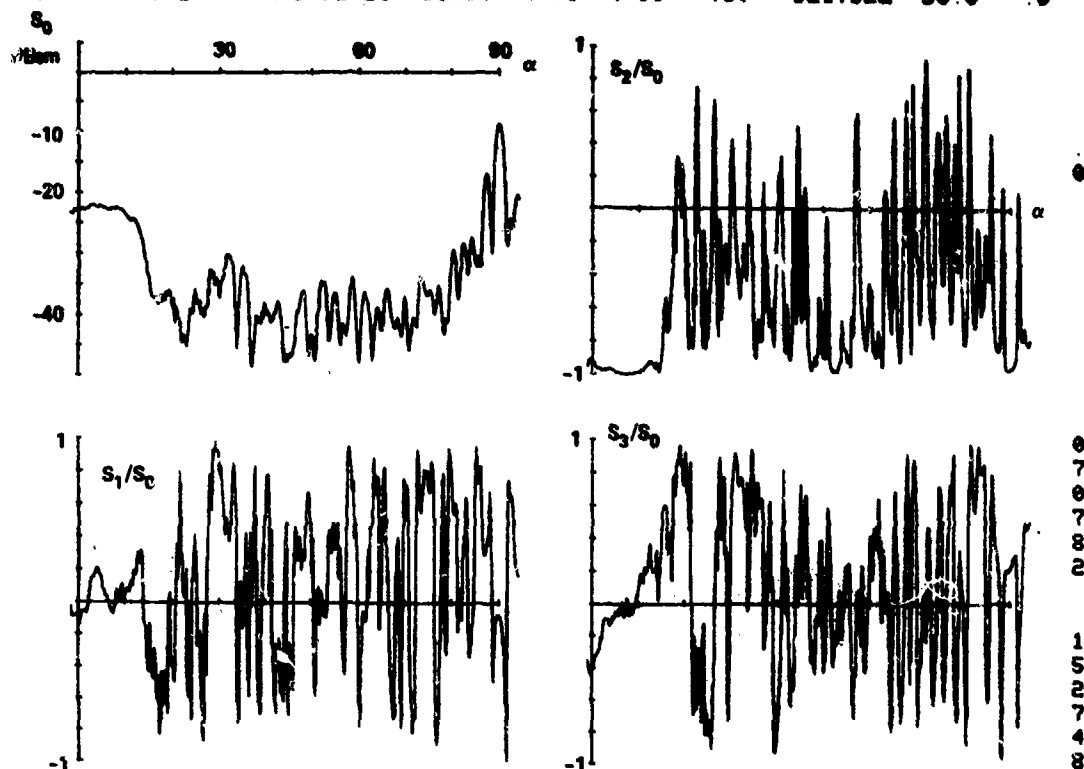


82-834

PCA3 - AIRCRAFT S0.1.2.3 VS ASPECT 4SLIN POLZII DATA P19R02 07-JUL-82

FIG. 63 Measured Stokes parameters vs. aspect of cylinder, Scale A; $ka = 5.24$; $\theta = 0^\circ$.

TH- 0 KA= 5.24 H.B.DZ.Z1= 10.00 4 71 4 00 -.30 BE1.BE2= 30.0 0

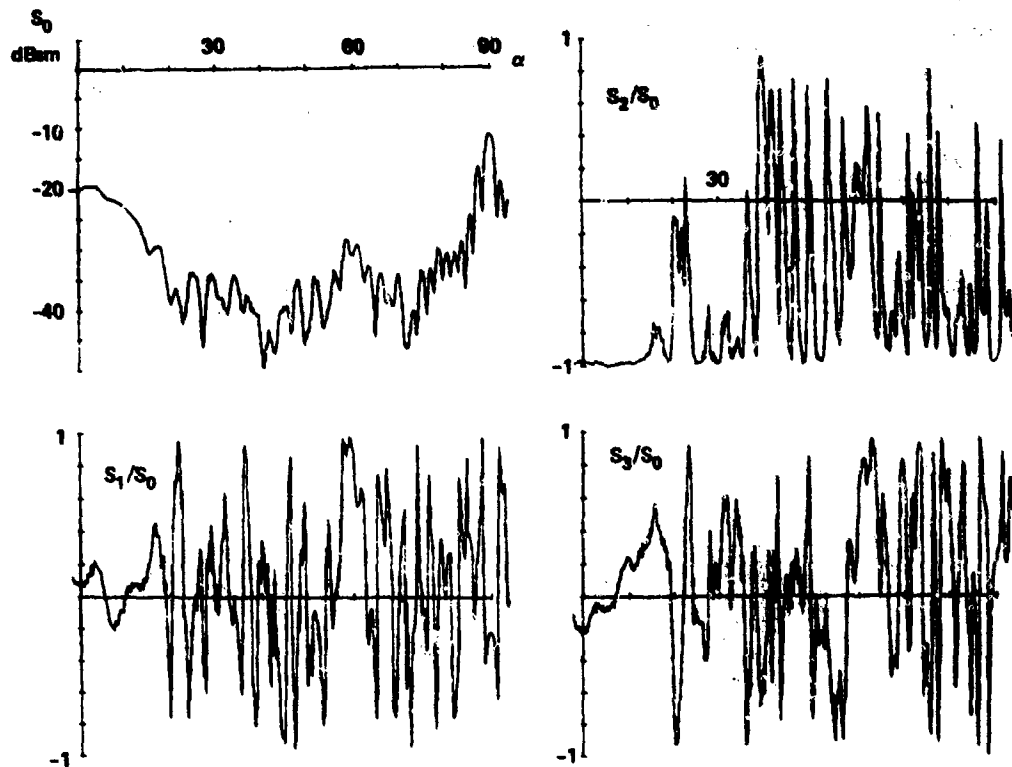


82-837

7 PCA3 - AIRCRAFT 50.1.2.3 US ASPECT 4SLIN POL2H DATA:P11R02 07-JUL-82

FIG. 64 Measured Stokes parameters vs. aspect of model 1, Scale A; $ka = 5.24$; $\theta = 0^\circ$.

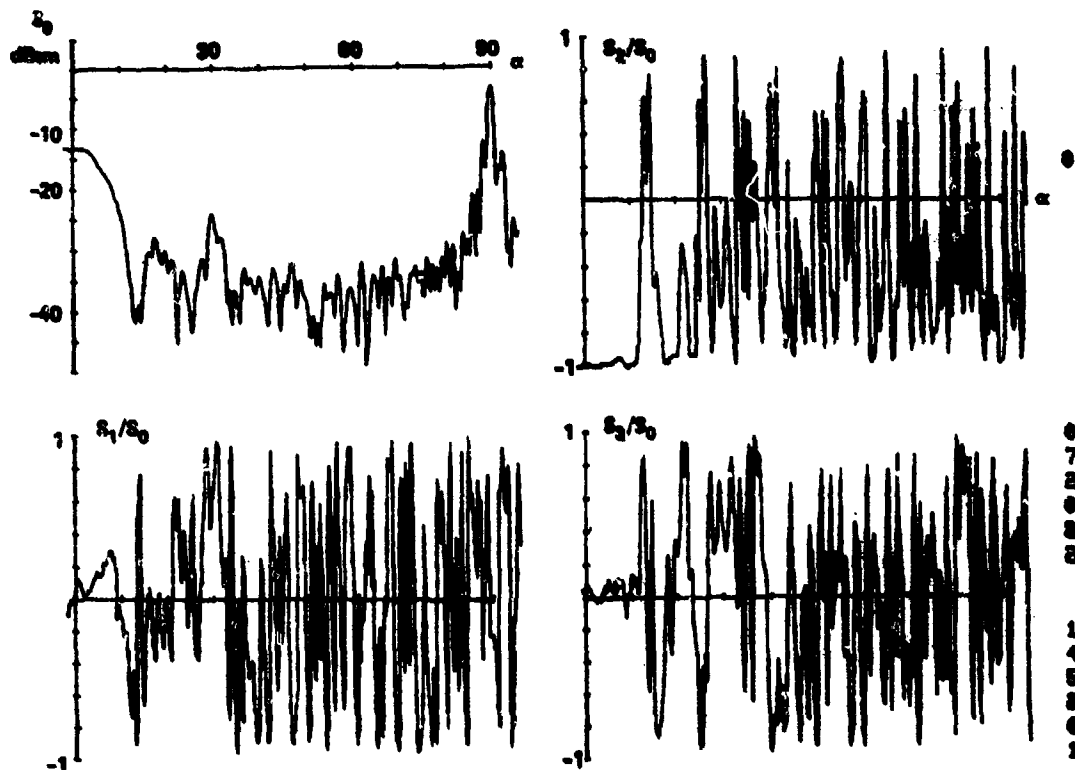
TH- 0 KA= 5.24 H.B.DZ.ZI= 00 3.86 7.40 2.00 BE1.BE2= 60.0 0



PCA5 - A/C-1000 S0.1.2.3 VS ASPECT POL2N -1.1 DATA: P12D01 16-JUL-82

FIG. 65 Measured Stokes parameters vs. aspect of rhodel 2, Scale A; $ka = 5.24$; $\theta = 0^\circ$.

TH- 0 KA= 8.14 H.B.DZ.21= 10.00 5.85 6.30 -.30 BE1,BE2= 30.0 0

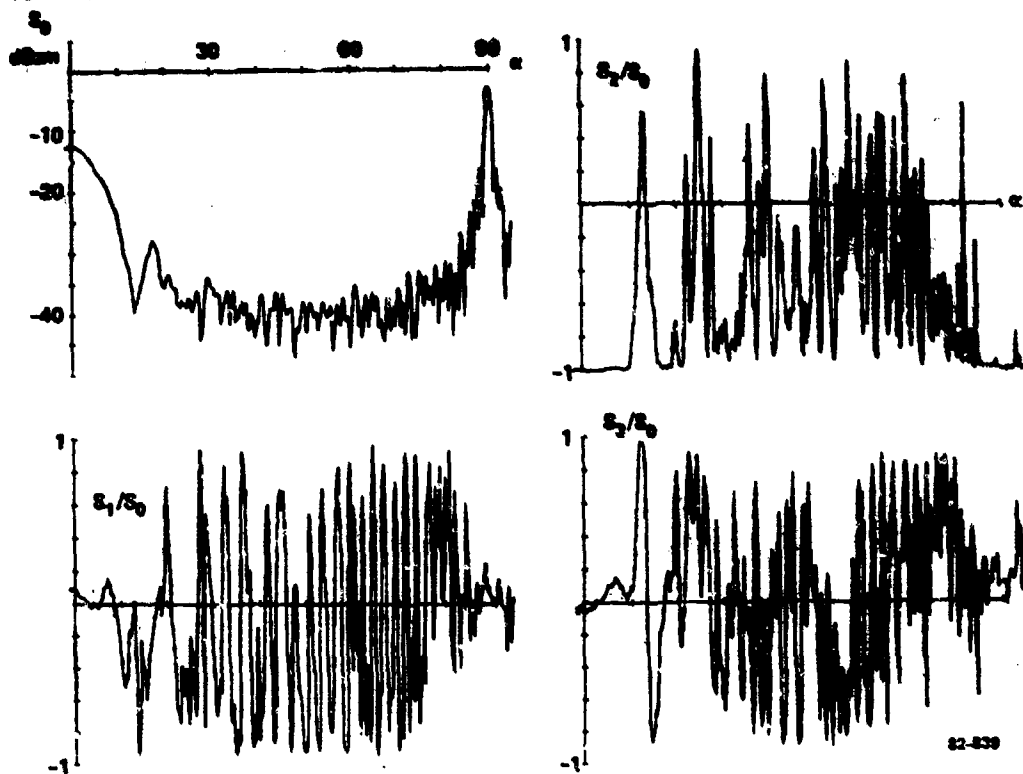


82-036

PCA3 - AIRCRAFT S0.1.2.3 US ASPECT 45LIN POLZN DATA P23R05 09-JUL-82

FIG. 06 Measured Stokes parameters vs. aspect of model 3, Scale A; $ka = 8.14$; $\theta = 0^\circ$.

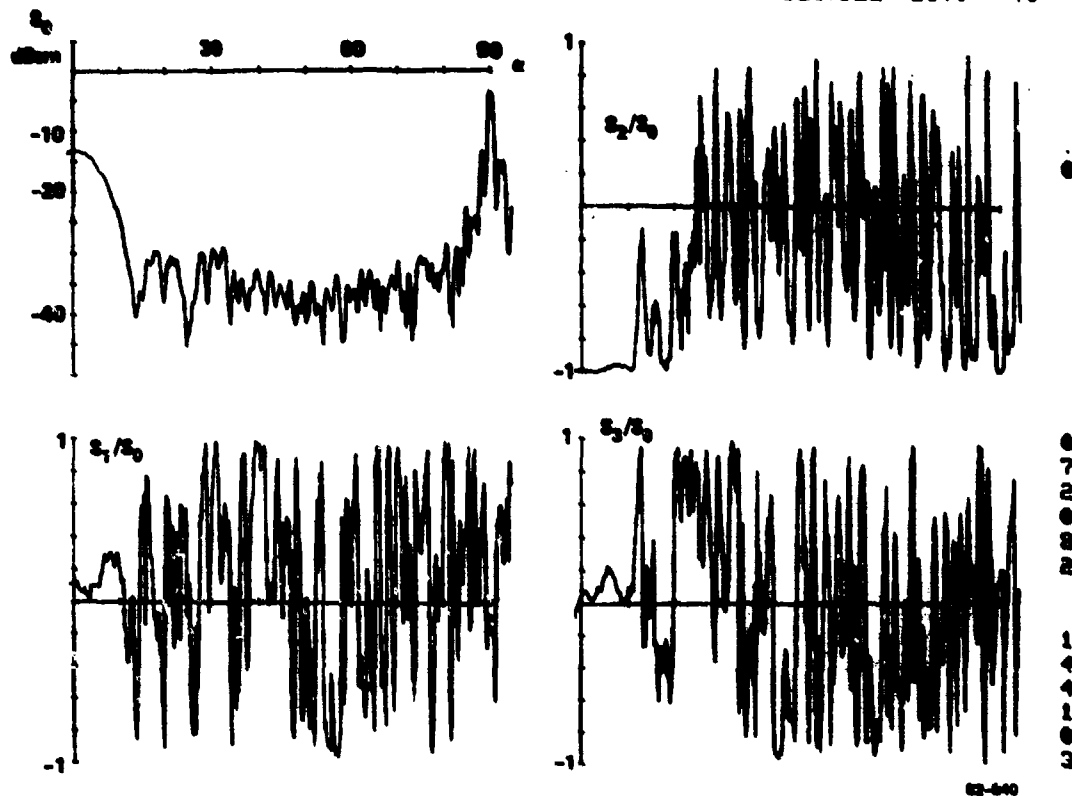
TH= .0 KA= 8.14 H.B.DZ.21= 10.00 .00 .00 .00 SE1.BER= .0 .0



3 PCA3 - AIRCRAFT SE.1.2.3 VS ASPECT 45LIN POLIN DATA P28R92 09-JUL-82

FIG. 67 Measured Stokes parameters vs. aspect of cylinder, Scale B; $ka = 8.14$; $\theta = 0^\circ$.

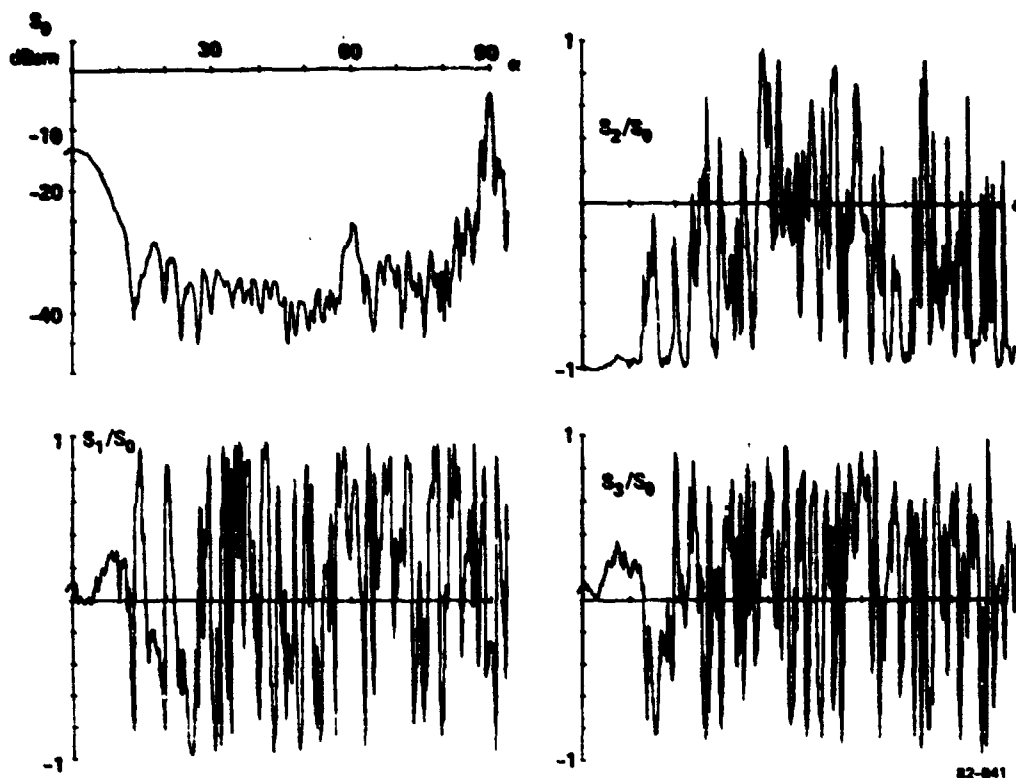
TH= 0 KA= 8.14 H.B.DZ.Z1= 10.00 4.71 4.00 -30 BE1.BE2= 30.0 0



PCA3 - AIRCRAFT 50.1.2.3 US ASPECT 45LIN POLZN DATA P21R02 08-JUL-82

FIG. 68 Measured Stokes parameters vs. aspect of model 1, Scale B; $ka = 8.14$; $\theta = 0^\circ$.

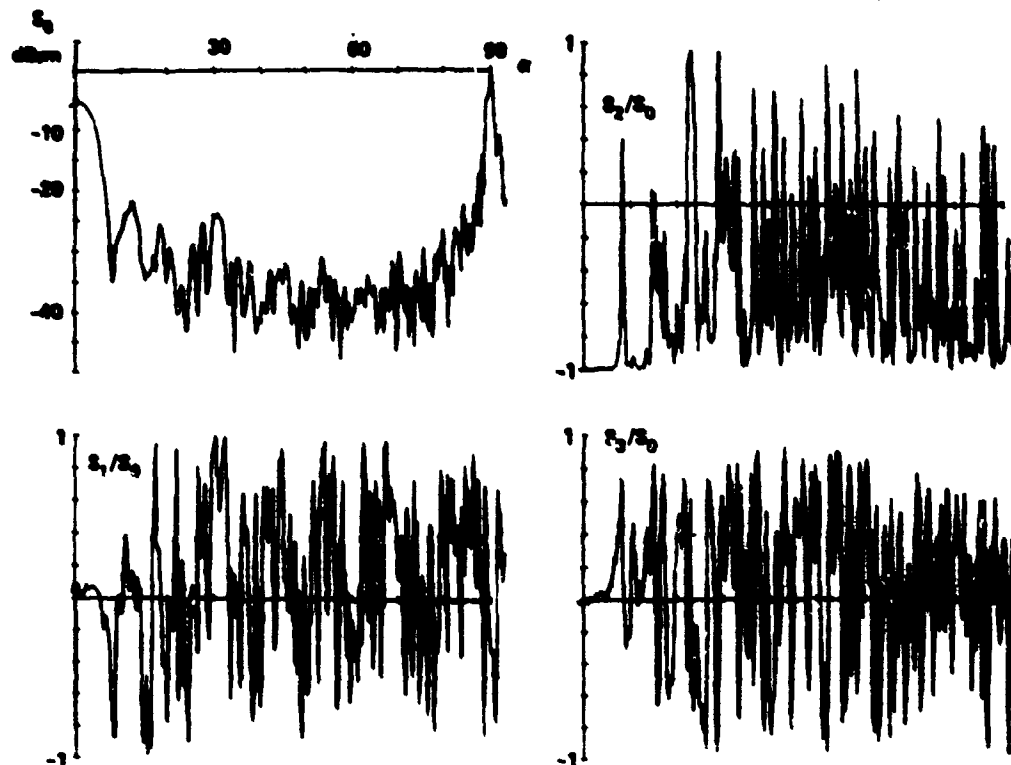
TH- 0 KA= 3.14 H.B.DZ.Z1- 10 00 3 26 7 40 2 00 BE1.BE2- 60 0 . 0



3 PCA3 - AIRCRAFT 50.1.2.3 US ASPECT 45LIN POLEN DATA P22R01 08-JUL-82

FIG. 69 Measured Stokes parameters vs. aspect of model 2, Scale B; $ka = 8.14$; $\theta = 0^\circ$.

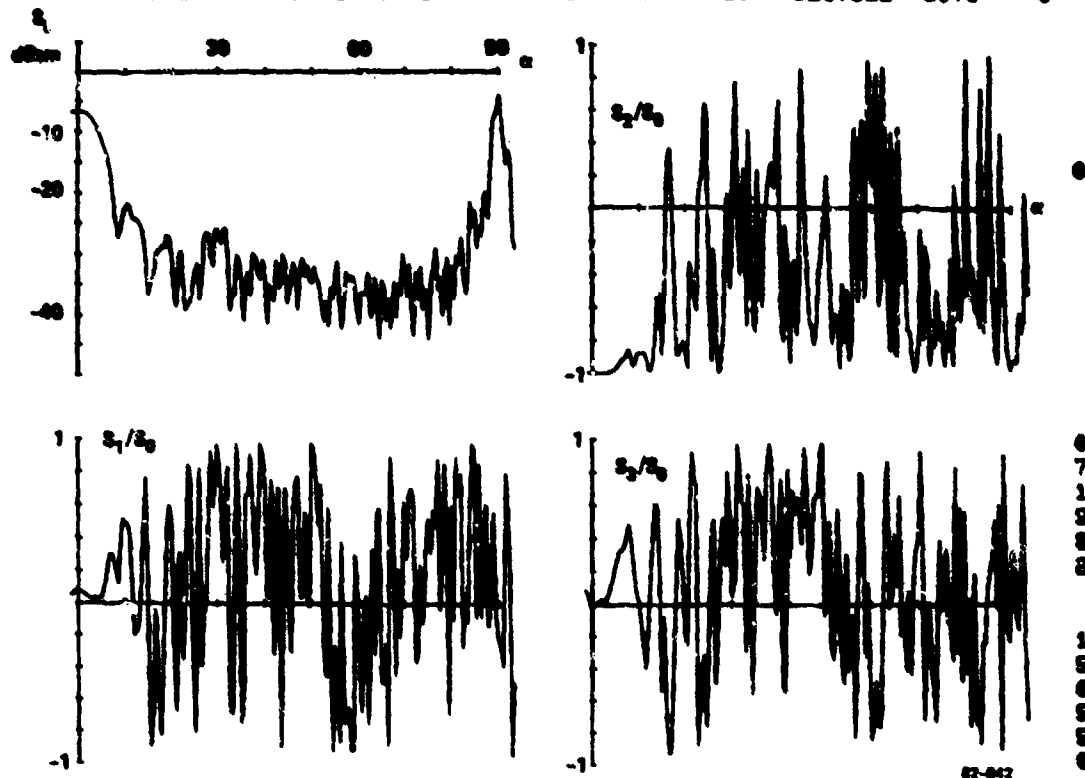
TH- 0 KA-12 80 H.P.DZ.21- 10.00 5.85 6.30 -.30 BE1.BE2- 30.0 0



PCA3 - A/C-1000 SO.1.2.3 VS ASPECT 45LIN POL2N DATA P33R02 09-JUL-82

FIG. 70 Measured Stokes parameters vs. aspect of model 3, Scale B; $ka = 12.8$; $\theta = 0^\circ$.

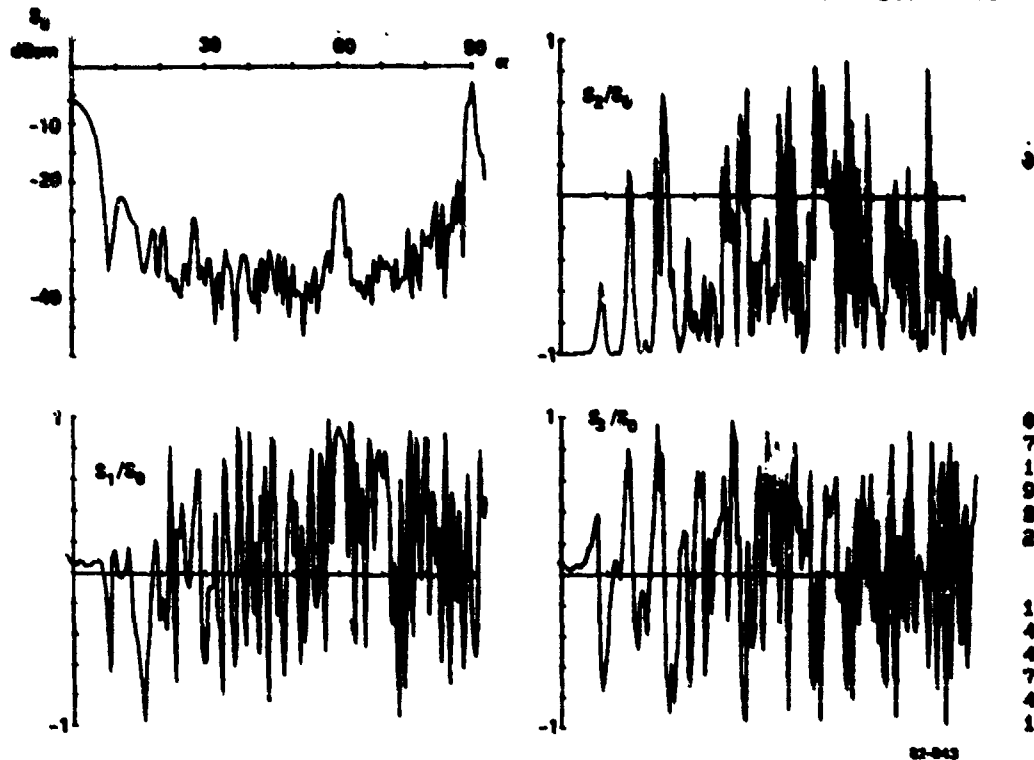
TH= .0 KA=12.80 H.B.DZ.Z1= 10.00 4.71 4.00 -.30 DE1.DE2= 30.0 0



PCAS - AIRCRAFT 50.1.2.3 US ASPECT POLZN -1.1 DATA P31D01 16-JUL-82

FIG. 71 Measured Stokes parameters vs. aspect of model 1, Scale C; $ka = 12.8$; $\theta = 0^\circ$.

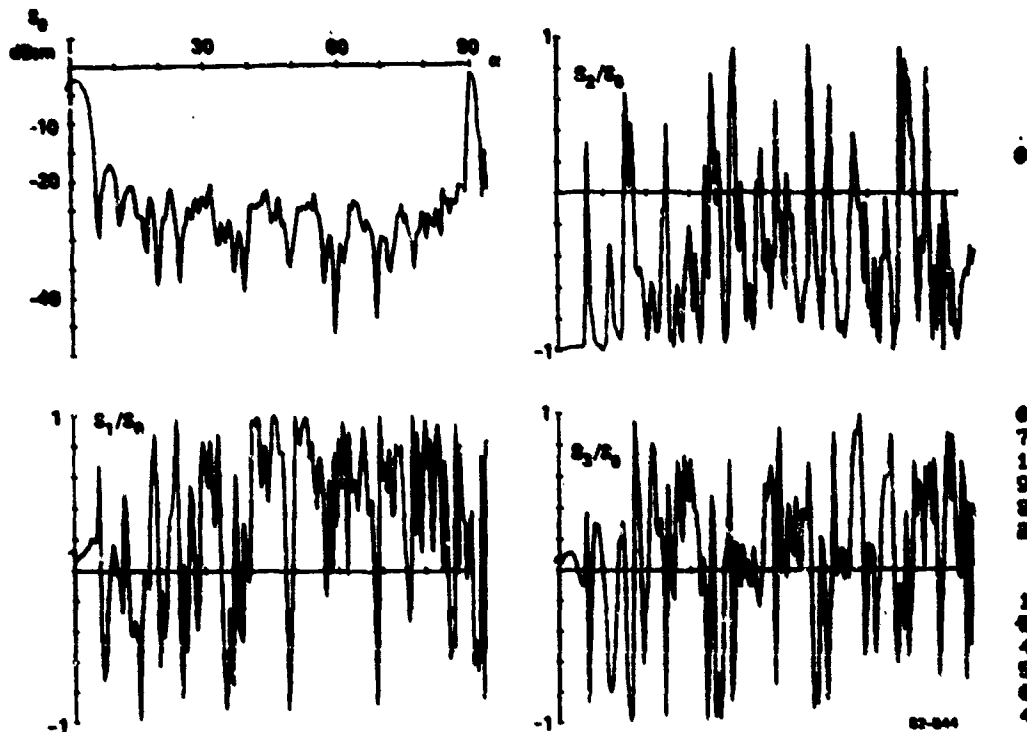
TH-10.0 KA-12.80 H.B.DZ.ZI- 10.00 3.26 7.40 2.00 SE1.BE2- 00.0 .0



■ PCAS - AIRCRAFT S0.1.2.3 VS ASPECT POLZN -1.1 DATA P32D01 16-JUL-82

FIG. 72 Measured Stokes parameters vs. aspect of model 2, Scale C; $ka = 12.8$; $\theta = 0^\circ$.

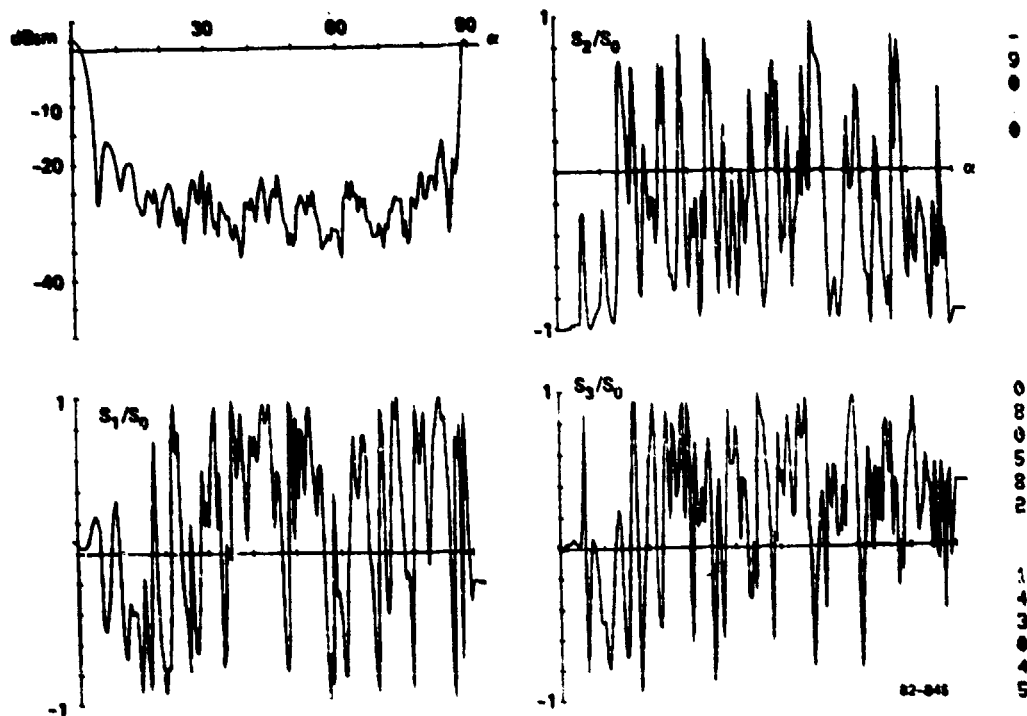
TH- .0 KA=18.60 H.B.DZ.Z1- 10.00 5.85 6.30 -.30 DE1.DZ2= 30.0 .0



PCAS - AIRCRAFT S0.1.2.3 US WSPECT POLZN -1.1 DATA P43D01 16-JUL-82

FIG. 73 Measured Stokes parameters vs. aspect of model 3, Scale C; $k_a = 18.6$; $\theta = 0^\circ$.

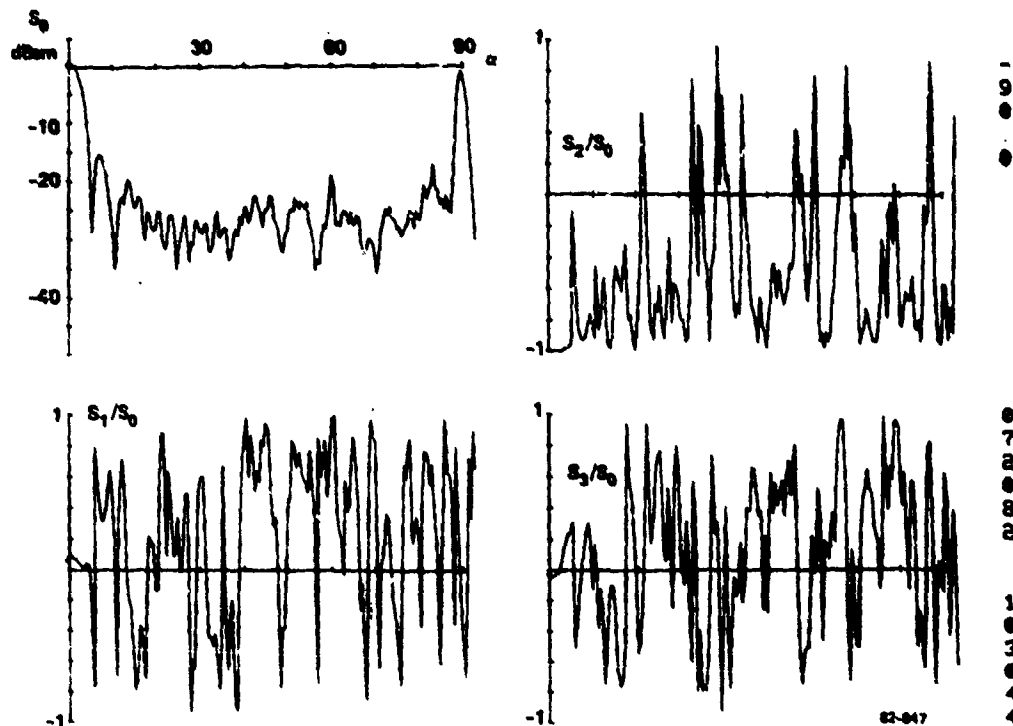
TH- 0 KA=18.60 H.P.DZ.21- 10.00 4 71 4 00 - 30 BE1.BE2- 30 0 0



9 PCAS - AIRCRAFT 50.1.2.3 VS ASPECT POLCH -1.1 DATA P41D01 16-JUL-82

FIG. 74 Measured Stokes parameters vs. aspect of model 1, Scale D; $ka = 18.6$; $\theta = 0^\circ$.

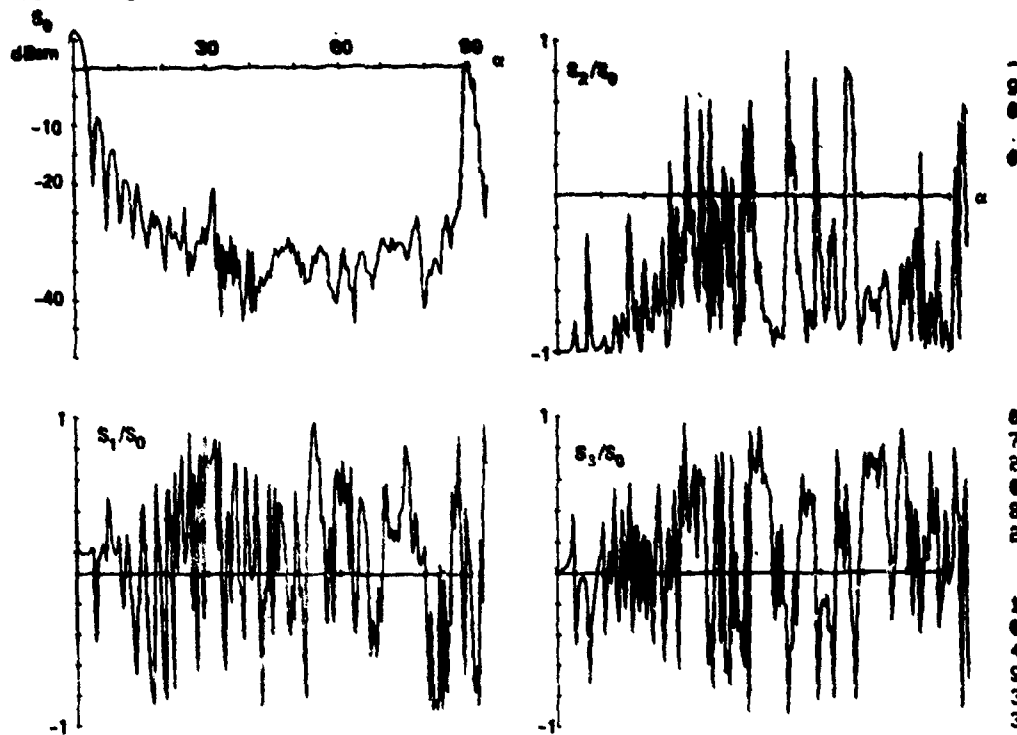
TH- 0 KA=18.60 H.B.DZ.Z1= 10 00 3 86 7 40 2 00 BE1.BE2= 60.0 .0



PCAS - AIRCRAFT 50.1.2.3 US ASPECT POLZN -1.1 DATA P42D01 16-JUL-82

FIG. 75 Measured Stokes parameters vs. aspect of model 2, Scale D; $ka = 18.6$; $\theta = 0^\circ$.

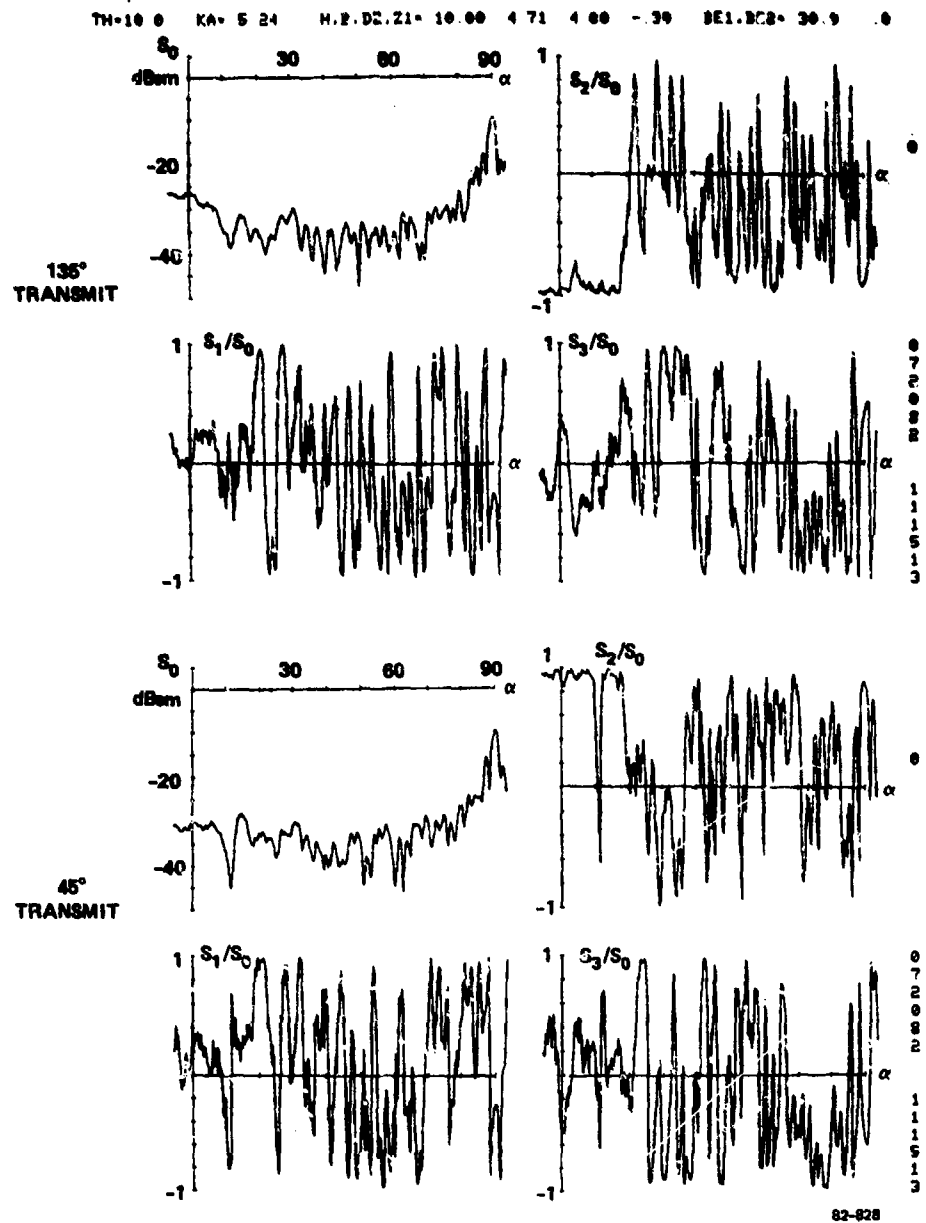
TH- 0 KA=27.90 H.B.DZ.Z1= 10.00 5.85 6.30 -.30 BE1.BE2= 30.0 .0



02-000

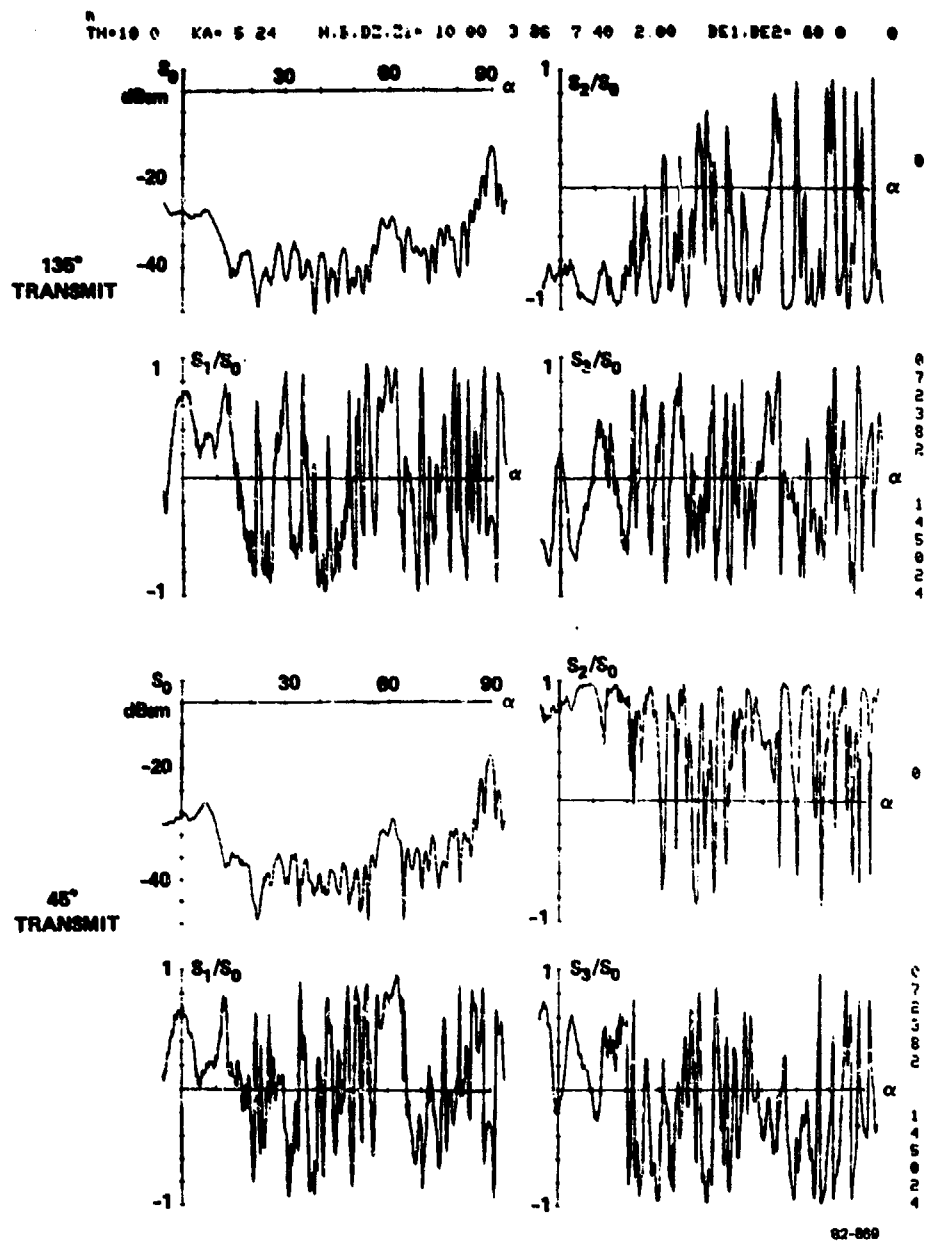
■ PCAS - AIRCRAFT 50.1.2.3 VS ASPECT POLZN -1.1 DATA P53D01 16-JUL-82

FIG. 76 Measured Stokes parameters vs. aspect of model 3, Scale D; $k_a = 27.9$; $\theta = 0^\circ$.



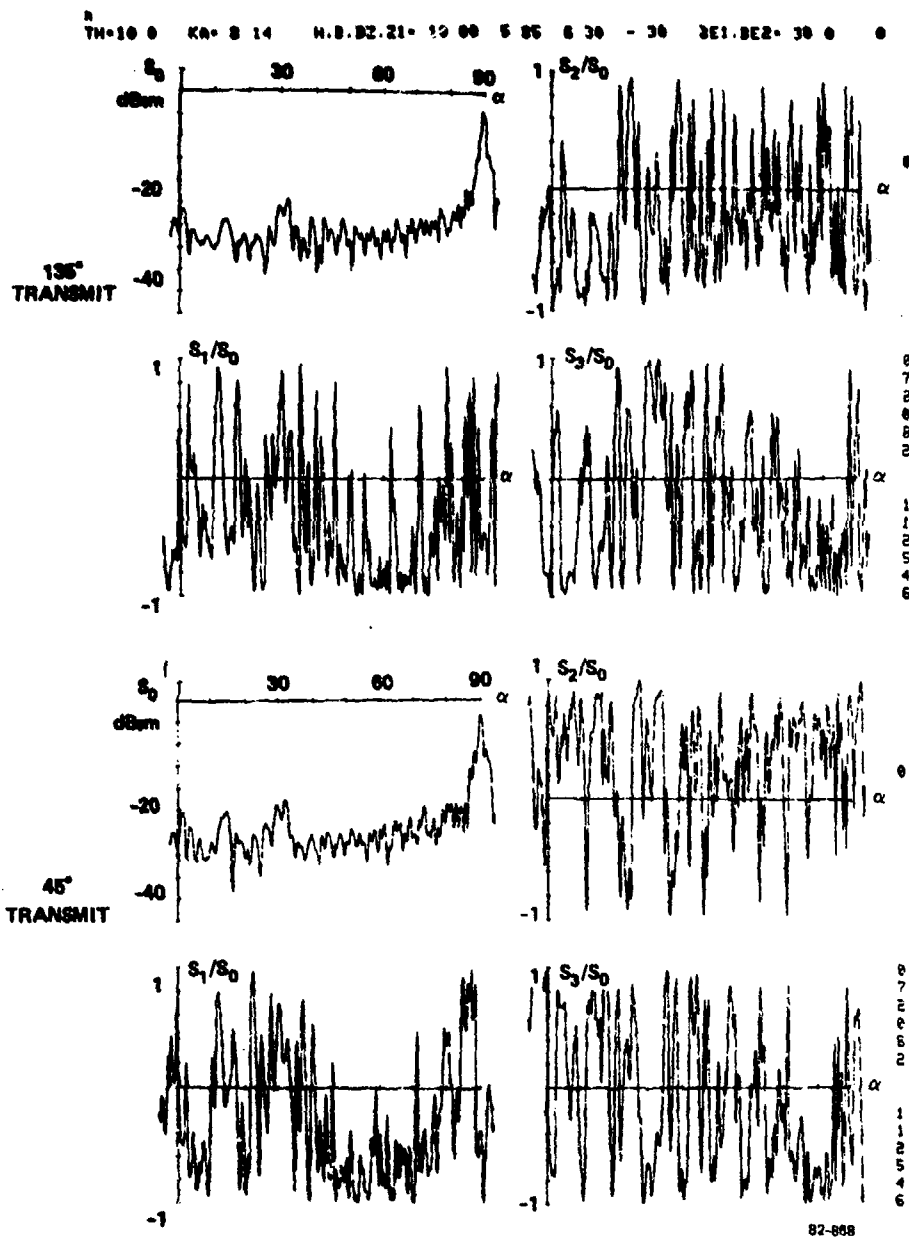
■ PCAS - AIRCRAFT 50.1.2.3 US ASPECT POLZM +1.1 DATA-P11A01 13-JUL-82

FIG. 77 Measured Stokes parameters vs. aspect of model 1, Scale A; $ka = 5.24$; $\theta = 10^\circ$.



PCAS - AIRCRAFT S0.1.2.3 VS ASPECT POLCN +1.1 DATA P18001 13-JUL-82

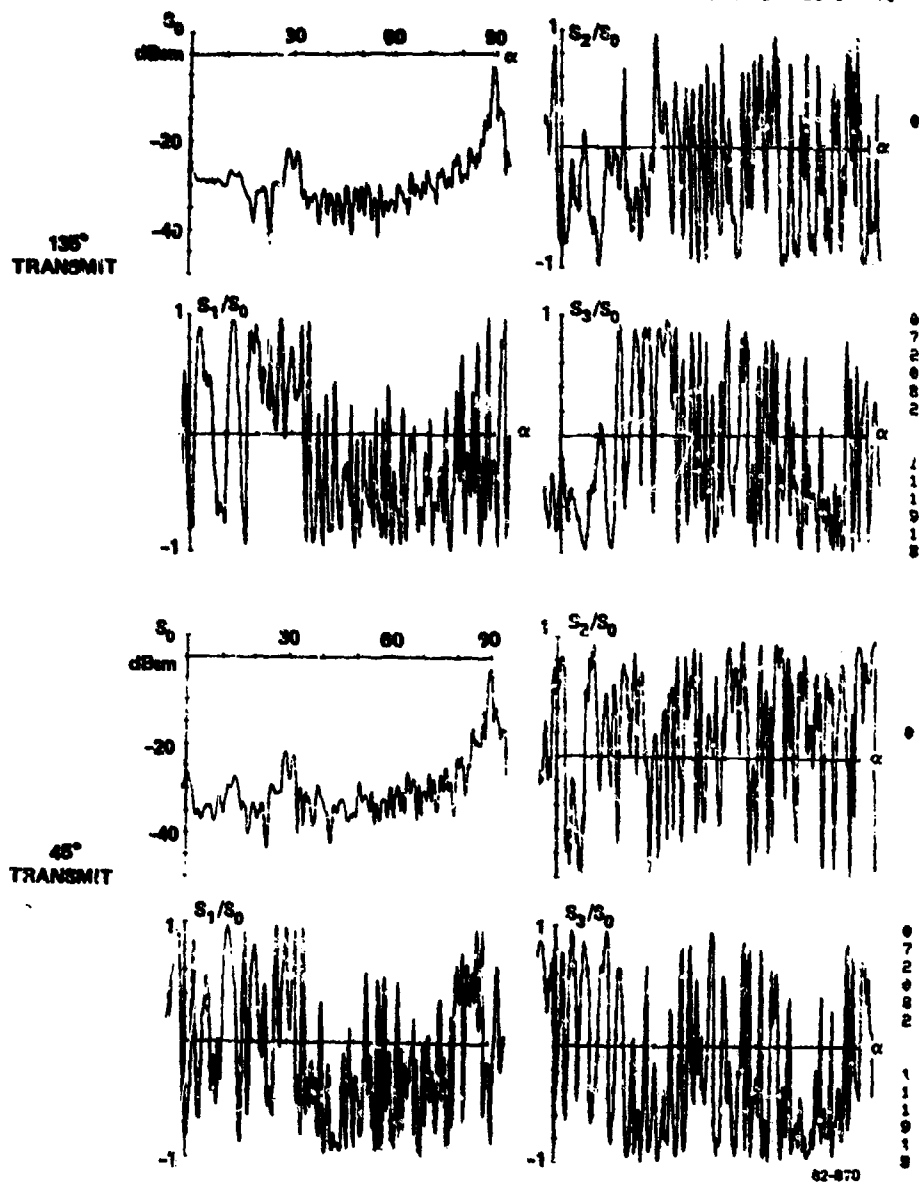
FIG. 78 Measured Stokes parameters vs. aspect of model 2, Scale A; $k_a = 5.24$; $\theta = 10^\circ$.



B PCAS - AIRCRAFT S0.1.2.3 VS ASPECT POLZM +1.1 DATA P83A01 13-JUL-82

FIG. 79 Measured Stokes parameters vs. aspect of model 3, Scale A; $ka = 8.14$; $\theta = 10^\circ$.

TH-10 0 KA-5 14 H.B.PC.21- 10 00 4 71 4 00 - 30 BE1.BE2- 30 0 0



B PCAS - AIRCRAFT 50.1.2.3 US ASPECT POLZN +1.1 DATA: PE1M01 13-11-88

FIG. 80 Measured Stokes parameters vs. aspect of model 1, Scale B; $ka = 0.14$; $\theta = 10^\circ$.

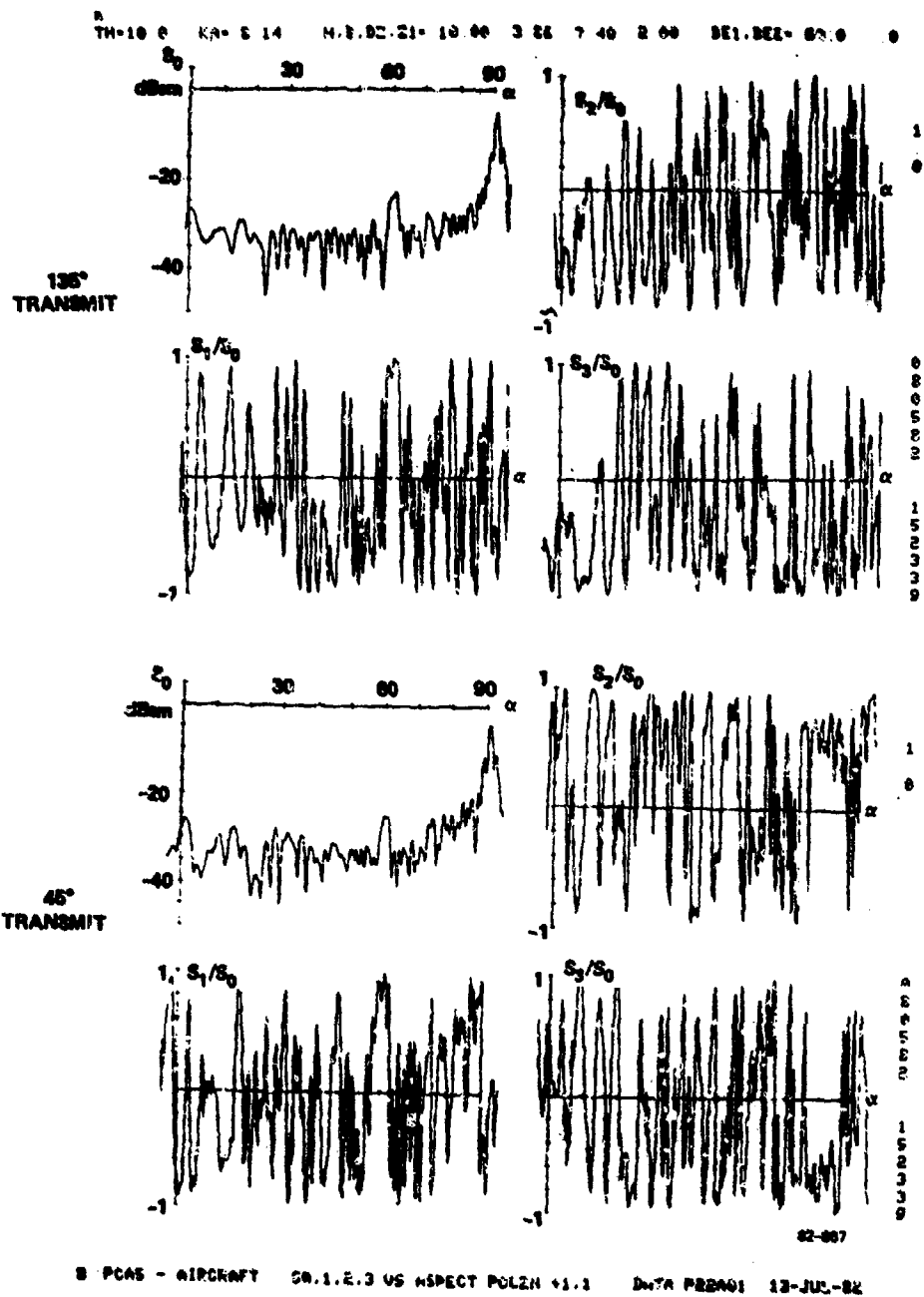
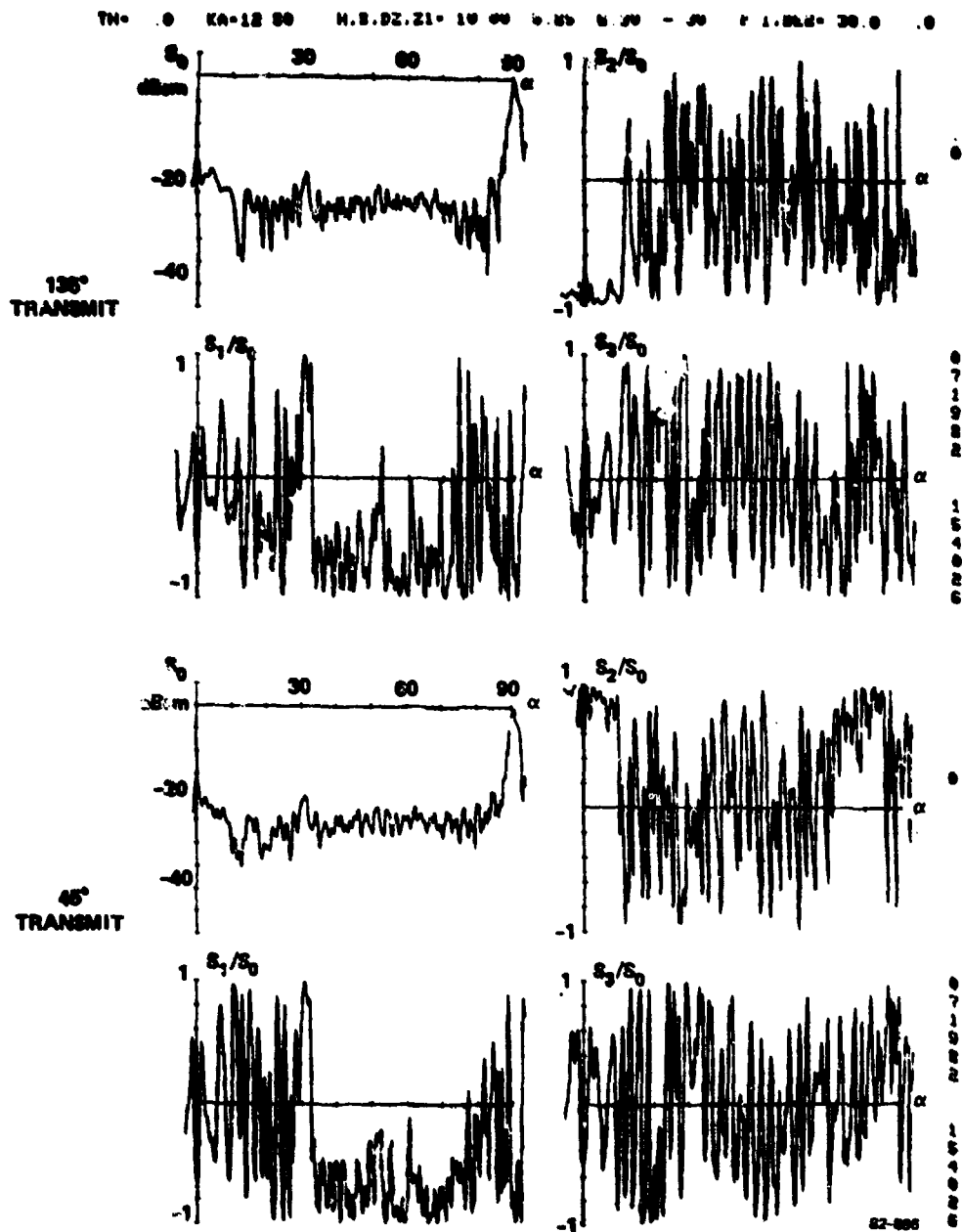
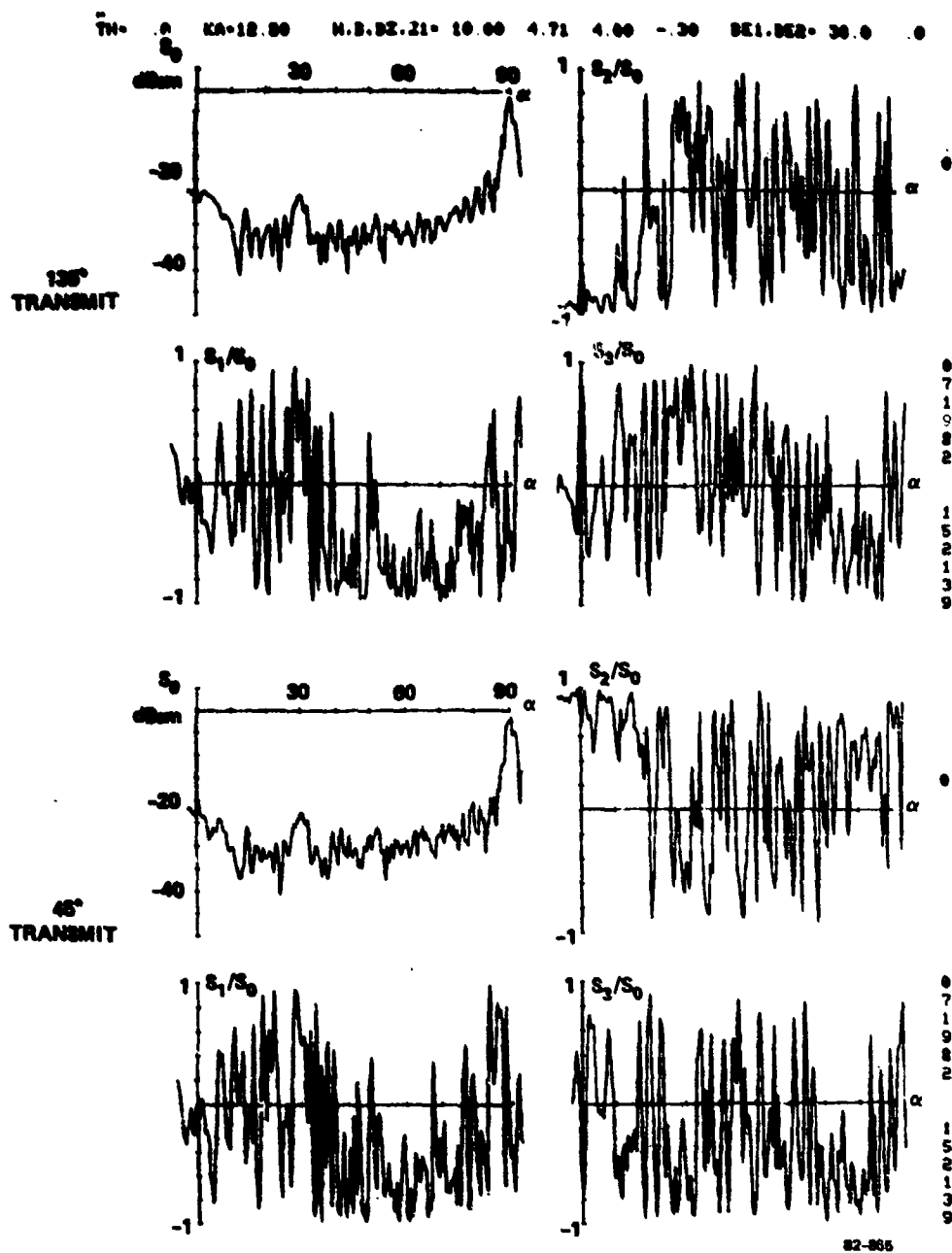


FIG. 81 Measured Stokes parameters vs. aspect of model 2, Scale B; $ka = 8.14$; $\theta = 10^\circ$.



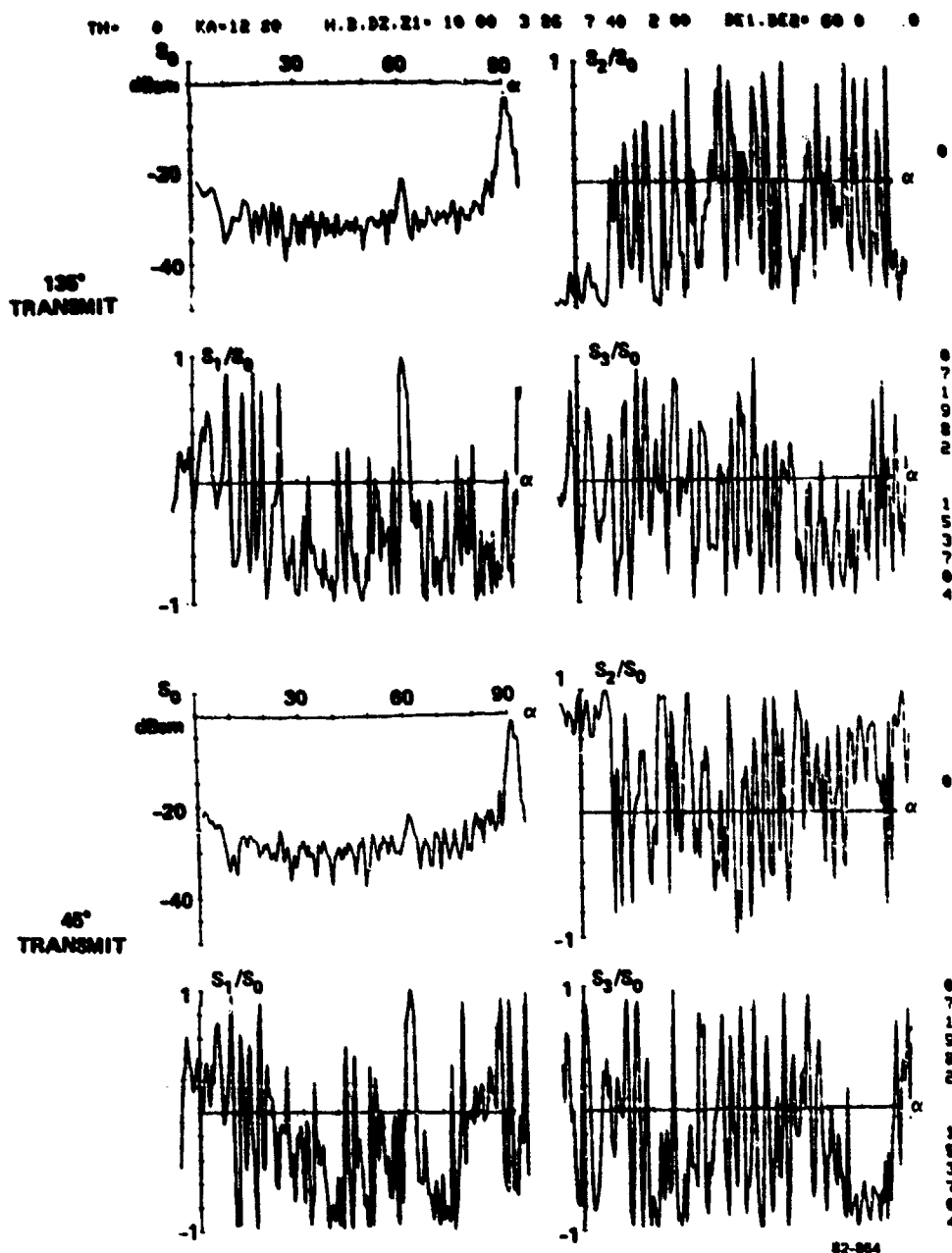
B PCAS - AIRCRAFT 50.1.2.3 US ASPECT POLZN +1.1 DATA P33A01 13-JUL-82

FIG. 82 Measured Stokes parameters vs. aspect of model 3, Scale B; $ka = 12.8$; $\theta = 10^\circ$.



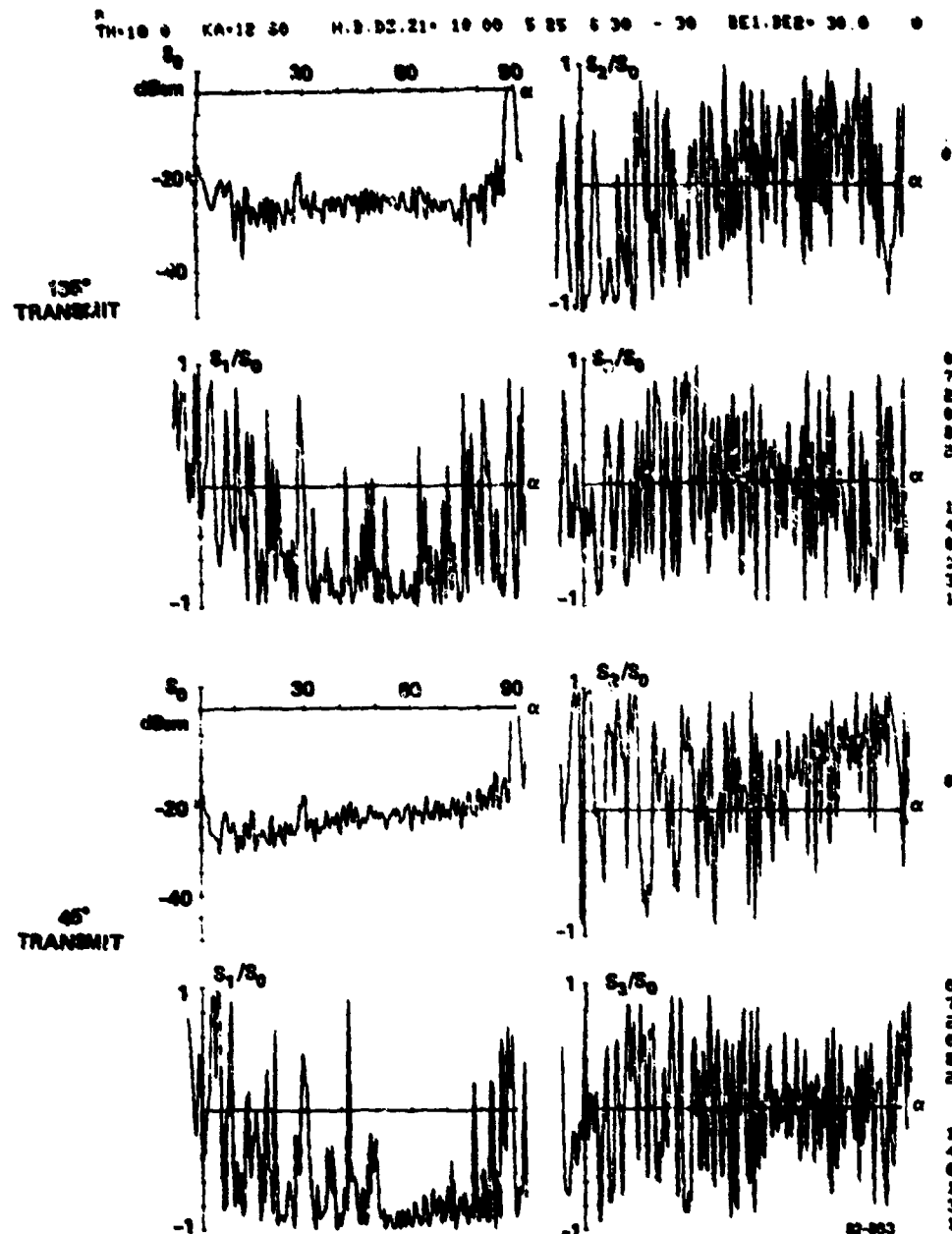
B PCAS - AIRCRAFT 90.1.2.3 US ASPECT POLZN +1.1 DATA P31A01 13-JUL-82

FIG. 83 Measured Stokes parameters vs. aspect of model 1, Scale C; $ka = 12.8$; $\theta = 10^\circ$.



B PCAS - AIRCRAFT S0.1.2.3 VS ASPECT POLZN +1.1 DATA P32A01 13-JUL-82

FIG. 84 Measured Stokes parameters vs. aspect of model 2, Scale C; $ka = 12.8$; $\theta = 10^\circ$.



8 PCAS - AIRCRAFT 80.1.2.3 US ASPECT POLIN +1.1 DATA P43401 13-JUL-82

FIG. 85 Measured Stokes parameters vs. aspect of model 3, Scale C; $ka = 18.6$; $\theta = 10^\circ$.

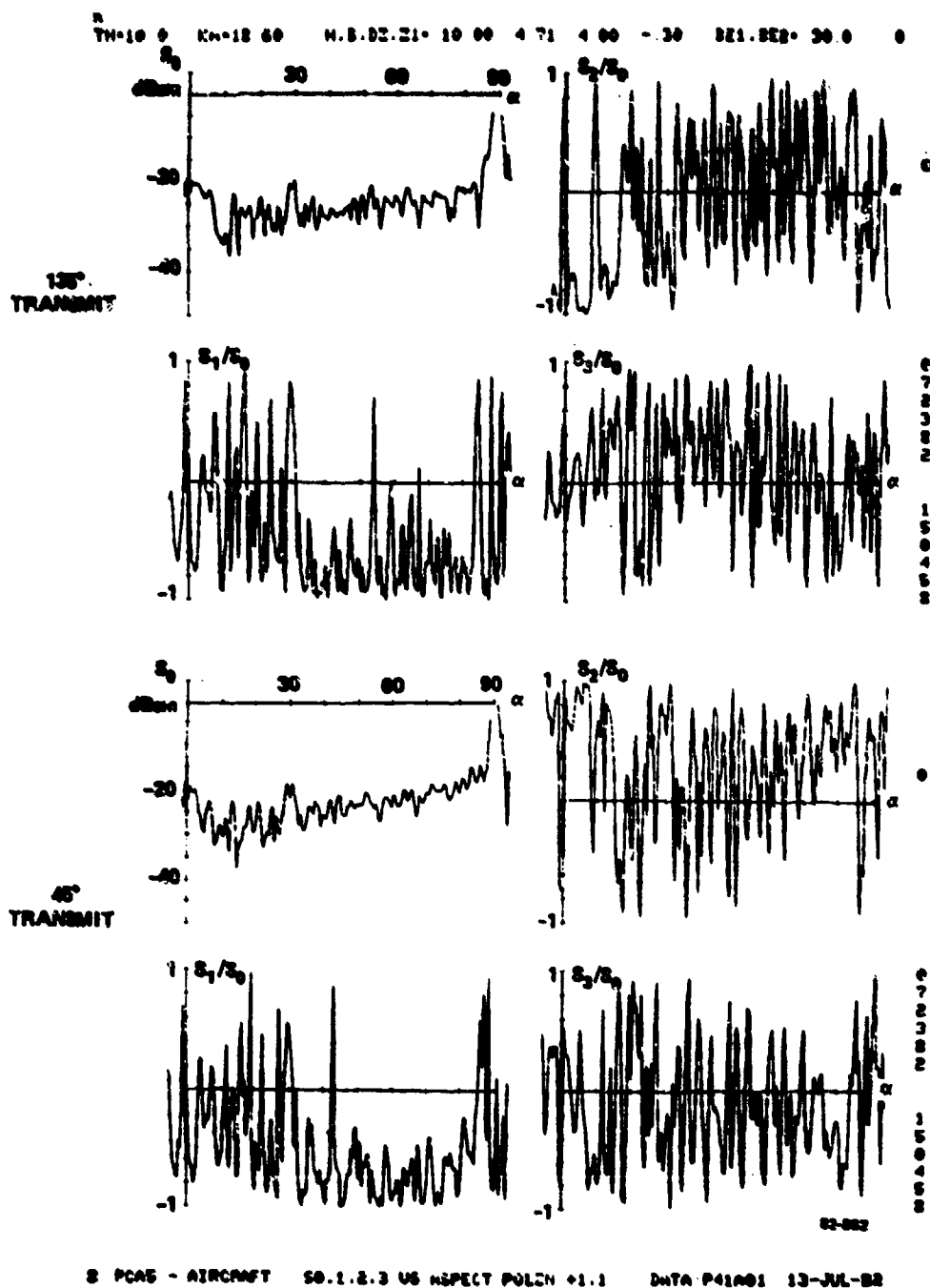
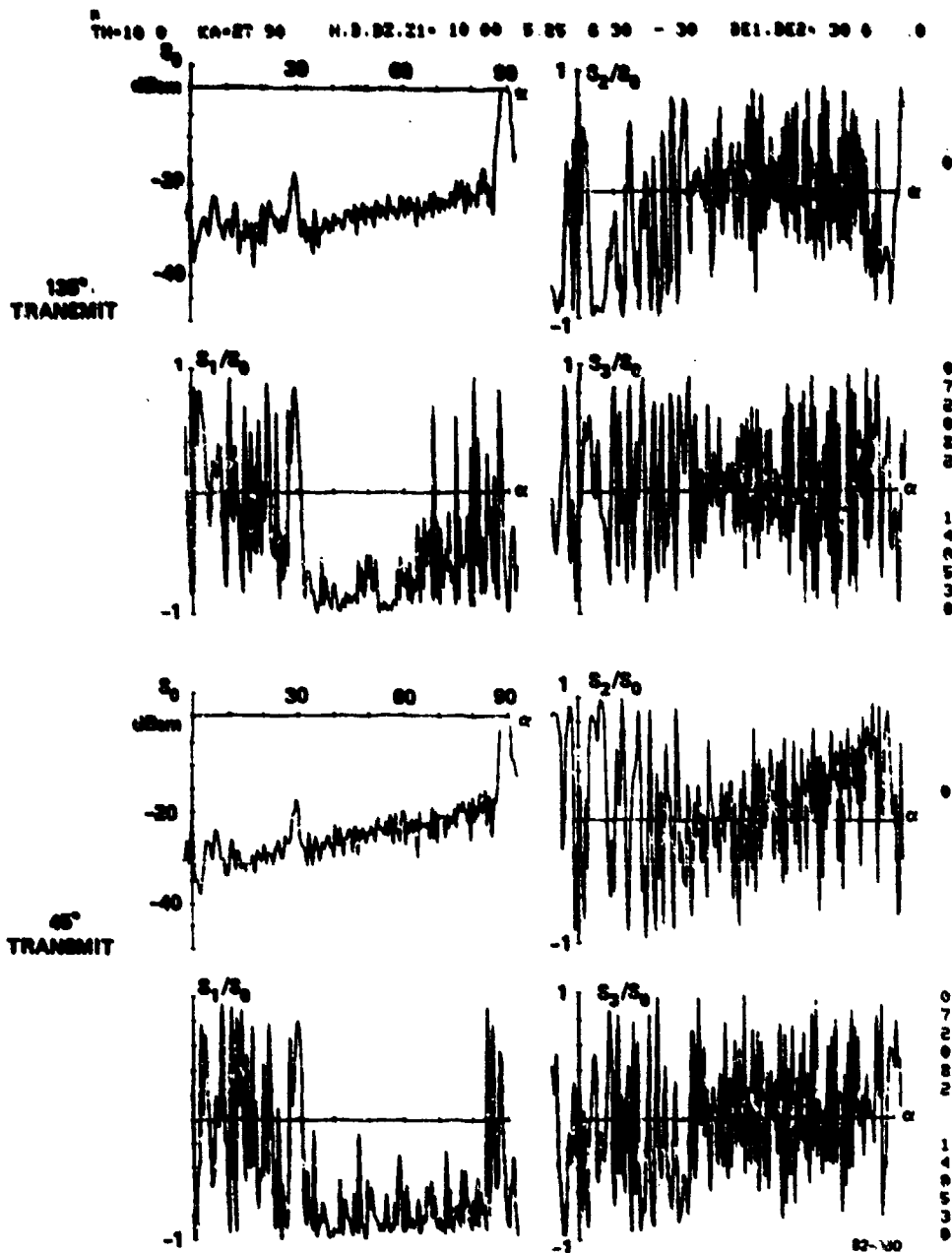
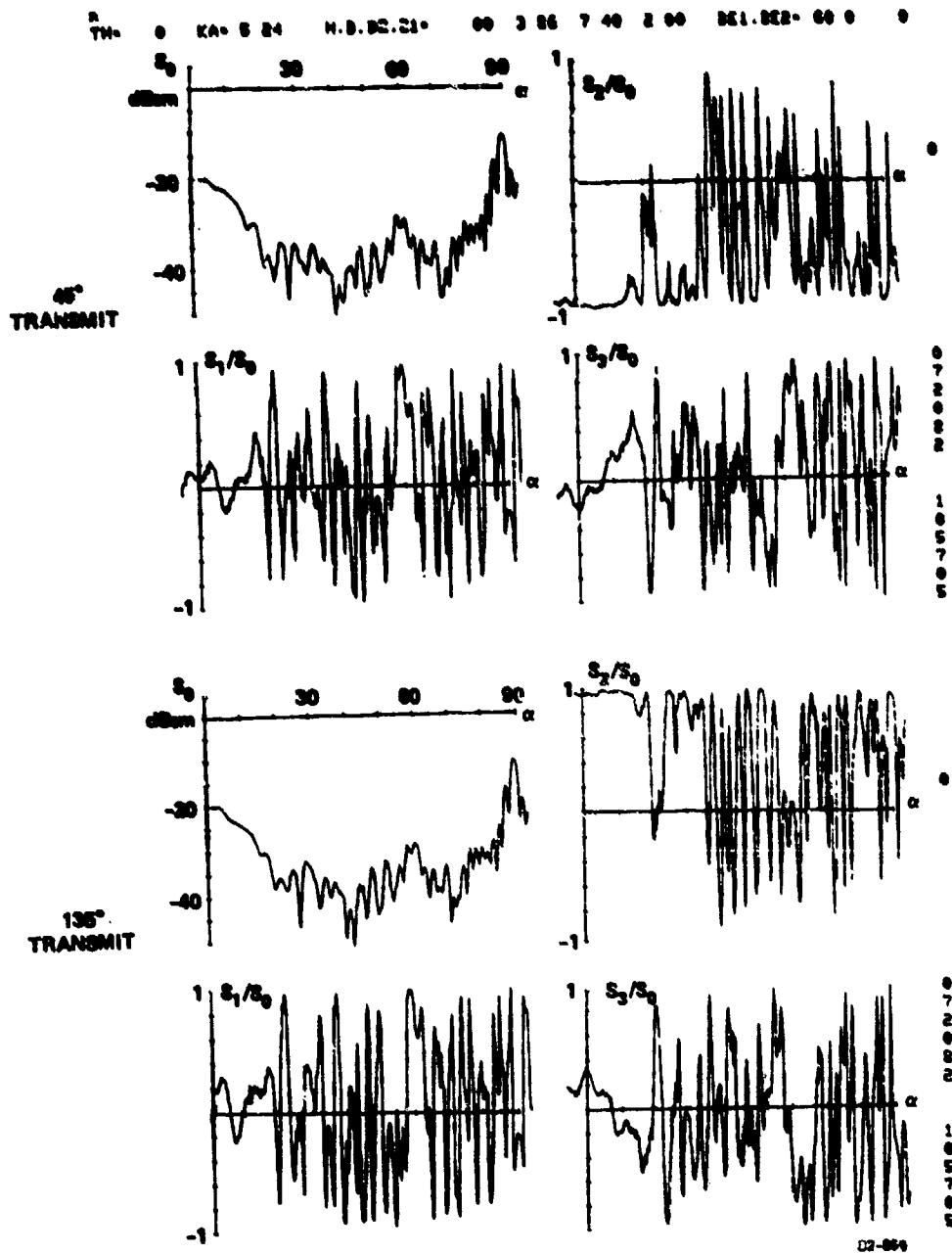


FIG. 86 Measured Stokes parameters vs. aspect of model 1, Scale D; $k_a = 18.6$; $\theta = 10^\circ$.



PCAS - AIRCRAFT 80.1.2.3 US ASPECT POLIN +1.1 DATA P53401 13-JUL-82

FIG. 83 Measured Stokes parameters vs. aspect of model 3, Scale D; $ka = 27.9$; $\theta = 10^\circ$.



8 PCAS - A/C-1000 S0.1.2.3 US ASPECT POLZM +1.1 DATA-P12001 16-JUL-82
 FIG. 89 Measured Stokes parameters vs. aspect of model 2, Scale A; $ka = 5.24$;
 $\theta = 0^\circ$. Note: demonstrates redundant data for symmetric target.

At 10° viewing aspect, the measured results found in Figures 77 through 88 show the nose-on total power response s_0 , in most cases, to be decreased in magnitude as it is expected to be. For example, consider the results corresponding to scale size A and aircraft Model 1 found in Figure 77. Although the 10° aspect results show the nose-on total power s_0 to be approximately 4 to 5 dB below that of the 0° aspect run, Figure 64, the azimuth extent around nose-on over which s_2/s_0 is approximately -1 is roughly the same.

A strong scatterer is also seen in the measurement results of total power s_0 near broadside for all target scales and models. This scatterer is identified as single-bounce specular most convincingly in the measurement results corresponding to cylinder only (aircraft without wings) for the scale sizes measured. It is clearly seen in Figures 63 and 67, corresponding to scale size A and B cylinder only, respectively, that s_2/s_0 is, on average, near -1, while both s_1/s_0 and s_3/s_0 are, on average, 0 near broadside, indicating a single-bounce specular scatterer. Somewhat surprising is the fact that the measurements of the aircraft models, regardless of scale or wing type, do not show this same polarization response as clearly as the cylinder only measurements. The wing causes a significant amount of fluctuation in the SP, particularly in s_1/s_0 and s_3/s_0 , which obscures the expected single-bounce specular scatterer response at broadside.

In general, at target azimuths that do not correspond to a clearly identifiable scatterer, such as the nose, wing, or broadside, the polarization signature as represented by the SP shows a great deal of fluctuation. The interaction between scatterers is extremely complicated and seems unlikely to be of use for target classification purposes. A method suggested elsewhere in this report, Section 6, considers using an average response for target classification which eliminates some of these fluctuations. Preliminary predicted response results show this technique to be worth further consideration.

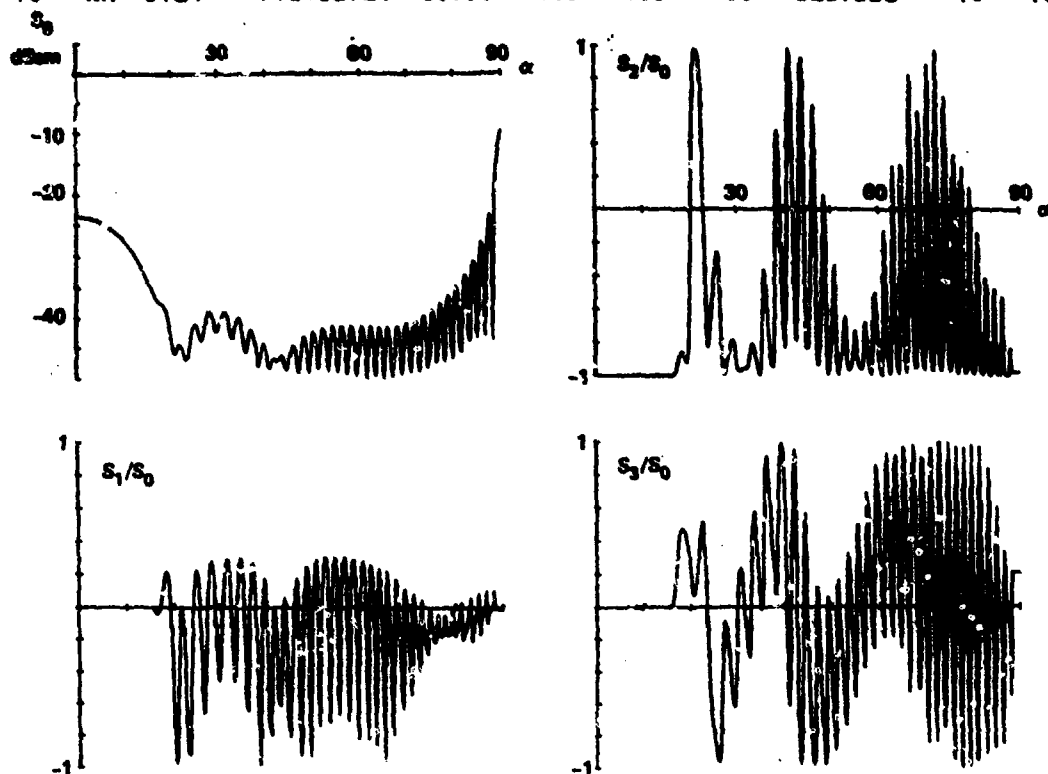
The measurement results reported in Figure 89 represent the scattering response of a 0° aspect or plane-symmetric target for two incident polarizations, 135° and 45° linear. Since the relative phase polarization scattering matrix for this target has zero off-diagonal elements, it is expected, and as indeed is the case, that s_0 should be identical for each transmit polarization, 135° and 45° linear. Similarly, s_1/s_0 should be identical, and is, for each transmit polarization. It can be shown, on the other hand, that s_2/s_0 for 135° linear transmit polarization should be the negative of s_2/s_0 for 45° linear transmit polarization. The measured data clearly shows this to be the case for s_2/s_0 and for s_3/s_0 , which should also exhibit this same phenomenon. A deviation from this relationship between the sets of SP could be an indication of the lack of system calibration or asymmetry of the aircraft target model.

The near field effects discussed in Section 8.9 are clearly visible, for example, in Figure 76, in which the broadside RCS for the Scale D Model 3 target is smaller than the nose-on RCS. Similar effects are seen for the other large scale targets when measured at the shorter (12 m) range (see Table 7). These effects are analyzed in Section 8.9. It is felt that even with degradation in the data due to near field effects, the polarization signatures of even the large models are qualitatively correct.

4.6 COMPARISON OF MEASURED AND CALCULATED RESULTS

Using the same modeling program that generated the polarization characteristics of Section 3, the Stokes vectors were computed, so that computed and measured data could be compared directly. In Figures 90, 91, 92, and 93, the computed Stokes vectors are presented for the cylinder, and Models 1, 2, 3, respectively at size scale A. These results are to be compared with the measured Stokes vectors for these targets given in Figures 63 through 66.

TH= .0 KA= 5.24 H.B.DZ.Z1= 10.00 .00 .00 .00 BE1,BE2= .0 .0

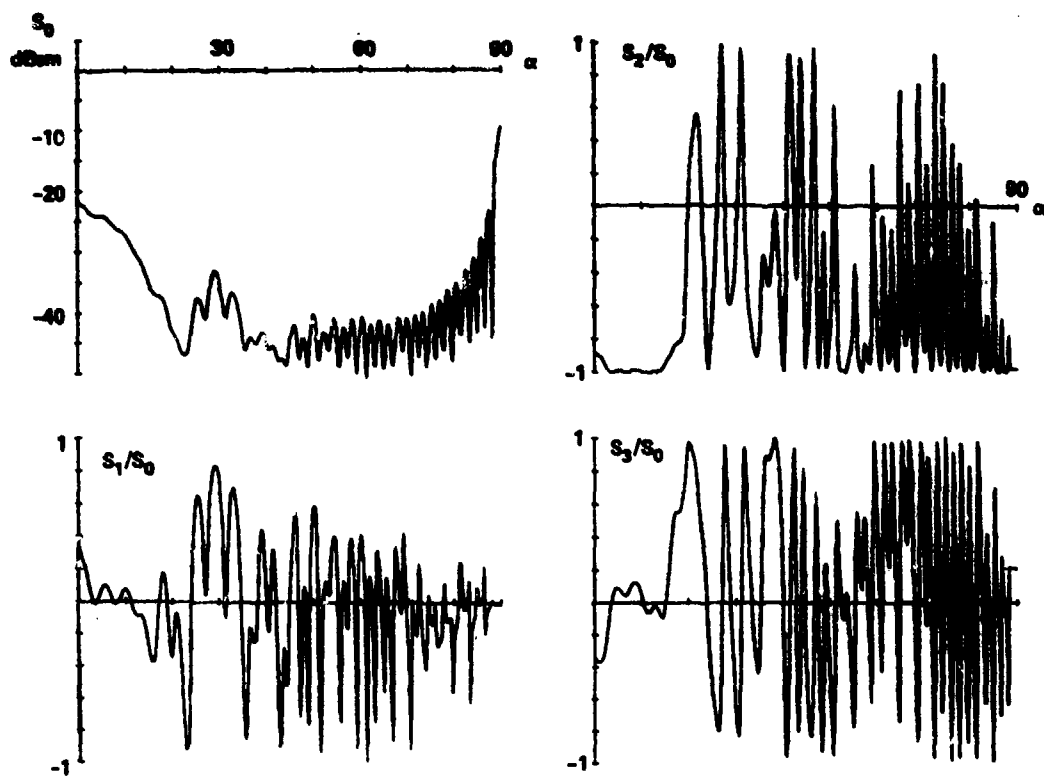


82-627

PCA3 - A/C-1000 50.1.2.3 US ASPECT 4SLIN POL2N DATA: ----

FIG. 90 Predicted Stokes parameters vs. aspect of cylinder, Scale A; $ka = 5.24$; $\theta = 0^\circ$.

TH- 0 KA= 5.24 H.B.DZ.Z1= 10.00 4.71 4.00 -.30 BE1,BE2= 30.0 .0



0
7
0
8
8
2
1
4
4
9
3
8

82-831

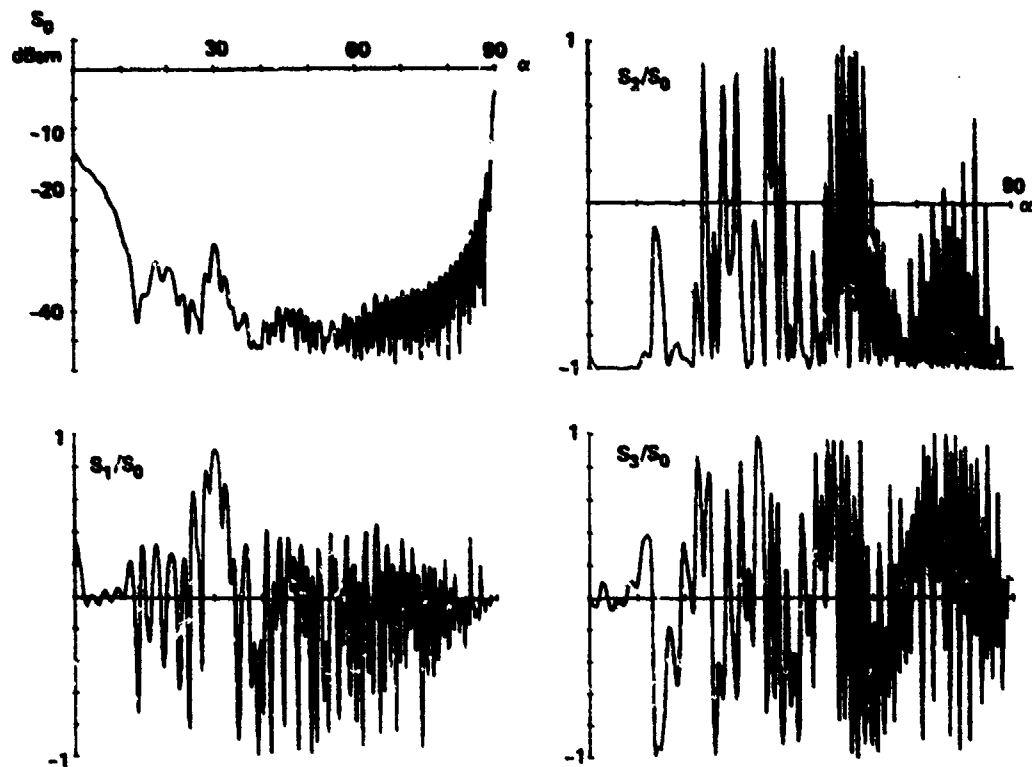
9 PCA3 - AIRCRAFT 50.1.2.3 VS ASPECT 45LIN POLZN DATA:-----

FIG. 91 Predicted Stokes parameters vs. aspect of model 1, Scale A; $ka = 5.24$; $\theta = 0^\circ$.

82-115

FIG. 92 Predicted Stokes parameters vs. aspect of model 2, Scale A; $k a = 5.24$; $\theta = 0^\circ$.

TH- 0 KA= 3.14 H.B.DZ.Z1= 10.00 5.85 6.30 - 30 DE1.DE2= 30.0 0



PCA3 - AIRCRAFT S0.1.2.3 VS ASPECT 4SLIN POLZM DATA:-----

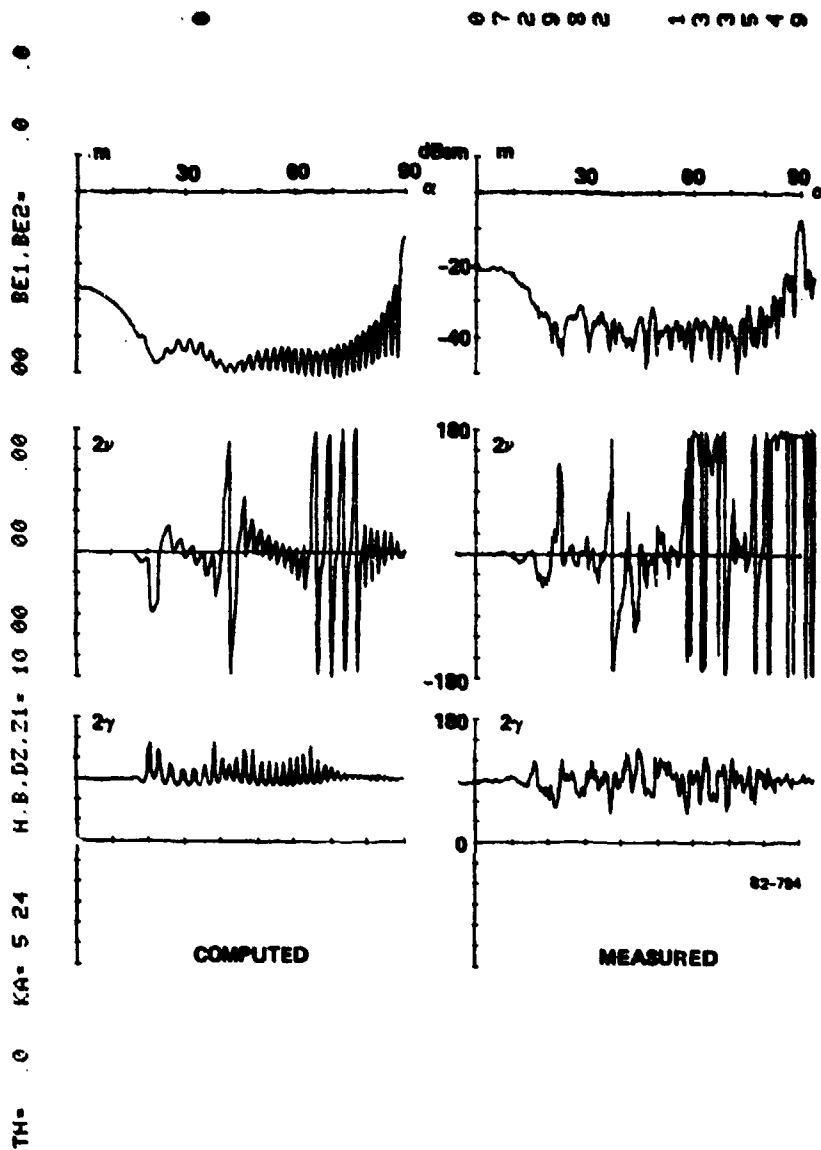
FIG. 93 Predicted Stokes parameters vs. aspect of model 3, Scale A; $ka = 8.14$; $\theta = 0^\circ$.

Consider first the response of the cylinder. The maxima in s_0 (representing the total power) at 0° and 90° aspect agree within 2 dB with measurements. The lobe peaks in the region 40° to 70° , where the response is lowest, are predicted 5 dB lower than measured. This discrepancy is thought to be due to noise and clutter and is supported by the unexpected envelope fluctuation in the lobe structure in the measured data. The lobe spacing agrees exactly. The normalized s_1 , s_2 , s_3 curves exhibit similar rapid fluctuations for the measured and predicted cases. The s_3 curves (which measure the cosine of the relative phase between the horizontal and vertical components of the scattering matrix) exhibit similar average structure for the measured and predicted cases. The details of the fluctuations (relative phase with respect to aspect) of the predicted s_1 , s_2 , s_3 curves differ from the measured cases. This is considered to be explained by the fact that the fluctuations are highly sensitive to relative scatter position at the high frequencies. We thus consider that agreement of the overall properties of the responses constitutes good agreement.

Similar observations hold for the comparisons between measured and computed Stokes vectors for Models 1, 2, and 3. Note that the effect of the wings (at 30° or 60°) shows up particularly in s_1 .

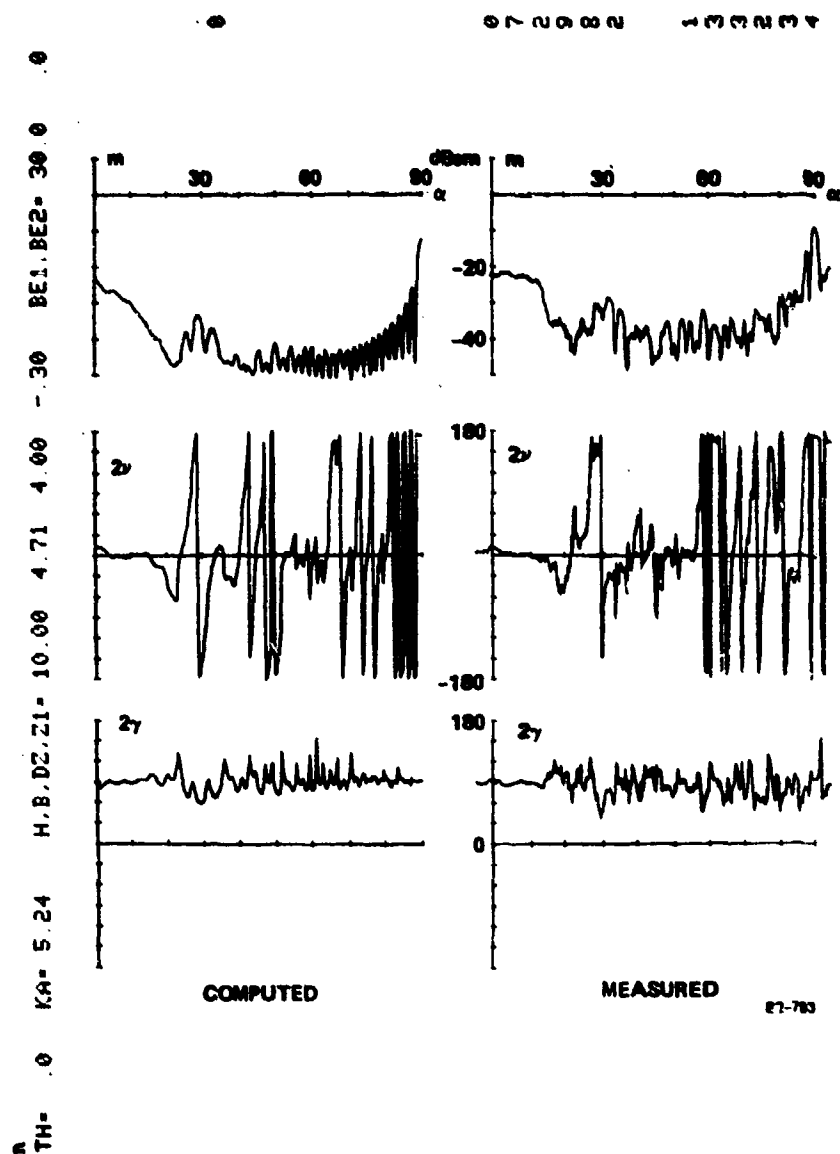
The polarization characteristics m , $2v$, 2γ were derived from the measured Stokes parameters. These results were also compared with predictions. Figures 94, 95, 96, and 97 compare the computed and measured characteristics respectively for the cylinder, Models 1, 2, 3, at size scale A, at $\theta = 0^\circ$. The left columns of these figures are the predicted m , $2v$, and 2γ ; these duplicate the results already given in Section 3. We see that the plots of m compare well, subject to the same comments made above for s_0 . The plots of $2v$ agree in their overall properties (rate of fluctuation), but disagree completely in detail. This parameter is most sensitive to uncertainties in the exact prediction and measurement of rapidly fluctuating targets. The 2γ curves show fair agreement, although they again disagree in the exact detail of the fluctuations. In particular, note that all 2γ curves are fairly constant near nose-on; and note the effect of the wings at 30° in Figure 95 and 97, and at 60° in Figure 96.

These curves also illustrate the need for averaging out the rapid fluctuations in the characteristics, as discussed in Section 3.4.



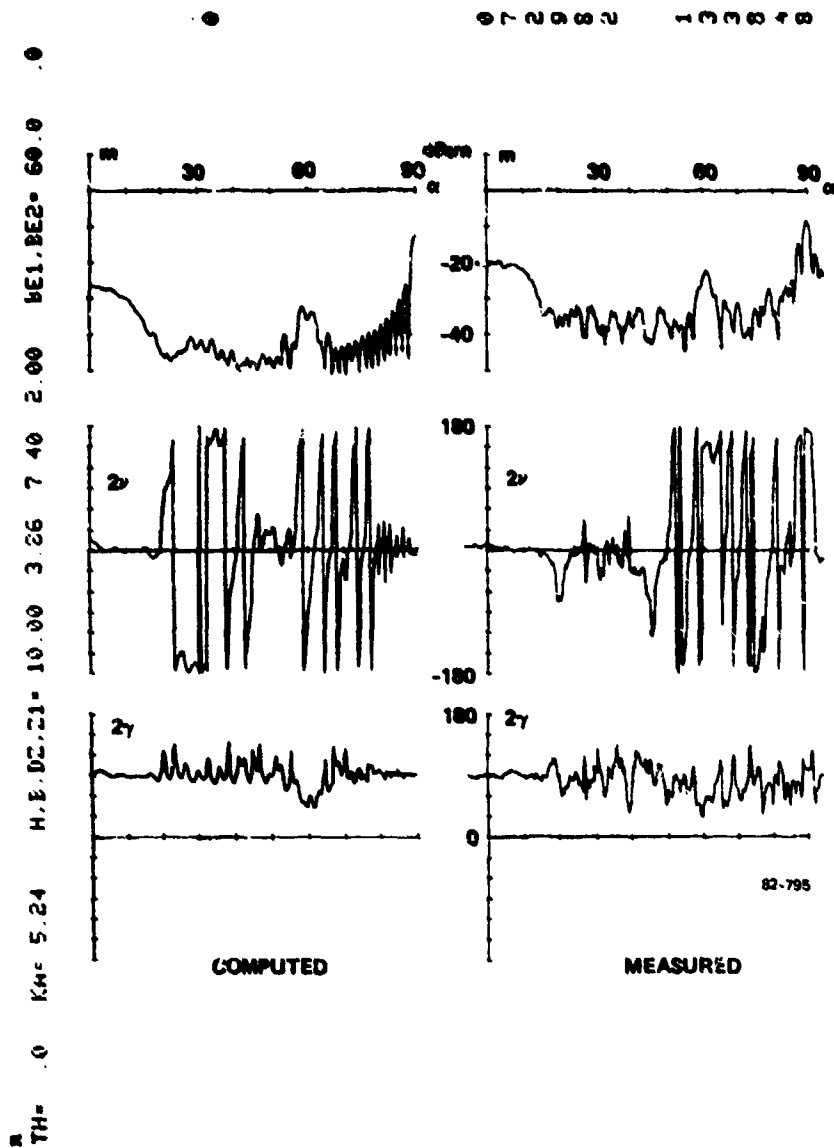
SPCA4 - A/C-1000 M.2NU.26H US WSPECT 45LIN POLZH DATA P10R02 07-JUL-82

FIG. 94 Predicted and measured polarization characteristics of cylinder, Scale A;
 $ka = 5.24$; $\theta = 0^\circ$.



SPCA4 - AIRCRAFT H.2111.25A US ASPECT 45LIN POL2N DATA:P11R02 07-JUL-82

FIG. 95 Predicted and measured polarization characteristics of model 1, Scale A;
 $ka = 5.24$; $\theta = 0^\circ$.



BPCA4 - AIRCRAFT M.2110.264 US ASPECT 45LIM POLCH DATA P12R06 07-JUL-82

FIG. 96 Predicted and measured polarization characteristics of model 2, Scale A;
 $ka = 5.24$; $\theta = 0^\circ$.

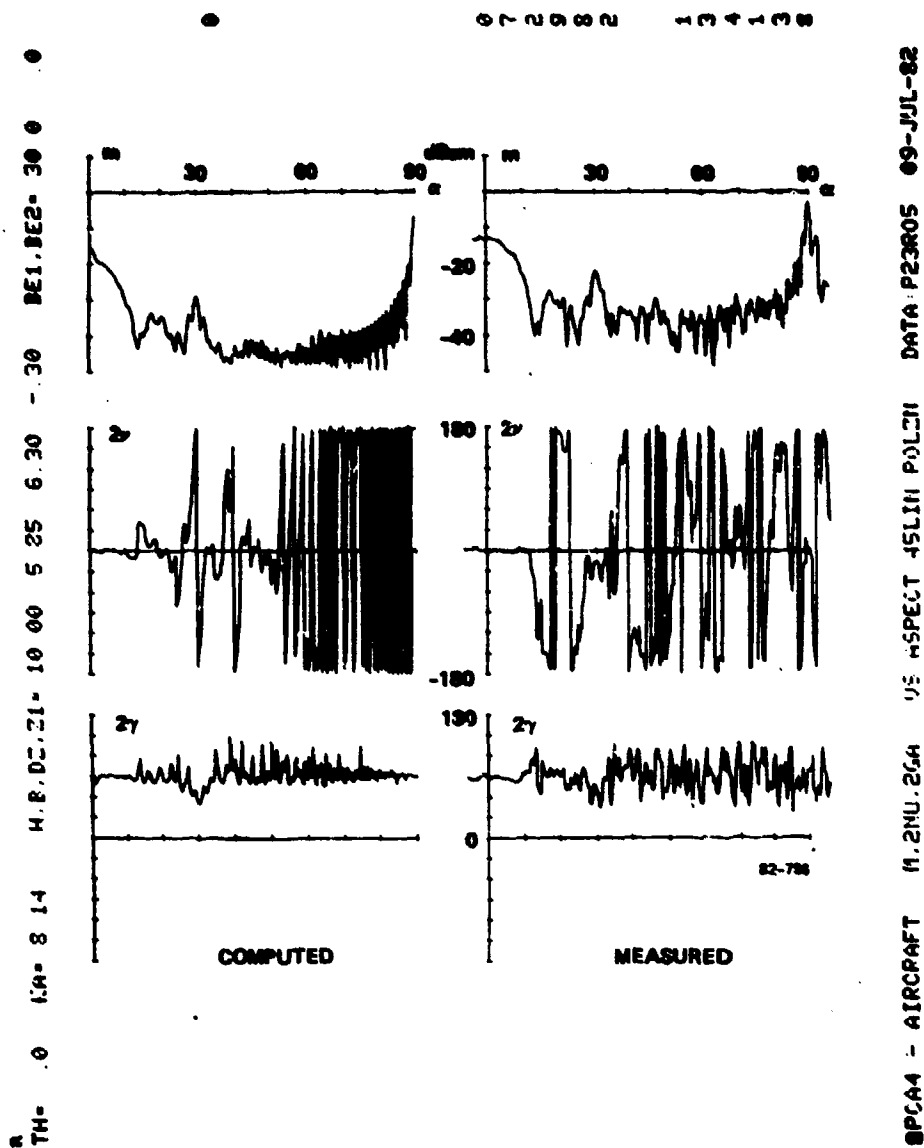


FIG. 97 Predicted and measured polarization characteristics of model 3, Scale A;
 $ka = 8.14$; $\theta = 0^\circ$.

SECTION 5

EFFECTS OF NOISE, CHAFF, AND JAMMING ON POLARIZATION NULLS

In this section the effects of noise, chaff, and jamming on polarization null estimation is investigated by obtaining a bound on the area of the concentration ellipse of the estimate probability distribution. This bound is used to evaluate the deterioration in accuracy of estimation of co-polarization null coordinates of a simple symmetric target. A technique to minimize the effect of a jammer is then postulated, in which receive polarizations are chosen parallel and perpendicular to the jammer, and transmit polarizations are chosen in orthogonal pairs at six antipodal points on the Poincare sphere. The gain afforded by this technique is evaluated for six different jammer polarizations, and is shown to be significant for some jammers, but a loss for others. The loss is attributed to improper choice of transmit polarizations.

5.1 INTERFERENCE EFFECTS

The return signal is first modeled when interference consists of receiver noise, chaff, and jamming. This leads to a probability distribution for the observed detector outputs of a polarization-sensitive radar. From this, a bound on the area of the concentration ellipse of any unbiased estimate of the co-polarization null coordinates of a symmetric target is obtained by evaluating the Fisher information matrix for this distribution. The bound is then evaluated for backgrounds of receiver noise plus chaff and receiver noise plus jamming.

5.1.1 Return Model

The complex voltage V measured by a coherent polarization-sensitive radar when chaff, jamming, and receiver noise are present can be represented as:

$$V = \underline{r}^T[(S + C)\underline{t} + \underline{x}_j] + n \quad , \quad (44)$$

where \underline{t} and \underline{r} are the transmit and receive polarization vectors of the radar;
 \underline{j} is the jammer polarization vector;
 S is the target scattering matrix
 C is the coherent sum of the scattering matrices of all chaff scatterers;
 x is a complex jammer waveform sample;
 n is a complex receiver noise sample.

For simplicity, we will restrict attention in this section to symmetric targets, for which the target scattering matrix S can be written, in an H,V basis, as

$$S = m \begin{pmatrix} e^{j2v} & 0 \\ 0 & e^{-j2v} \tan^2 \gamma \end{pmatrix} e^{j\theta_t} \quad (45)$$

where v and γ are the coordinates of the co-polarization nulls of the target, and m^2 is proportional to the signal return power. The phase angle θ_t is determined by the two-way propagation distance to the target, which is a very large number of wavelengths. Modulo 2π , θ_t can therefore be considered to be a random phase, uniformly distributed on a 2π interval.

The chaff voltage is the coherent sum of contributions from all chaff scatterers, and so is the overall scattering matrix:

$$C = \sum_k C_k \quad (46)$$

If a chaff scatterer is modeled as a dipole at orientation ϕ_k to the horizontal, then the chaff scattering matrix from the k^{th} such dipole is

$$C_k = \sqrt{P_c} \begin{pmatrix} \cos^2 \phi_k & \cos \phi_k \sin \phi_k \\ \cos \phi_k \sin \phi_k & \sin^2 \phi_k \end{pmatrix} e^{j\theta_k} \quad (47)$$

where p_c is proportional to the mean return power from such a dipole for H-H transmit/receive, averaged over the distribution of ϕ_k , and where ϕ_k is analogous to ϕ_c , and is uniformly distributed on $(0, 2\pi)$. In a cloud of many chaff scatterers, the sum of the returns may be well approximated as a complex Gaussian random variable.

The jammer is modeled as having a fixed polarization vector \underline{j} , with a common random modulation, x . The modulation is modeled as a complex Gaussian random process. The receiver noise, n , is also modeled as complex Gaussian.

The observable quantity is the magnitude or envelope of V , for each of several pairs of transmit and receive vectors:

$$z = |V| \quad (48)$$

Since, by the above models, V is the sum of a fixed but unknown signal and an additive complex Gaussian random variable, z has a Rician distribution, with parameters A and σ :

$$p(z) = \frac{z}{\sigma^2} \exp\left[-\frac{1}{2\sigma^2}(z^2 + A^2)\right] I_0\left(\frac{Az}{\sigma^2}\right) \quad (49)$$

where A and σ^2 are given by

$$A = \bar{z}, \text{ signal only,} \quad (50)$$

$$\sigma^2 = \bar{z^2}, \text{ no signal.} \quad (51)$$

For large signal-to-interference ratios (large A/σ), this distribution is well-approximated as a Gaussian, with mean value A and variance σ^2 .

When the target is symmetric, as in Equation (45), A is given by

$$A = m |r_1 t_1 + r_2 t_2 \tan^2 \gamma e^{-j4v}| \quad (52)$$

where the transmit and receive polarizations are written (H-V basis):

$$\underline{t} = \begin{pmatrix} t_1 \\ t_2 \end{pmatrix} \quad (53)$$

$$\underline{r} = \begin{pmatrix} r_1 \\ r_2 \end{pmatrix} \quad (54)$$

The variance, σ^2 , is the sum of three components. The component due to chaff, when the chaff dipole orientation ϕ_k is presumed to be uniform on $(0, 2\pi)$, can be shown to be

$$\sigma_c^2 = \frac{1}{2} P_c \left\{ \frac{|r_1 t_1 + r_2 t_2|^2 + 2|r_1 t_1|^2 + 2|r_2 t_2|^2 + |r_1 t_2 + r_2 t_1|^2}{3} \right\} \quad (55)$$

where $1/2(P_c)$ is the variance due to chaff when H-H transmit/receive polarization is used (i.e., $r_1 = t_1 = 1$, $r_2 = t_2 = 0$). The component due to jamming is

$$\sigma_j^2 = \frac{1}{2} P_j |r_1 j_1 + r_2 j_2|^2 \quad (56)$$

where $P_j = \overline{|x|^2}$ (57)

and the jammer polarization vector is

$$\underline{j} = \begin{pmatrix} j_1 \\ j_2 \end{pmatrix} \quad (58)$$

The component due to receiver noise is simply

$$\sigma_N^2 = \frac{1}{2} P_N \quad (59)$$

where $P_N = \overline{|n|^2}$ (60)

When \underline{z} is observed sequentially for N different pairs of transmit and receive vectors, and when sequential observations are sufficiently separate in time to assure independent chaff, jammer, and receiver noise samples, the observations are independent Gaussians, whose joint distribution can be written

$$p(\underline{z}) = \prod_{i=1}^N \frac{1}{2\pi\sigma_i^2} \exp\left[-\frac{1}{2\sigma_i^2} (z_i - A_i)^2\right], \quad (61)$$

where A_i and σ_i correspond to the i^{th} transmit and receive polarization vectors. Target polarization null classification then requires estimation of the target parameters ν and γ , given these N observations. For example, one such estimation technique would be to calculate the maximum likelihood estimates, which are the values of ν and γ which maximize Equation (61).

5.1.2 Fisher Information Matrix for Estimating ν and γ

A convenient mechanism for investigating the accuracy with which ν and γ may be estimated is the Fisher information matrix, J , obtained from the probability distribution of the voltage envelopes \underline{z} , given in Equation (61).

The Fisher information matrix J is defined as

$$J = \begin{bmatrix} j_{11} & j_{12} \\ j_{21} & j_{22} \end{bmatrix}, \quad (62)$$

where

$$j_{11} = E \left[\left(\frac{\partial \ln p(\underline{z})}{\partial \gamma} \right)^2 \right] \quad (63)$$

$$j_{12} = j_{21} = E \left[\left(\frac{\partial \ln p(\underline{z})}{\partial \gamma} \right) \left(\frac{\partial \ln p(\underline{z})}{\partial v} \right) \right] \quad (64)$$

$$j_{22} = E \left[\left(\frac{\partial \ln p(\underline{z})}{\partial v} \right)^2 \right] \quad (65)$$

This matrix is useful in the following way: Any estimates \hat{v} and $\hat{\gamma}$ will be random variables themselves, since they are functions of the random observations \underline{z} . If the mean value of \hat{v} and $\hat{\gamma}$ are the true values of v and γ , then the estimates are said to be unbiased. From trial to trial, the estimate values will be randomly scattered about their mean values according to some probability distribution. The scatter can be described by the concentration ellipse, which is defined by

$$\underline{\varepsilon}^T \Lambda_e^{-1} \underline{\varepsilon} = c^2 \quad (66)$$

where

$$\underline{\varepsilon} = \begin{pmatrix} \hat{\gamma} - \gamma \\ \hat{v} - v \end{pmatrix} \quad (67)$$

is the estimate error vector, Λ_e is the estimate error covariance matrix;

$$\Lambda_e = E[\underline{\varepsilon}^T \underline{\varepsilon}] , \quad (68)$$

and c^2 is a constant. If the error distribution is joint Gaussian, the probability P that the error vector is within the concentration ellipse is a function of c^2 :

$$P = 1 - \exp\left(-\frac{c^2}{2}\right) . \quad (69)$$

The Fisher information matrix is useful because, for any unbiased estimate of v and γ , the concentration ellipse defined by Equation (66) lies either outside of or on the bound ellipse defined by

$$\underline{\varepsilon}^T J \underline{\varepsilon} = c^2 \quad (70)$$

where J is the Fisher information matrix (see, for example, page 81 of reference 15). In particular, if we use as a measure of estimation accuracy the area of the concentration ellipse of the estimates, this area can be no

smaller than the area of the ellipse defined by Equation (70). This is the approach taken here. Equation (70) will be evaluated for $c^2 = 2$ ($P = 1 - e^{-1}$) and the area of the concentration ellipse investigated and compared for various types of interference.

Application of Equations (63), (64), and (65) to Equation (61), when the target is symmetric, results in a Fisher information matrix of the form:

$$J = \sum_{i=1}^N J_i = \sum_{i=1}^N \frac{m^2}{\sigma_i^2} B_i, \quad (71)$$

where

$$B_i = \begin{bmatrix} b_{\gamma i}^2 & b_{\gamma i} b_{v i} \\ b_{v i} b_{\gamma i} & b_{v i}^2 \end{bmatrix}, \quad (72)$$

$$b_{\gamma i} = \frac{i}{m} \frac{\partial A_i}{\partial \gamma} = \frac{2|r_2 t_2|^2 \frac{\tan^3 \gamma}{\cos^2 \gamma} + 2\text{Re}[r_1 t_1 r_2^* t_2^* e^{j4v} \frac{\tan \gamma}{\cos^2 \gamma}]}{|r_1 t_1 + r_2 t_2 \tan^2 \gamma e^{-j4v}|}, \quad (73)$$

and

$$b_{v i} = \frac{1}{m} \frac{\partial A_i}{\partial v} = \frac{-4\text{Im}[r_1 t_1 r_2^* t_2^* e^{j4v} \frac{\tan \gamma}{\cos^2 \gamma}]}{|r_1 t_1 + r_2 t_2 \tan^2 \gamma e^{-j4v}|}. \quad (74)$$

In Equations (73) and (74), the i -dependence of r_1 , r_2 , t_1 , and t_2 has been suppressed for notational simplicity.

The area of the concentration ellipse of Equation (70), for $c^2 = 2$, can be shown to be given by

$$\text{area} = \frac{\pi}{\sqrt{J_{11}J_{22} - J_{12}^2}}. \quad (75)$$

Thus, small concentration ellipse areas are produced by large diagonal elements in J (J_{11} and J_{22}) and small off-diagonal elements (J_{12}). Large diagonal elements are produced by large signal-to-interference ratios (m^2/σ_i^2), and by large values of the partial derivatives of Equations (73) and (74). Small off-diagonal terms are obtained by selecting, where possible, transmit and receive polarization vectors in complementary pairs, so that the off-diagonal terms have equal magnitude but opposite sign, and thus cancel when the J_i 's are summed over all polarizations i . This technique will be illustrated in Section 5.2.

5.1.3 Effects of Chaff and Jamming Using Nominal Polarization Sets

In the presence of receiver noise, a nominal set of $N = 12$ pairs of transmit and receive polarizations has been selected. They are sufficient to allow estimation of target polarization nulls for an arbitrary target. In this section, the effect of chaff and jamming will be evaluated on the area of the concentration ellipse of estimates of γ and ν , when the target is symmetric and the nominal set of twelve pairs of polarizations are used. The equations developed in the previous section will be used.

The nominal set of polarizations are the twelve pairwise combinations of two transmit polarizations (45° and -45° linear)

$$\underline{t} = \begin{pmatrix} 1 \\ 1 \end{pmatrix} \text{ and } \begin{pmatrix} 1 \\ -1 \end{pmatrix} \quad (76)$$

and six receive polarizations (45° and -45° linear, H and V, and RC and LC):

$$\underline{r} = \begin{pmatrix} 1 \\ 1 \end{pmatrix}, \begin{pmatrix} 1 \\ -1 \end{pmatrix}, \begin{pmatrix} 1 \\ 0 \end{pmatrix}, \begin{pmatrix} 0 \\ 1 \end{pmatrix}, \begin{pmatrix} j \\ 1 \end{pmatrix}, \begin{pmatrix} 1 \\ j \end{pmatrix}. \quad (77)$$

The target is a symmetric target, with

$$\begin{aligned} \gamma &= 45^\circ, \\ \nu &= 0^\circ, \end{aligned} \quad (78)$$

i.e., a sphere or flat plate. The signal-to-receiver noise ratio (m^2/P_N) is +20 dB. Figure 98 is a plot of the concentration ellipse area of Equation (70) as a function of chaff-to-receiver-noise ratio, when the interference background is receiver noise plus chaff. The effect of chaff on the ellipse area is essentially the same as an equal amount of receiver noise. For example, at a chaff-to-receiver-noise ratio of 0 dB, the total background power is twice that of receiver noise only, and the ellipse area is also twice that for receiver noise. This property is not surprising in view of the fact that the chaff model used contains no preferred dipole orientation.

When the interference is a jamming, however, the result is a function of the jammer polarization vector. Figure 99 shows seven jammer polarizations chosen for calculations. Figure 100 shows the variation of concentration ellipse area with jammer-to-noise ratio, when the interference background is receiver noise plus a jammer. The target is again a sphere or flat plate, and the signal-to-receiver-noise ratio is +20 dB. In this case, each jammer polarization has a somewhat different effect on the estimate accuracies.

5.2 ECCM TECHNIQUES

In this section, the properties of the Fisher information matrix which lead to small concentration ellipse areas, which were identified in Section 5.1.2, will be exploited to obtain an ECCM technique for countering the effects of jamming when estimating γ and ν of a symmetric target. First, a specific example will be discussed to motivate the postulation of a counter-jamming technique for a more general situation. The technique will then be evaluated in the more general situation.

5.2.1 Example Case

When the target polarization parameters are estimated from a sequence of N independent voltage envelope measurements, \underline{z} , the Fisher information matrix, J , as we have seen, is the sum of N terms, one for each

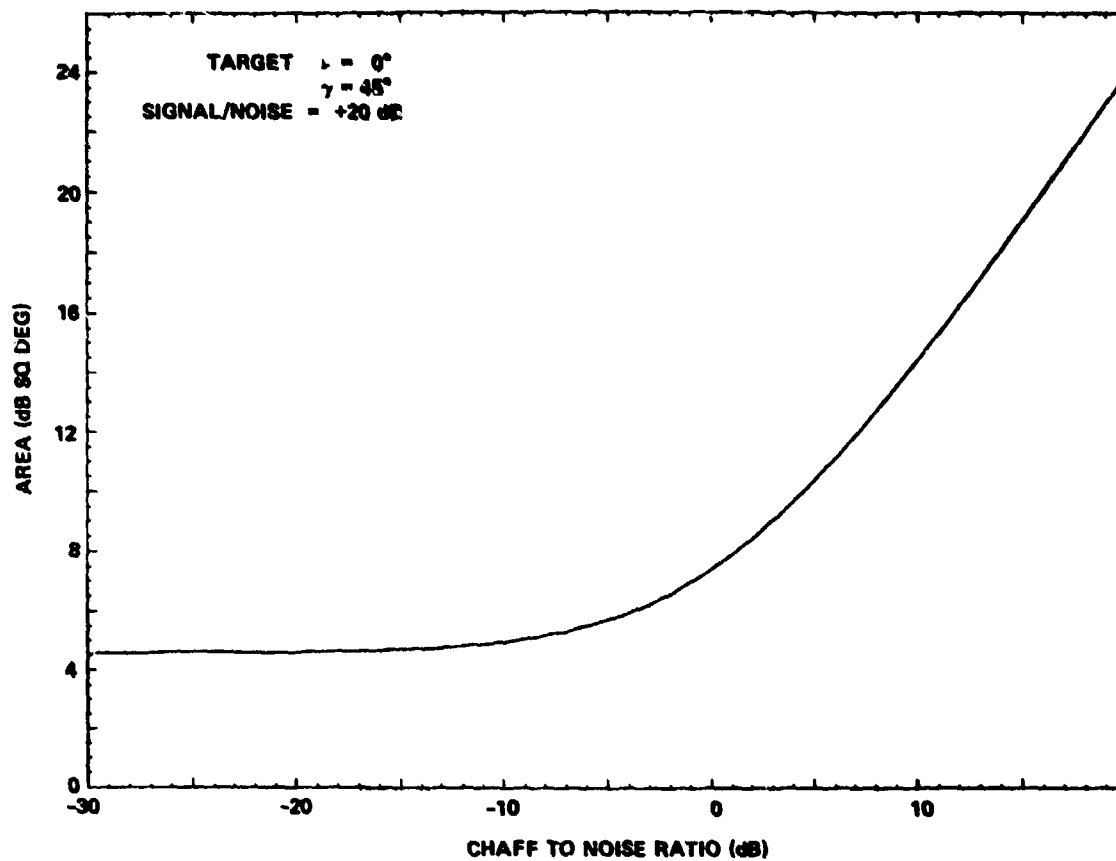
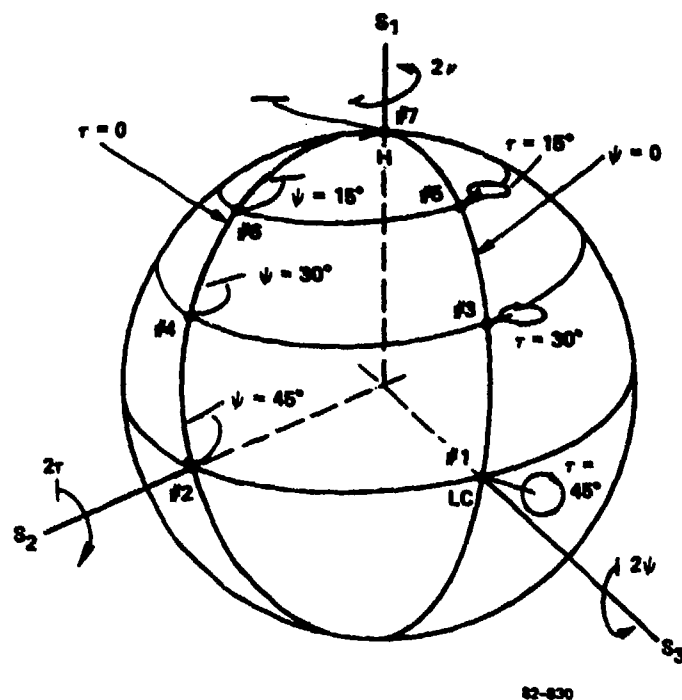


FIG. 98 Polarization null estimation accuracy of chaff.



82-830

FIG. 99 Jammer polarization on the Poincaré sphere.

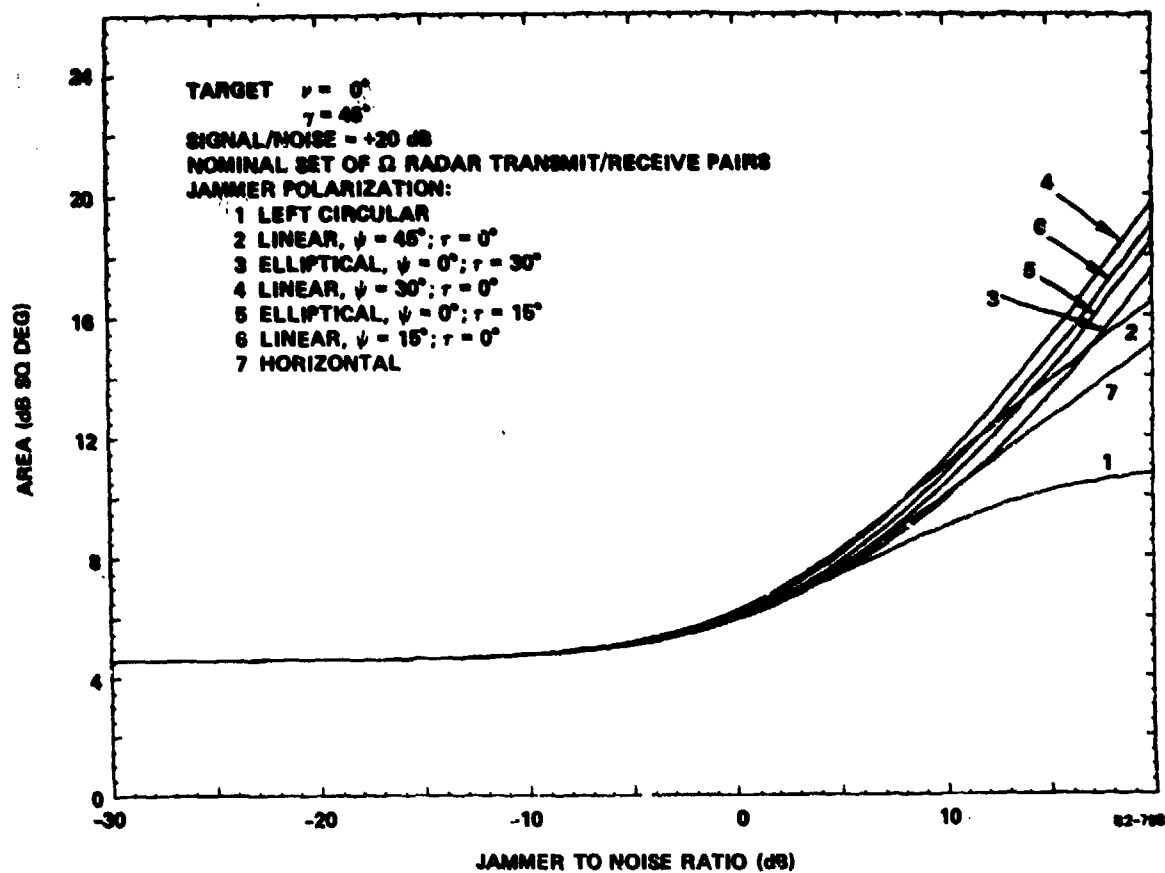


FIG. 100 Polarization null estimation accuracy in jamming.

measurement. Each term is dependent on the signal-to-interference ratios and the partial derivatives of the mean return, for the associated transmit and receive polarizations. The concentration ellipse area can be made small if the diagonal terms of the sum J are large, and the off-diagonal terms are small. If at least one of the N terms in the sum has a large diagonal term for each parameter, and if the terms can be grouped in pairs such that the off-diagonal terms are of equal magnitude but opposite sign, the desired net effect will be achieved. Therefore, the key to good performance in an ECCM environment is to examine the J_i 's for various transmit and receive polarizations, and select polarizations to produce the desired effect on the sum.

As an illustration, consider the symmetric target again, with $\gamma = 45^\circ$, $\nu = 0^\circ$, in a background of receiver noise plus jamming. Table 8 is a tabulation of the terms of the B_i matrix (Equation (72)) for each of 36 pairings of transmit and receive polarizations chosen from the set: 45° linear, -45° linear, H, V, LC, and RC.

Suppose we were to choose from these polarizations the set $\underline{t}_1 = 45^\circ$ linear, $\underline{r}_1 = \text{LC}$, and $\underline{t}_2 = 45^\circ$ linear, $\underline{r}_2 = \text{RC}$. Then

$$J_1 = \frac{m^2}{\sigma_1^2} \begin{pmatrix} 2 & 2 \\ 2 & 2 \end{pmatrix} \quad (79)$$

$$J_2 = \frac{m^2}{\sigma_2^2} \begin{pmatrix} 2 & -2 \\ -2 & 2 \end{pmatrix} \quad (80)$$

TABLE 8
ELEMENTS OF B MATRIX FOR EXAMPLE CASE
SYMMETRIC TARGET
 $\gamma = 45^\circ, \nu = 0^\circ$

Transmit	Receive	b_{ξ}^2	$b_{\gamma}b_{\nu}$	b_{ζ}^2
H	H	0	0	0
	V	0	0	0
	45L	0	0	0
	-45L	0	0	0
	LC	0	0	0
	RC	0	0	0
V	H	0	0	0
	V	16	0	0
	45L	8	0	0
	-45L	8	0	0
	LC	8	0	0
	RC	8	0	0
45L	H	0	0	0
	V	8	0	0
	45L	4	0	0
	-45L	0	0	0
	LC	2	2	2
	RC	2	-2	2
-45L	H	0	0	0
	V	8	0	0
	45L	0	0	0
	-45L	4	0	0
	LC	2	-2	2
	RC	2	2	2
LC	H	0	0	0
	V	8	0	0
	45L	2	2	2
	-45L	2	-2	2
	LC	0	0	0
	RC	4	0	0
RC	H	0	0	0
	V	8	0	0
	45L	2	-2	2
	-45L	2	2	2
	LC	4	0	0
	RC	0	0	0

If $\sigma_1^2 = \sigma_2^2$, the desired cancellation of off-diagonal terms occurs. However, since $\underline{r}_1 \neq \underline{r}_2$, we may have $\sigma_1^2 \neq \sigma_2^2$. If we add to the set, $\underline{t}_3 = -45^\circ$ linear, $\underline{r}_3 = \text{LC}$, $\underline{t}_4 = -45^\circ$ linear, $\underline{r}_4 = \text{RC}$, then two more terms are added:

$$J_3 = \frac{m^2}{\sigma_3^2} \begin{pmatrix} 2 & -2 \\ -2 & 2 \end{pmatrix} \quad (81)$$

$$J_4 = \frac{m^2}{\sigma_4^2} \begin{pmatrix} 2 & 2 \\ 2 & 2 \end{pmatrix} \quad (82)$$

Since $\underline{r}_1 = \underline{r}_3 = \text{LC}$, $\sigma_1^2 = \sigma_3^2 = \sigma_{\text{LC}}^2$, and $J_1 + J_3$ is diagonal. Similarly, $J_2 + J_4$ is diagonal, and hence so is J :

$$J = \left(\frac{m^2}{\sigma_{\text{LC}}^2} + \frac{m^2}{\sigma_{\text{RC}}^2} \right) \begin{pmatrix} 4 & 0 \\ 0 & 4 \end{pmatrix} \quad (83)$$

An alternate choice of \underline{r} and \underline{t} pairs would be to interchange the transmit and receive polarizations in the above selection, so that transmit polarizations are LC and RC, and receive polarizations are $\pm 45^\circ$ linear. The partial derivatives of A_i are unchanged by the interchange of \underline{t} and \underline{r} , but the σ_i^2 values are. Thus, we get

$$J = \left(\frac{m^2}{\sigma_{45}^2} + \frac{m^2}{\sigma_{-45}^2} \right) \begin{pmatrix} 4 & 0 \\ 0 & 4 \end{pmatrix} \quad (84)$$

The better technique depends on the jammer polarization. If the jammer polarization is 45° linear,

$$\underline{j} = \frac{1}{\sqrt{2}} \begin{pmatrix} 1 \\ 1 \end{pmatrix} \quad (85)$$

then

$$\sigma_{LC}^2 = \frac{1}{2} \{ P_N + P_J |r_1 J_1 + r_2 J_2|^2 \}$$

$$= \frac{1}{2} \left\{ P_N + \frac{1}{2} P_J \right\} \quad (86)$$

$$\sigma_{RC}^2 = \frac{1}{2} \left\{ P_N + \frac{1}{2} P_J \right\}. \quad (87)$$

and

$$\frac{\frac{m^2}{2}}{\sigma_{LC}^2} + \frac{\frac{m^2}{2}}{\sigma_{RC}^2} = \frac{4 \frac{S}{N}}{1 + \frac{1}{2} \frac{J}{N}} \quad (88)$$

For the $\pm 45^\circ$ linear polarization reception case, we get

$$\sigma_{45}^2 = P_N + P_J \quad (89)$$

$$\sigma_{-45}^2 = P_N \quad (90)$$

and

$$\frac{\frac{m^2}{2}}{\sigma_{45}^2} + \frac{\frac{m^2}{2}}{\sigma_{-45}^2} = 2 \left(\frac{S}{N} \right) \left(1 + \frac{1}{1 + \frac{J}{N}} \right) \quad (91)$$

For all J/N ratios, we have

$$\frac{\frac{m^2}{2}}{\sigma_{45}^2} + \frac{\frac{m^2}{2}}{\sigma_{-45}^2} \geq \frac{\frac{m^2}{2}}{\sigma_{LC}^2} + \frac{\frac{m^2}{2}}{\sigma_{RC}^2} \quad (92)$$

so that the latter choice of polarization sets is better.

When the jammer is LC or RC, the opposite conclusion is true. This suggests the following counter jamming scheme:

1. Choose receive polarization vectors parallel and orthogonal to the jammer polarization vector.
2. For each of these two receive polarizations, transmit on pairs of polarization vectors chosen so that the off-diagonal terms of the pair of corresponding B_i matrices are of equal magnitude but opposite sign, and thus cancel when the J_i terms are summed.

Step 1 requires knowledge of the jammer polarization, which should be feasible as long as the jammer polarization does not change rapidly. For Step 2 it is not clear how to choose the appropriate transmit polarizations. The above example suggests that if transmit pairs are orthogonal, the desired property will be achieved for the particular target and jammer. The correct transmit polarization set choice is not fully understood for a general target and jammer combination.

5.2.2 Calculation of ECCM Effectiveness for Six Jammer Polarizations

To test the above conjecture, the concentration ellipse area was calculated when measurements are made with twelve pairs of transmit and receive polarizations, for six jammer types. In all cases, the transmit/receive pairs are obtained by combining six different transmits with two different receive polarizations. The six transmit polarization vectors are the six antipodal polarization vectors used on receive in the nominal set: $\pm 45^\circ$ linear, H, V, LC, and RC. The two receive polarizations are determined by the jammer polarization: one is parallel to the jammer, and the other is orthogonal. The target is a symmetrical target, $\gamma = 45^\circ$, $\nu = 0^\circ$. The signal-to-receiver-noise ratio in all cases is +20 dB. Figure 101 plots the ellipse area versus jammer-to-noise ratio for all six cases. Comparison to Figure 99 shows the gain (or loss) achieved by the technique. Curves 1, 2, 4, and 6 show a significant gain at high jammer-to-noise ratio. These curves correspond to a LC jammer and three different linearly-polarized jammers. At +20 dB J/N, the gain ranges from 3 dB for LC to 13 dB for 30° linear. For the two cases of elliptical jammer polarizations, however, there is a net loss of about 4 dB. This loss is believed to have occurred because of improper selection of transmit polarizations for the jammer-driven receive polarizations, and for the particular target. The desired cancellation of the off-diagonal terms probably did not occur. More work needs to be done to determine how the transmit set should be chosen. However, the correct choice may be target-dependent, thereby defeating the utility of the technique for classification of an unknown target.

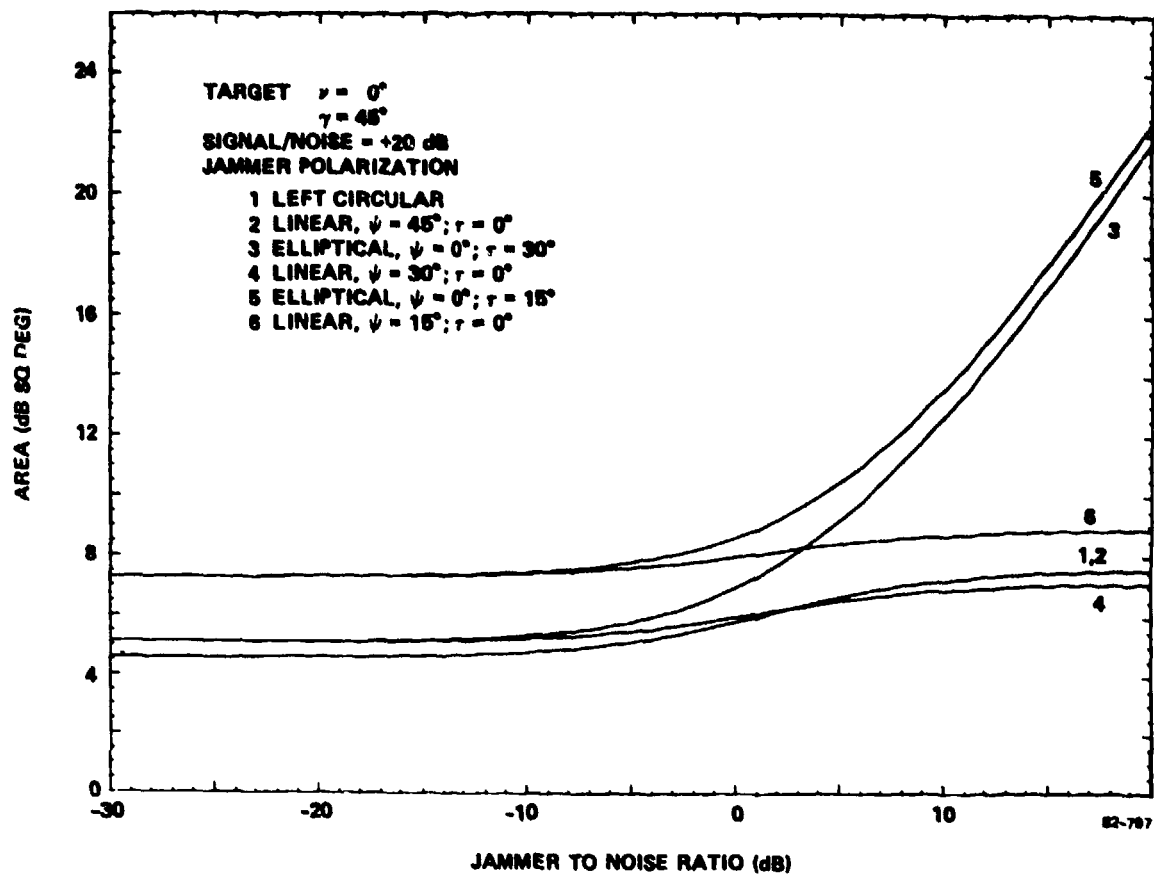


FIG. 101 Polarization null estimation accuracy using counter-jamming scheme.

SECTION 6

SUMMARY AND CONCLUSIONS

We have given the theoretical background of polarization null and maximum properties of simple and compound targets as functions of aspect and frequency. A measurement system was described which obtains Stokes vectors of the scattered radiation, from which the polarization null and maximum properties are derived. Computed and measured results are given for three simplified aircraft models at several size scales. The effect of noise, clutter, and jamming on polarization characteristics, and the use of polarization agility to reduce the effect of jamming was investigated.

The object of this study was to assess the efficacy of polarization null and maximum concepts for aircraft identification at practical, single radar frequencies. It was found that simple targets have highly distinctive polarization characteristics, but that the dynamic behavior of the polarization nulls and maxima of compound targets is very complex. The conclusion of this study is that, in general, single-frequency, instantaneous polarization characteristics are not useful for discrimination of extended targets (see Section 3.2). An exception could be certain distinctive targets over certain restricted aspect bins. The reason for the failure is purely due to the complexity of the dynamic null and max loci. It remains true that the polarization characteristics of targets are highly distinctive and contain more information about a target than does data taken at a single polarization.

It is necessary to find another approach to utilize the polarization information. Two methods are suggested here. One way is to overcome the rapid fluctuations in polarization data by averaging over frequency and/or aspect, and is discussed in a preliminary fashion in Section 3.4. The result is that different aircraft models are readily distinguishable over certain aspect bins. A more complex but promising approach is to subresolve the target, that is utilizing frequency and/or aspect diversity. (It should be noted that the nulls of simple scattering centers are highly characteristic and do not change rapidly with frequency or aspect.) Full analysis of these two methods are beyond the scope of this report and are suggested for future investigation.

The restriction of this study to practical frequencies and aircraft targets resulted in compound targets which are many wavelengths long. We may expect quite different behavior of polarization nulls and maxima at much lower frequencies or for much smaller targets, that is in the resonance region where the largest target dimension is of the order of a wavelength. Such targets are expected to show slow variation of null characteristics with changes in frequency or aspect. (This could have application to discrimination against small decoys.) To analyze complex targets in the resonance region requires (computationally intensive) target modeling by means of integral equations, since scattering center concepts do not apply. Such methods are available, e.g. [8,13] and could be pursued.

In the presence of jamming, the accuracy of the measurement of polarization characteristics will deteriorate. By proper choice of measurement polarizations, the effect of a jammer may be overcome in many cases. It was found that for some jammer polarizations a simple prescription for measurement polarizations gives good results; while at other polarizations, the search for optimum measurement polarizations is complex.

Acknowledgment

The authors of this report acknowledge the contributions of Dr. H-M. Boerner who acted as an expert consultant and provided an extensive summary of the state of the art in radar polarimetry [18].

SECTION 7
REFERENCES

- [1]. C-Y. Chan, "Studies on the Power Scattering Matrix of Radar Targets," Dept. of Information Engineering, University of Illinois, Chicago, IL, M.Sc. Thesis, May 1981.
- [2]. E. W. Kennaugh, "Polarization Properties of Radar Reflections," Ohio State University, Project Report Contract No. RADC-AF28(099)-90, Report 389-12(AD2494), March 1952.
- [3]. J. R. Huynen, "Phenomenological Theory of Radar Targets," D.Sc. Thesis, Delft, 1970.
- [4]. W.-M. Boerner and M. B. El-Arini, "Polarization Utilization in Radar Target Reconstruction; Buoy Targets," Final Report Contract NAV-AIR-N00019-80-C-0620, September 1981.
- [5]. C. E. Heath, "Properties of the Linear Polarization Bistatic Scattering Matrix," Tech. Note 1980-7, MIT Lincoln Laboratory, March 1980.
- [6]. E. M. Kennaugh, "Polarization Dependence of RCS - A Geometrical Interpretation," IEEE Trans AP-29, No. 2, March 1981.
- [7]. J. R. Huynen, "Radar Target Sorting Based Upon Polarization Signature Analysis," Lockheed Aircraft Corp., Final Report on Contract AF19(604)5550, Report AFCRC-TN-60-588, May 1960.
- [8]. C. L. Bennett, H. Mieras, S. L. Teeter, and J. P. Toomey, "Low EM Signature Response Techniques," Final Report on Contract F30602-77-C-0166, October 1978.
- [9]. R. A. Ross, "Investigation of Scattering Principles," Cornell Aeronautical Lab., Inc., May 1969.
- [10]. G. T. Ruck, et al, Radar Cross Section Handbook, Plenum Press, NY, 1970.

REFERENCES (Cont'd.)

- [11]. E. L. O'Neill, Introduction to Statistical Optics, Addison Wesley, Reading, MA, 1963, Chapter 9.
- [12]. R. A. Ross, "Radar Cross Section of Rectangular Flat Plates as a Function of Aspect Angle," IEEE Trans. AP, Vol. AP-14 No. 3, p. 329, May 1966.
- [13]. C. L. Bennett, H. Mieras, "Wideband Scattering Target Response Validation," Final Report F30602-80-C-0019, Sperry Research Center, SRC-CR-81-7, Dec. 1980.
- [14]. J. R. Huynen, "A Revisitation of the Phenomenological Approach with Applications to Radar Target Decomposition," Communications Lab., Electromagnetic Imaging Division, Univ. Illinois at Chicago, Report No. EMID-CL-82-05-18-01, 18 May 1982.
- [15]. Van Trees, Harry L., Detection, Estimation, and Modulation Theory, Part I, John Wiley and Sons, New York, 1968.
- [16]. W-M. Boerner, "List of References on Broadband Radar Polarimetry in the dm-mm Wave Spectral Region", Univ. of Illinois at Chicago, Department of Information Engineering, Communications Laboratory, available in the ICL "UNIX" System.
- [17]. A.J. Poelman, "Polarization Vector Translation in Radar Systems," Proc. IEEE, Part F, accepted for publication in 1983.
- [18]. W-M. Boerner, "Historical Development of Radar Polarimetry," App. 8-12 of Final Report on Contract F30602-81-C-0254, September 1982.

SECTION 8

APPENDICES

8.1 UNITARY TRANSFORMATION PROPERTIES

$$\text{Let } b = Qa, \text{ where } Q \text{ is } 2 \times 2. \quad (93)$$

Then to preserve the inner product, $(a_1, a_2) = a_1 a_2^* = a_1^T a_2^*$,

we must have $b_1^T b_2^* = a_1^T Q^T Q^* a_2^* = a_1^T a_2^*$. This

is satisfied if

$$Q^T Q^* = I, \text{ or } Q^{-1} = Q^*{}^T; \quad (94)$$

that is, Q is unitary. In particular, Q will preserve an orthonormal basis. Writing out Equation (94) in full, it is easily found that the rows of Q are orthonormal and that the magnitude of $\det(Q) = 1$. We will further restrict the phase of the determinant to be zero.

$$Q = \begin{pmatrix} q_1 & q_2 \\ -q_2^* & q_1^* \end{pmatrix} \quad (95)$$

If b and a are any unit polarization vectors, then Equation (93) can be solved for Q in the above form, namely $q_1 = b_1 a_1^* + b_2^* a_2^*$ and $q_2 = -a_1 b_2^* + b_1 a_2^*$. Hence, there is a Q for every polarization basis transformation. We have that

$$\begin{aligned} 1 &= |q_1|^2 + |q_2|^2 \\ \det(Q) &= 1 \end{aligned}$$

and that the product of two such matrices is a matrix of the same form.

It is not, in general, true that a Q of form (Equation (95)) can be found which transforms any orthogonal pair of basis vectors into any other orthogonal pair. For that we would have to maintain a more general form with $\det(Q) = e^{j\phi}$. The reason is that a pair of basis vectors is still orthogonal if one of them is multiplied by a constant phase. Suppose \hat{A}_1, \hat{A}_2 are orthogonal with

$$\hat{A}_1 = \begin{pmatrix} a_1 \\ a_2 \end{pmatrix} \text{ and } \hat{A}_2 = \begin{pmatrix} a_2^* e^{j\phi_a} \\ -a_1^* e^{j\phi_a} \end{pmatrix} ; \text{ and that } \hat{B}_1, \hat{B}_2 \text{ are}$$

orthogonal with $\hat{B}_1 = \begin{pmatrix} b_1 \\ b_2 \end{pmatrix} \text{ and } \hat{B}_2 = \begin{pmatrix} b_2^* e^{j\phi_b} \\ -b_1^* e^{j\phi_b} \end{pmatrix}$. Then we can solve

for the more general Q_G , obtaining

$$Q_G = \begin{pmatrix} q_1 & q_2 \\ -q_2^* e^{j(\phi_b - \phi_a)} & q_1^* e^{j(\phi_b - \phi_a)} \end{pmatrix} \quad (96)$$

with $\det(Q_G) = e^{j(\phi_b - \phi_a)}$.

In our case, we will always deal with relative phase polarizations, so that we can use the more restricted form (Equation (95)).

8.2 THE ELEMENTARY TRANSFORMATIONS OF POLARIZATION AND STOKES VECTORS

Let $\begin{pmatrix} b_1 \\ b_2 \end{pmatrix} = Q \begin{pmatrix} a_1 \\ a_2 \end{pmatrix}$, with respective Stokes vectors

$$s_b = \begin{bmatrix} |b_1|^2 + |b_2|^2 \\ |b_1|^2 - |b_2|^2 \\ 2\text{Re}(b_1 b_2^*) \\ -2\text{Im}(b_1 b_2^*) \end{bmatrix} \quad \text{and} \quad s_a = \begin{bmatrix} |a_1|^2 + |a_2|^2 \\ |a_1|^2 - |a_2|^2 \\ 2\text{Re}(a_1 a_2^*) \\ -2\text{Im}(a_1 a_2^*) \end{bmatrix}.$$

We want to find V such that $s_b = V s_a$, in terms of q_1, q_2 of Equation (95). This can be done directly by writing out the matrix multiplication and identifying terms. The result is

$$V = \begin{bmatrix} 1 & 0 & 0 & 0 \\ 0 & |q_1|^2 - |q_2|^2 & 2\text{Re}(q_1 q_2^*) & 2\text{Im}(q_1 q_2^*) \\ 0 & -2\text{Re}(q_1 q_2) & \text{Re}(q_1^2 - q_2^2) & \text{Im}(q_1^2 + q_2^2) \\ 0 & 2\text{Im}(q_1 q_2) & -\text{Im}(q_1^2 - q_2^2) & \text{Re}(q_1^2 + q_2^2) \end{bmatrix} \quad (97)$$

We now note that rotations about the axes s_1, s_2, s_3 , respectively, (refer to Figure 2 in Section 2.1), have the matrices

$$\begin{aligned}
 V_v &= \begin{bmatrix} 1 & 0 & 0 & 0 \\ 0 & 1 & 0 & 0 \\ 0 & 0 & \cos 2v & -\sin 2v \\ 0 & 0 & \sin 2v & \cos 2v \end{bmatrix} & -\frac{\pi}{4} \leq v \leq \frac{\pi}{4} \\
 V_\tau &= \begin{bmatrix} 1 & 0 & 0 & 0 \\ 0 & \cos 2\tau & 0 & -\sin 2\tau \\ 0 & 0 & 1 & 0 \\ 0 & \sin 2\tau & 0 & \cos 2\tau \end{bmatrix} & -\frac{\pi}{4} \leq \tau \leq \frac{\pi}{4} \\
 V_\psi &= \begin{bmatrix} 1 & 0 & 0 & 0 \\ 0 & \cos 2\psi & -\sin 2\psi & 0 \\ 0 & \sin 2\psi & \cos 2\psi & 0 \\ 0 & 0 & 0 & 1 \end{bmatrix} & -\frac{\pi}{2} \leq \psi \leq \frac{\pi}{2}
 \end{aligned} \tag{98}$$

These correspond respectively (as can be seen from Equation (97) to

$$\begin{aligned}
 Q_v &= \begin{bmatrix} e^{-jv} & 0 \\ 0 & e^{jv} \end{bmatrix} \\
 Q_\tau &= \begin{bmatrix} \cos \tau & j \sin \tau \\ j \sin \tau & \cos \tau \end{bmatrix} \\
 Q_\psi &= \begin{bmatrix} \cos \psi & -\sin \psi \\ \sin \psi & \cos \psi \end{bmatrix}
 \end{aligned} \tag{99}$$

The decomposition $V = V_\psi V_\tau V_v$ corresponds to
 $Q = Q_\psi Q_\tau Q_v$.

The elementary V transformations applied successively are Euler rotations (about the transformed axes). The indicated angle restrictions ensure uniqueness, for a fixed order ψ, τ, v .

A more elegant method of relating the transformations of polarization and Stokes vectors and of relating the scattering matrix to the Mueller matrix, is by means of the Kronecker product. This may be found in [11]. It has the advantage of providing a formalism for transforming from one representation to another, from which properties can be rigorously derived.

One form of the Kronecker product of two complex vectors $a = \begin{pmatrix} a_1 \\ a_2 \end{pmatrix}$, $b = \begin{pmatrix} b_1 \\ b_2 \end{pmatrix}$ is defined as

$$a \otimes b = \begin{bmatrix} a_1 b_1 \\ a_1 b_2 \\ a_2 b_1 \\ a_2 b_2 \end{bmatrix}.$$

In particular, for $E = \begin{pmatrix} e_x \\ e_y \end{pmatrix}$;

$$E \otimes E^* = \begin{bmatrix} |e_x|^2 \\ e_x e_y^* \\ e_y e_x^* \\ |e_y|^2 \end{bmatrix} \quad (100)$$

We can then define the Stokes vector corresponding to E (in accordance with Equation (4)) as

$$s = T E \otimes E^*, \quad (101)$$

where

$$T = \begin{bmatrix} 1 & 0 & 0 & 1 \\ 1 & 0 & 0 & -1 \\ 0 & 1 & 1 & 0 \\ 0 & j & -j & 0 \end{bmatrix},$$

for a right-hand coordinate system. (For the left-hand coordinate system, which also appears in our scattering formulation, we must use $T_L = T^*$. See discussion in Appendix 8.3.

We also need the identity $(A \otimes B)(a \otimes b) = Aa \otimes Bb$, where the Kronecker product of two matrices is defined as

$$A \otimes B = \begin{pmatrix} A_{11}[B] & A_{12}[B] \\ A_{21}[B] & A_{22}[B] \end{pmatrix}.$$

Let the scattered polarization vector be given by

$$E_s = A E_t.$$

Then the scattered Stokes vector (defined in the left-hand system) is

$$\begin{aligned} s_s &= T^* E_s \otimes E_s^* \\ &= T^* (A E_t) \otimes (A E_t)^* \\ &= T^* (A \otimes A^*) (E_t \otimes E_t^*) \\ s_s &= M s_t \end{aligned}$$

where

$$s_t = T E_t \otimes E_t^*$$

and

$$M = T^* A \otimes A^* T^{-1}. \quad (102)$$

M is the Mueller matrix corresponding to A . It is readily verified that

$$T^{-1} = 1/2(T^* T).$$

For a coordinate transformation (no change of handedness)

$$b = Q a,$$

we derive similarly the corresponding Stokes vector transformation

$$s_b = V s_a, \quad (103)$$

where

$$V = T Q \otimes Q^* T^{-1}.$$

The latter equation can be worked out to give Equation (97). Equation (103) can be used to derive M_0 of Equation (20) in terms of the components of S_0 of Equation (16).

8.3 SYMMETRY RELATIONS FOR SCATTERING MATRIX AND TRANSMIT-RECEIVE CONVENTIONS

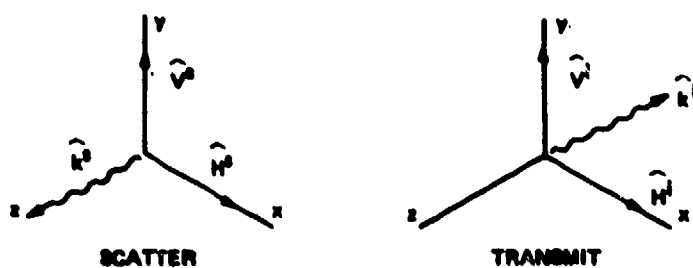
The linear scattering matrix is written

$$\begin{bmatrix} E_H^s \\ E_V^s \end{bmatrix} = \begin{bmatrix} a_{HH} & a_{HV} \\ a_{VH} & a_{VV} \end{bmatrix} \begin{bmatrix} E_H^i \\ E_V^i \end{bmatrix} \quad (104)$$

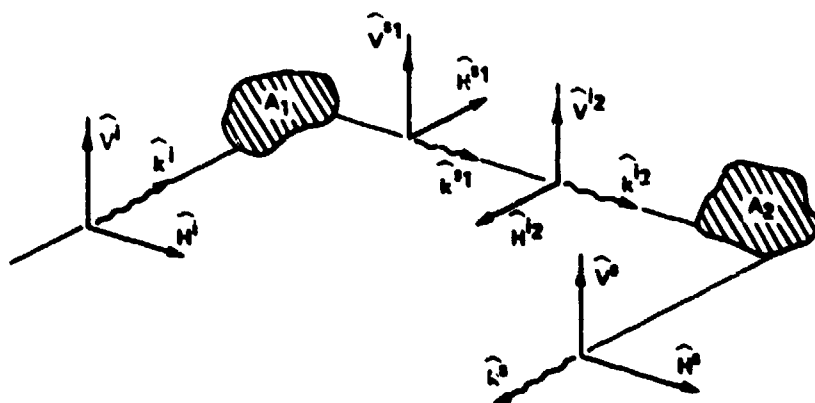
Sign conventions for the "monostatic convention" are that $\hat{V}^i = \hat{V}^s$; $\hat{H}^i = \hat{H}^s$ for receiver and transmitter at the same location. Identifying \hat{H} , \hat{V} with \hat{x} , \hat{y} and writing \hat{k} for the direction of propagation, we see (Figure 102a) that \hat{H}^i , \hat{V}^i , \hat{k}^i form a left-handed triplet if \hat{H}^s , \hat{V}^s , \hat{k}^s are chosen to be right-handed.

Since much of the theory of polarization phenomenology treats the symmetric case $a_{HV} = a_{VH}$, it is important to identify when this relation holds. This is done carefully in [5]. First consider when $a_{HV} = a_{VH} = 0$. Define a "bistatic plane" which contains \hat{k}^i and \hat{k}^s . Define the "polarization reference" planes for \hat{E}^i and \hat{E}^s independently as the plane containing \hat{k} and \hat{H} . Then $a_{HV} = a_{VH} = 0$ when

- (1) the bistatic plane is a symmetry plane of the target, and
- (2) the bistatic plane is the polarization reference plane for both \hat{E}^i and \hat{E}^s .



(a) MONOSTATIC CONVENTION: $\hat{V} = \hat{V}^0$, $\hat{H} = \hat{H}^0$, FOR $\hat{k} = -\hat{k}^0$



(b) MULTIPLE SCATTERING IN A PLANE

62-111

FIG. 102 Propagation and scattering sign conventions.

The above are shown to be true readily by reciprocity. For the monostatic case, given a plane symmetric target, it is always possible to align all the reference planes such that $a_{HV} = a_{VH} = 0$. Based on the above, one can readily see the general condition for $a_{HV} = a_{VH} \neq 0$, namely perform the spatial rotation Q_ψ defined in Section 2, which rotates both polarization reference planes by ψ . The conditions for which $a_{HV} = a_{VH}$ are

- (1) the bistatic plane is a symmetry plane of the target, and
- (2) transmitter and receive polarization reference planes are rotated by the same angle with respect to the symmetry plane.

In general it is true that $a_{HV} = a_{VH}$ if and only if there exist a polarization for which the transformed A is diagonal. This observation agrees with the results of Section 2.3. For the monostatic case, reciprocity directly results in $a_{HV} = a_{VH}$ for any target.

The above holds for linear isotropic media and targets, and breaks down when reciprocity does not hold.

Because of the reversal of the basis triplet, one has to be careful when multiplying scattering matrices in order to represent multiple scattering. The simple case of all propagation vectors in the same plane is illustrated in Figure 102b. A left-hand triplet is incident upon A_1 and scattered, by convention, as a right-hand triplet. Before applying the next scattering matrix A_2 , it is necessary to reverse the basis back to a left-hand one, using the matrix $\begin{pmatrix} 1 & 0 \\ 0 & -1 \end{pmatrix}$. The total transformation is then

$$A = A_2 \begin{pmatrix} 1 & 0 \\ 0 & -1 \end{pmatrix} A_1 \quad (105)$$

For example, for double-bounce scattering from two specular surfaces with $A_1 = A_2 = I$, we obtain $A = \begin{pmatrix} 1 & 0 \\ 0 & -1 \end{pmatrix}$.

The use of the monostatic convention introduces a confusion in the definition of s_3 in the Stokes vector (Equation (4) in Section 2.1). For the right-handed system (H, V, k) we defined $s_3 = -2\text{Im}(e_H e_V^*)$. But then in a left-handed system $(H, V, -k)$, we must take $s_3 = +2\text{Im}(e_H e_V^*)$. With this convention, transmission of LC with $t = \begin{pmatrix} 1 \\ j \end{pmatrix}$ and $s_3 = 1$ in a right-handed system results in a specularly back-scattered field given by $\begin{pmatrix} 1 \\ j \end{pmatrix}$ in a left-handed system with $s_3 = -1$ (RC). On the other hand, 45° linear polarization $t = \begin{pmatrix} 1 \\ 1 \end{pmatrix}$ with $s_2 = 1$, upon back-scattering results in $\begin{pmatrix} 1 \\ 1 \end{pmatrix}$ also with $s_2 = 1$.

8.4 DIAGONALIZATION OF SCATTERING MATRIX AND EIGENVALUES

The object is to diagonalize the scattering matrix with a unitary transformation. This will be achieved by solving the eigenvalue problem

$$Ae = \lambda e^* \quad (106)$$

First we note that if λ, e is an eigenvector, eigenvalue pair, then so are $\underline{\lambda} = \lambda e^{j2\phi}$, $\underline{e} = e e^{j\phi}$. See this by multiplying through by $e^{j\phi}$:

$$Ae e^{j\phi} = (\lambda e^{j2\phi})(e^* e^{-j\phi});$$

hence

$$A\underline{e} = \underline{\lambda} \underline{e}^*.$$

We can therefore require the eigenvalues λ_1, λ_2 to be positive real.

To solve Equation (106), premultiply by A^* :

$$He = (A^* A)e = \lambda A^* e^* = |\lambda|^2 e \quad (107)$$

For the monostatic case $A = A^T$ (some of this analysis fails when $a_{12} \neq a_{21}$); hence $(A^* A)^* = A^* A = H$ is hermetian which is known to have real eigenvalue solutions $|\lambda_1|^2, |\lambda_2|^2$ to the ordinary eigenvalue problem (107), with orthogonal eigenvectors, e_1, e_2 .

The solution is given by

$$|\lambda_1 \lambda_2|^2 = \det(H) = |\det(A)|^2 \quad (108)$$

$$|\lambda_1|^2 + |\lambda_2|^2 = \text{tr}(H) = |a_{11}|^2 + |a_{22}|^2 + |a_{12}|^2 + |a_{21}|^2. \quad (109)$$

$$= \text{norm}^2(A)$$

(The last equation does not hold if A is not symmetric.)

That is:

$$|\lambda_1|^2 = \left(\frac{\text{norm}^2(A)}{2} \right) \pm \sqrt{\left(\frac{\text{norm}^2(A)}{2} \right)^2 - |\det(A)|^2} \quad (110)$$

and the eigenvectors are

$$e_1 = \begin{pmatrix} e_{11} \\ e_{12} \end{pmatrix} = \frac{1}{E} \begin{pmatrix} \lambda_1^2 - (|a_{12}|^2 + |a_{22}|^2) \\ a_{11}^* a_{12} + a_{12}^* a_{22} \end{pmatrix} \quad (111)$$

and

$$e_2 = \begin{pmatrix} -e_{12}^* \\ e_{11}^* \end{pmatrix}, \quad (112)$$

where E is the normalizing factor.

Define $Q = \begin{pmatrix} [e_1] & [e_2] \end{pmatrix}$, and $\Lambda = \begin{pmatrix} \lambda_1 & 0 \\ 0 & \lambda_2 \end{pmatrix}$.

Then Q is unitary ($Q^{*T} = Q^{-1}$ with $|\det(Q)| = 1$). Equation (106) can then be written

$$Q^T A Q = \Lambda \quad (113)$$

The phases of λ_i are arbitrary so far. Let us choose some phase such that $\lambda_1 \lambda_2 = \det(\Lambda) = \det(A) = e^{-j\theta} |\det(A)|$. Then we must have $\det(Q) = 1$, which makes it a unitary transformation in our restricted form. Further, choose $m = |\lambda_1| \geq |\lambda_2| = s$ and take the phase factor out:

$$S_0 = \begin{pmatrix} m & 0 \\ 0 & s \end{pmatrix} = e^{j\theta} Q^T A Q. \quad (114)$$

There are several invariants under a unitary transformation that are immediately apparent from this derivation: If matrix B is related to A by a unitary transformation:

$$B = Q^T A Q,$$

then it has the same eigenvalues as A , which satisfy the same characteristic equation, namely, the relations (108) and (109). That is, the norm and determinant are invariant.

There are two degenerate cases. The first is $\det(A) = 0$. Then $m = \text{norm}(A)$ and $s = 0$. This happens when $|a_{11} a_{22}| = |a_{12}|^2$ and $(a_{12}^{*2} a_{11} a_{22})$ is real. The other case is

$$|\det(A)| = \frac{\text{norm}^2(A)}{2}.$$

In that case, $m^2 = s^2 = |\det(A)|$. This happens when $|a_{11}| = |a_{22}|$ and $a_{12} = 0$ or when $a_{11} = a_{22} = 0$. The degenerate cases are discussed in Section 2.4.

8.5 EQUAL AREA PROJECTION FOR POLARIZATION CHART

The Huynen polarization chart [4,7] is an orthogonal projection of the Poincare sphere with circular polarization at the center. Two charts: one for left-sense polarization and another for right-sense represent the entire sphere. This chart is ideal for the purpose of plotting null loci, except for the fact that with an orthogonal projection the area nearest the outer perimeter is compressed. Since in the present study we want to examine the separability of null loci, it is desirable to avoid that distortion. We therefore use a polar equal area projection, so that the separation between two loci near the outer perimeter appears visually the same as for loci near the center.

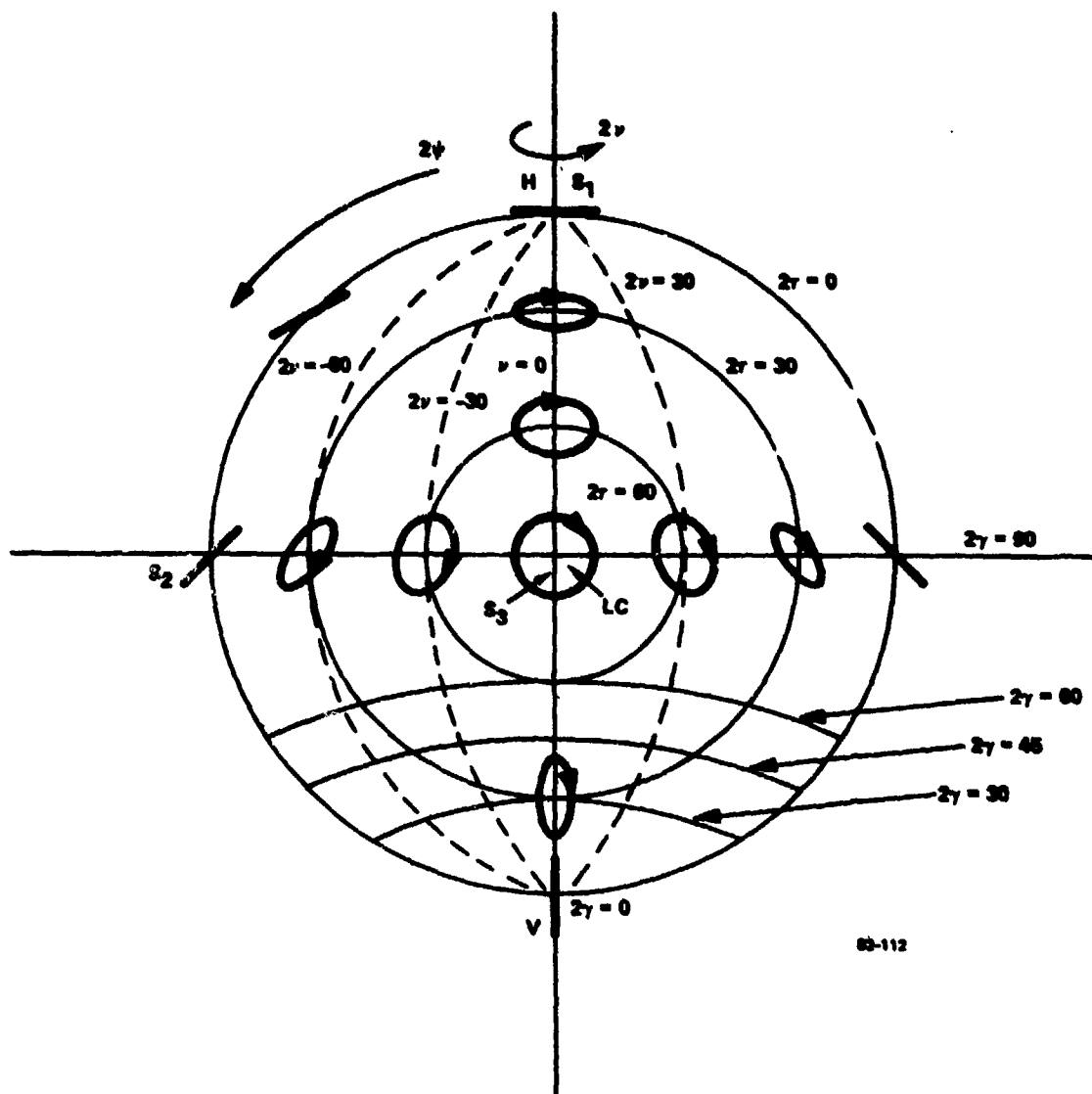
The equal area polarization chart is shown in Figure (103). At its center is the axis s_3 and LC polarization. The perimeter is linear polarization with H (axis s_1) at the top and V at the bottom. The rotation 2ψ corresponds to the polarization tilt angle ψ . The radius from the center is related to the ellipticity by

$$r = \sqrt{1 + \cos 2\tau} - \sqrt{1 - \cos 2\tau} \quad (115)$$

(By contrast, in the Huynen polarization chart, $r = \cos 2\tau$.) Except for the distortion in the radius and our usage here of placing H on top, the chart is the same as the Huynen chart.

8.6 MODELED RESPONSE OF RIGHT-CIRCULAR CYLINDER

The cylinders used in this report all have length, L , much greater than the radius, a , with the radius in the upper end of the resonance region and much higher. Approximate analytic expressions exist for this case which exhibit the proper polarization dependence. The response curves as a function aspect, a , are divided into three sections: near nose-on ($\alpha \approx 0$), near



63-112

FIG. 103 Equal area polarization chart, showing left-sense hemisphere.

broadside ($\alpha \approx 90$), and oblique. We will give the responses as coefficients G , normalized such that the RCS is

$$\sigma = \pi a^2 |G|^2. \quad (116)$$

Near nose-on, we have simply the response of a flat disc. Creeping waves can be neglected due to the great length of the cylinder. A physical optics approximation can be made, because we will use this model only in the main lobe of the return. Then

$$G = (jka) \cos \alpha \left(\frac{2J_1(x)}{x} \right) e^{j\phi} \quad (117)$$

where

$$x = 2ka \sin \alpha$$

$$\phi = (ka) \frac{L}{a} \cos \alpha.$$

(The factor j , often not written in published results, is included to give the proper 90° phase shift.) The phase, ϕ , is with respect to the cylinder center.) This expression is used over $0 \leq x \leq 3.83$, where 3.83 is the first zero of $J_1(x)$.

At oblique angles the GTD expressions are useful, as given in [9]. For the RCC, for the monostatic case, the expression for scattering from cylinder edge, k , is

$$G_k = \frac{2}{3} \sin \nu \sqrt{\frac{1}{\pi ka \sin |\alpha_k|}} \left[\frac{1}{\cos \nu - \cos(\nu + \frac{4}{3} \alpha_k)} \pm \frac{1}{\cos \nu - 1} \right] \quad (118)$$

where

$$\nu = 120^\circ,$$

the top sign is for horizontal (TM) polarization ($H \perp$ to symmetry plane).

For aspect α measured with respect to the cylinder axis, α_k in the above has the values

$$\alpha_1 = \alpha, \quad \alpha_2 = -\alpha, \quad \alpha_4 = \alpha - 180^\circ,$$

the edge in the third quadrant is shadowed and does not contribute. The total cylinder response is then

$$G = |G_1| e^{j(\phi_1 - \pi/4)} + |G_2| e^{j(\phi_2 + \pi/4)} + |G_4| e^{j(\phi_4 - \pi/4)} \quad (119)$$

where the ϕ_i are due to the edge position:

$$\phi_1 = 2ka(\sin \alpha + \frac{L}{2a} \cos \alpha),$$

$$\phi_2 = 2ka(-\sin \alpha + \frac{L}{2a} \cos \alpha),$$

$$\phi_4 = 2ka(\sin \alpha - \frac{L}{2a} \cos \alpha).$$

Note that (118) only has a $(ka)^{-1/2}$ dependence on frequency, and will fail at low frequency. Also, typically for GTD, the expressions fail near grazing angles.

Near broadside, we use an approximation derived from the exact infinite cylinder result [10]. This is a good approximation, because the length, L , is much larger than the radius, a . The expression includes polarization dependence in the specular part of the response and a polarization dependent creeping wave contribution. In the following, three terms must be retained of the series expansion, which is then applicable for $ka \geq 2$. For horizontal (TM) polarization:

$$G_H = G \frac{L/a}{\sqrt{\pi}} \left((jka)^{1/2} \left(1 + \frac{127}{128(2ka)^2} \right) + \frac{5}{16}(jka)^{-1/2} + \dots + (\text{creep})_H \right) e^{j\phi}.$$

where

$$(\text{creep})_H = -1.82(jka)^{-1/6} e^{-(5.05+j2.94)(ka)^{1/3}} e^{j\phi_{cr}},$$

$$\phi = 2 ka \sin \alpha,$$

$$\phi_{cr} = ka(2 + \pi) \left(\frac{1 - 0.25 \cos^2 \alpha}{\sin \alpha} \right), \quad (120)$$

$$F = \frac{\sin(ka \frac{L}{a} \cos \alpha)}{ka \frac{L}{a} \cos \alpha} \sqrt{\sin \alpha}.$$

The factor, F , represents the effect of looking slightly off-broadside; the creep phase, ϕ_{cr} , contains an adjustment for looking off-broadside. The creeping wave magnitude is not quite correct for $\alpha \neq 90^\circ$, but its contribution is small.

For vertical (TE) polarization:

$$G_V = F \frac{L/a}{\sqrt{\pi}} \left((jka)^{1/2} \left(1 - \frac{353}{128(2ka)^2} \right) - \frac{11}{16}(jka)^{-1/2} \dots + (\text{creep})_V \right) e^{j\phi},$$

where

$$(\text{creep})_V = 3.06(jka)^{-1/6} e^{-(2.2+j1.27)(ka)^{1/3}} e^{j\phi_{cr}}.$$

These expressions are used in the main lobe of the broadside specular, namely, $0 \leq (ka)(L/a) \cos \alpha \leq \pi$.

The broadside specular expressions go smoothly into the GTD expressions [9], but not if polarization dependence is included in the broadside return. Near nose-on the GTD expressions do not at all converge to the specular expressions. To obtain a smooth response versus aspect, the cylinder model computer program interpolates between the two expressions over a small interval about the transition point.

For reference, the responses of a $L/D = 10$ cylinder are given in Figures 104 and 105 at $ka = 5.24$ and 8.15 , respectively.

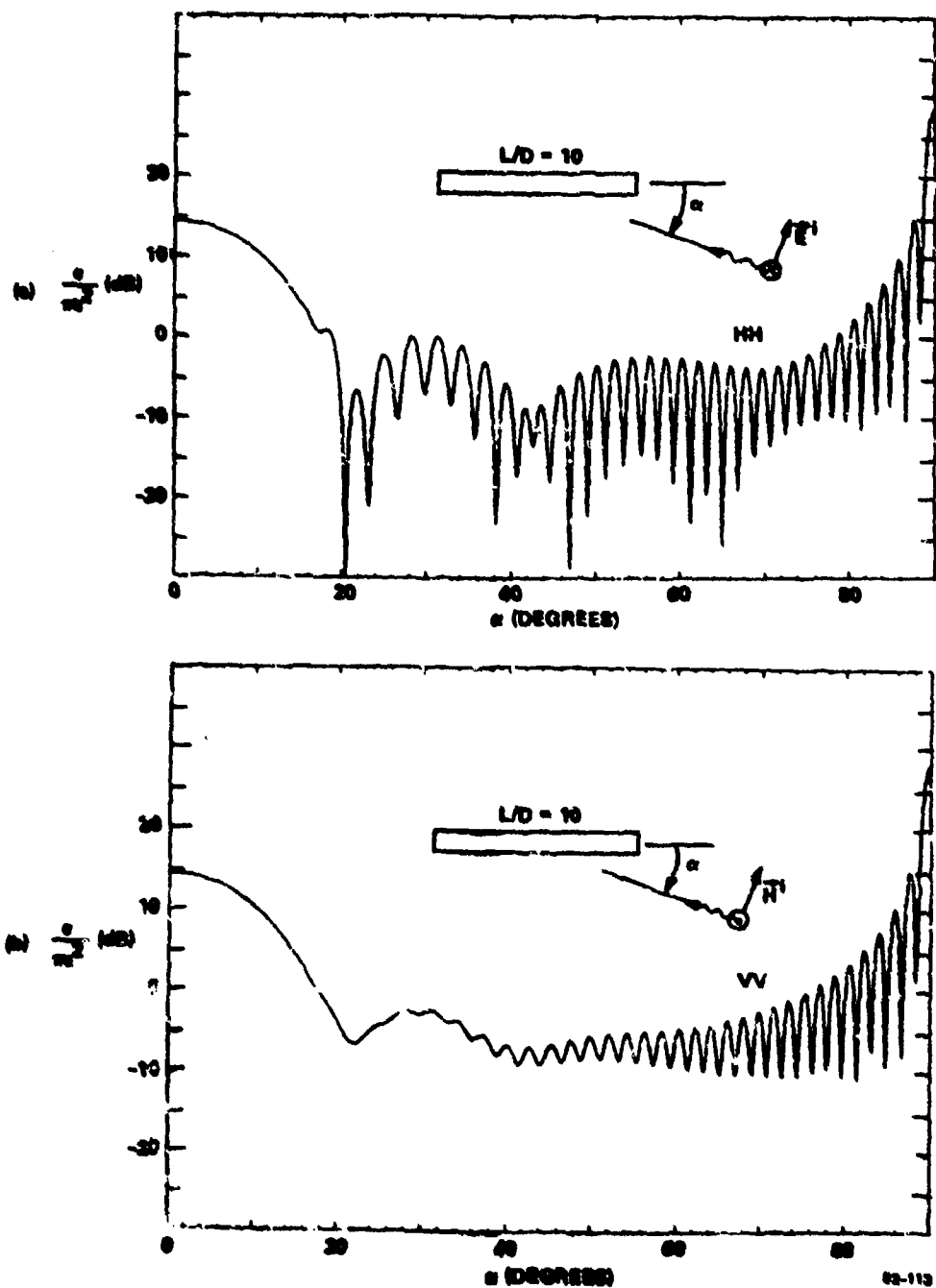


FIG. 104 Backscatter RCS of right circular cylinder, $L/D = 10$, at $ka = 5.24$; (a) HH, (b) VV.

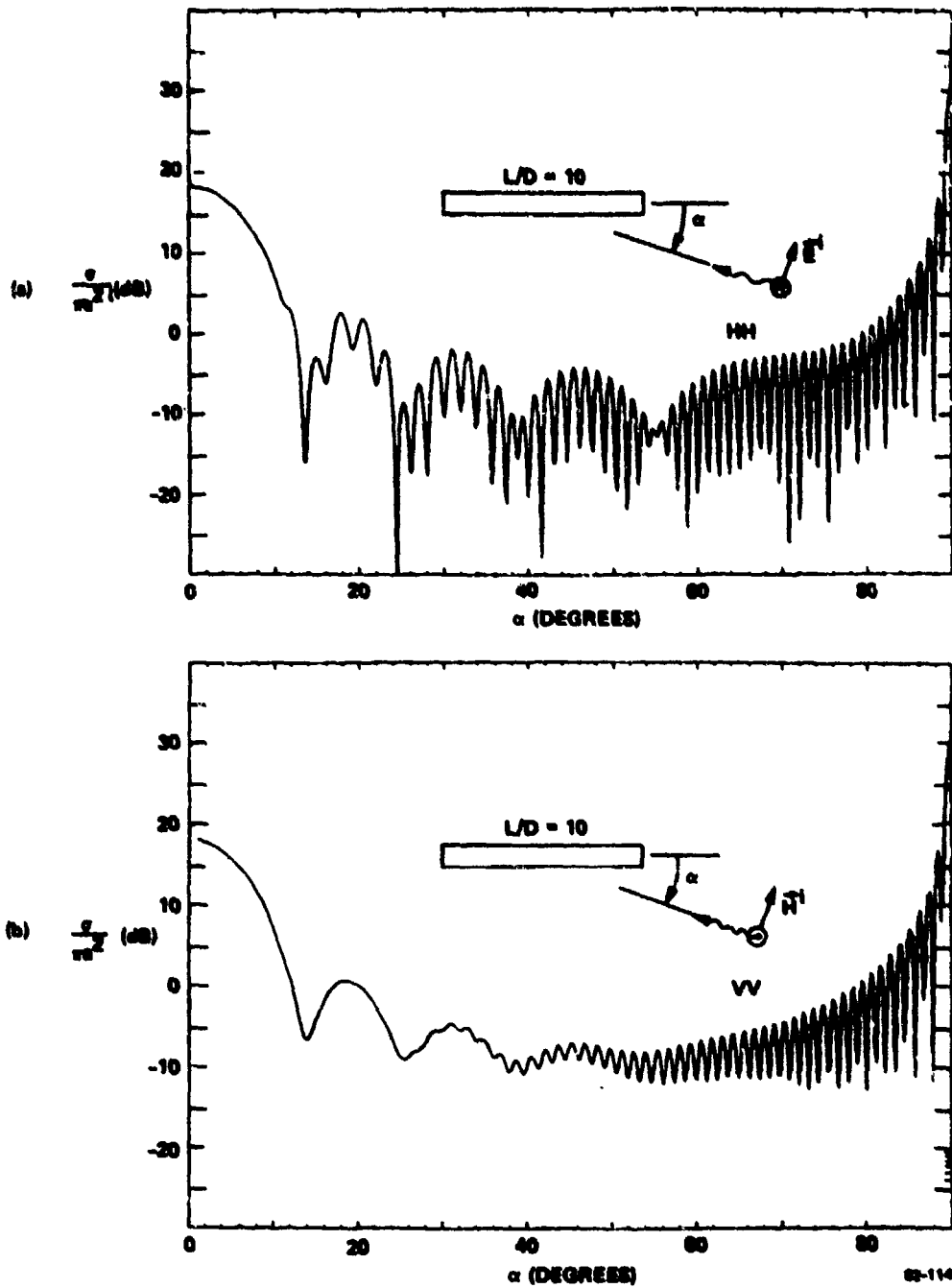


FIG. 105 Backscatter RCS of right circular cylinder, $L/D = 10$, at $ka = 8.25$; (a) HH, (b) VV.

General features of the RCC response that are pertinent to polarization null behavior are: for VV the leading edge scatterer is dominant; the other two edges are weak becoming larger in their respective specular directions. For HH the two edges at opposite ends of the cylinder have strengths on the same order of magnitude. Consequently, the HH nulls are deeper than the VV nulls, because the interference is stronger. At broadside, the polarization dependence of the specular and the creeping wave contribution are strongest for VV polarization. Consequently, the VV broadside response oscillates slightly with increasing ka , and is usually somewhat smaller than the HH response. At higher frequencies ($ka > 6$), the HH and VV responses are almost the same.

8.7 MODELED RESPONSE OF FINS

The aircraft wings were modeled as flat plates of general quadrilateral contour. There are no closed-form expressions which give the response at all aspects. Because of the large number of response calculations that are to be made, it was necessary to use simple expressions. On the other hand, it was desired that these expressions give a good approximation to the polarization dependent response to assure meaningful interpretation of the computed polarization characteristics. The expressions used were basically those of Physical Optics (PO) and the geometrical theory of diffraction (GTD), but modified in accordance with experimental results and results from exact calculations in the regions where the PO and GTD expressions fail.

In summary, GTD was used for incidence normal to an edge. This gives a response dependent on polarization and elevation with respect to the plane of the wing. For aspects in the plane of the wing, a $(\sin x)/x$ dependence was imposed (as predicted from PO interpretation of edge currents). At large elevations, the expressions for leading and trailing wing edges combine to form the simple PO expression for a flat plate. Near grazing angle, the simple GTD results fail drastically [12, 13] for the trailing edge of a plate

and are incorrect for the trailing edge even at larger elevations. The effect may be interpreted as due to the existence of traveling waves on the plate. Using Space Time Integral Equation (STIE) results [13], a simple expression was formed giving the elevation and polarization dependent correction to the GTD expressions. The expression was based on educated guesses as to functional behavior and forced to fit the data found in [12, 13].

A summary of the plate model follows, given in terms of the coefficient G , where the RCS is $\sigma = \pi |G|^2$ (refer to Figure 106). In the main lobe of the flat plate specular return (θ close to 90°)

$$G = j \frac{Ak}{\pi} \left(\frac{\sin x}{x} \right) \quad (121)$$

where

A = the area of the plate

$x = kL \cos \theta$

L = the dimension projected in the observation plane.

(This has no polarization dependence. It applies only in the main lobe, since it does not include any dependence on the plate contour.) Out of the main specular lobe, GTD expressions are used for the individual edges. For the leading edge:

$$G = \frac{D}{2\pi} \left(\frac{1}{\cos \theta} \pm 1 \right) \left(\frac{\sin x}{x} \right) e^{-j\frac{\pi}{4}}, \quad (122)$$

where the top sign is for \vec{E} in the plane of the plate,
the bottom sign for the perpendicular polarization
 D = edge length
 $x = kD \sin(\alpha - \alpha_n)$,
 $(\alpha - \alpha_n)$ is the aspect in the plane of the plate with
respect to the edge normal.

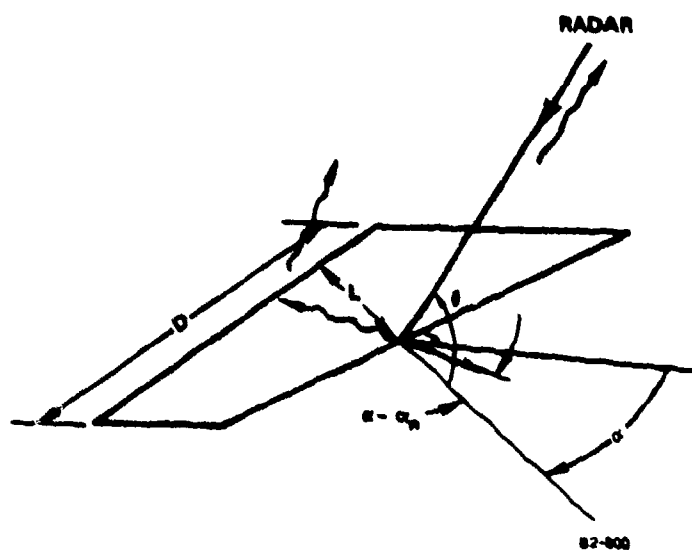


FIG. 108 Flat Wing Model, showing leading and trailing edge responses and traveling wave interaction.

This expression has been shown by exact (STIE) calculations to be very accurate for all θ . Not so accurate is the expression for the trailing edge:

$$G = \frac{D}{2\pi} \left(-\frac{1}{\cos \theta} \pm 1 \right) \left(\frac{\sin x}{x} \right) e^{-j\frac{\pi}{4}} \quad (123)$$

For $\theta = 0$ this gives a large value for perpendicular polarization, whereas actually a sharp null is observed; and gives zero for parallel polarization, whereas actually a finite response is observed. To this is added a "traveling wave contribution":

$$G = -\frac{D}{2\pi} f_{\pm} 2 \cos^2 \theta e^{-jkL(1+\cos \theta) \pm j\frac{\pi}{2}} \left(\frac{\sin x}{x} \right) \quad (124)$$

where L and \pm have the same meaning as above, the factor f is chosen as $f_{+} = e^{-kD \sin^2 \theta / 2}$ to obtain agreement with exact calculation for parallel polarization and $f_{-} = 1$ (perpendicular polarization). The above gives good agreement also with perpendicular polarization data, but still fails at $\theta = 0$, for which a null is desired. Hence the entire (sum) result for perpendicular polarization is multiplied by

$$g = (1 - e^{-kD \sin^2 \theta / 2}) \quad (125)$$

The factors f_{\pm} and g are not based on theory, but appear to result in plate responses which agree with experiment and exact computations using STIE. Figure 107 shows the computed response of a plate versus aspect at 0° and 10° elevation. The perpendicularly polarized return is zero at 0° and small at 10° .

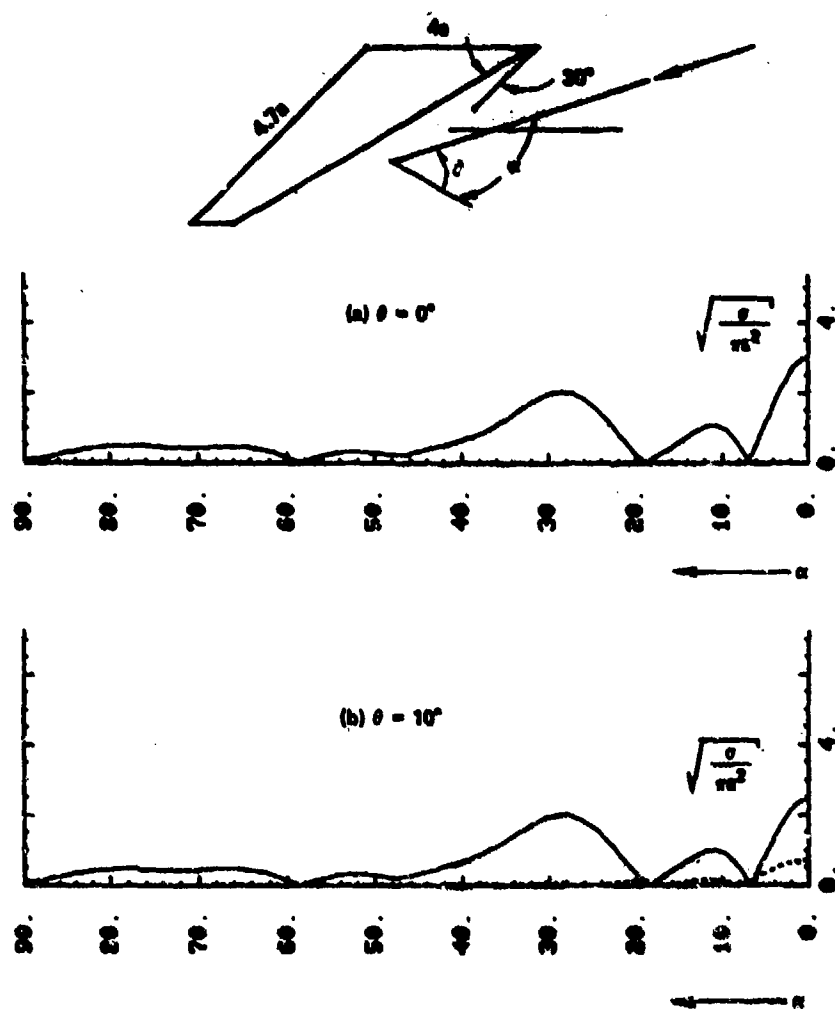


FIG. 107 Computed wing response versus aspect. At 0° and 10° elevation. (Wing for aircraft model 1 at $ka = 2.4$.)

8.8 MULTIPLE SCATTERING - AIRCRAFT MODELS

For wings attached to a cylinder, the wing is reflected in the cylinder, resulting in an even-bounce return. This may be important for polarization dependent modeling, since the signatures of even- and odd-bounce scattering are different. For small elevation angles, the following approximate expressions were used (applied only to leading wing edges):

$$\begin{aligned} D_{\text{eff}} &= 2D_m \cdot \min(\sin \alpha, \cos \alpha) , \\ D_m &= \min(D, L_c \cos \theta \tan \alpha) , \end{aligned} \tag{126}$$

where L_c is the fuselage length available for mirroring;
 D is the edge length.

Then the response is given by the specular GTD leading edge expression for an effective length, D_{eff} , and with opposite sign for perpendicular polarization. If the wing edge is slanted, the main lobe of the even-bounce return is bistatic and the response is multiplied by a $(\sin x)/x$ factor.

There are also triple bounce, partial mirroring, and shadowing effects: for the thin fuselages considered here, these effects nearly cancel. Hence the total odd-bounce return from two wings was modeled as a single-bounce return from only one wing and its full image.

There are also double-bounce returns for $\theta > 0$ due to the cylinder reflection in the plate. These were also modeled, but turned out to be small.

8.9 FRESNEL REGION RESPONSES

It was unfortunately not possible to satisfy the far field conditions for the largest of the targets. We attempt to estimate the severity of the

Fresnel region effects in this appendix. The exact transmitted field equation for a uniform source $\vec{J}_s(\vec{r}') = -\hat{x}$ over a square region $2a \times 2a$ in the x', y' plane, for transmission in direction \hat{z} is given by

$$\vec{H}(x, y, z) = \frac{1}{4\pi} \iint_{-a}^a \left(-\frac{1}{R^2} + \frac{jk}{R} \right) (\hat{x} \times \hat{R}) e^{-jkR} dx' dy' \quad (127)$$

where

$$R = |\vec{r} - \vec{r}'|$$

In the Fresnel region: $(x - x')^2 + (y - y')^2 \ll z^2$

and

$$\lambda \ll z$$

this can be written

$$\vec{H}(x, y) = \hat{y} H_{\text{far}} \left[\frac{1}{2a} \int_{-a}^a e^{\frac{-j\pi(x-x')^2}{\lambda z}} dx' \right] \left[\frac{1}{2a} \int_{-a}^a e^{\frac{-j\pi(y-y')^2}{\lambda z}} dy' \right] \quad (128)$$

where

$$H_{\text{far}} = \frac{jke^{-jkz}}{4\pi z} (2a)^2 \quad \text{is the ideal farfield.}$$

Writing one of these in standard form for $y = 0$:

$$I_{y0} = \int_{-a}^a e^{-j\pi y'^2} dy' = \sqrt{\lambda z/2} \int_{-t_0}^{t_0} e^{-j\frac{\pi}{2} t^2} dt = 2\sqrt{\lambda z/2} \left[C(t_0) - jS(t_0) \right]$$

where

$$t = y' / \sqrt{\lambda z/2}, \quad t_0 = a / \sqrt{\lambda z/2}$$

C and S are the Fresnel integrals

$$C(t_0) = \int_0^{t_0} \cos\left(\frac{\pi}{2} t^2\right) dt$$

$$S(t_0) = \int_0^{t_0} \sin\left(\frac{\pi}{2} t^2\right) dt$$

$I_{y0}/2a$ is the on-axis Fresnel-zone correction. We can then rewrite Equation (128) at a point x with $y = 0$:

$$H(x) = H_{\text{far}} \left[\frac{I_{y0}}{2a} - \frac{I_{x0}}{2a} \right] F(x) \quad , \quad (129)$$

where $I_{x0} = I_{y0}$ and

$$F(x) = \int_{-t_0(1+x/a)}^{t_0(1-x/a)} e^{-j\pi t^2/2} dt \cdot \frac{\sqrt{\lambda z/2}}{I_{x0}} \quad ,$$

using $t = (x' - x)/\sqrt{\lambda z/2}$.

$F(x)$ is the off-axis correction factor, normalized such that $F(0) = 1$. Writing this out

$$F(x) = \frac{\sqrt{\lambda z/2}}{I_{x0}} \left\{ [C(t_0(1 - \frac{x}{a})) + C(t_0(1 + \frac{x}{a}))] - j[S(t_0(1 - \frac{x}{a})) + S(t_0(1 + \frac{x}{a}))] \right\} \quad (130)$$

This factor applies to both receive and transmit patterns, for scattering from the point x . The magnitude of the two-way amplitude pattern, $|F|^2$, is plotted in Figure 108 as a function of the displacement x in cm off-axis for the antenna ($a = 15$ cm) used in these measurements, at the distance $z = 12$ m. Indicated on the plot are the maximum extents (broadside view) of the targets at sizes A, B, and C . It is seen that target size B extends significantly into the edge of the radar beam. Target C at broadside is poor.

The effect of the Fresnel pattern is principally the apparent shortening of the cross-range dimensions of the target. The result of this is to decrease the response and to increase the spacing of the lobes near broadside. The effect can be estimated and was observed for target size B . At aspects closer to nose-on, the target cross-range extent is smaller and these effects do not matter much.

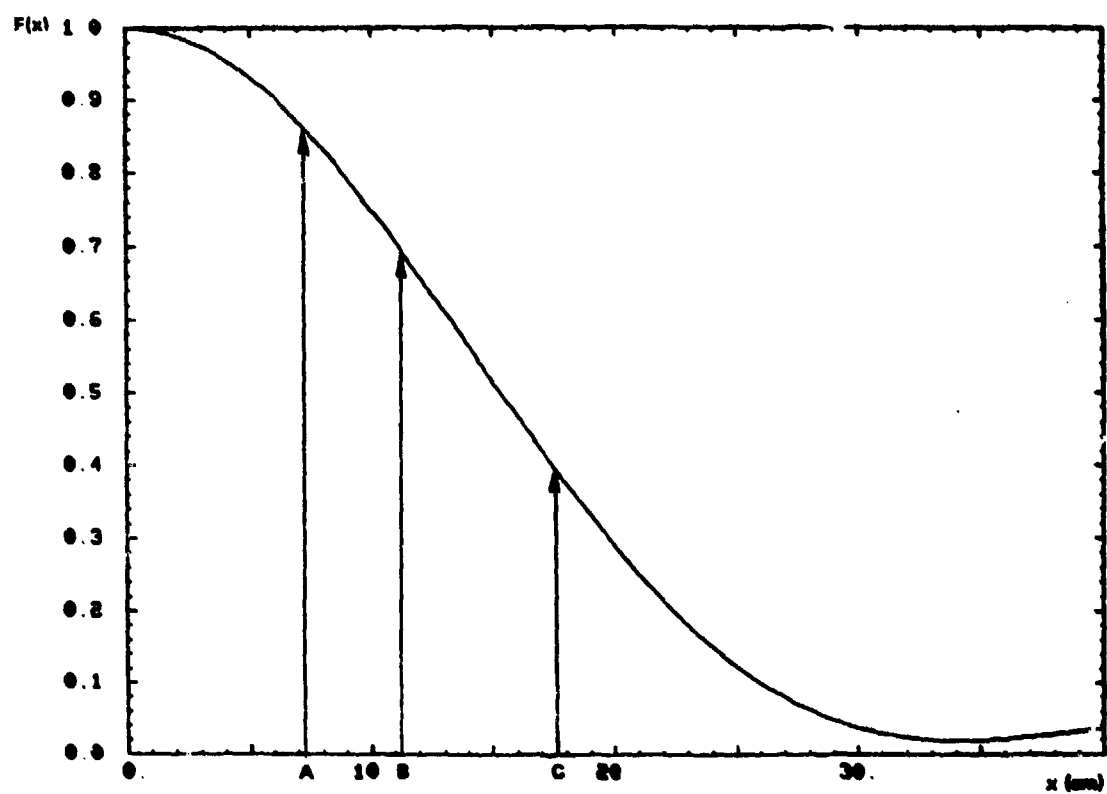


FIG. 108 Two-way Fresnel pattern factor vs. off-axis position at $Z = 12$ m.

The larger targets were measured at a range of 21 m, in an effort to reduce the Fresnel effects (the limitation was reduced SNR). The factor $|F(x)|^2$ is shown for this case in Figure 109. It is seen that target size D is still poor, and that E (signifying target model 3 at size scale D) extends hopelessly out of the beam. The measured responses of the larger targets are therefore only valid for aspects of less than about 45° .

Although some details of the measured responses are inaccurate, such as amplitude and lobe-spacing, the general nature of the polarization characteristics will still be exhibited. This justifies the use in this study of Fresnel-region conditions.

8.10 RELATION BETWEEN SYMMETRIC PSM AND SIX POWER MEASUREMENTS

For a plane-symmetric target, the relative phase polarization scattering matrix (RPSM) may be written as

$$\begin{bmatrix} |a_{11}|e^{j\Delta\psi} & 0 \\ 0 & |a_{22}| \end{bmatrix} \quad (131)$$

where $a_{11} = |a_{11}|e^{j\phi_{11}}$, $a_{22} = |a_{22}|e^{j\phi_{22}}$ are the diagonal elements of the scattering matrix and $\Delta\psi = \phi_{11} - \phi_{22}$. When the polarization of the signal incident on such a target is 135° linear, the scattered electric field is:

$$\begin{bmatrix} E_1^s \\ E_2^s \end{bmatrix} = \begin{bmatrix} |a_{11}|e^{j\Delta} & 0 \\ 0 & |a_{22}| \end{bmatrix} \begin{bmatrix} -1 \\ 1 \end{bmatrix}. \quad (132)$$

The Stokes parameters describing the polarization of this scattered field are:

$$\begin{aligned} s_0 &= |a_{11}|^2 + |a_{22}|^2 \\ s_1 &= |a_{11}|^2 - |a_{22}|^2 \\ s_2 &= -2|a_{11}||a_{22}|\cos \Delta\psi \\ s_3 &= -2|a_{11}||a_{22}|\sin \Delta\psi \end{aligned} \quad (133)$$

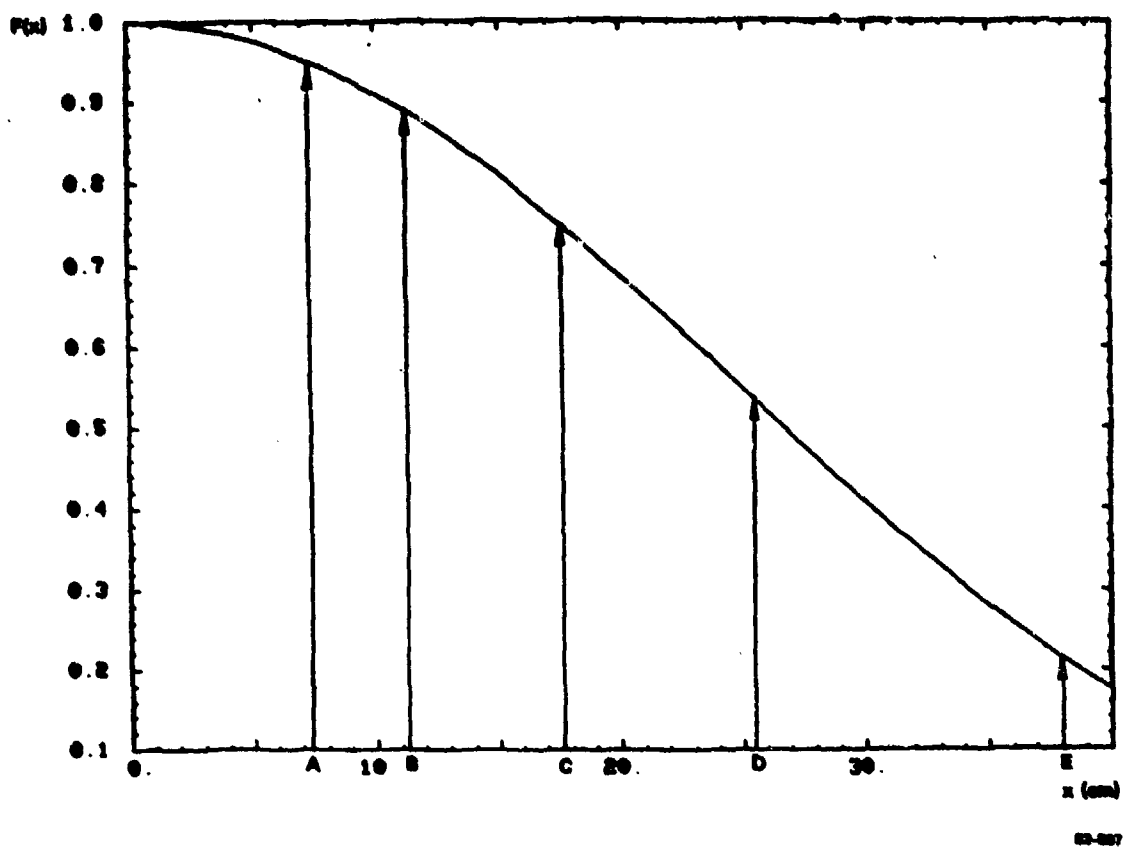


FIG. 109 Two-way Fresnel pattern factor vs. off-axis position at $Z = 21$ m.

and it is not difficult to then show that

$$\begin{aligned} |a_{11}| &= (s_0 + s_1)/2 \\ |a_{22}| &= (s_0 - s_1)/2 \\ \Delta\psi &= \tan^{-1}(s_3/s_2) \end{aligned} \quad (134)$$

It was decided to measure the power at six different receiver polarizations, V' and H' linear, 135° and 45° linear, and LH and RH circular and call these powers P_1 , P_2 , P_3 , P_4 , P_5 , and P_6 , respectively. The SP may then easily be related to these powers as follows:

$$\begin{aligned} s_0 &= \sqrt{(P_2 - P_1)^2 + (P_4 - P_3)^2 + (P_6 - P_5)^2} \\ s_1/s_0 &= (P_2 - P_1)/s_0 \\ s_2/s_0 &= (P_4 - P_3)/s_0 \\ s_3/s_0 &= (P_6 - P_5)/s_0 \end{aligned} \quad (135)$$

By combining the relationship between the elements of the RPSM and the SP and the expressions above, the elements of the RPSM may be expressed in terms of the six measured powers for each target aspect.

8.11 RELATION BETWEEN PSM AND TWELVE POWER MEASUREMENTS

The purpose of this appendix is to describe the procedure used to determine the elements of the relative phase polarization scattering matrix for an asymmetric target in the target coordinate system. Remember that the radar coordinate system is rotated +45° relative to the target coordinate system. That is, given a polarization scattering matrix (PSM) in the target coordinate system H,V

$$A_{H,V} = \begin{bmatrix} a_{11} & a_{12} \\ a_{12} & a_{22} \end{bmatrix} \quad (136)$$

the PSM in the radar coordinate system is

$$A_{H',V'} = R^T A_{H,V} R \quad (137)$$

where R is the rotation matrix

$$R = \begin{bmatrix} \cos \alpha & -\sin \alpha \\ \sin \alpha & \cos \alpha \end{bmatrix} \quad (138)$$

and where α is specified to be $+45^\circ$. Performing the matrix multiplication

$$A_{H',V'} = \frac{1}{2} \begin{bmatrix} a_{11} + 2a_{12} + a_{22} & -a_{11} + a_{22} \\ -a_{11} + a_{22} & a_{11} - 2a_{12} + a_{22} \end{bmatrix} = \begin{bmatrix} p_{11} & p_{12} \\ p_{12} & p_{22} \end{bmatrix} \quad (139)$$

where the $p_{i,j}$'s are complex and defined as above.

The procedure used to measure the elements of the relative phase scattering matrix (RPSM) $e^{-j\phi_{12}} A_{H,V}$ where $a_{ij} = |a_{ij}| e^{j\phi_{ij}}$, $i,j = 1,2$ consists of four parts or steps.

First, illuminate the target with two transmit polarizations, 135° and $+45^\circ$ linear (in the target coordinate system) and receive the power in six polarizations, V' and H' linear, 135° and $+45^\circ$ linear and LH and RH circular (in the radar coordinate system) for each transmit polarization for a total of twelve power measurements at each target aspect. Call these powers $P_{1V'}$, $P_{2V'}$, $P_{3V'}$, $P_{4V'}$, $P_{5V'}$, and $P_{6V'}$, respectively, for the 135° linear or V' transmit polarization and similarly $P_{1H'}$, $P_{2H'}$, $P_{3H'}$, $P_{4H'}$, $P_{5H'}$, and $P_{6H'}$, respectively, for the $+45^\circ$ linear or H' transmit polarization.

Second, given these twelve power measurements form two sets of Stokes parameters

$$\begin{aligned}
 s_{0x} &= \sqrt{(P_{2x} - P_{1x})^2 + (P_{4x} - P_{3x})^2 + (P_{6x} - P_{5x})^2} \\
 s_{1x}/s_{0x} &= (P_{2x} - P_{1x})/s_{0x} \\
 s_{2x}/s_{0x} &= (P_{4x} - P_{3x})/s_{0x} \\
 s_{3x}/s_{0x} &= (P_{6x} - P_{5x})/s_{0x}
 \end{aligned} \tag{140}$$

where x denotes either V' or H' . Notice that all twelve measurements are used and that the SP in each set s_{1x} , s_{2x} , and s_{3x} are guaranteed to sum square to one as they should for monochromatic radiation.

The third step is to relate these two sets of SP to the elements of $A_{H',V'}$, up to a relative phase. Assuming that $p_{12} \neq 0$, then it is possible to show that

$$\begin{aligned}
 |p_{11}| &= \sqrt{(s_{0H'} + s_{1H'})/2} \\
 |p_{22}| &= \sqrt{(s_{0V'} - s_{1V'})/2} \\
 |p_{12}| &= \sqrt{(s_{0V'} + s_{1V'})/2} = \sqrt{(s_{0H'} - s_{1H'})/2} \\
 \tan \Delta\psi_{22} &= -s_{3V'}/s_{2H'} \\
 \tan \Delta\psi_{11} &= s_{3H'}/s_{2H'}
 \end{aligned} \tag{141}$$

where $p_{ij} = |p_{ij}|e^{j\phi_{ij}}$, $i, j = 1, 2$ and $\Delta\psi_{11} = \phi_{11} - \phi_{12}$, $i = 1, 2$.

Once these p_{ij} 's, the elements of the RPSM in the radar coordinate system, have been found, then the a_{ij} 's, the elements of the RPSM in the target coordinate system, may be determined. Specifically it can be shown that

$$\begin{aligned}
A_{H,V} &= e^{j\phi_{12}} \begin{bmatrix} a_{11} e^{-j\phi_{12}} & |a_{12}| \\ |a_{12}| & a_{22} e^{-j\phi_{12}} \end{bmatrix} \\
&= \frac{e^{j\phi_{12}}}{2} \begin{bmatrix} |p_{11}| e^{j\Delta\psi_{11}} - 2|p_{12}| + |p_{22}| e^{j\Delta\psi_{22}} & |p_{11}| e^{j\Delta\psi_{11}} - |p_{22}| e^{j\Delta\psi_{22}} \\ |p_{11}| e^{j\Delta\psi_{11}} - |p_{22}| e^{j\Delta\psi_{22}} & |p_{11}| e^{j\Delta\psi_{11}} + 2|p_{12}| + |p_{22}| e^{j\Delta\psi_{22}} \end{bmatrix} \\
&= \frac{e^{j\phi_{12}}}{2} \begin{bmatrix} q_{11} & q_{12} \\ q_{12} & q_{22} \end{bmatrix} \tag{142}
\end{aligned}$$

and then that

$$\begin{aligned}
2|a_{11}| &= |q_{11}| \\
2|a_{22}| &= |q_{22}| \\
2|a_{12}| &= |q_{12}| \tag{143}
\end{aligned}$$

Letting

$$\begin{aligned}
m_{11} &= q_{11} e^{-j\angle q_{12}} \\
m_{22} &= q_{22} e^{-j\angle q_{12}} \tag{144}
\end{aligned}$$

where

$$\angle q_{12} = \tan^{-1} \left(\frac{\text{Im} \{ q_{12} \}}{\text{Re} \{ q_{12} \}} \right)$$

then

$$\begin{aligned}\Delta\phi_{11} = \phi_{11} - \phi_{12} &= \tan^{-1} \left(\frac{\text{Im}\{m_{11}\}}{\text{Re}\{m_{11}\}} \right) \\ \Delta\phi_{22} = \phi_{22} - \phi_{12} &= \tan^{-1} \left(\frac{\text{Im}\{m_{22}\}}{\text{Re}\{m_{22}\}} \right) .\end{aligned}\tag{145}$$

The two relative phases $\Delta\phi_{11}$ and $\Delta\phi_{22}$ of the diagonal elements of the scattering matrix in the target coordinate system and the three magnitudes $|a_{11}|$, $|a_{22}|$, and $|a_{12}|$ of that matrix are written in terms of the twelve powers actually measured by the radar. Using these relative phase scattering matrix elements, the polarization nulls and maxima may be determined as described in Sections 2.10 and 3.3.

HISTORICAL DEVELOPMENT OF RADAR POLARIMETRY

The history of polarimetric radar can be traced from the phenomenon of polar electromagnetic energy dating back to 1669, when the first work on the subject was published by Erasmus Bartholinus. It contained his observations that objects viewed through a crystal doubled and that an incident light ray split into ordinary and extraordinary rays (see Können, 1982).

Bartholinus was followed by Christian Huygens, who contributed most significantly to the field of optics by proposing the wave nature of light and by discovering polarized light (1677). E. Louis Mallus proved Newton's suggestion that polarization is an intrinsic property of light and not something added by a crystal (1808).

The next significant contribution to this field was added by Augustine Fresnel (1788-1827), who proposed that light could be considered as a transverse wave. His reflection formulas are still in use today and have been rederived using electromagnetic theory by Drude (twentieth century).

The last of the early pioneers was Sir David Brewster who, by extending the work of Mallus, discovered the relationship between the polarizing angle and the relative refractive power of dielectric materials (1816).

The work of all of these scientists is available in a translated form in the literature by William Swindell (1975).

The modern application of radio waves began with the postulation of electromagnetic theory by Michael Faraday in 1832, and James Clerk Maxwell's mathematical formulation of the behavior of these fields in 1873. Soon to

follow, in 1886, was Heinrich Hertz's demonstration of the application of the theory as it applies to radio waves, but the usage was mainly restricted to ship range detecting in darkness and fog throughout the first three decades of the twentieth century. A good paper on the first applications of radio waves was done by Marconi (1922).

The use of RF waves for aircraft detection and the design of the first radar was accomplished by the 1930's and further advanced during World War II (1939).

The first extensive polarimetric wave propagation analyses were carried out for the description of optical transmission devices by R. C. Jones (1941-1944) under the guidance of Professor Hans Mueller (MIT); and extensive studies on radar polarization were initiated in 1946 by G. Sinclair (1948) at the Ohio State University, ElectroScience Laboratory.

These studies were further pursued by Rumsey (1949-1951) and particularly by Kennaugh (1948-1954).

Basic papers appear in a series of papers in the Proc. IRE, May 1951, in which the paper by Deschamps (1951) is of particular use. Utilizing matrix algebra, Kennaugh introduced a new approach to radar and developed the "Optimal Target Polarization" concept for the monostatic relative phase case (Kennaugh, 1950-1954) which became of particular interest to meteorological radar studies (circular polarization clutter cancellation). There were a number of isolated other studies going on as, for example, GIT-Project A235 (July 1955) for the purpose of using polarization to distinguish between targets and clutter, which is well reviewed and summarized in Root (1980). The decade of the fifties closed without any real recognition for the need of decoy discrimination, and polarimetric radar still remained highly underdeveloped.

The ballistic missile defense program gave birth to the first real need for decoy discrimination and target classification, and in May 1960, J. R. Huynen, of Lockheed Aircraft Corporation, supported by AFCRL Hanscom Field, reported the first attempts of decoy discrimination utilizing Kennaugh's optimal target polarization concept. A very extensive amount of measurements on the relative phase scattering matrix were made, and the most important finding of Huynen is the phenomenon of aspect invariance of a radar target's characteristic (co-polarization) angle, i.e., that the spherical angle between the two co-polarization null locations on the Poincare sphere is almost aspect independent for simple targets. Unfortunately, his studies were terminated, and we refer to his excellent dissertation which summarizes the deep insight Huynen gained into radar target polarization properties. We note here that Huynen (1970, 1978) developed in his clutter decomposition theorem a very powerful tool for clutter/target analysis which requires extensive further studies. Again, we note that in the Russian literature (Kanareykhin, et al. 1965, 1968; Varshavchuk and Kobak, 1971; Zhivotovski, 1973-1978) the potential applicability to target/clutter analysis was recognized long ago. We also note here that Copeland (1960), under the guidance of Kennaugh, developed a practical scheme for "classification and possible identification of targets", based on radar polarimetric concepts for purely symmetrical, reciprocal targets.

Instead of vigorously pursuing polarimetric radar technology, it was set aside in favor of electromagnetically incomplete methods of wake analysis, Doppler studies, and the like; all concerned with the recognition of re-entry bodies. The main bulk of polarimetric studies still existing during the sixties and seventies stem from programs initiated within the Army Missile Research and Development Labs for specific missions of discriminating between airborne targets and decoys (Root, 1980). However, we must note that several important papers on the subject of polarimetric radar were published in the Russian literature, and we refer to the two excellent text books by Kanareykhin, et al., (1966, 1968), which should be published in English: immediately!

Systematic polarimetric analyses of radar backscatter from hydrometeors in isolation and/or distribution supplemented by rigorous experimental and theoretical studies were most likely first initiated by Glendon C. McCormick, Laverne E. Allan, and Archibald Hendry at NRC/Ottawa in conjunction with the radar meteorological field studies at Penhold, Alberta, of Brian L. Barge and Robert G. Humphries of the Alberta Research Council. Based upon extensive background research studies on available polarization diversity radar techniques, McCormick/Allan/Hendry systematically developed the most economical polarization radar systems applicable to hydrometeorological backscatter analysis using circular polarization base vectors [Allan and McCormick, 1978]. Particular emphasis is being placed on experimental, theoretical, as well as computer-verificational radar backscatter studies of oblate, prolate dielectric spheroids in isolation and distribution. For these specific classes of targets the relative phase backscattering matrix of a "reciprocal body of revolution ($S_{AB} = S_{BA}$)" was written in terms of a system of coordinates and selected parameters useful in describing this class of lossy dielectric spheroidal scatterers. In addition, in utilizing properties of reduced polarization phase extraction of a circular polarization base vector measurement system, most likely the simplest polarimetric radar measurement system for hydrometeorological scatter analysis was designed [Allan and McCormick, 1978, 1980; McCormick and Hendry, 1979, 1981; McCormick, 1981], which yet represents an incomplete polarimetric measurement system.

We have had many discussions with this very talented group, and we were disappointed to learn that they did not consider the optimal polarization null theory useful, although they had been aware of the studies of Kennaugh [1948-1952, and later], Huynen [1965, but not his Doctoral thesis or later publications], and Kanareykhin, et al., [1966, 1968]. McCormick flatly opposed until recently, the fact that the optimal polarization null theory is of any usefulness to radar hydrometeorological analyses. However, this personal view on his part is slowly subsiding, and he has rewritten his results in terms of the optimal polarization null concept, which clearly establishes the usefulness of the concept to radar meteorology (private

communications, 1982): In truth, our elaborate meticulously deep studies show that they "disguised" Kennaugh's optimal polarization null theory into their approach!

We also note that for hostile radar target discrimination, classification and identification in meteorological clutter, the polarimetric radar measurement system proposed and designed at NRC-EMD is not suitable; because, for man-made targets, the co-pol nulls may occur close to linear as well as circular polarization; whereas, the assumption of their measurement system squarely lies on the assumption of near circular co-pol null location on the polarization sphere.

In our opinion, it is this very fact of not recognizing the great potential of the optimal polarization null theory that device technology related to radar polarimetry is so retarded. Although the research of McCormick, et al., has found full recognition among meteorologists, it still needs to be translated into the formulation competitive with utilizing the "dynamic polarization fork concept" (Huynen, 1970; Poelman, 1980; Root, 1980; Bnerner, 1982). We emphasize that it is the specific, unique property of the optimal polarization nulls below the decorrelation threshold that will become so decisive in target-versus-clutter discrimination in the problem considered here: (i) "The electromagnetic wave propagation assessment in the ocean environment for the marine boundary layer characterization"; (ii) "The electromagnetic wave interrogation assessment in ground-based battlefield environment, where dust, smog, smoke, muzzle blast, and precipitation/hydrometeoric clutter screen the radar vision", and last but not least, (iii) "The electromagnetic wave interrogation with general-motional or stationary ground-based targets observed from an aerospace platform incorporating the naval, as well as ground-base clutter aspects". We emphasize here that polarimetric radar technology has advanced to a state-of-art that broadband polarimetric radar systems can be designed which recover complete scattering matrix information within time frames below the decorrelation (reshuffling) threshold times of the vector scattering centers of clutter/chaff.

During his dissertation studies at the Technical University Delft under Professor J. P. Schouten, Huynen strongly influenced (1970 to 1975) a young technician at SHAPE-TC and engineering student at THD, Mr. Andre J. Poleman, who then realized the dreams of Huynen by creating a complete polarimetric X-band radar (9.95 GHz) with real-time optimal polarization post-processing facility of his own. This Polarimetric Radar System of SHAPE-TC is certainly one of the most advanced measurement facilities now available for analyzing radar target acquisition, tracking, discrimination, classification and imaging problems (Poelman, 1981) in most adverse clutter conditions. Unfortunately, that system is stationary and we would require a mobile system to analyze various target shapes as well as various kinds of precipitation, land and sea clutter, and such systems need to be made available immediately within all relevant dm-to-mm wave propagation windows of interest.

In recent years, there has been a renaissance of research in radar polarimetry from both a theoretical and experimental point of view directed toward the determination of the characteristic properties of radar targets utilizing a scatterer's optimal polarization properties. It has been established experimentally (Daley, 1978-1981, Weisbrod and Morgan, 1979-1981), that the null polarizations can be used in order to discriminate targets against scattering sea clutter which is of particular importance to naval operations. This meets greatly the existing tremendous need for improved clutter rejection methods in order to detect accurately small targets, which is also of great significance to avionics, geophysical, and environmental remote sensing. It has been shown (Weisbrod, et al., 1979), in the case of sea clutter, that its non-random behavior manifests itself as a characteristic clustering of co-polarized and cross-polarized nulls as plotted on the Poincare sphere. This clustering was noticeably disturbed with the presence of a target. This phenomenon could lead to low false alarm rate discriminants with the use of theoretical models extending existing clutter statistics sensitive to the changes in the clustering of co-pol and cross-pol nulls.

Again, we emphasize that Poelman (1981) clearly verified these aspects and has without any doubt, demonstrated with his polarimetric radar at SHAPE-TC, that target versus clutter discrimination is possible under the most adverse clutter conditions as long as the target and clutter co-polarization nulls are separated on the Poincare sphere.

Other recent studies include polarization effects for millimeter wave propagation in rain done by W. S. Vogel at the University of Texas in 1975. The work of S. I. Metcalf (1977), formerly of GIT, provides a survey of research relevant to the measurement of atmospheric parameters with polarization diversity radar.

A study of volumetric effects in depolarization of electromagnetic waves scattered from a rough surface was done by Andrew J. Blanchard (1977), in which he verified the thesis that depolarization of backscatter from a finitely conducting media is predominately a multiple scatter volumetric effect. He developed a mathematical model capable of describing the volumetric effect in the depolarization of EM waves scattered from rough surfaces, collected data in the microwave and optical frequency regions, and compared model performance with depolarization results accumulated in the measurement program. Another more advanced study of the same problem was carried out by Fung and Eom (1980, 1981) and is being further extended, incorporating the optimal polarization null concept (Fung and Eom, 1982), which proved to be very successful. We note here that Blanchard and Theiss have been able to substantiate this finding in more detail (Blanchard and Theiss, 1982).

Recently, another area to which polarization has been applied is its incorporation into the equations of transfer, or to be more specific, equations of radiation hydrodynamics. The work on the subject is summarized, for example, in Ishimaru (1978), Born and Wolf (1964), Wolf (1976), Zubairy and Wolf (1977), as well as in G. C. Pomraning (1973).

As far as the analytical theory of polarization is concerned, one of the latest summaries was done by R. M. Azzan and N. M. Bashara of the University of Nebraska in 1977. This work offers a beginner in polarization studies a concrete foundation into the basic theory of polarization. We also refer to Gerard and Burch (1975) in which the transformations from the Mueller matrix to the Jones matrix representation are provided in the appendix, and in which the case of partially polarized wave interaction is treated. A succinct but good introduction for the radar case is given in R. E. Collin and F. J. Zucker, Antenna Theory, McGraw Hill Co., 1969, providing a discussion on how the Stokes parameters are useful to polarimetric antenna design.

Ellipsometric measurements for laser light scattering from metallic and dielectric rough surfaces of identical surface profiles were carried out and reported by Gough and Boerner (1978), showing that the difference in measured values for the various Mueller matrix elements as function of incidence angle are primarily dependent on the volumetric scatter from the underburden rather than due to surface roughness. We note that Blanchard et al. (1981), and Fung and Eom (1982), came to the same conclusions.

Dr. W-M. Boerner and his research associates of the Communications Laboratory at UIC (January 1981), investigated the basic theory for polarization utilization in radar target reconstruction, which is presented and verified by computer computation. The study clearly demonstrated that the optimal polarization concept is very useful in radar target analysis.

This work was followed by a second report (Boerner, et al., September 1981), in which the objectives of the analysis carried out are directed toward extracting useful target classification algorithms utilizing experimental and amplitude-plus-phase matrix data measured by Weisbrod and Morgan of Teledyne-Micronetics and comparing those with amplitude-only data obtained in the late fifties by Huynen of Lockheed (1960). For this purpose, the rudimentary properties required with its transformation invariants, and the optimal polarization descriptors, are summarized in the previous report (Boerner, et al., June 15, 1981).

The measurements by Weisbrod and Morgan of Teledyne-Micronetics were carried out for 18 buoy targets located above a sea-bed surface. Two specific, rather different buoy shapes are used, where six of the targets are "4-corner" dihedral reflectors with a yaw angle of 90° , and the rest of the targets are horizontal open pipe sections with varying sizes and displacement height above sea-bed level. We note here that Huynen in his May 1960 report presented most excellent data on 24 different isolated missile decoy shapes measured at 9.735 GHz.

The scattering matrix data of Weisbrod and Morgan were measured at only one frequency of 3.150 GHz as functions of the aspect angle and presented to us in printed and/or tape format. Their results and own analyses are summarized in (Morgan and Weisbrod, "RCS Matrix Studies of Sea Clutter", Final Report, March 1982), which are reproduced here with their consent: (1) In general, RCS matrix response of a target mounted over water will be significantly different from those of free space. This effect is attributed to illumination taper caused by interference between the direct and the reflected components. (2) Of various targets which were put together, only the dihedral was readily identifiable under most conditions. Other targets, which were primarily cylinders mounted on a vertical buoy, were identifiable part of the time, but the buoy support structure tended to dominate and mask inner signatures of other targets. (3) Single parameter results as $|\sigma_{LL}| |\sigma_{RR}| - |\sigma_{LR}|^2$ turned out quite effective in separating a dihedral from any other simple target. A flat plate type of target could also be successfully separated from other targets using a single parameter classifier. Utilizing single parameter classifiers and sifting, it was found to be possible to classify targets as dihedrals, flat plates, or neither with about 70 to 80 percent probability of being correct. (4) When used alone, the single frequency RCS matrix is primarily useful in classifying objects whose scattering centers are separated by a small fraction of a wavelength. Larger, more complex objects should, however, be classifiable using multifrequency RCS matrix data. This can be done by breaking the complex target into simpler elements through transformation to the time domain and identifying the components. Alternatively, the signature in the frequency domain could be matched to a library of reference signatures with the different elements of the RCS matrix being used to multiply the dimensions.

In our NAV-AIR effort (Boerner, et al., September 15, 1981), we developed computer-assisted programs to determine the optimal polarization characteristics, and we compared the measured RCS with that obtained from approximate scattering formulae developed for these shapes. All of our results are compared with those obtained by J. Richard Huynen in the late fifties and as reported in his May 1960 report, and with results reported in previous reports by Morgan and Weisbrod (1960, 1981, 1982). Our specific novel contributions to the interpretations of the results of Weisbrod and Morgan (1982) are contained in the M.Sc. thesis;

B-Y. Foo, "A High Frequency Inverse Scattering Model to Recover the Spectral Point Curvature from Polarimetric Scatter Data", CL-EMID-82-02, M.Sc. thesis, College of Graduate Studies, UICC, May 1982.

In another very thoughtful and excellent M.Sc. thesis,

C-Y. Chan, "Studies on the Power Scattering Matrix of Radar Targets, CL-EMID-81-02, M.Sc. thesis, College of Graduate Studies, UICC, May 1982.

various complete polarimetric measurement techniques as compared to the incomplete techniques proposed in Huynen (1960, 1970, 1978), McCormick/Allan/Hendry (1975-1981), Root (1980) are identified. These initial studies require immediate advancement.

TARGET VECTOR SCATTERING CENTER ANALYSIS

Scalar Case

The scalar scattering center discrimination technique was derived from geometrical optics considerations to a large extent at the Cornell Aeronautical Laboratories (CAL: Kell, 1965; Bechtel and Ross, 1966; Hammer, 1967), and it draws heavily from the monostatic-bistatic equivalence theorem derived by Kell (1965) and extended to the general bistatic case in (Bickel, 1965). Starting from the Stratton-Chu vector diffraction integral (Stratton, 1941), Kell (1965) derives the "bistatic scattering integral"

$$\sigma = \frac{\pi}{\lambda^2} \left| \int T(z) \exp[j2k_0 z \cos(\theta/2)] dz \right|^2$$

where $T(z)$, not precisely known, is a composite expression of surface geometry,

of illuminating and observing ray geometry, and of surface/creeping wave propagation effects. A cylindrical coordinate system (ρ, θ, z) was assumed to relate monostatic and bistatic properties such that its z -axis is coincident with the bisector of the bistatic angle β formed by the transmitter, target centroid, and receiver. It is found that the above integral can be subdivided into a sum of integrals, each of which is taken over the range of z within which its integrand is continuous and contributions only come at end points of each subregion integral which define the scattering centers. The contribution of each scattering center to the total bistatic integral corresponds to the neighborhood of the scattering center over which the phase of the net phase of the integrand in the above equation remains within $\pi/2$ of its value at the scattering center and which applies to both monostatic and bistatic scattering. Phase changes are indicated by the factor $k_0 \cos(\beta/2)$, and it follows that small bistatic angles (less than 10°) have little effect on wavelength, whereas, at larger bistatic angles the reradiation characteristics of the scattering centers are most important.

Evaluation of the above equation over the various separated scattering centers or "cophased areas" yields the total RCS

$$\sigma = \left| \sum_{m=1}^M \sqrt{\sigma_m} \exp j\phi_m \right|^2$$

with

$$\sigma_m = 2k_0 z_m \cos \beta/2 + \epsilon_m$$

where σ_m , ϕ_m , z_m , and ϵ_m denote the RCS, individual phase, distance to first phase center, and residual phase contribution of the m^{th} center including creeping wave path-length phase corrections, where $\sqrt{\sigma_m}$, z_m , and ϵ_m are insensitive to the bistatic angle β over the range of β considered, for those centers which are significant in σ . It then follows that the bistatic cross-section of aspect angle α and bistatic angle β is equal to the monostatic RCS measured on the bisector at a frequency lower by a factor $\cos \beta/2$.

Using a narrowband reconstruction approach, it was shown mainly by CAL (Hammer, 1967) how the scattering centers can be determined and allocated from lack-scattered data. Using principles of synthetic aperture radar (Harger, 1970), it is shown in (Graf, 1972) and in (Gniss, Magura, 1976) how Doppler phase information can be used to identify scattering centers of rotating bodies. It should be noted that narrowband reconstruction requires considerably increased efforts in data processing as compared to wideband short-pulse techniques in which case the complexity can be built into the radar itself (Ross, 1978), though both narrowband (MITRE, CAL, RRE-UK-Malvern, RCA-Moorestown, NYU) and wideband (Westinghouse-Baltimore, SURC/Rome AFB, MIT-Lincoln Labs/Kwajalein, and Pattern Recogn. Inc./Rome) systems are required simultaneously in efficient pattern recognition schemes (Goggins, 1978; Ksienski, et al., 1973; Repjar, 1970). It should be noted that narrowband interferometric methods (Tomljanovich, et al., 1968) have been developed also in other fields such as aperture synthesis (Harger, 1970), speckle interferometry (Dainty, 1975) and in synthetic interferometer radar (Porcello and Allan, 1974).

VECTOR CASE: HUYNEN'S N-TARGET DECOMPOSITION THEORY

Of particular relevance to this electromagnetic target scattering problem is the interaction of polarization/depolarization sensitive scattering centers on a single closed target of irregular shape, which was first attacked rigorously by Huynen (1960) in his dissertation. In this masterpiece, he developed his little understood "N-target decomposition theorem", utilizing canonical properties of Kennaugh's optimal target polarization null theory, which specifically applies to clutter analysis and multiple vector scattering center interaction of single targets. This theory is of paramount importance to further advancement in radar polarimetry. Although it still requires extensive extension, it clearly paves the way to a single unique method of complete polarimetric description of an extended target in clutter, an immensely complicated electromagnetic inverse problem.

VECTOR TARGET SCATTERING CENTER MODEL ANALYSES

In collaboration with Morgan and Weisbrod (Teledyne-Micronetics), in our studies of polarimetric CW radar target characteristics, we are following the direction of examining a set of simple canonical target shapes such as the sphere, the linear wire target, the n-bounce corner reflector, the left/right winding helices, the cone-tip/ogival and/or spherical capped cylinders with and without fins, bumps, protrusions, etc. These are treated in (Boerner, et al., January 15/September 15, 1981). Second, in consultation with Mieras and Bennett, Sperry Research Center, (see present RADC contract report), a CW vector dumbell scattering center (matrix) interaction was chosen. Both methods have proven to provide useful results and can be used for interpretation of the motion of the Huynen polarization fork as a function of frequency, relative aspect angle (with respect to the line joining the vector scattering centers) and the electric separation of component scattering centers.

DYNAMICS OF POLARIZATION FORK

Specifically, for the dumbell target, we observe that for linear (H, V) polarization base pair anchoring, the cross-polarization nulls move only whenever the principal target symmetry axis is rotated about the line of sight orthogonal to (H, V); and that the co-polarization null locations move on quasi-circular spiral non-closing paths as functions of differential change in aspect angle: for small differences in component scattering center strengths, the circles remain within isolated patches, whereas for large differences, the nulls move on large circles encircling the total polarization sphere. Furthermore, the electric separation of the scattering centers dictates the relative differential speed with which these loci are traversed (slow versus rapid) as functions of differential aspect angle. We also note that for a large ensemble of closely packed vector scattering centers, the loci of the co-polarization nulls remain within rather small isolated patches on the polarization sphere which is indicative of clutter-type. Furthermore,

the specific quasi-circular paths drawn are indicative of clutter motion. We note that the analytical result was verified experimentally by Poelman (1980-82) as explained in detail in (Boerner, STAS 1914, September 30, 1981), and this specific phenomenon of the dynamic fork motion of time frames of below the vector scattering center reshuffling time requires further extensive analytical and experimental studies. In general, the cross-polarization null location for linear symmetric targets is of slow precession type, and the rapid quasi-circular path motion of the co-polarization null location is nutative gyroscopic in nature. We note that this specific dynamic polarization fork behavior is well described by Huynen's "single target" decomposition into five target characteristic parameters $(p_m, \gamma, \nu, \tau_m, \psi)$.

However, the electromagnetic inverse problem of decomposing a single radar target into its characteristic polarimetric target vector scattering centers is very complicated and still not resolved. In a joint research effort with ESL-OSU, EML-UIU, SRC, BAC, we at the EMID-CL-UIC are planning to attack this problem in the near future.

REFERENCES

- L. E. Allan, G. C. McCormick, "Measurements of the Backscatter Matrix of Dielectric Bodies", IEEE Trans. Antennas and Propagation, Vol. AP-22, March 1980.
- L. E. Allan, G. C. McCormick, "Measurements of the Backscatter Matrix of Dielectric Spheroids", IEEE Trans. Antennas and Prop., Vol. AP-26, No. 4, July 1978.
- B. L. Barge, R. G. Humphries, "Identification of Rain and Hail with Polarization and Dual-Wavelength Radar", 19th Conf. on Radar Meteor., Miami, FL, 1982.
- M. E. Bechtel, R. A. Ross, "Radar Scattering Analysis", CAL Rept. FR IRIS-10, August 1966.
- S. H. Bickel, "Some Invariant Properties of the Polarization Scattering Matrix", Proc. IEEE, Vol. 53, pp. 1070-1072, August 1965.
- A. J. Blanchard and S. W. Theiss, "Measurement Error Considerations in Polarization and Phase Retrieval", IGARSS '82 (IEEE Geoscience and Remote Sensing Society), Vol. 2, Sec. FA-7, p. 4, Munich, FRG-West Germany, 1982.
- A. J. Blanchard, "Volumetric Effects in the Depolarization of Electromagnetic Waves Scattered from Rough Surfaces", NASA Grant NAL 44-001-001, May 1977, Texas A and M University, RSC, College Station, Tech. Rept. RSC-83.
- A. J. Blanchard, B. R. Jean, "Antenna Effects in Depolarization Measurements", Texas A and M University, Remote Sensing Center, College Station, TX 77843, May 11, 1981.
- W-M. Boerner, M. B. El-Arini, S. Saatchi, M. Davidovitz, J. Nespor, "Polarization Utilization in Radar Target Reconstruction: Buoy Targets", Final Report, UICC, EL-EMID, NNRAR, 81-03, (NAV-AIR Contract N00019-80-C-0620, September 15, 1981).
- W-M. Boerner, C. M. Ho, "Analysis of Physical Optics Far Field Inverse Scattering for the Limited Data Case Using Radon Theory and Polarization Information", WAVE MOTION, pp. 311-333, North Holland Publ. Co., 1981.
- W-M. Boerner, C. M. Ho, B. Y. Foo, "Use of Radon's Projection Theory in Electromagnetic Inverse Scattering", IEEE Trans. AP-29(2), pp. 336-341, March 1981.
- W-M. Boerner, "Inverse Modeling in Remote Sensing", XXth General Assembly, URSI, Washington, DC, August 12, 1981 (invited).
- W-M. Boerner, "Use of Polarization in Active and Passive Precipitation Radar Measurements", Workshop in Precipitation Measurement from Space NASA, Goddard Space Flight Center, Greenbelt, MD, April 28-May 1, 1981.

REFERENCES (Cont'd.)

- W-M. Boerner, "Polarization Sensitivity of Near-to-Ground Clutter at mm- and Near-mm Wavelengths", Battelle Delivery No. STAS 1904, Contract No. DAAG 29-76-D-0100, USA-MICOM-DRSMI-REL, September 30, 1981.
- W-M. Boerner, M. B. El-Arini, C-Y Chan, P. Mastoris, "Polarization Dependence in Electromagnetic Inverse Problems", IEEE Trans. Antennas and Prop., AP-29(2), pp. 262-274, 1981.
- W-M. Boerner, M. B. El-Arini, C-Y Chan, S. Saatchi, W. S. Ip, M. Mastoris, B. Y. Foo, "Polarization Utilization in Radar Target Reconstruction", Tech. (Interim) Report, UICC, CL-EMID-NANRAR-81-01, Communications Lab, Information Eng. Dept., SEC-1104, UICC, Chicago, IL, January 1981.
- W-M. Boerner, M. B. El-Arini, "Optimal Polarization Concept in Electromagnetic Inverse Problems", 1981 Intern. Geo-Science and Remote Sensing Symp. (IGARSS, 81), Washington, DC, June 8-10, 1981.
- W-M. Boerner, "Imaging Radar Polarimetry (invited base-lecture), Workshop on Fundamental Research in Active Microwave Remote Sensing, Jet Propulsion Laboratory, Bldg. 264, Room 461-B, February 1-2, 1982, Pasadena, CA.
- V.V. Bogorodsky, D.B. Kanareykin, A.I. Kozlov, "The Polarization of Scattered and Self Radioemission of the Earth's Covers", Leningrad, Hydrometeoizdat, 1981.
- M. Born, E. Wolf, "Principles of Optics, 3rd Ed.", Pergamon, London, NY, 1965.
- C-Y. Chan, "Studies on the Power Scattering Matrix of Radar Targets", M.Sc. Thesis, May 1981, Inf. Eng. Dept., UICC, Chicago, IL, Dept. No. CL-EMID-81-02 — A Tutorial Exposition on the Power Scattering Matrix.
- J. R. Copeland, "Radar Target Classification by Polarization Properties", Proc. IRE, Vol. 48, pp. 1290-1296, July 1960.
- J. C. Dainty, "Laser Speckle and Related Phenomena", Topics in Applied Phys. 9, Springer, NY, 1975.
- J. C. Daley, "Radar Target Discrimination Based on Polarization Effects", NRL Rept., Washington DC, March 1978.
- J. C. Daley, "Radar Target Discrimination", NAVAIR REVIEW, January 1979.
- G. A. Deschamps, "Part II-Geometrical Representation of the Polarization of a Plane Electromagnetic Wave", Proc. IRE, Vol. 39, pp. 540-544, May 1951.
- A. K. Fung, H. J. Eom, "Multiple Scattering and Depolarization by a Randomly Rough KIRCHHOFF Surface", IEEE Trans. AP-29, pp. 463-471, May 1981.
- A. K. Fung, H. J. Eom, "A Theory of Wave Scattering from Air Inhomogeneous Layer with an Irregular Interface", IEEE Trans. AP-29, pp. 899-910, November 1981.

REFERENCES (Cont'd.)

- A. K. Fung, H. J. Eom, "Effects of a Rough Boundary Surface on Polarization of the Scattered Field From an Inhomogeneous Medium", Proc. IGARSS, June 1-4, 1982, Munich, IRD.
- A. Gerard and J. M. Burch, "Introduction to Matrix Methods in Optics", John Wiley and Sons, Ltd., London, 1975.
- H. Gniss and K. Magura, "mm-Wave of Ground Based Objects", Rept. 1-78-153 (FHP-FGAN), Wachtbert-Werthoven, FRG-West Germany, January 1978.
- W. B. Goggings, Jr., "Identification of Radar Targets by Pattern Recognition", Ph.D. Thesis USAF Institute of Technology, Air University, Dayton OH, June 1973.
- P. T. Gough, W-M. Boerner, "Depolarization of Scatter as an Aid to Identical Rough Metallic Surface", J. Opt. Soc. Am., 69(9), pp. 1212-1217, November 1979.
- G. Graf, "Analyse des Dopplerfrequenzspektrums rotierender Korper", DFVLR 46, 1972, DK535.338.34, Oberpfaffenhofen, FRG.
- J. A. Hammer, "A Method to Determine the Scattering Centers From the Back Scatterer Pattern of a Body", Proc. GISAT II Symposium, Vol. 2, Part I, pp. 223-235, MITRE Corp., Bedford, MA, 1967 (available as AD839-700 from Nat'l Tech. Inf. Serv., Springfield, VA).
- R. O. Harger, "Synthetic Aperture Radar Systems: The Dry and Design", NY, Academic, 1970.
- J. R. Huynen, "Study on Ballistic-Missile Sorting Based on Radar Cross Section Data", Scientific Rept. No. 4; Radar Target Sorting Based on Polarization Signature Analysis, Lockheed Aircraft Corp., Missiles and Space Division, Rept. LMSD-288216, Contract No. AF 19(604)5550, May 1960 (AD318597).
- J. R. Huynen, "Radar Backscatter from Distributed Targets with Emphasis on Polarization Dependence", Lockheed Missiles and Space Co., Sunnyvale, CA, Rept. L-86067-2, May 1967.
- J. R. Huynen, "Measurement of the Target Scattering Matrix", Proc. IEEE 53(8), pp. 936-946, 1965.
- J. R. Huynen, "Phenomenological Theory of Radar Targets", Ph.D. Dissertation, Drukkerij Bronder-Offset, N.V. Rotterdam, 1970.
- J. R. Huynen, "Radar Measurements on Scattering Operators", Proc. 6th Symp. on Ballistic Missile and Aerospace Technology, Vol. II, Academic Press, NY, 1961.

REFERENCES (Cont'd.)

A. Ishimaru, "Wave Propagation and Scattering in Random Media", Vol. I: "Single Scattering and Transport Theory", Vol. II: "Multiple Scattering Turbulence, Rough Surfaces and Remote Sensing", Acad. Press, NY, 1973.

A. Ishimaru, "Diffusion of a Pulse in Densely Distributed Scatterers", J. Opt. Soc. Am., Vol. 68, No. 8, August 1978.

R. C. Jones, "New Calculus for the Treatment of Optical Systems. III. The Sohncke Theory of Optical Activity," J. Opt. Soc. Am. 31, 500(1941).

R. C. Jones, "New Calculus for the Treatment of Optical Systems. IV." Opt. Soc. Am. 32, 486 (1942).

R. C. Jones, "New Calculus for the Treatment of Optical Systems I. Description and Discussion of the Calculus", J. Opt. Soc. Am. 31, 488 (1941).

D. B. Kanareykin, N. F. Pavlov, and V. A. Potekhin, "The Polarization of Radar Signals", Sovyetskaye Radio, Moscow 1966 (in Russian): (English translation of Chapters 10-12: Radar Polarization Effects, CCM Inf. Corp., G. Collier and McMillan, 900 Third Avenue, NY, NY 10023).

D. B. Kanareykin, V. A. Potekhin and M. F. Shisikin, "Maritime Polarimetry", Sudostroyenie, Leningrad, 1968.

R. E. Kell, "On the Derivation of Bistatic RCS from Monostatic Measurements", Proc. IEEE 53, pp. 983-988, 1965.

E. M. Kennaugh, "Effects of Type of Polarization on Echo Characteristics Monostatic Case, Reports 389-1 (Sept. 16, 1949) and 389-4 (June 16, 1950), Ohio State University, Antenna Laboratory, Columbus, OH 43212.

E. M. Kennaugh, "Effects of Type of Polarization on Echo Characteristics", Reports 389-1 to 389-24, Ohio State University, Antenna Laboratory, Columbus, OH 43212, 1949-1954.

E. M. Kennaugh, "Polarization Properties of Radar Reflections", Antenna Lab., Ohio State University Research Foundation, Columbus, OH, ZRADC Contract F28(099)-90, Project Report 389-12 (AD2494), March 1, 1952.

E. M. Kennaugh, "Polarization Properties of Radar Reflections", M.Sc. thesis, Dept. of Electrical Engineering, Ohio State University, Columbus, OH 43212, 1952.

G. P. Konnen, "Gepolariseerde Licht in de Natuur", B.V.W.J. Thieme Cie.-Zutphen 1982.

REFERENCES (Cont'd.)

- A. A. Ksienski, "Radar Target Identification and Imaging", The Radar Signatures Workshop, Patrick Air Force Base, FL, July 24, 1975.
- E. Marconi, "Radio Telegraphy", Proc. IRE, Vol. 10, page 237, 1922.
- G. C. McCormick, A. Hendry, "Radar Measurement of Precipitation-Related Depolarization in Thunderstorms", IEEE Trans. on Geoscience Electronics, Vol. GE-17, No. 4, pp. 142-150, 1979.
- G. C. McCormick, "Polarization Errors in a Two-Channel System", Radio Science, Vol. 16, No. 1, pp. 67-75, 1981.
- G. C. McCormick, A. Hendry, L. E. Allan, "Depolarization Over a Link Due to Rain: Measurements of the Parameters", Radio Science, Vol. 11, No. 8,9, pp. 741-749, August-September 1976.
- J. I. Metcalf, "Polarization-Diversity Radar and Lidar Technology in Meteorological Research: A Review of Theory and Measurements", Eng. Exper. Georgia Inst. of Tech., Atlanta, Georgia 30332, July 31, 1977.
- H. Mieras, et al., "Polarization Null Characteristics of Simple Targets", Final Report on Contract No. F30602-81-C-0254, Sperry Research Center, Sudbury, MA, September 1982.
- L. A. Morgan and S. Weisbrod, "RCS Matrix Analyses of Sea Clutter and Targets", Teledyne-Micronetics, San Diego, CA. Final Report, Naval Air Systems Command, Contract No. N00019-C-80-0595, December 1981.
- L. A. Morgan and S. Weisbrod, "RCS Matrix Studies of Sea Clutter", Teledyne-Micronetics, Final Report, San Diego, CA, March 1982.
- L. A. Morgan, S. Weisbrod, "RCS Matrix Studies of Sea Clutter", GACIAC PR-81-02, pp. 103-119.
- A. J. Poelman, "Features of Multipurpose Experimental X-Band Radar Facility", Informationen anlässlich eines Besuchs am SHAPE Technical Centre, Den Haag, Holland, 1981.
- G. C. Pomraning, "Radiation Dynamics", Pergamon Press Ltd., Headington Hill Hall, Oxford, 1973.
- A. G. Repjar, A. A. Ksienski and L. J. White, "Object Identification from Multifrequency Radar Returns", Radio and Electronic Engineer, 45, pp. 161-167, April 1975.
- L. W. Root, Chairman, Workshop on: "Polarimetric Radar Technology", 25-26 June 1982, USA-MICOM-DRSMI-REG, Redstone Arsenal. Proc. GACIAC, Vol. 1, 11TR1, 10 W. 35th St., Chicago, IL 60616, GACIAC PR-81-02, February 1981.

REFERENCES (Cont'd.)

V. H. Rumsey, "Part I - Transmission Between Elliptically Polarized Antennas", Proc. IRE, Vol. 39, pp. 535-540, May 1951.

G. Sinclair, "Modification of the Radar Equation for Arbitrary Targets and Arbitrary Polarization", Rept. No. 302-19, Antenna Laboratory, Ohio State University, Columbus, OH, 1948.

N. M. Tomljanovich, M. S. Ostrowsky, J. F. A. Urmsby, "Narrowband Interferometer Imaging", MITRE Corp., Prop. 4966, November 1968, AD 679-208.

M. L. Varshanchuk and V. O. Kobay, "Cross-Correlation of Orthogonally Polarized Components of the Electromagnetic Field Scattered by an Extended Object", Radio Eng. and Electr. Phys. 16, pp. 201-205, 1971.

A. Weisbrod and L. A. Morgan, "RCS Matrix Studies of the Sea Clutter", NAVAIR Review, January 1979.

E. Wolf, E. Collett and J. T. Foley, "On Tatarskii's Investigations into the Foundations of the Theory of Radiative Energy Transfer", J. Opt. Soc., Vol. 66, p. 1065, 1976.

L. A. Zhivotovskiy, "Calculation of the Depolarization Properties of Radar Targets", Radio Eng. 31 (Part 2), pp. 46-48, 1976.

L. A. Zhivotovskiy, "Dependence of the Power Flux Density of Echo Signals on Radar Signal Polarization", Radio Eng. 31 (Part 2), pp. 49-53, 1976.

L. A. Zhivotovskiy, "Optimum Polarization of Radar Signals", Radio Eng. and Electronic Phys. 18(4), pp. 630-632, 1973.

M. S. Zubairy and E. Wolf, "Exact Equations for Radiative Transfer of Energy and Momentum in Free Electromagnetic Fields", Opt. Comm., Vol. 20, pp. 321-324, March 1977.

MISSION of Rome Air Development Center

RADC plans and executes research, development, test and directed acquisition programs in support of Command, Control, Communications and Intelligence (C³I) activities. Technical and engineering support within areas of technical competence is provided to ESD Program Offices (POs) and other ESD elements. The principal technical mission areas are: communications, electromagnetic guidance and control, surveillance of ground and aerospace objects, intelligence data collection and handling, information systems, weapons, propulsion, solid state sciences, microwave physics and electronic reliability, maintainability and supportability.